

# Atomic doping & coating for Electrocatalysis & Li-ion batteries

Présentée le 18 février 2022

Faculté des sciences de base  
Laboratoire de synthèse et de catalyse inorganique  
Programme doctoral en chimie et génie chimique

pour l'obtention du grade de Docteur ès Sciences

par

**Albert Claude Jean-Pierre DAUBRY**

Acceptée sur proposition du jury

Prof. K. Sivula, président du jury  
Prof. X. Hu, directeur de thèse  
Prof. L. Liu, rapporteur  
Prof. D. Tilley, rapporteur  
Prof. R. Buonsanti, rapporteuse

"If you want to find secrets of the universe, think in terms of energy, frequency and vibration"

**-Nikola Tesla**

**-Никола Тесла**



# Acknowledgements

First, I would like to thank Professor Xile Hu, director of the Laboratory of Inorganic Synthesis and Catalysis (LSCI), for giving me the opportunity to pursue my doctoral thesis within his research group. During the last four years, I have been grateful for the projects he has offered to me, for his guidance and his help. Thank you for giving me the possibility to express my creativity without limitations; I will always value your opinion and direction regarding my scientific work.

I also want to thank the jury members for reviewing and grading the work accomplished during my thesis, namely Prof. Raffaella Buonsanti, Prof. David Tilley, Prof. Lifeng Liu as members, and Prof. Kevin Sivula as president.

I owe Professor Dr. Yajun Cheng and his group special thanks for their help, and gratitude for their significant contributions regarding the lithium-ion battery performance tests. Our collaboration was fruitful mainly due to their generous help.

I thank Dr. Pierre Mettraux for all the XPS measurements and for always being so helpful and kind. I am also grateful to Dr. Victor Boureau for the High-Resolution and Aberration-Corrected TEM measurements. To Christina Zamanos Epremian, thank you for all your help with administrative work since the beginning of my Ph.D. To Anne-Lene Odegaard and to Karine Brahimi, thank you for your time and assistance throughout the years.

I want to take the time to thank all present and past co-workers with whom I had the chance to spend time and collaborate with during the past four years. Meeting people from all around the world has definitely helped me grow as a better person. I would like to thank all the LSCI

lab members for the nice moments, the discussions about science and life and the international dinners; Weiyan, Renyi, Zhikun, Miyeon, Xiangli, Runze, Pengzuo, Wenhao, Lei, Deyun, Srikrishna, Seunghwa and Lara. Special thanks to Laurent for helping me with my research, my career objectives and for collaborating with me.

My acknowledgements to Thomas Di Franco, who took the time to mentor me during my master project within LSCI lab. To this day, I am grateful for everything you have taught me.

I am really fortunate to have shared my time with Céline Prange, the lab-mom, and Xingyu Wu, my lab-roommate, for their friendliness and support during the majority of my time spent in this group.

I also want to take the time to thank all my Swiss friends that supported me throughout this journey, namely André Douverny Roque Dos Santos, Daniel Chernis and Thomas Baumeler. To my flatmate Christophe Gaillet for your hospitality and joy. To my friend Victor Stokowski, for changing my mind-set. To my dearest friend Gabriel Day Boulougne, for your warm heart and brilliant intellect, thank you.

I could not thank my family more, without whom I would not be where I am today. Firstly to my mother and my father, Emmanuelle and Philippe, without whom I would not be here at all. Thank you for supporting and believing in me and giving me the chance to study at EPFL. Secondly to my brothers, Gustave and Eugène, who I look up to and who give me the strength to keep on going every day. To my grandparents who have always believed in me and helped me move forward, while reminding me where I am from. To the rest of my family, thank you.

I finally want to express my kindness and my love to Laureen; you help me become a better version of myself each and every day.

Albert Claude Jean-Pierre Daubry

Lausanne, August 2021

# Abstract

In order to face the urgency of energetic and climate challenges, the "Hydrogen economy" based on renewable sources is necessary. To implement such an economy, bottlenecks such as electrochemical water splitting, and electrosynthesis of ammonia need to be tackled. The development of new non-precious atomically dispersed electrocatalysts is desirable, as an efficient, sustainable and scalable solution. For such an economy, mostly based on intermittent solar energy production, an energetic grid is necessary. Such a grid relies on the implementation of energy storage systems in order to account for the local on-demand distribution of energy. The development of lithium-ion batteries is considered one way to ensure sufficient capacity storage for domestic and mobility demand.

In Chapter 2, molybdenum atomic-doping on bio-waste derived nitrogen-doped conductive carbon electrocatalyst was synthesized and investigated for the dinitrogen reduction to ammonia in alkaline media. The assessment of the catalytic activity was found to be non-trivial as nearly any external source can be the cause of ammonia contamination. In a closed-cell set-up using isotopically labelled  $^{15}\text{N}_2$  as feed gas for 48h chronoamperometry at  $-0.1\text{ V}$  vs RHE that the current density was correlated to the availability of the gas. Non-precious metals were incorporated in an oxidized carbon black conductive matrix and investigated for their activity towards oxygen evolution reaction in  $0.1\text{ M H}_2\text{SO}_4$ ,  $0.5\text{ M H}_2\text{SO}_4$  and  $0.1\text{ M HClO}_4$ . The stability of the deposited catalyst was insufficient and their deterioration was attributed to the oxidation of the carbon support as well as the dissolution of the metal ions upon high anodic potentials.

In chapter 3, the same metal-incorporated oxidized conductive carbon black agents were investigated for the enhancement of the performance of Si/C anodes in lithium-ion batteries. It was found that cobalt incorporation in the oxidized matrix displayed a significant influence in the electrochemical kinetics and consequent rate performances. With 0.8% cobalt ions by mass incorporated in oxidized KetJen Black the average capacity of the Si/C anode was increased by 180% at 1.5 A.g-1. This metal incorporation approach was extended to other ionic species (copper, iron and nickel) and other carbon conductive agents (SuperP). The electrolyte affinity, the desolvation process and the improved electronic conductivity synergistically improved the rate performance without compromising the gravimetric capacity of the electrode.

In Chapter 4, the deposition of ultra-thin aluminium oxide by atomic layer deposition on the surface of  $\text{LiNi}_{0.5}\text{Co}_{0.2}\text{Mn}_{0.3}\text{O}_2$  cathode material in lithium-ion batteries for the improvement of cyclic performances at high voltages (4.3-4.6 V) was investigated. One source of the failure mechanisms of the battery comes from unwanted side reactions between surface species and the electrolyte. The aluminium oxide layers of 1.42 nm and 2,36 nm were found to be beneficial at current densities exceeding 1.0 C (1 C = 170 mAh.g-1), and especially at 5.0 C with an increase of about 20 mAh.g-1 and 35 mAh.g-1 compared to uncoated NCM523, respectively. The capacity retention was found to be improved for all coated samples compared to pristine upon 140 cycles at 1.0 C. Mitigating side reactions and increasing the specific capacity at higher C-rates by atomically controlled layered deposition of inexpensive metal oxides is desirable for the implementation next-generation of safer and stable fast-charging high-voltage lithium-ion batteries.

**Keywords:** atomic doping, electrochemical dinitrogen reduction, acidic oxygen evolution reaction, lithium-ion battery, atomic layer deposition.

# Résumé

Pour faire face à l'urgence des défis énergétiques et climatiques, "l'économie de l'hydrogène" basée sur des sources renouvelables de production est nécessaire. Pour mettre en œuvre une telle économie, les obstacles tels que la séparation électrochimique de l'eau et l'électrosynthèse de l'ammoniac doivent être résolus. Le développement de nouveaux électro-catalyseurs non précieux dispersés atomiquement est souhaitable, en tant que solution efficace, durable à grande échelle. Pour une telle économie, principalement basée sur la production solaire d'énergie, un réseau de distribution énergétique est nécessaire. Un tel réseau repose sur la mise en œuvre de systèmes de stockage d'énergie afin de prendre en compte une distribution locale et à la demande. Le développement des batteries au lithium est considéré comme un moyen d'assurer une capacité de stockage suffisante pour la demande domestique et pour la mobilité des personnes.

Dans le chapitre 2, le dopage atomique de molybdène sur du carbone conducteur dopé à l'azote -dérivé de biodéchets- a été synthétisé et étudié comme électrocatalyseur pour la réduction du diazote en ammoniac dans un milieu alcalin. L'évaluation de l'activité catalytique s'est avérée complexe car de nombreuses sources externes peuvent être à l'origine de contaminations à l'ammoniac. Dans une configuration de cellule étanche utilisant l'isotope  $^{15}\text{N}_2$  comme gaz d'alimentation pour une expérience chronoampérométrique de 48 h à -0,1 V vs RHE, la densité de courant mesurée était corrélée à la disponibilité du gaz, suggérant une possible activité. Des métaux non-précieux ont été incorporés dans une matrice conductrice de carbone oxydée et, ces échantillons ont été étudiés pour leur activité vis-à-vis de la réaction de production d'oxygène dans 0,1 M  $\text{H}_2\text{SO}_4$ , 0,5 M  $\text{H}_2\text{SO}_4$  et 0,1 M  $\text{HClO}_4$ . La

stabilité des catalyseurs déposés était insuffisante et leurs détériorations a été attribuée à l'oxydation du support ainsi qu'à la dissolution des ions métalliques dans l'électrolyte lors de l'application de potentiels anodiques élevés.

Dans le chapitre 3, les mêmes métaux incorporés dans le carbone conducteur ont été étudiés pour améliorer les performances des anodes Si/C dans les batteries au lithium. Il a été constaté que l'incorporation de cobalt dans la matrice oxydée présentait une influence significative sur la cinétique électrochimique et les performances de vitesse de réaction qui en résultent. Avec 0,8 % par masse d'ions cobalt incorporés dans le KetJen Black oxydé, la capacité moyenne de l'anode Si/C a été augmentée de 180 % à  $1,5 \text{ A.g}^{-1}$ . Cette approche d'incorporation de métal a été étendue à d'autres espèces ioniques (cuivre, fer et nickel) et à d'autres agents conducteurs de carbone (SuperP). L'affinité de l'électrolyte, le processus de désolvatation et la conductivité électronique ont amélioré de manière synergique les performances de débit sans compromettre la capacité gravimétrique de l'électrode.

Dans le chapitre 4, le dépôt d'une couche ultra fine d'oxyde d'aluminium par ALD sur la surface du matériau cathodique  $\text{LiNi}_{0.5}\text{Co}_{0.2}\text{Mn}_{0.3}\text{O}_2$  (NCM523) pour l'amélioration des performances cycliques à haute tension (4,3-4,6 V) des batteries au lithium a été enquêté. Une des sources de défaillance de la batterie provient de réactions secondaires indésirables entre les espèces en surface et l'électrolyte. La couche protectrice d'oxyde d'aluminium de 1,42 nm et 2,36 nm s'est avérée bénéfique à des densités de courant dépassant 1,0 C (1 C =  $170 \text{ mAh.g}^{-1}$ ), et surtout à 5,0 C avec une augmentation d'environ  $20 \text{ mAh.g}^{-1}$  et  $35 \text{ mAh.g}^{-1}$  par rapport au NCM523 non revêtu, respectivement. Sur 140 cycles à 1,0 C, la rétention de capacité s'est avérée améliorée pour tous les échantillons revêtus. L'atténuation des réactions secondaires et l'augmentation de la capacité spécifique à des densités de courants plus élevés



grâce à un dépôt peu coûteux et de précision atomique d'oxydes métalliques est souhaitable pour la mise en œuvre d'une nouvelle génération de batteries au lithium à haute tension qui se recharge rapidement tout en étant sûres et stables

**Mot-clé :** dopage atomique, réduction électrochimique du diazote, réaction de l'évolution d'oxygène en milieu acide, batterie lithium-ion, dépôt atomique en couches minces.

# Riassunto

Per far fronte all'urgenza delle sfide energetiche e climatiche è necessaria "l'economia dell'idrogeno" basata su fonti rinnovabili. Tra i principali ostacoli che si incontrano nell'implementare tale economia, sono la scissione elettrochimica dell'acqua e l'elettrosintesi dell'ammoniaca. Lo sviluppo di nuovi elettrocatalizzatori non preziosi a dispersione atomica è auspicabile, come soluzione efficiente, sostenibile e potenzialmente espandibile ad una produzione industriale. Per una tale economia, basata principalmente sulla produzione intermittente di energia solare, è necessaria una rete energetica. Tale rete si basa sull'implementazione di sistemi di accumulo di energia per tenere conto della distribuzione locale di energia su richiesta. Lo sviluppo delle batterie al litio è considerato un modo per garantire una capacità energetica sufficiente alla domanda domestica e di mobilità.

Nel capitolo 2, un elettro catalizzatore è stato sintetizzato a base di carbonio conduttivo, e drogato con molibdeno e azoto derivato da rifiuti organici. La riduzione in mezzi alcalini dell'azoto in ammoniaca è stata studiata per differenti quantità di molibdeno. La valutazione dell'attività catalitica è risultata piuttosto complicata poiché numerose fonti esterne possono causare la contaminazione di ammoniaca. In un impianto a celle chiuse utilizzando  $^{15}\text{N}_2$  etichettato con isotopi come gas di alimentazione per la cronoamperometria di 48 ore a  $-0,1\text{ V}$  rispetto a RHE, la densità di corrente era correlata alla disponibilità del gas. I metalli non preziosi sono stati incorporati in una matrice conduttiva di nerofumo ossidato e studiati per la loro attività verso la reazione di evoluzione dell'ossigeno in  $0,1\text{ M H}_2\text{SO}_4$ ,  $0,5\text{ M H}_2\text{SO}_4$  e  $0,1\text{ M HClO}_4$ . La stabilità del catalizzatore depositato era insufficiente e il loro deterioramento è

stato attribuito all'ossidazione del supporto carbonioso nonché alla dissoluzione degli ioni metallici su alti potenziali anodici.

Nel capitolo 3, lo stesso nerofumo conduttivo ossidato incorporato in metallo è stato studiato per il miglioramento delle prestazioni degli anodi Si/C nelle batterie agli ioni di litio. È stato scoperto che l'incorporazione di cobalto nella matrice ossidata mostrava un'influenza significativa nella cinetica elettrochimica e nelle prestazioni di velocità conseguenti. Con lo 0,8% di ioni di cobalto in massa incorporati nel KetJen Black ossidato, la capacità media dell'anodo Si/C è stata aumentata del 180% a 1,5 A.g<sup>-1</sup>. Questo approccio all'incorporazione dei metalli è stato esteso ad altre specie ioniche (rame, ferro e nichel) e ad altri agenti conduttori di carbonio (SuperP). L'affinità elettrolitica, il processo di solvatazione e la superiore conducibilità elettronica hanno migliorato sinergicamente le prestazioni di velocità senza compromettere la capacità gravimetrica dell'elettrodo.

Nel capitolo 4, la prestazione ciclica ad alte tensioni (4,3-4,6 V) è stata indagata nelle batterie al litio modificate attraverso la deposizione atomica stratificata di ossido di alluminio ultra sottile sulla superficie del materiale catodico LiNi<sub>0.5</sub>Co<sub>0.2</sub>Mn<sub>0.3</sub>O<sub>2</sub>. Lo strato di ossido di alluminio di 1,42 nm e 2,36 nm è risultato vantaggioso alle densità di corrente superiore a 1,0 C (1 C = 170 mAh.g<sup>-1</sup>), con un aumento di circa 20 mAh.g<sup>-1</sup> (e un aumento di 35 mAh.g<sup>-1</sup> a 5,0 C), con rispetto a NCM523 non rivestito. È stato riscontrato che la ritenzione della capacità è migliorata per tutti i campioni rivestiti rispetto a quelli incontaminati su 140 cicli a 1,0 C. Per l'implementazione futura di batteri a basi di litio, con buone prestazioni ad alta tensione, ricarica rapida, stabilità e oscurità, è auspicabile attenuare le reazioni collaterali e aumentare la capacità specifica a tassi di C più elevati, tramite la deposizione atomica stratificata e controllata degli ossidi metallici poco costosi.

**Parole chiave:** drogaggio atomico, riduzione elettrochimica del diazoto, reazione di evoluzione acida dell'ossigeno, batteria agli ioni di litio, deposizione atomica stratificata.

# Zusammenfassung

Um der Dringlichkeit der energetischen und klimatischen Herausforderungen zu begegnen, ist die „Wasserstoffwirtschaft“ auf Basis erneuerbarer Energien notwendig. Um eine solche Wirtschaftlichkeit umzusetzen, müssen Engpässe wie die elektrochemische Wasserspaltung und die Elektrosynthese von Ammoniak angegangen werden. Die Entwicklung neuer unedler atomar dispergierter Elektrokatalysatoren ist als effiziente, nachhaltige und skalierbare Lösung wünschenswert. Für eine solche Wirtschaft, die meist auf intermittierender Solarenergieerzeugung basiert, ist ein Energienetz notwendig. Ein solches Netz ist auf die Implementierung von Energiespeichersystemen angewiesen, um die lokale bedarfsgesteuerte Energieverteilung zu berücksichtigen. Die Entwicklung von Lithium-Batterien gilt als ein Weg, um eine ausreichende Kapazitätsspeicherung für den Haushalts- und Mobilitätsbedarf sicherzustellen.

In Kapitel 2 wurde die Molybdän-Atom Dotierung an einem aus Bioabfällen gewonnenen Stickstoff-dotierten leitfähigen Kohlenstoff-Elektrokatalysator synthetisiert und auf die Distickstoffreduktion zu Ammoniak in alkalischen Medien untersucht. Die Bewertung der katalytischen Aktivität erwies sich als nicht trivial, da nahezu jede externe Quelle die Ursache für eine Ammoniak Kontamination sein kann. In einem geschlossenen Zellaufbau unter Verwendung von isotopen markiertem  $^{15}\text{N}_2$  als Speisegas für die 48h-Chronoamperometrie bei -0,1 V vs. RHE wurde festgestellt, dass die Stromdichte mit der Verfügbarkeit des Gases korreliert. Nichtedelmetalle wurden in eine oxidierte leitfähige Ruß Matrix eingebaut und auf ihre Aktivität bezüglich der Sauerstoffentwicklung Reaktion in 0,1 M  $\text{H}_2\text{SO}_4$ , 0,5 M  $\text{H}_2\text{SO}_4$

und 0,1 M  $\text{HClO}_4$  untersucht. Die Stabilität des abgeschiedenen Katalysators war unzureichend und ihre Verschlechterung wurde der Oxidation des Kohlenstoffs Trägers sowie der Auflösung der Metallionen bei hohen anodischen Potentialen zugeschrieben.

In Kapitel 3 wurde derselbe oxidierte leitfähige Ruß mit eingebautem Metall zur Verbesserung der Leistung von Si/C-Anoden in Lithium-Ionen-Batterien untersucht. Es wurde festgestellt, dass der Einbau von Kobalt in die oxidierte Matrix einen signifikanten Einfluss auf die elektrochemische Kinetik und die daraus resultierenden Geschwindigkeitsleistungen aufwies. Mit 0,8 Masse-% Kobalt-Ionen in oxidiertem KetJen Black wurde die durchschnittliche Kapazität der Si/C-Anode um 180 % bei 1,5 A.g<sup>-1</sup> erhöht. Dieser Metalleinbau-Ansatz wurde auf andere ionische Spezies (Kupfer, Eisen und Nickel) und andere kohlenstoff leitende Stoffe (SuperP) ausgedehnt. Die Elektrolyt Affinität, der Desolvatisierung Prozess und die verbesserte elektrische Leitfähigkeit verbesserten synergistisch die Geschwindigkeit Leistung, ohne die gravimetrische Kapazität der Elektrode zu beeinträchtigen.

In Kapitel 4 wurde die Abscheidung von ultradünnen Aluminiumoxid durch atomare Schichtabscheidung auf der Oberfläche von  $\text{LiNi}_0.5\text{Co}_0.2\text{Mn}_0.3\text{O}_2$ -Kathodenmaterial in Lithium-Ionen-Batterien zur Verbesserung der Zyklen Leistung bei hohen Spannungen (4,3–4,6 V) beschrieben untersucht. Eine Quelle für die Ausfallmechanismen der Batterie sind unerwünschte Nebenreaktionen zwischen Oberflächen Spezies und dem Elektrolyten. Die Aluminiumoxidschicht von 1,42 nm und 2,36 nm erwies sich bei Stromdichten über 1,0 C (1 C = 170 mAh.g<sup>-1</sup>) als vorteilhaft, und insbesondere bei 5.0 C mit einer Zunahme von etwa 20 mAh.g<sup>-1</sup> bzw. 35 mAh.g<sup>-1</sup> im Vergleich zu unbeschichtetem NCM523. Es wurde festgestellt, dass die Kapazitätsvorhaltung bei allen beschichteten Proben im Vergleich zu

reinen nach 140 Zyklen bei 1.0 C verbessert wurde. Die Abschwächung von Nebenreaktionen und die Erhöhung der spezifischen Kapazität bei höheren C-Raten durch atomar kontrollierte Schichtabscheidung kostengünstiger Metalloxide ist für die nächste Implementierung wünschenswert -Generierung sicherer und stabiler schnell ladender Hochvolt-Lithium-Ionen-Batterien .

**Schlüsselbegriffe:** atomare Dotierung, elektrochemische Die Stickstoffreduktion, saure Sauerstoffentwicklung Reaktion, Lithium-Ionen-Batterie, Atomlagenabscheidung.

# Symbols and Abbreviations

**Abs** absolute

**AFC** Alkaline Fuel Cell

**ALD** Atomic Layered Deposition

**CA** ChronoAmperometry

**CNT** Carbon Nanotube

**CO<sub>2</sub>RR** Carbon dioxide Reduction Reaction

**CSP** Concentrated Solar thermal Power

**CV** Cyclic Voltammetry

**DFT** Density Functional Theory

**DMFC** Direct Methanol Fuel Cell

**ESS** Energy Storage Systems

**EXAFS** Extended X-ray Absorption Fine Structure

**FE** Faraday Efficiency

**GDL** Gas Diffusion Layer

**HAADF** High-Angle Annular Dark Field

**HER** Hydrogen Evolution Reaction



**HR-TEM** High-Resolution Transmission Electron Microscopy

**LAADF** Low-Angle Annular Dark Field

**LIB** Lithium Ion Battery

**LSV** Linear Sweep Voltammetry

**MCFC** molten carbonate fuel cells

**MvK** Mars van Krevelen

**N<sub>2</sub>RR** Dinitrogen Reduction Reaction

**NdC** Nitrogen doped Carbon

**NHE** Normal Hydrogen Electrode

**iR** Current Interrupt

**OER** Oxygen Evolution Reaction

**PAFC** Phosphoric Acid Fuel Cell

**ppm**: parts per million

**PCET** Proton-coupled electron transfer

**PEM** Polymer Electrolyte Membrane/ Proton Exchange Membranes

**PEMFC** Proton Exchange Membranes Fuel Cells

**PV** PhotoVoltaic

**RDS** Rate Determining Step

**RHE** Reversible Hydrogen Electrode

**SAC** Single Atom Catalysts

**SEI** Solid Electrolyte Interface

**SHE** Standard Hydrogen Electrode

**SOFC** Solid Oxide Fuel Cell

**STEM** Scanning Transmission Electron Microscopy

**TOF** TurnOver Frequency ( $\text{s}^{-1}$ )

**XANES** X-Ray Absorption Near Edge Structure

**XRD** X-Ray diffraction

# Chemicals

**Al** Aluminium

**ADP** Adenosine DiPhosphate

**ATP** Adenosine TriPhosphate

**C** Carbon

**C<sub>2</sub>H<sub>2</sub>** Acetylene

**C<sub>2</sub>H<sub>4</sub>** Ethylene

**Co** Cobalt

**CO<sub>2</sub>** Carbon dioxide

**Cr** Chromium

**Cu** Copper

**ddH<sub>2</sub>O** double-distilled water = bidistilled water = ultrapure water

**e<sup>-</sup>** Electron

**EtOH** Ethanol

**Fe** Iron

**H<sup>+</sup>** Proton

**HClO<sub>4</sub>** Perchloric Acid

**H<sub>2</sub>** Dihydrogen

**H<sub>2</sub>O** Water

**H<sub>3</sub>O<sup>+</sup>** Hydronium

**H<sub>2</sub>SO<sub>4</sub>** Sulphuric Acid

**Ir** Iridium

**KOH** Potassium Hydroxide

**Li** Lithium

**Li-CF<sub>x</sub>** Lithium-Carbon Monofluoride

**M** Metal

**Mo** Molybdenum

**MOF** Metal-organic framework

**N** Nitrogen

**Nb** Niobium

**NH<sub>3</sub>** Ammonia

**NH<sub>4</sub><sup>+</sup>** Ammonium

**N<sub>2</sub>H<sub>2</sub>** Diazene

**N<sub>2</sub>H<sub>4</sub>** Hydrazine

**NMC** Ni<sub>x</sub>Mn<sub>y</sub>Co<sub>1-x-y</sub> Nickel Managanese Cobalt

**NMP** N-Methyl-2-pyrrolidon

**O** Oxygen

**O<sub>2</sub>** Dioxygen

**P** Phosphorus

**P<sub>i</sub>** inorganic Phosphate

**Pt** Platinum

**PVDF** Polyvinylidene fluoride

**Q** Charge

**Ru** Ruthenium

**Si** Silicon

**SiO<sub>2</sub>** Silica = Silicon dioxide

**Sn** Tin

**Ti** Titanium

**V** Vanadium

**W** Tungsten

**Zn** Zinc

**Zr** Zirconium

# Units

**A** Ampere

**atm** atmospheric pressure:  $1.01325 \text{ hPa} = 1.01 \times 10^5 \text{ Pa}$

**at%** atomic percentage

**bar**  $10^5 \text{ Pa}$

**C** Coulomb =  $1 \text{ A.s}^{-1}$

**dec** decade

**EJ** ExaJoules  $10^{18} \text{ J}$

**eV** electron Volt

**h** hour

**K** Kelvin;  $0 \text{ K} = -273.15 \text{ }^{\circ}\text{C}$

**kg** kilogram =  $10^3 \text{ g}$

**L** liters

**M** molar:  $\text{mol.L}^{-1}$

**m** meter

**m<sup>2</sup>** square meter

**mins** minutes

**mol** 1 mole =  $6.022 \times 10^{23}$  atoms

**oz** Once

**Pa** Pascal =  $1 \text{ kg.m}^{-1}.\text{s}^{-2}$

**rpm** rotations per minute

**s** second

**\$** Dollar

**V** volts

**W** Watt :  $1 \text{ kg.m}^2.\text{s}^{-3}$

**wt%** weight percentage

**μm** micrometer=  $10^{-6} \text{ m}$

**°C** degrees Celsius

**%** Percentage

# List of Figures and Tables

<b>Figure 1-1</b> Physical and chemical dihydrogen storage media.	39
<b>Figure 1-2.</b> Fuel Cell technology overview.	41
<b>Figure 1-3.</b> Volmer-Heyrovský and Volmer-Tafel mechanisms for HER.	45
<b>Figure 1-4.</b> Overall (top) and step-by-step (bottom) proposed mechanisms for OER in acidic (red) and alkaline (blue) media.	47
<b>Figure 1-5.</b> Proposed mechanisms for OER in acid: adsorbate evolution mechanism (AEM, left) and lattice oxygen mediated mechanism (LOM, right).	51
<b>Figure 1-6.</b> Proposed mechanism for the reduction of dinitrogen on FeMo cofactor.	56
<b>Figure 1-7.</b> Structure (left) and catalytic cycle with hexaisopropylterphenyl substituents (right) adapted from <sup>133</sup> .	57
<b>Figure 1-8.a-c)</b> Scheme of the different proposed mechanisms for the catalytic conversion of dinitrogen to ammonia.	60
<b>Figure 1-9.</b> Scheme of the different type of electrochemical cells tested for the ambient dinitrogen reduction (a) Back-to-back cell, b) Proton-Electron-Membrane –type cell, c) Hydrogen-type cell and d) Single chamber cell, adapted from <sup>151</sup> .	63
<b>Figure 1-10.</b> Schematic representation of the Mars van Krevelen mechanism on metal nitrides. M, N and H stand for metal, nitrogen and hydrogen, respectively.	67
<b>Figure 1-11.</b> Schematic representation of charge-discharge process on a lithium-ion cell using graphite and LiMO <sub>2</sub> electrodes.	73
<b>Figure 1-12.</b> Mechanisms of Li unwanted side reactions leading to battery failure.	75
<b>Figure 1-13.</b> Mechanism of materials interacting with lithium.	77



**Figure 1-14.** Si as anode for LIB, overview of advantages, drawbacks, shortcomings and coping strategies. 81

**Figure 2-1.** a) Synthesis scheme, b) recorded XRD pattern for Mo-N-C, c) TEM images, d) Aberration-corrected STEM-HAADF images, e) and f) STEM-EDS element mapping showing the distribution of Mo (red) and N (green), respectively. 121

**Figure 2-2.** High-resolution XPS spectra of Mo-N-C powder for a) C1s region, b) N1s region and c) of Mo 3d region. 122

**Figure 2-3.** HR-TEM images of Mo-N-C. 123

**Figure 2-4.** Linear Sweep Voltammetry results for Mo-N-C in N<sub>2</sub> and Ar saturated 0.1 M KOH. 125

**Figure 2-5.** 1h electrolysis at constant voltage of Mo-N-C in N<sub>2</sub> saturated 0.1M KOH. 127

**Figure 2-6.** Calculated Faraday efficiencies and ammonia production rates for 1h electrolysis at constant voltage of Mo-N-C in N<sub>2</sub> saturated 0.1M KOH. 128

**Figure 2-7. a)** Calculated Faraday efficiencies and b) associated partial current densities for 1h electrolysis at constant voltage of Mo-N-C in N<sub>2</sub> (blue), Ar (red) and of Ctrl in N<sub>2</sub> (green) saturated 0.1M KOH. 130

**Figure 2-8. a)** Calculated Faraday efficiencies and b) associated partial current densities for 1h and 2h electrolysis at constant voltage of Mo-N-C in N<sub>2</sub> (blues), and of Ctrl in N<sub>2</sub> (green) saturated 0.1M KOH. 132

**Figure 2-9.** <sup>15</sup>N<sub>2</sub> isotopic labelling 48h electrolysis at -0.2 V vs RHE using Mo-N-C in 0.1M KOH. 134

**Figure 2-10.** Calibration and reaction for Salicylate/Indophenol blue detection by UV-Vis. 142

**Figure 2-11.** H-type Cell used with Nafion117 membrane. 143

**Figure 2-12.** H-type Cell used with porous frit. 143

**Figure 2-13.** Scheme of the general synthesis of M-SAC-OxKJB, of the catalyst ink composition and of the catalyst drop-deposited on a hydrophilic carbon cloth. 147

**Figure 2-14.** a-b) TEM images; c) HAADF images; d-e) EDS-STEM element mapping showing the distribution of C and O, respectively; f) EDS survey of KJB. g-h) High-resolution XPS spectra of C1s and O1s, respectively. 149

**Figure 2-15.** a-b) TEM images; c) HAADF images; d-e) EDS-STEM element mapping showing the distribution of C and O, respectively; f) EDS survey of Ox-KJB. g-h) High-resolution XPS spectra of C1s and O1s, respectively. 150

**Figure 2-16.** a-b) TEM images; c) HAADF images; d-f) EDS-STEM element mapping showing the distribution of N, O, and Cu in Cu-Ox-KJB, respectively. g-j) High-resolution XPS spectra of C1s, O1s, N1s and Cu2p3 respectively. 152

**Figure 2-17.** a-b) TEM images; c) HAADF images; d-f) STEM-EDS element mapping showing the distribution of N, Fe, and O in Fe-Ox-KJB, respectively. g-j) High-resolution XPS spectra of C1s, O1s, N1s and Fe2p3 respectively. 154

**Figure 2-18.** a-b) TEM images; c) HAADF images; d-f) EDS-STEM element mapping showing the distribution of N, Ni, and O in Ni-Ox-KJB, respectively. g-j) High-resolution XPS spectra of C1s, O1s, N1s and Ni2p3 respectively 156

**Figure 2-19.** Linear sweep voltammetry at  $5 \text{ mV.s}^{-1}$ , obtained after the activation procedure (left) and related Tafel slopes @  $10 \text{ mA.cm}^{-2}$  (right) for M-SAC-OxKJB in Ar saturated  $0.1 \text{ M H}_2\text{SO}_4$ . 158

**Figure 2-20.** Linear sweep voltammetry at  $5 \text{ mV.s}^{-1}$ , obtained after the activation procedure (left) and related Tafel slopes @  $10 \text{ mA.cm}^{-2}$  (right) for M-SAC-OxKJB in Ar saturated  $0.5 \text{ M H}_2\text{SO}_4$ . 159

**Figure 2-21.** Linear sweep voltammetry at  $5 \text{ mV.s}^{-1}$ , obtained after the activation procedure (left) and related Tafel slopes @  $10 \text{ mA.cm}^{-2}$  (right) for M-SAC-OxKJB in Ar saturated  $0.1\text{M HClO}_4$ . 160

**Figure 3-1.** a) Nitrogen adsorption/desorption isotherm curves of Co-Ox-KJB (red), Ox-KJB (blue) and KJB (black). b) Pore size distribution curves of Co-Ox-KJB (red), Ox-KJB (blue) and KJB (black). c) XRD Pattern of Co-Ox-KJB (red), Ox-KJB (blue) and KJB (black). d-g) High resolution XPS spectra for d) C 1s, e) Co 2p, f) O 1s and g) N 1s regions of Co-Ox-KJB, respectively. 181

**Figure 3-2.** a-b) TEM images of Co-Ox-KJB. c) HAADF images of Co-Ox-KJB. d-f) STEM-EDS element mapping showing the distribution of N, O, and Co of Co-Ox-KJB, respectively. g) STEM-EDS survey from HR-TEM and h) LAADF of Co-Ox-KJB. 182

**Figure 3-3.** a-c) Typical  $I-V$  curves of Co-Ox-KJB, Ox-KJB and KJB at different temperatures. d) Temperature-dependent resistivity profiles of Co-Ox-KJB, Ox-KJB and KJB at different temperatures. 183

**Figure 3-4.** a-b) CV curves of pristine KJB and Ox-KJB. c-d) Discharge and charge curves of pristine KJB and Ox-KJB at  $0.05 \text{ A g}^{-1}$ . 184

**Figure 3-5.** a) CV curves and b) Discharge and charge curves of Co-Ox-KJB at  $50 \text{ mA g}^{-1}$ . c) Long-term cycling performance at  $50 \text{ mA g}^{-1}$  of Co-Ox-KJB (red), Ox-KJB (blue) and KJB (black). d) Rate capability test from  $0.05 \text{ A g}^{-1}$  to  $1.50 \text{ A g}^{-1}$ , followed by returning to  $0.10 \text{ A g}^{-1}$  with 5 cycles of Co-Ox-KJB (red), Ox-KJB (blue) and KJB (black). 187

**Figure 3-6.** a-b) TEM images, c) HAADF images d-f) EDS element mapping showing the distribution of Co, C and O of Co-Ox-super P, respectively. g) EDX image of Co-Ox-super P. h-k) High resolution XPS spectra for h) C1s, i) O1s, j) N1s and k) Co2p regions of Co-Ox-SuperP, respectively. 188

**Figure 3-7.** Cyclic (a) and rate (b) performance of the Si/C electrode with pristine SuperP, ox-super P, and Co-Ox-SuperP. 189

**Figure 3-8.** Cyclic (a) and rate (b) performance of the Si/C electrode with pristine KJB, Cu-Ox-KJB, Fe-Ox-KJB, and Ni-Ox-KJB. 190

**Figure 4-1.** Sequence for Al<sub>2</sub>O<sub>3</sub> deposition by ALD 202

**Figure 4-2.** a) Schematic top-view representation of the ALD set-up, b) Picture of the overall system and, c) Glass wool covered vacuum chamber. 206

**Figure 4-3.** Atomic concentration of C, O, Al, and Si for a) 26, b) 79, c) 158 and d) 316 Al<sub>2</sub>O<sub>3</sub> ALD cycles d; e) SEM image of 400 Al<sub>2</sub>O<sub>3</sub> ALD cycles; f) Growth per cycle rate of Al<sub>2</sub>O<sub>3</sub> deposited on Si (100) wafer substrate. 208

**Figure 4-4.** Capacity retention and Coulombic efficiency for a) NCM523-Al<sub>2</sub>O<sub>3</sub>-(2), b) NCM523-Al<sub>2</sub>O<sub>3</sub>-(4), c) NCM523-Al<sub>2</sub>O<sub>3</sub>-(6), d) NCM523-Al<sub>2</sub>O<sub>3</sub>-(8), e) NCM523-Al<sub>2</sub>O<sub>3</sub>-(10) cycling at 1.0 C. 211

**Figure 4-5.** Rate performance of a) NCM523-Al<sub>2</sub>O<sub>3</sub>-(2), b) NCM523-Al<sub>2</sub>O<sub>3</sub>-(4), c) NCM523-Al<sub>2</sub>O<sub>3</sub>-(6), d) NCM523-Al<sub>2</sub>O<sub>3</sub>-(8), e) NCM523-Al<sub>2</sub>O<sub>3</sub>-(10) at various current densities from 0.1 to 5.0 C. 213

# Contents

"If you want to find secrets of the universe, think in terms of energy, frequency and vibration"

1

Acknowledgements 2

Abstract 4

Résumé 6

Riassunto 9

Zusammenfassung 11

Symbols and Abbreviations 14

Chemicals 17

Units 20

List of Figures and Tables 22

Chapter 1: Introduction to Energy and Storage 32

1.1 Introduction: The Energy Crisis 33

1.2 Hydrogen and Energy Storage 36

1.2.1 Fuel Cells 39

1.2.2 Water Splitting 41

1.2.3 Hydrogen Evolution Reaction (HER) 45

1.2.4 Oxygen Evolution Reaction (OER) 46

1.2.5 Dinitrogen Reduction Reaction ( $\text{N}_2\text{RR}$ )	54
1.3 Energy Storage Systems: Battery	68
1.3.1 Li-ion Batteries	71
1.4 Context of the thesis	84
1.5 References	85
Chapter 2: Single-Atom Electrocatalysts for electrochemical Dinitrogen Reduction and Atomic doping for Oxygen Evolution Reaction in acidic media	114
2.1 Introduction to Single atom catalysts	115
2.2 Single Atom Electrocatalysts for Dinitrogen reduction ( $\text{N}_2\text{RR}$ )	117
2.3 Results	119
2.3.1 Synthesis and Characterization	119
2.3.2 Electrochemical Performances	123
2.3.3 Other Samples: MOFs and ZIFs	135
2.3.4 Discussion	136
2.3.5 Conclusion	138
2.3.6 Experimental Section	139
2.4 Single-atom Electrocatalysts for Acidic Oxygen Evolution Reaction	145
2.5 Results	146
2.5.1 Synthesis	146
2.5.2 Characterization	148

2.5.3 Electrochemical Performance	157
2.5.4 Discussion	161
2.5.5 Conclusion	163
2.5.6 Experimental Section	164
2.6 References	167
Chapter 3: Co-incorporated Carbon Black for Lithium-ion Batteries	177
3.1 Introduction to Electron conductive Carbon agents	178
3.2 Results	179
3.2.1 Characterization	179
3.2.1 Electrochemical Performances	183
3.3 Discussion	190
3.4 Conclusion	192
3.5 Experimental Section	192
3.6 Références	196
Chapter 4: Atomic Layered Deposition of Aluminium Oxide for stabilizing LiNi <sub>0.5</sub> Co <sub>0.2</sub> Mn <sub>0.3</sub> O <sub>2</sub> cathode in Lithium-ion Batteries	200
4.1 Introduction to Atomic Layer Deposition	201
4.2 ALD Principle and Set-up	205
4.3 Results:	206
4.3.1 Calibration	206

4.3.2 Electrochemical Performances	209
4.4 Discussion	214
4.5 Conclusion	215
4.6 Experimental Section	216
4.6.1 Deposition procedure	216
4.7 References	219
Conclusion and Outlooks	225
References	228
Transcript of Results	229
Curriculum Vitae	230





# Chapter 1: Introduction to Energy and Storage

## 1.1 Introduction: The Energy Crisis

"Energy" is defined as the ability to do work (to alter the environment). It can be found in many different forms such as thermal, electricity, chemical, mechanical, motion, gravitational, nuclear, radiant, and acoustic. Energy sources can be either fossil (e.g. petroleum, coal, natural gas, oil,...) or renewable (biomass, hydro, wind, geothermal, solar, tidal,...). In 2019, the world total primary energy supply was estimated to be 583.9 EJ and is still expected to rise in the future. Fossil sources of energy, such as oil (33.1%, 193.0 EJ), coal (27.0%, 157.9 EJ), natural gas (24.2%, 141.5 EJ), still represent 84.3% (492.2 EJ) of the total primary energy supply. The remaining is supplied by nuclear (4.3%, 24.9 EJ), leaving only 11.4% (66.6 EJ) from renewable sources<sup>1,2</sup>

Unsustainable energy consumption is a major cause of global environmental deterioration, including overexploitation of renewable resources and pollution caused by fossil fuels<sup>3</sup>. Energy is therefore the primary factor in many aspects of human activity<sup>4</sup>. Moreover, the global population continues to grow by 82 million people a year and is expected to reach 9.7 billion by 2050, adding further demands on the energy system<sup>5</sup>.

How will we sustain an ever-growing energy demand while transitioning to a global renewable energy grid? Answering this question is the biggest challenge humanity has to solve within the end of the 21<sup>st</sup> century.

Indeed, the combustion of fossil fuels, our primary source of energy, releases immense amounts of carbon dioxide (CO<sub>2</sub>) into the atmosphere. In 2019, a new world record for the average amount of atmospheric CO<sub>2</sub> was recorded at 409.8 parts per million (ppm); the highest value for the past 800 000 years<sup>6</sup>. About half of the CO<sub>2</sub> released during the industrial

revolution is still present in the atmosphere. The rest of it is partially dissolved in the world's oceans, lowering its pH by 0.1 units in form, resulting in a 30% acidity increase<sup>7</sup>. Anthropogenic CO<sub>2</sub> emissions are responsible for the disturbance and collapse of terrestrial and marine ecosystems, rise of sea level and global climate change<sup>8</sup>.

To limit climate change between 1.5° and 2 °C (Paris agreement), replacing fossil fuels with low- and no-carbon alternatives is critical<sup>9</sup>. Fortunately, many pathways are available to decarbonize the global economy. One promising path is via "Carbon capture and sequestration" (CCS), where CO<sub>2</sub> is collected, purified, and concentrated from large emitters and then transported to storage sites where it is sequestered underground several hundred meters below the surface. Within such conditions, CO<sub>2</sub> can undergo mineral carbonation and be immobilized in the ground as carbonate, preventing atmospheric release<sup>10</sup>. Alternatively, carbon dioxide could potentially be used as a C1 carbon source for the generation of many valuable chemicals<sup>11–13</sup>. Carbon dioxide capture, sequestration and functionalization exist as potential solutions to emissions from fossil fuel consumption. Nonetheless, the total fossil fuel resources are limited and will become scarce with time. Ultimately, new renewable energy sources have to replace fossil fuels in our energy mix to ensure a sustainable lifestyle.

Among all the previously mentioned renewable energy sources available, solar energy is a promising and freely available energy source for managing long-term issues in an energy crisis. Indeed, solar energy is the most abundant, inexhaustible source in the renewable energy family<sup>14</sup>, with more energy reaching Earth in one hour than what humanity consumes in a year<sup>15</sup>. Solar energy can be exploited directly to generate electricity in two ways. Either the heat from the sun can be concentrated and used to drive a heat engine, or energy can be harvested from photons in a solid-state device, a solar cell, providing a source of electric

power. Solar thermal power plants come in four main varieties, solar towers, parabolic trough power plants, Fresnel lens plants and solar dishes, each defined by the method used to concentrate the sun's heat energy. Solar thermal collection can also be added to a combined cycle gas turbine plant. Solar cells capture light energy directly. These simple solid-state devices are the third most important renewable source of electricity after hydropower and wind power.<sup>15</sup> A worldwide solar industry would definitely be the best option for future energy demand since it is now superior in terms of availability, cost-effectiveness, accessibility, capacity and efficiency compared to other renewable energy sources.<sup>16</sup>

Sunlight energy can be harvested by either producing electricity or heat. The solar thermal applications rely on devices capable of converting solar energy to thermal energy, which is then transferred to a caloric fluid to be transported and further utilized. Solar energy may also be harvested in the form of electricity thanks to devices such as concentrated solar thermal power (CSP)<sup>17</sup> or photovoltaics (PV)<sup>18</sup>. CSP devices consist of an arrangement of mirrors that redirect sunlight to be concentrated on towers, usually filled with a molten salt. This heated molten salt provides the necessary energy for the functioning of a steam turbine connected to an electrical power plant. PV cells are based on semiconductors that, upon photon irradiation, promote an electron from their valence band to their conduction band, generating a current<sup>19,20</sup>.

Unfortunately, as the earth rotates around the sun and about its own polar axis, accounting for our natural day/night and the seasonal cycles, the solar irradiation is intermittent. This prevents a stable local solar to electricity conversion. A way to tackle this problem is by utilizing energy storage systems (ESS) that store solar energy during production and restore it upon consumption. Viable and scalable ESS are necessary for solar

energy applications. One of these methods consist in mechanical energy storage: using ground level potential differences to store energy. For example by using "pumped-storage hydropower"<sup>21,22</sup> where excess solar electricity drives turbines that pump water from a lower to a higher ground, creating artificial lakes, and when the energy demands exceed the supply, the water flows down the turbines to generate electricity. Even if this storage method is environmentally friendly and quite inexpensive, the requirements for the terrain are strict (hills, mountains) and it presents only modest charge and discharge rates, which are not well matched for a 24h diurnal cycle.

Another storage method consists in producing high energy density fuels from artificial photosynthesis. Hydrogen gas ( $H_2$ ) has been explored as an energy carrier<sup>23</sup>, while generating electricity from hydrogen using a fuel cell causes no local pollution as it only generates pure water when utilized together with oxygen ( $O_2$ ). Another advantage of hydrogen lies in its high specific energy density, providing three times more energy than gasoline combustion per unit mass<sup>24</sup>, and being sustainable when produced from a wide range of renewable sources<sup>25</sup>. All things considered, a "Hydrogen Economy" is our best solution for long-term resolution of the energy crisis and global warming<sup>26</sup>, accounting for a better and brighter future.

## 1.2 Hydrogen and Energy Storage

Hydrogen, the most abundant element in our universe (around 73% by mass), present since the beginning of time<sup>27</sup>, is believed to be the mother of all elements, the substance from which every other element was made as suggested by the Prout hypothesis of 1815<sup>28</sup>. This hypothesis is supported by the idea that the atomic weights of other elements were integer

multiples of that of the hydrogen atom; it was later dismissed by the discovery of the neutron by Chadwick in 1932<sup>29</sup>. H<sub>2</sub> is invisible, non-toxic, and is scarce in Earth's atmosphere, as it is such a light gas that it can escape Earth's gravity.

In the past decades, a new highlight on using hydrogen as an energy carrier emerged, which could solve our dependence on conventional fossil fuels to satisfy our energy demand. The term "Hydrogen Economy" was first introduced by Professor John O'M Bockris in 1972 in a paper co-written with Dr. John Appleby entitled "The Hydrogen Economy: An Ultimate Economy?"<sup>30</sup>. This publication already analysed the feasibility of a society implementing hydrogen as a substitute to petroleum derivatives, and the cost of its implementation.

Compared with other traditional fuels (hydrocarbons and nitrogen-based fuels), hydrogen is sustainable, non-toxic, being the lightest element (molecular weight of 2.016 g.mol<sup>-1</sup>) with the highest energy density by mass (143 MJ.kg<sup>-1</sup>). It can be generated from both non-renewable such as coal, natural gas and nuclear energy sources, and renewable such as hydro, wind, tidal, solar, biomass and geothermal energy sources<sup>31</sup>. When used as a clean energy carrier, hydrogen gas is utilized as a fuel in transportation, and combustion engines or turbines, as well as in power generation within fuel cells, releasing only water as exhaust gas<sup>32</sup>.

Gradually, hydrogen could replace conventional fossil fuels in the energy sector, greatly reducing the emission of CO<sub>2</sub> and other harmful pollutants. Ultimately, the hydrogen economy needs to utilize renewable hydrogen as an energy carrier in order to satisfy the ever-growing energy demand of our society, without compromising our environment.

Despite the aforementioned advantages of the hydrogen economy, the path of transitioning from a fossil fuel energy system to a hydrogen energy system still suffers from

significant scientific, technological and socioeconomic roadblocks. Molecular hydrogen has to be produced from hydrogen-rich compounds with an energy input. Due to economic reasons, 95% of hydrogen production comes from fossil fuels that also generate significant amounts of carbon dioxide<sup>33,34</sup>. For example, hydrogen can be produced by steam reforming of methane, which generates carbon and carbon monoxide species as a side product. Also, mixed together with carbon monoxide, hydrogen forms the synthetic gas mixture (syngas) that is widely used building blocks for synthesis and technological applications globally<sup>35,36</sup>. Nowadays, hydrogen is mainly used industrially in fertilizer production (ammonia)<sup>37-39</sup>, hydrocarbon refining by hydrocracking<sup>40</sup>, production of valuable chemicals<sup>41</sup>, and sometimes (though rarely) as fuel for spacecraft propulsion<sup>42</sup>.

A full development of a hydrogen economy also requires improvement in hydrogen storage, transportation and distribution<sup>43</sup>. Hydrogen<sup>44</sup> gas is highly flammable and burns in air at a very wide range of concentrations; it has an extremely low volumetric density, and is so small that it can diffuse through most materials, including existing pipeline networks. Dihydrogen can be stored as pressurized gas, cryogenic liquid, or chemically bonded or physically adsorbed on solid-state materials (Fig.1-1).

Regarding physical storage, uncompressed hydrogen weighs 0.09 g.L<sup>-1</sup> at room temperature, pressurizing it to 150 bar steel tank increases it to 10 g.L<sup>-1</sup>. Further pressurized and cooled down, it can reach 40 g.L<sup>-1</sup>. Hydrogen liquefies at -253 °C (20 K) and weighs 71g.L<sup>-1</sup><sup>45</sup>. Already, such conditions require safe, leak-proof and expensive infrastructure, and a high amount of energy input to pressurize it and additional continuous energy input to keep it at low temperature<sup>46</sup>. Hydrogen may also be stored chemically within complex hydrides (70-150 g.L<sup>-1</sup>)<sup>47</sup> or on carbon or nitrogen-rich compounds (70-150 g.L<sup>-1</sup>)<sup>48</sup>. Hydrogen can also



be physisorbed on solid surfaces by Van der Waals interactions on materials such as metal organic frameworks (i.e. MOF-5 < 70 g.L<sup>-1</sup>), zeolites and carbon based materials (nanotubes and nanofibers)<sup>49</sup>. Carbon based physisorption, compared with heavier elements, is considered to be the most promising as it maximizes the hydrogen weight percentage while being safe, abundant, inexpensive and non-toxic.

Recently, metal hydrides emerged as promising H<sub>2</sub> storage media as many metals can reversibly store large amounts, either through gas or electrolyte absorption (100-150 g.L<sup>-1</sup>) (Fig.1-1)<sup>50,51</sup>.

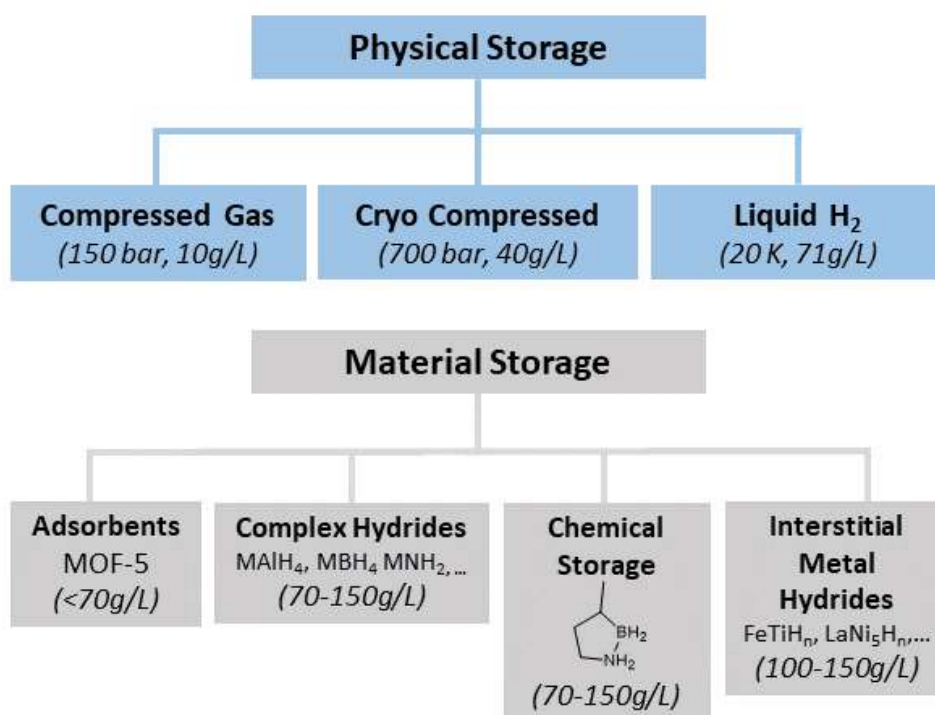


**Figure 1-1** Physical and chemical hydrogen storage media.

Altogether, storage and transportation seem to be the main bottlenecks in fully adopting the Hydrogen Economy. Once stored, the energy needs to be released and utilized; for that,

hydrogen can be burnt in combustion engines<sup>52</sup>, or used as a fuel in a fuel cell device, generating heat<sup>53</sup> and electricity.

### 1.2.1 Fuel Cells

Historically, water electrolysis was first described in 1800 by British scientists William Nicholson and Sir Anthony Carlisle; which is considered the first chemical reaction utilizing electricity. In 1838, Sir William Robert Grove immersed two platinum electrodes: one in sulphuric acid, and the other in a separately sealed container filled with oxygen and hydrogen gas. He observed a constant current flowing between the electrodes, and that water was produced; the fuel cell was born. By combining in series pairs of electrodes, the voltage drop increased, and he decided to give his invention the name of "gas battery". For the last two centuries, this technology has evolved significantly thanks to the collective efforts of scientists around the globe<sup>54</sup>. Nowadays, different types of fuel cell exist and are utilized in a wide range of applications, from domestic W-range, use such as consumer electronics and off-grid residential<sup>55</sup>. And also in industrial MW-range, with for example FuelCellEnergy supplying their SureSource product line of fuel cells from 1.4 to 3.7 MW of ultra-clean power with an electrical efficiency nearing 60%<sup>56</sup>. Fuel Cell technologies are classified in six different groups depicted in Figure 1-2. Namely, alkaline fuel cells (AFC)<sup>57</sup>, direct methanol fuel cells (DMFC)<sup>58</sup>, molten carbonate fuel cells (MCFC)<sup>59</sup>, phosphoric acid fuel cells (PAFC)<sup>60</sup>, proton exchange membranes fuel cells (PEMFC)<sup>61</sup> and solid oxide fuel cells (SOFC)<sup>62</sup>. In general, fuel cells are compartmented into three sections, one consisting of the anode where fuel is fed (usually H<sub>2</sub>), another is the cathode where oxygen is fed, both of which are separated by an electrolyte or a membrane. Both electrodes are covered with electrocatalysts that, on the anode, oxidize the fuel yielding electrons; these electrons travel

through an external circuit bringing an electrical load, and are then consumed on the cathode side to reduce oxygen. Fuel cells provide power continuously as long as fuel and oxygen are supplied.

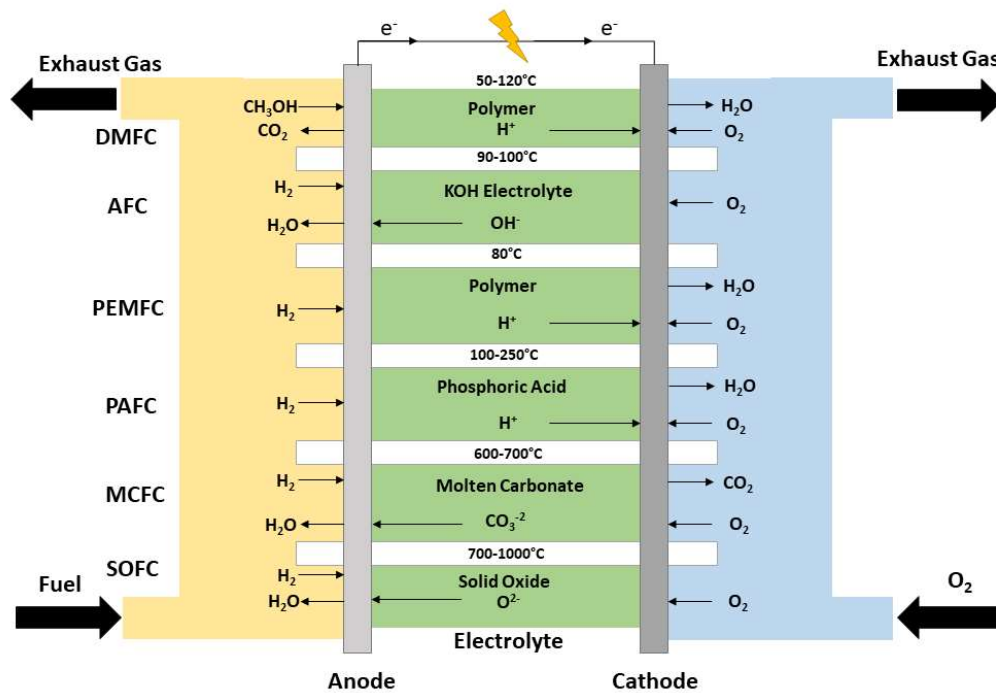


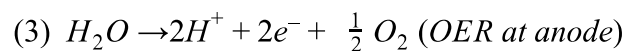
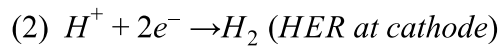
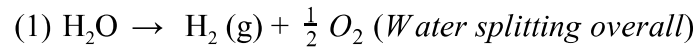
**Figure 1-2.** Fuel Cell technology overview.

### 1.2.2 Water Splitting

In terms of sustainability and with consideration of minimizing the amount of carbon emissions, water is the most promising source of hydrogen. In principle, dissociating the molecule will yield H without worries of generating carbon by-products. However, the atoms are strongly bonded with each other in the molecule. In the gas phase, it requires  $\sim 5.0$  eV to dissociate the molecule into its component atoms<sup>63</sup>. Hence, catalysts and energy sources are necessary to assist the dissociation process.

This chemical reaction is referred to as "water splitting" (Eq.1). Water (H<sub>2</sub>O) is separated into dihydrogen gas (H<sub>2</sub>) and dioxygen gas (O<sub>2</sub>). This reaction was first mentioned in 1789 by the two Dutch experimenters Deiman and Van Troostwijk, in a letter written in French to M. de la Mètherie. They described how they were able with hermetically sealed tubes, gold wires and power supply to separate water into "inflammable air" and "vital air". Shortly after, in 1797, the English Royal Society concluded that "hydrogen and oxygen gas were produced by passing electric discharges through water"<sup>64</sup>. Water splitting was born.

This reaction can be performed electrocatalytically, where at the cathode water is reduced to form dihydrogen, referred to as the hydrogen evolution reaction (HER, Eq.2), and simultaneously oxidized at the anode to form dioxygen, namely the oxygen evolution reaction (OER, Eq.3). The overall water splitting and the two half reactions, namely HER and OER, are described as the following:



Also, the standard Free energy ( $\Delta G^0$ , standard conditions of 25°C and 1 bar), also referred to as Gibbs energy, can be expressed in function of the standard enthalpy ( $\Delta H^0$ ), the entropy ( $\Delta S^0$ ) and the temperature (in Kelvin) of that reaction as:

$$(4) \Delta G^0 = \Delta H^0 - T\Delta S^0$$

The standard chemical potential of a reaction in an electrochemical cell ( $\Delta E_{cell}^0$ ) can be expressed as:

$$(5) \Delta E_{cell}^0 = -\frac{\Delta G^0}{zF}$$

Where,  $z$  is the number of electrons involved in the reaction, and  $F$  is the Faraday constant (96485 C.mol<sup>-1</sup>). For the two-electron water splitting reaction at standard conditions:

$\Delta G^0 = 285.8 \text{ kJ.mol}^{-1}$ , the entropy  $\Delta S^0 = 0.163 \text{ kJ.mol}^{-1}.\text{K}^{-1}$ , calculated from:

$$(6) \Delta S^0 = \left[ \sum nS^0(\text{products}) \right] - \left[ \sum nS^0(\text{reactants}) \right]$$

$$\Delta S^0 = [S^0(H_2) + \frac{1}{2}S^0(O_2)] - [S^0(H_2O)] = 131.0 + \frac{205.0}{2} - 69.9 \text{ J.mol}^{-1}.\text{K}^{-1}$$

$$S^0 = 163.6 \text{ J.mol}^{-1}.\text{K}^{-1}$$

Where  $S^0(H_2)$ ,  $S^0(O_2)$ , and  $S^0(H_2O)$  correspond to the standard entropy of formation of one mole of dihydrogen, dioxygen and water respectively. Therefore, the cell potential ( $\Delta E_{cell}^0$ ) is equal to -1.23V, which is considered to be the minimum potential necessary to generate hydrogen and oxygen from water at standard conditions. Thus, in a real system, an overpotential ( $\eta$ , defined as the difference between the applied potential and the thermodynamic potential, Eq.8) needs to be applied to split water. In order to improve the performances, hence reduce the overpotential ( $\eta$ ), electrocatalysts are deposited on both the anode and the cathode to efficiently catalyse the reduction and oxidation. In an electrochemical reaction, kinetics depend directly on the applied potential at the electrodes and can be described by the Butler-Volmer equation (7):

$$(7) \quad j = j_0 \left( e^{\frac{-\alpha z F (E - E_{eq})}{RT}} - e^{\frac{(1-\alpha) z F (E - E_{eq})}{RT}} \right)$$

Where,  $j$  is the current density ( $\text{A.m}^{-2}$ ),  $j_0$  the exchange current density ( $\text{A.m}^{-2}$ ),  $\alpha$  the charge transfer coefficient,  $z$  the number of electrons involved in the reaction,  $E$  the electrode potential (V),  $E_{eq}$  is the equilibrium potential (V),  $F$  is the Faraday constant ( $96485 \text{ C.mol}^{-1}$ ),  $R$  the universal gas constant ( $8.314 \text{ J.K}^{-1}.\text{mol}^{-1}$ ), and  $T$  the temperature (K).

The overpotential, that is the extra voltage that needs to be applied for the reaction to proceed, can be described as:

$$(8) \quad \eta = E - E_{eq}$$

Where,  $E$  the electrode potential (V) and  $E_{eq}$  is the equilibrium potential (V). This overpotential  $\eta$  is a critical factor for the kinetic evaluation of electrocatalysts. And in the case of  $|\eta| > 0.1 \text{ V}$ , where the concentrations at the electrode are equal to the concentration at the bulk electrolyte, the equation (8) can be rearranged to the Tafel equation:

$$(9) \quad \eta = a + b \log \log (i)$$

Where,  $i$  is the current, while  $a$  and  $b$  are parameters characteristic of the reaction and the electrodes which are defined as:

$$(10) \quad a = \frac{2.3 RT}{\alpha z F} \log \log i_0$$

$$(11) \quad b = \frac{-2.3 RT}{\alpha z F}$$

Where,  $b$  is referred to the Tafel slope when  $\log \log(i)$  is plotted in function of overpotential  $\eta$ . The Tafel slope provides valuable kinetic insight, especially for the elucidation of the rate determining step (RDS) and to further understand fundamental relationships between the reactants and the electrocatalysts.

### 1.2.3 Hydrogen Evolution Reaction (HER)

During water splitting, the hydrogen evolution half-reaction takes place at the cathode, utilizing hydronium ions ( $\text{H}_3\text{O}^+$ ) or water molecules as proton sources in acidic and alkaline media, respectively. The reaction is believed to take place by either the Volmer-Heyrovský or the Volmer-Tafel mechanisms<sup>65</sup>, depicted below:

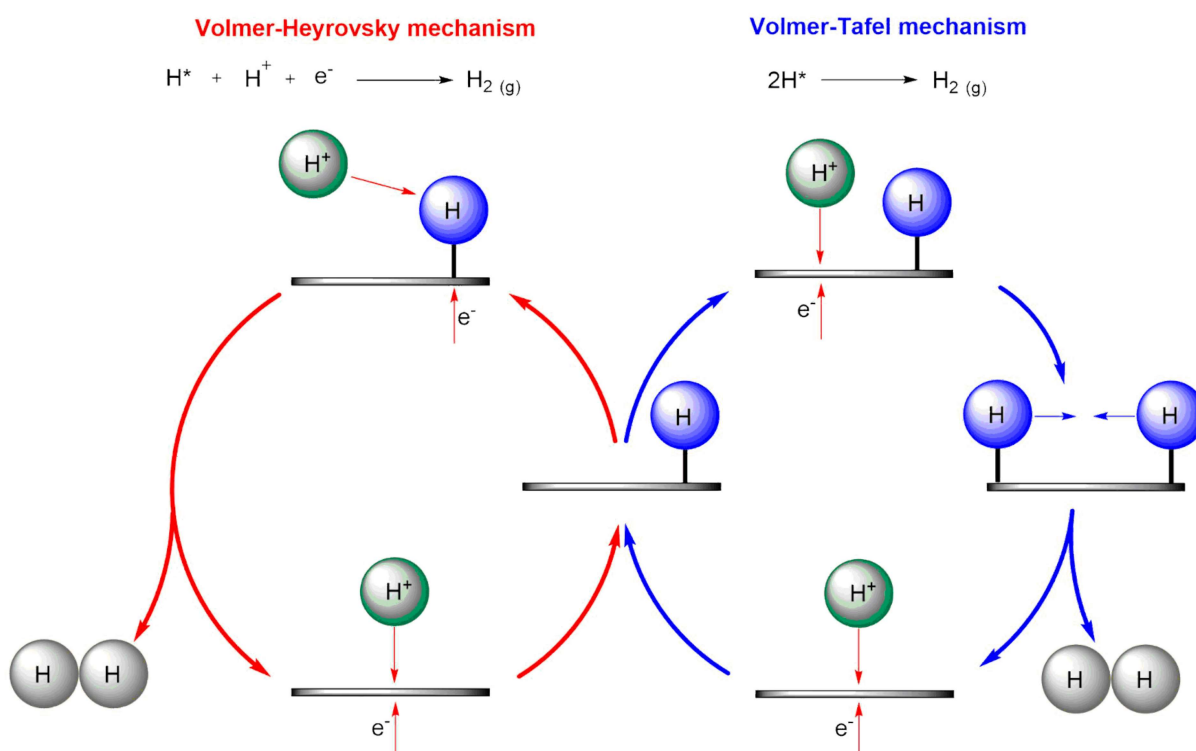


**Figure 1-3.** Volmer-Heyrovský and Volmer-Tafel mechanisms for HER.

In the Volmer-Heyrovský mechanism (red, left), a hydrogen ion from the electrolyte and an electron, as a concerted electron-proton coupled step, react with a hydrogen atom adsorbed on the surface of the electrocatalyst and generate dihydrogen.

In the Volmer-Tafel mechanism (blue, right), hydrogen ions are reduced by an electron and adsorbed on the surface of the electrocatalyst. Two adsorbed hydrogen form a hydrogen molecule and are desorbed from the surface of the catalyst.

Regardless of the mechanism, H adsorption is crucial, and should be facilitated by the electrocatalyst. Platinum (Pt) is known as the best HER catalyst, as its adsorption free energy of H is close to zero ( $\Delta G_H \cong 0$ ), binding neither too strongly nor too weakly the adsorbed H atom and H<sub>2</sub> molecule<sup>66,67</sup>. A large effort is made to use non-noble metal based HER electrocatalysts<sup>68,69</sup>, which is necessary for scaling up hydrogen production.

#### 1.2.4 Oxygen Evolution Reaction (OER)

One of the major issues holding back the implementation of water electrolyzers, fuel cells or even metal-air batteries are the sluggish kinetics of the oxygen evolution reaction (OER). OER is a four electron-proton coupled reaction, while HER is only a two electron-transfer reaction, therefore OER is usually the bottleneck requiring a higher energy input to overcome the kinetic barrier.

In a common research effort, many different groups tried to describe from experiments or computational calculations all the possible OER mechanisms either in alkaline or acidic media (Fig.1-4)<sup>70</sup>. Within most proposed mechanisms, the formation of metal-hydroxide (M-OH) or metal-oxide (M-O) intermediates is observed. The major divergence appears upon



the formation of these intermediates with oxygen. A mechanism hypothesis for the formation of  $O_2$  is by direct combination of 2 M-O intermediates (purple pathway, Fig.1-4). Another mechanism revolves around the formation of the M-OOH superoxide intermediate (black pathway, Fig.1-4) before the formation of  $O_2$ . Regardless of the mechanistic differences, OER is believed to be a heterogeneous reaction, where the metal-oxygen bonding interactions in all possible intermediates (and all possible pathways) are key descriptors for the performance of the studied electrocatalysts<sup>71</sup>.

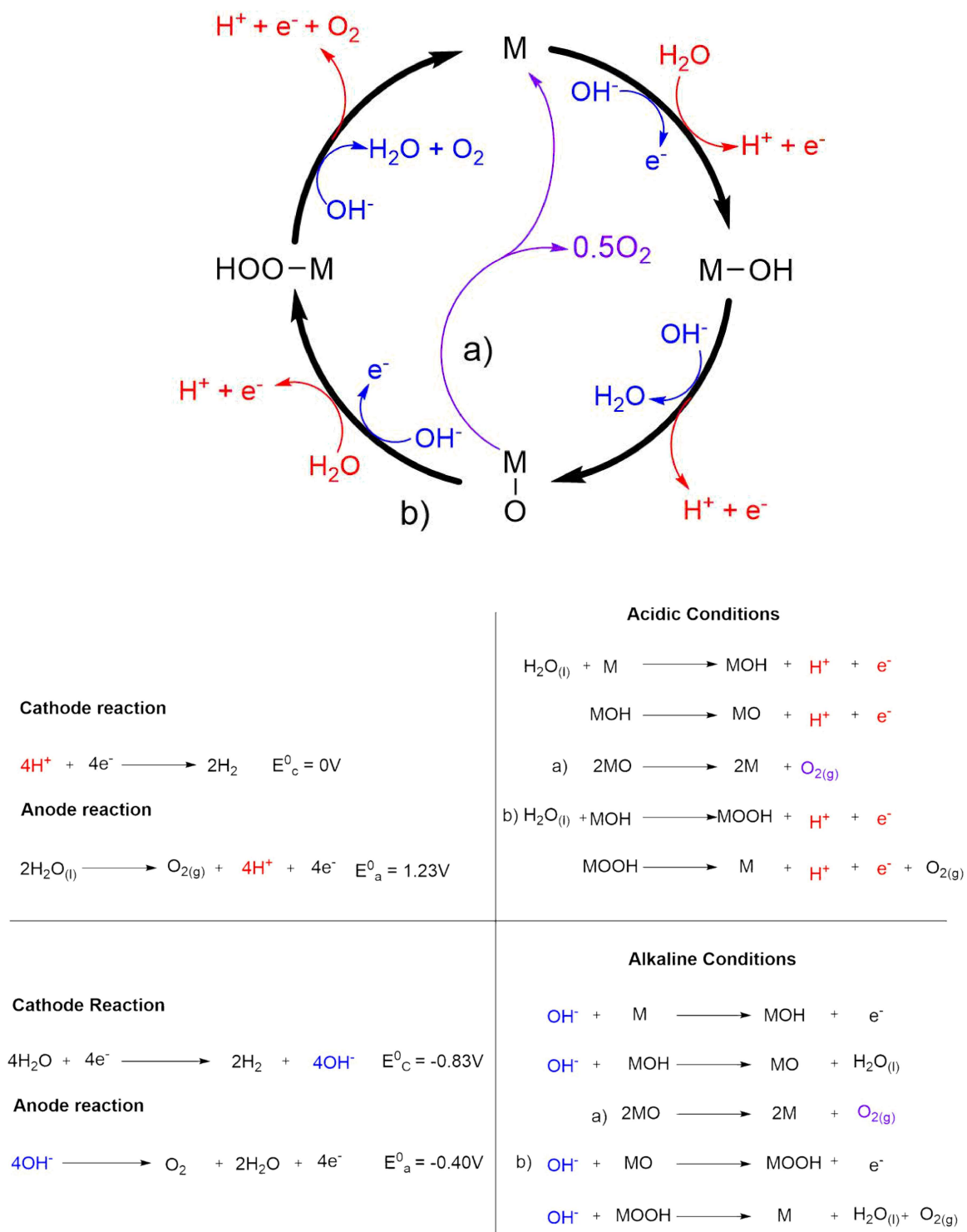


**Figure 1-4.** Overall (top) and step-by-step (bottom) proposed mechanisms for OER in acidic (red) and alkaline (blue) media.

Due to the complexity of the OER reaction, many different research groups attempt to solve this issue using conventional electrochemistry techniques. Thus, the reliability and

reproducibility of the published data is dependent on the conditions of measurement, which may vary from group to group for the same studied material<sup>72</sup>. In order to cope with this phenomenon, Prof. Jaramillo and his group<sup>73</sup> have published a standard experimental flow chart to have reliable and comparable measurement of key parameters of tested electrocatalysts such as chemical composition, Faraday efficiency (FE), catalytic activity and stability. Finally, for the determination of the overpotential ( $\eta$ ), they suggested applying 10 mA.cm<sub>geo</sub><sup>-2</sup> as current density per geometric area at room temperature. This corresponds to roughly the same current density as 10% efficiency at the anode under one sun illumination (around 1 kW.m<sup>-2</sup> by convention) for a solar water-splitting device.

Until now, the best performing catalysts are rutile-type RuO<sub>2</sub> and IrO<sub>2</sub>, precious metal oxides, that exhibit excellent OER activity in both acidic and alkaline electrolytes<sup>72,74–76</sup>. Ruthenium and iridium oxide-based materials present high electric conductivity from their rutile crystallographic structure<sup>77</sup>. IrO<sub>2</sub> is more stable than RuO<sub>2</sub>, but the contrary is observed regarding OER activity, with RuO<sub>2</sub> being more active<sup>78</sup>. Thus, RuO<sub>2</sub> was demonstrated to be unstable under high anodic potentials and will dissolve over time due to the formation of hydrous RuO<sub>2</sub>(OH)<sub>2</sub>, which can be further deprotonated to RuO<sub>4</sub>, a soluble specie in electrolyte<sup>72,79</sup>. While IrO<sub>2</sub> is more stable than RuO<sub>2</sub>, upon high anodic potential, soluble IrO<sub>3</sub> and IrO<sub>4</sub><sup>2-</sup> may also be formed, limiting the performances of the catalyst for prolonged use<sup>80–82</sup>. Hence, to improve the stability of RuO<sub>2</sub> (or the performance of IrO<sub>2</sub>), bimetallic oxide systems such as Ru<sub>x</sub>Ir<sub>1-x</sub>O<sub>2</sub> were investigated, by using doping techniques<sup>83,84</sup> or core-shell structures<sup>85,86</sup>.

Unfortunately, both ruthenium and iridium are scarce elements in the Earth's crust (both around 0.001ppm<sup>87,88</sup>) and are consequently expensive (with a price reported in May 2021 by

J. Matthey of 440\$.oz<sup>-1</sup> and 6,300\$.oz<sup>-1</sup>, for Ru and Ir, respectively)<sup>89</sup>, limiting scale-up applications.

Therefore, developing low-cost, robust, and earth-abundant OER catalysts is crucial, as it represents the main bottleneck for a hydrogen economy<sup>70</sup>.

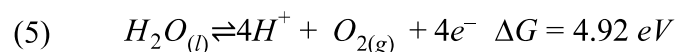
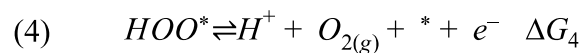
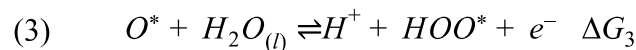
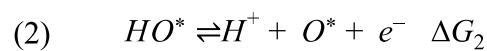
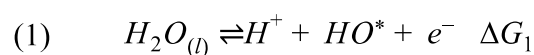
### *Acidic Mechanism*

During the past decades, the scientific energy community concentrated their efforts on the development of better OER electrocatalysts, most of which are transition-metal-based for alkaline media<sup>90,91</sup>. However, three major issues are associated with alkaline electrolyzers: low partial load range, limited current density and low operating pressure<sup>92</sup>. Plus, oxygen can diffuse to the cathode chamber, reducing the overall efficiency, as it will be catalysed back to water in the presence of hydrogen. In addition, diffusion of hydrogen<sup>93</sup> to the anodic chamber may cause a decrease in efficiency, as well as being a serious safety issue – a hydrogen and oxygen gas mixture is explosive starting from 4 mol% H<sub>2</sub><sup>94</sup>. Another drawback for alkaline electrolyzers is the high ohmic resistance across the electrolyte, yielding low maximum achievable current densities (0.2-0.4 mA.cm<sup>-2</sup>)<sup>92</sup>. Progress made within the field of acidic OER was significantly lesser compared to the process in alkaline media.

The advantage of conducting water electrolysis in acid is the availability of protons in solution, exhibiting higher ionic conductivity, which improves the kinetics for HER compared with neutral and alkaline medias<sup>95,96</sup>. In the 1960s, based on the concept of W. T. Grubb<sup>97,98</sup>, General Electrics developed the first water electrolyzer based on solid polymer electrolytes. This concept is also referred to as proton exchange membrane or polymer electrolyte membranes (PEM). It was presented as an alternative to alkaline electrolyzers that could overcome previously mentioned drawbacks. Also, well studied PEM are suitable for

separating the anodic and cathodic compartments in acid conditions. Such membranes are based on fluorocarbon and hydrocarbon backbones decorated with sulfonic-acid side chains<sup>99</sup>. PEM (i.e. Nafion®, fumapem®) permit high proton conductivity, high pressure operation<sup>100</sup>, compact designs (versus stack design for alkaline electrolyzers) and avoid gas cross-over<sup>101</sup>. They can be obtained as very thin membranes (20-300 µm) with excellent chemical, mechanical, and thermal stability, resulting in many advantages<sup>102</sup>. Thus, such membranes can be expensive, and a common effort is made to drive their price down<sup>103</sup>.

Most mechanisms proposed within the last century, namely; the electrochemical metal peroxide, electrochemical oxide pathway, and the oxide pathway<sup>104</sup>, are based on the adsorbate evolution mechanism (AEM, Fig.1-5). In this mechanism, water molecules are at first adsorbed on the surface of the catalyst and undergo a series of transformations, formation of a hydroxide complex, proton-electron coupled transfers, bond cleavage and formation, and oxygen desorption. Within a joined effort, the groups of Jaramillo and Nørskov together with Rossmeisl<sup>105</sup> proposed a density functional theory (DFT) pathway based on four concerted proton-electron transfer, such as:



Where \* represents an available active site. At first, the water molecule is adsorbed on the active site while dissociating a proton, yielding HO\* (1), followed by a second proton

dissociation to yield  $O^*$  (2). From here, another water molecule acts as a nucleophile and attack the  $O^*$ , and dissociating from a hydrogen, it yields the superoxide intermediate  $HOO^*$  (3). Finally, the last hydrogen is removed and the oxygen molecule desorbs from the active site (4). The overall oxygen evolution half-reaction is depicted in (5). The Gibbs free energy ( $\Delta G$ ) of the overall reaction is estimated to be 4.92 eV under equilibrium conditions, which represents a theoretical potential for the oxygen evolution under standard conditions of 1.23 V, without considering any kinetic barriers.

In real life examples, there is generally a step with a  $\Delta G$  larger than theoretical 1.23 eV, this step will lead to a large overpotential and will be the bottleneck for the entire reaction, it is referred to as the potential determining step (PDS)<sup>106</sup>. For the well-studied  $RuO_2$ , the PDS is described by reaction (3), where  $O^*$  is strongly adsorbed, preventing the formation of  $HOO^*$ <sup>107</sup>.

Today, transition metal ions, usually present in rutile<sup>108,109</sup>, perovskite<sup>110,111</sup> and pyrochlore-type<sup>112</sup> catalysts as coordinatively unsaturated octahedral  $MO_6$  structures, are believed to be the active site for the AEM<sup>113–115</sup>.

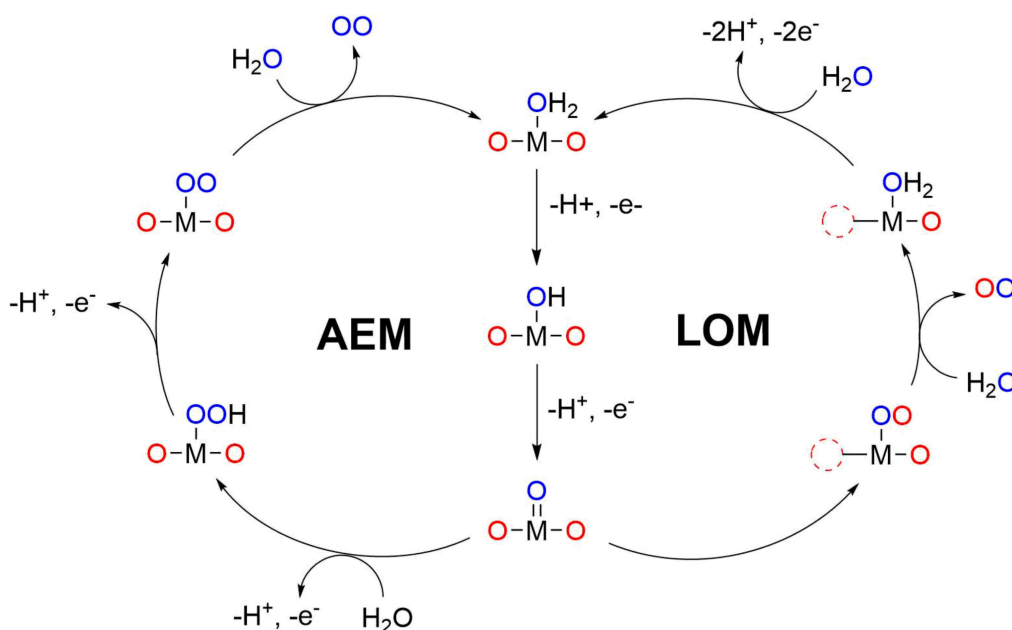
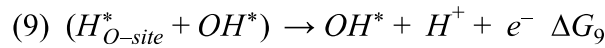
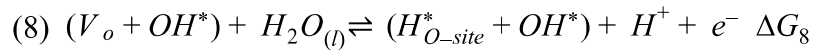
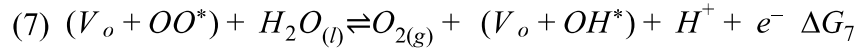
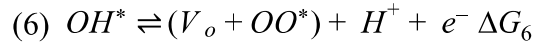


**Figure 1-5.** Proposed mechanisms for OER in acid: adsorbate evolution mechanism (AEM, left) and lattice oxygen mediated mechanism (LOM, right).

Upon investigation of a large panel of electrocatalysts for OER arose catalytic behaviours that could not be explained by the AEM. Indeed, following the discovery of materials exceeding predicted limitations while also having pH-dependent performances versus the reversible hydrogen electrode (RHE)<sup>116–118</sup>, the hypothesis of another OER mechanism emerged. The most studied among the new proposition is the lattice oxygen mechanism (LOM). From the mid-1970s to the early 1980s, several research groups worked on the elucidation of this proposed mechanism<sup>119,120</sup>. Thus, due to the poor stability of the catalysts in acidic environment, the study of the LOM in alkaline media is more suitable. In this process, lattice oxygen of catalysts directly participates in the formation of a new oxygen molecule, creating a vacancy within the oxygen lattice. The mechanism was demonstrated experimentally by the use of isotopic labelling:  $^{16}\text{O}$   $^{18}\text{O}$  molecules were formed from a  $\text{H}_2^{16}\text{O}$  solution on a ruthenium oxide ( $\text{Ru}^{18}\text{O}_2$ ) layer, previously formed in  $\text{H}_2^{18}\text{O}$ ; and  $^{16}\text{O}^{18}\text{O}$  molecules were observed when the OER was performed on  $\text{Ru}^{16}\text{O}_2$  in  $\text{H}_2^{18}\text{O}$  solution<sup>121</sup>.

However, even if the results confirmed this possible mechanism, the actual pathway is still under debate. Based on DFT calculations, Rong *et al.*<sup>122</sup> proposed a reaction pathway involving lattice oxygen in the reversible formation of surface oxygen vacancies ( $V_o$ ) was proposed<sup>123</sup>, such as:



From the study of the activity of perovskite catalysts, Yoo *et al.*<sup>122</sup> suggested that LOM, from equation (7), had a relatively constant value of  $\Delta G_7$  corresponding to minimum overpotential of 0.17-0.41 V. From the overpotential point of view, LOM could be superior to the AEM, as the AEM has an overpotential around 0.37 V<sup>105</sup>. In their proposition, the metal ion is still considered as the active site for the oxygen evolution, as the  $OH^*$  intermediate binds to the metal ion and then reacts with a surface oxygen yielding the  $OO^*$  intermediate and the  $V_o$  vacancy. From this intermediate, the oxygen molecule is formed, and the vacancy is replenished by water (7). With the hypothesis of the metal ion being the active site, AEM and LOM can coexist and/or compete with each other. This phenomenon was highlighted by the work of Macounová *et al.*<sup>124</sup>, where they revealed that both mechanisms coexisted at high potentials. However, in the LOM proposed by Rong *et al.*<sup>123</sup> each step is an electron-proton coupled step, resulting in a pH-independence<sup>125</sup>.

To explain the observed pH-dependence observed on several types of perovskites<sup>117</sup>, another mechanism was hypothesized where lattice oxygen acts as the active site and no redox chemistry is observed on the metal centres. In this mechanism, lattice oxygen reacts



with adsorbed oxygen to form an O-O bound, followed by oxygen molecule release leading to an oxygen vacancy. Thus, they also observed from isotopic labelling experiments that oxygen molecules could be produced solely from lattice oxygen, leading to another mechanistic possibility. In the two proposed pathways, elementary steps involving non-concerted proton-electron transfer steps could explain the pH dependency of the oxygen evolution ability. Nevertheless, it is important to signal that all above-mentioned mechanistic propositions were based on OER within alkaline media, therefore acidic pathways may differ.

Upon the study of  $\text{La}_2\text{LiIrO}_6$ , Tarascon *et al.*<sup>118</sup> proposed another catalytic pathway. At first, (1) a surface oxidation/delithiation step, followed by (2) the formation of O-O bond through either the reaction of water with surface oxygen followed by a deprotonation, or (2') the O-O formation from two surface oxygen, both followed by oxygen release yielding oxygen vacancies. These vacancies can be either refilled by (3) bulk migration of lattice oxygen or by (4) water. In this pathway, electrophilic surface oxygen may be considered as the active site. The replenishment of oxygen vacancies, inducing migration of ions, leads to modification of the coordination environment of surface Ir, leading to soluble Ir species owing for the instability of the electrocatalyst over prolonged OER periods.

While mechanistic controversy continues, several features of the AEM compared to LOM can be resumed as in following Table 1-1:

**Table 1-1-1.** Possible OER mechanisms: AEM vs LOM.

Mechanism	AEM	LOM
Catalytic Redox process	Cationic	Anionic
Overpotential	0.37 V	0.17-0.41 V
Active Site	Surface coordinating unsaturated metal ion	Surface coordinating unsaturated oxygen ion
Main Feature	pH independence	Oxygen vacancy participation

From this mechanistic comparison, it can be concluded that in the OER potential region the ease of the redox of either cations or anions will dictate which of the pathways is preferable for a given electrocatalyst.

### 1.2.5 Dinitrogen Reduction Reaction ( $N_2RR$ )

Another alternative to the OER half-reaction for water splitting is the reduction of dinitrogen molecules ( $N_2$ ) into ammonia ( $NH_3$ ). Indeed,  $NH_3$ , an activated nitrogen building block essential to the fertilizer, pharmaceuticals, and explosives industry<sup>126,127,128</sup>; could also be utilized as a carbon-neutral liquid fuel, presenting high energy density ( $4.32 \text{ kWh.L}^{-1}$ ), high hydrogen content (17.6 wt%), and low boiling point ( $-33.3^\circ\text{C}$  at 1 atm), in a hydrogen based economy<sup>129,130</sup>.

Dinitrogen ( $N_2$ ), the most abundant gas in our atmosphere (78%), is particularly inert; it has a highly stable triple bond ( $940.95 \text{ kJ.mol}^{-1}$ ), no dipole moment and a very low polarizability. The first bond cleavage energy of dinitrogen is very high ( $410 \text{ kJ.mol}^{-1}$ )

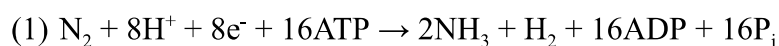
compared with other small molecules with triple bonds (ex  $C_2H_2$ ) and the addition of the first H atom to the dinitrogen molecule is an endothermic process ( $+37.6 \text{ kJ.mol}^{-1}$ )<sup>131</sup>. The high ionization potential (15.8 eV) and negative electron affinity (-1.9 eV) hinders the activation of dinitrogen by Lewis acid and/or base<sup>132</sup>. Therefore, nitrogen fixation currently represents one of the major challenges in chemistry.

### *Haber-Bosch*

Industrially, the reduction of  $N_2$  to  $NH_3$  is globally sustained by the Haber-Bosch process, which is performed at high pressure and high temperature (150-350 atm, 350-550°C). It is currently a centralized process which requires a continuous pure dihydrogen ( $H_2$ ) flow, usually originated from fossil fuels; and combined with such harsh conditions, it leads to substantial emissions of  $CO_2$ <sup>133,134</sup>. Indeed, it has accounted for the consumption of more than 1% of the world's energy supply and generates more than 300 million metric tons of fossil fuel derived  $CO_2$  every year<sup>135</sup>. Therefore, it is strongly desirable to develop alternative processes to Haber-Bosch's in order to overcome its limitations, which include harsh conditions, complex and centralized infrastructures, transportation, high energy consumption and finally the drastically disastrous environmental impacts.

### *Nitrogenase*

In nature, plants and bacteria carry out nitrogen fixation using nitrogenase metalloenzymes under ambient reaction conditions, converting gaseous dinitrogen into ammonia<sup>136</sup>. These enzymes are formed by the combination of two proteins; where the first protein operates as an electron carrier for the reduction of dinitrogen via an iron sulphur cluster ( $Fe_4S_4$ ). The second protein, containing FeMo, FeV, or FeFe cofactors, acts as catalytic sites for the actual nitrogen fixation according to the following reaction<sup>137–139</sup>:



Where the transformation of adenosine triphosphate (ATP) to adenosine diphosphate (ADP) acts as the driving force for the reaction. As shown in equation (1) the reduction of dinitrogen to ammonia is not an efficient process, as it requires the consumption of 16 equivalents of ATP per  $\text{N}_2$  molecule. Still, per each  $\text{NH}_3$  molecule released, 8 equivalents of ATP are consumed, corresponding to an energy of  $244 \text{ kJ.mol}^{-1}$ , making this process more efficient than the Haber-Bosch process. In addition, for every reduced molecule of dinitrogen with a partial pressure of 50 atm, a molecule of dihydrogen is generated. At ambient pressure, more equivalents of dihydrogen are formed, implying that additional equivalents of ATP must be consumed in order to overcome this increase in energy consumption<sup>140</sup>. Hydrogen production at FeMo cofactor nitrogenase under deuterium atmosphere ( $\text{D}_2$ ) shows the formation of HD gas. Moreover, the formation of HD increases together with the partial pressure of dinitrogen, suggesting a dependency between hydrogen scrambling and the turnover of dinitrogen. Therefore, in the catalytic dinitrogen reduction on nitrogenases, the formation of dihydrogen is an intrinsic phenomenon rather than just being a side reaction. From the reaction kinetics, stoichiometry and probing of reaction intermediates (i.e. hydrazine and diazene), Dean, Hoffman and Seefeldt proposed a reaction mechanism for the reduction of dinitrogen to ammonia on the FeMo cofactor, such as<sup>140,141</sup>:

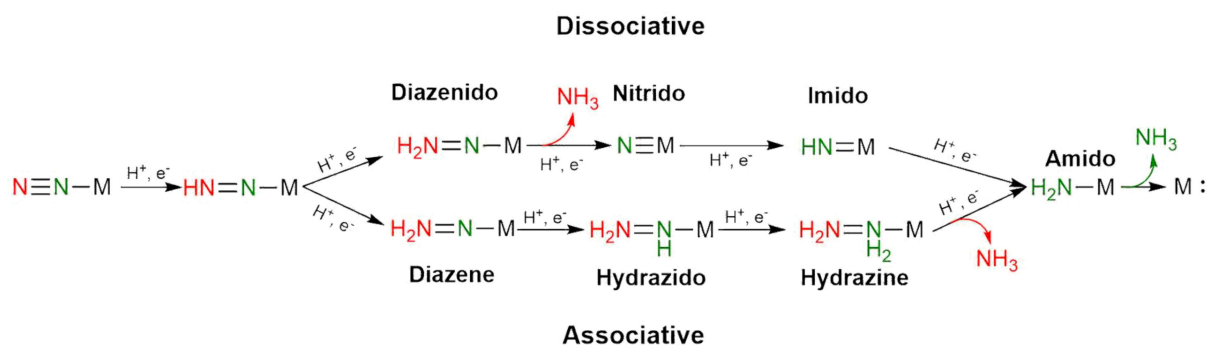


**Figure 1-6.** Proposed mechanism for the reduction of dinitrogen on FeMo cofactor.

As traces of hydrazine were detected as an intermediate for the dinitrogen reduction on FeV cofactor, it suggests an alternating mechanism pathway. In this mechanism, both N-atoms are hydrogenated simultaneously. As both FeV and FeMo cofactors are believed to undergo dinitrogen via the same mechanism, it is most likely that nitrogenases operate via an enzymatic pathway (Fig.1-8, b)).

### Heterogeneous

Up to now, the Mo based artificial molecular systems for the catalytic reduction of dinitrogen to ammonia were shown to be the most successful. The most outstanding examples of active catalysts are derivatives of Schrock systems<sup>142</sup>, where most species of the hypothesized catalytic cycle have been isolated and thoroughly characterized and remaining species resulted in disproportionation reactions yielding other intermediates of the catalytic cycle and generation of ammonia<sup>143,144</sup>. Thanks to this very intensive work, a clear catalytic pathway can be depicted for the reduction of dinitrogen on these trisamidoamine molybdenum systems, illustrated as the following:

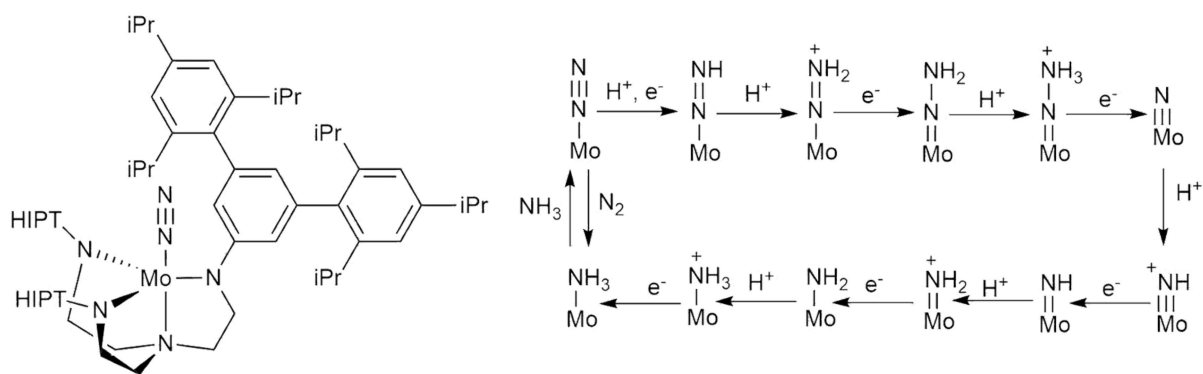


**Figure 1-7.** Structure (left) and catalytic cycle with hexaisopropylterphenyl substituents (right) adapted from<sup>133</sup>.

The dinitrogen coordinates follow an end-on fashion to the molybdenum center and the reduction to ammonia occurs via a so-called distal pathway, wherein the N-atoms are protonated and reduced sequentially, as shown in Figure 1-7. The first reduction step is believed to proceed via a proton-coupled electron transfer (PCET) mechanism, resulting in the formation of MoNNH species. These species are the most sensitive in the reaction pathway, and if steric bulk is lacking around the Mo centre, then H<sub>2</sub> is rapidly produced by  $\beta$ -elimination of hydrogen, regenerating the initial dinitrogen complex<sup>145</sup>. Just like for the natural systems, it emphasizes that formation of dihydrogen is not simply a side reaction, but may also result from the decomposition of partly hydrated intermediate species from the catalytic cycle. Moreover, for both natural and artificial systems, hydrogen is an inhibitor for dinitrogen reduction catalytic activity as it coordinates more strongly to the Mo centre than ammonia or dinitrogen<sup>146</sup>.

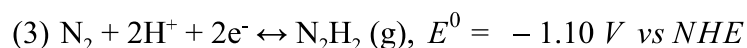
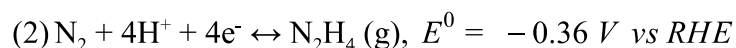
### Thermodynamics

Theoretically, electrochemical<sup>147</sup> and photochemical<sup>148–150</sup> reduction of dinitrogen to ammonia, from water and air, using heterogeneous catalysts is possible. It would benefit from possible clean and renewable energy sources for achieving NH<sub>3</sub> production. Electrochemical

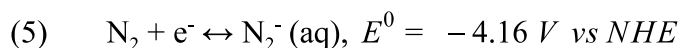
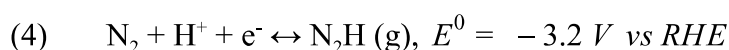
reduction of dinitrogen can be more efficient than photochemical alternatives, as not all photons can be converted to electrons, due to multiple wavelength and fast charge carrier recombination. Thermodynamically speaking<sup>151</sup>, the fundamental challenges affiliated with the electrochemical reduction of dinitrogen by PCET are imposed by the relevant intermediates of the following overall reaction, here in acidic media:



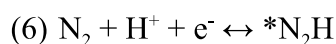
The equilibrium potential for the two most important and detectable intermediates of the dinitrogen reduction through an alternating mechanism, i.e. hydrazine ( $\text{N}_2\text{H}_4$ ) and diazene ( $\text{N}_2\text{H}_2$ ), is also known<sup>8</sup>:



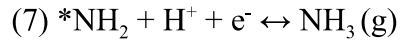
Such negative equilibrium potential illustrates the thermodynamic difficulty of hydrogenation of dinitrogen. Also, the thermodynamic potential for the first electron transfer have been estimated<sup>131</sup>:



If a PCET mechanism is considered for the electrochemical dinitrogen reduction, the most likely first formed specie corresponds to  $\text{*N}_2\text{H}$  species.

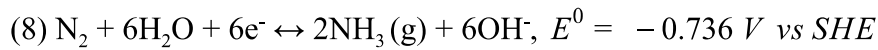


Following this mechanism, the most likely last step is desorption of the  $\text{NH}_2^*$  species, such as:

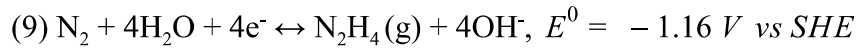


Where \* is a free active site on the catalyst surface. From reaction (5),  $\text{N}_2\text{H}^*$  needs to bind very strongly for the reaction (7) to have the best equilibrium potential. Thus, the binding energies of  $\text{NH}_2$  and  $\text{N}_2\text{H}$  species are not independent, and therefore favouring the binding of  $\text{N}_2\text{H}$  species will lead to over binding of the  $\text{NH}_2$  species. Additionally, having a weak binding of  $\text{NH}_2$  to optimize the conditions required by equation (7) will lead to weak absorption of the  $\text{N}_2\text{H}$  and disfavour the reaction depicted in equation (6). In this energetic relationship, the relative adsorption energy of the intermediates are intertwined, this is referred to as the "scaling relations"<sup>151</sup>.

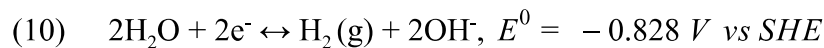
In alkaline media (pH=14) the overall reaction can be described as:



The formation of the hydrazine was also simulated to be:



The competing HER reaction at the same pH can be expressed as:



Making this process more favourable to be performed in alkaline media, due to the hindrance of HER compared to acidic conditions, where the proton availability will be a driving force for HER.

Plus, electrochemically speaking, splitting the  $\text{N}_2$  triple bond requires a reduction overpotential where the eminent competing hydrogen evolution reaction (HER) occurs, which needs to be suppressed by intelligent design<sup>147</sup>. Kinetically, the rate determining step



(RDS) is usually suggested to be the proton-coupled electron transfer process yielding the  $*N_2H$  intermediate (7), where  $*$  is a surface active catalytic site<sup>133,147,152–156</sup>. As it requires a solvated  $N_2$  molecule, an electron from the working electrode, and a proton from the electrolyte. This charge transfer requires a high solvent reorganization energy to occur, which is rare, resulting in slow kinetics as well<sup>157</sup>.

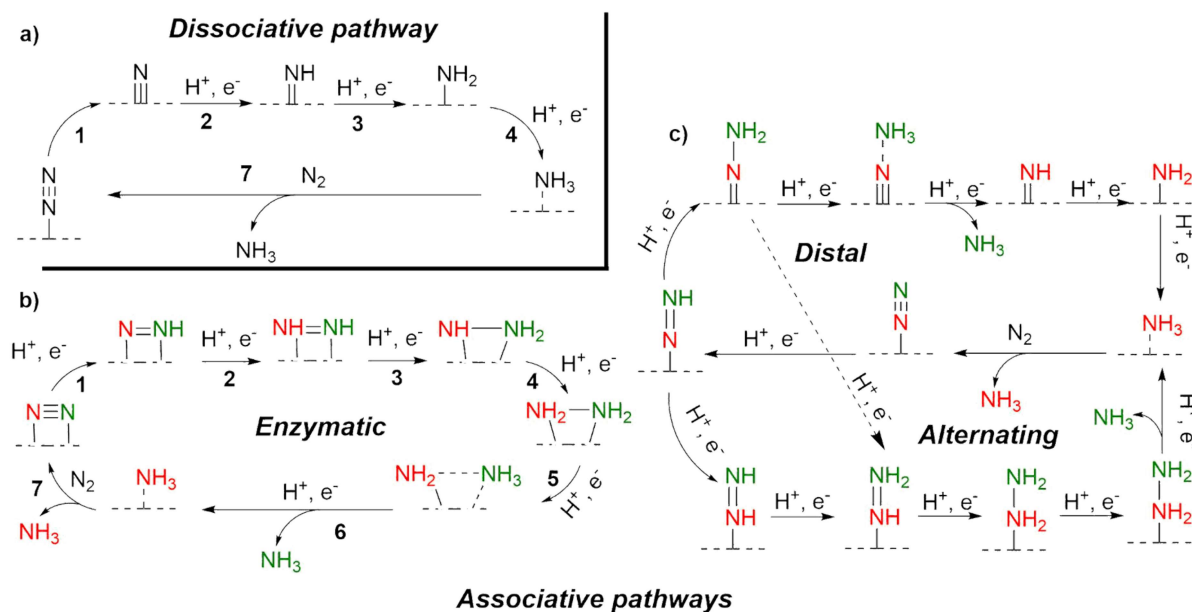


**Figure 1-8.a-c)** Scheme of the different proposed mechanisms for the catalytic conversion of dinitrogen to ammonia.

The different proposed mechanisms for the reduction of dinitrogen to ammonia depicted in Fig.1-8 can be classified into a) the dissociative pathway; b) and c) the associative pathways. For the dissociative pathway, the first step consists in breaking the highly stable N-N triple bond, and will therefore require high energy in order to proceed; it is the most plausible pathway for the highly energy demanding Haber-Bosch process. The associative pathways -b) and c)- share the same first step, after the adsorption of the dinitrogen molecule, the proton-electron addition step leading to the formation of  $*N=NH$  intermediate, where  $*$  is

an active catalytic site. From there, the successive adsorption of electrons and protons on the peripheral nitrogen will lead to the formation of one  $\text{NH}_3$  molecule, then following the same mechanism, another  $\text{NH}_3$  molecule is liberated, it is the "distal" pathway. Thus, upon the formation of the  $^*\text{NNH}_2$  intermediate in the distal pathway, it is possible that the next PCET will lead to the formation of  $^*\text{NHNH}_2$ , therefore following an "alternating" pathway. In the alternating pathway, after the formation of the common  $^*\text{NNH}$  intermediate, the PCET are alternated on the nitrogen centres, leading to the formation of notably  $^*\text{NHNH}$  and  $^*\text{NH}_2\text{NH}_2$  intermediates. From these intermediates, diazene ( $\text{N}_2\text{H}_2$ ) and hydrazine ( $\text{N}_2\text{H}_4$ ) molecules can be liberated, and therefore probing for such intermediates gives mechanistic information on the favoured catalytic pathway.

### *Electrochemical Design*

Electrochemical synthesis of  $\text{NH}_3$  from  $\text{N}_2$  and  $\text{H}_2\text{O}$ , utilizing power generated from renewables, could sustain a distributed  $\text{NH}_3$  production<sup>158</sup>. Although an electrochemical approach to the ammonia synthesis under aqueous conditions has been demonstrated on several catalysts in very diverse conditions<sup>151,159–164</sup>, the catalysts are scarce and generally perform poorly, achieving moderate yields and poor Faraday efficiency (FE).

Since the beginning of the 21<sup>st</sup> century, the electrochemical synthesis of ammonia over heterogeneous catalysts under ambient conditions has gained considerable interest as a replacement strategy for the Haber-Bosch process. So far, attempts utilizing noble metals<sup>157,165</sup>, transition metals<sup>166</sup>, metal oxides<sup>134,167,168</sup>, metal-free catalysts<sup>169</sup>, and their hybrid materials have been investigated. In order to test the performances of electrocatalysts, a large range of electrochemical set-ups have been developed worldwide by the different research

groups, where liquid aqueous to solid electrolytes are utilized in systems from back-to-back to single-chamber cells, illustrated in Fig.1-9.

The back-to-back cells utilizing solid-state electrolyte for the dinitrogen electroreduction to ammonia can be operated within a wide range of temperatures (25-800°C)<sup>170,171</sup>. Usually, both the cathode and anode are made from porous material and the two cell compartments are separated by a polymer membrane. Among the membranes used at ambient conditions, the most used are perfluorosulfonic acid proton-exchange membranes such as Nafion membranes, as previously discussed in the acidic PEM fuel cells and electrolyzers subchapter.

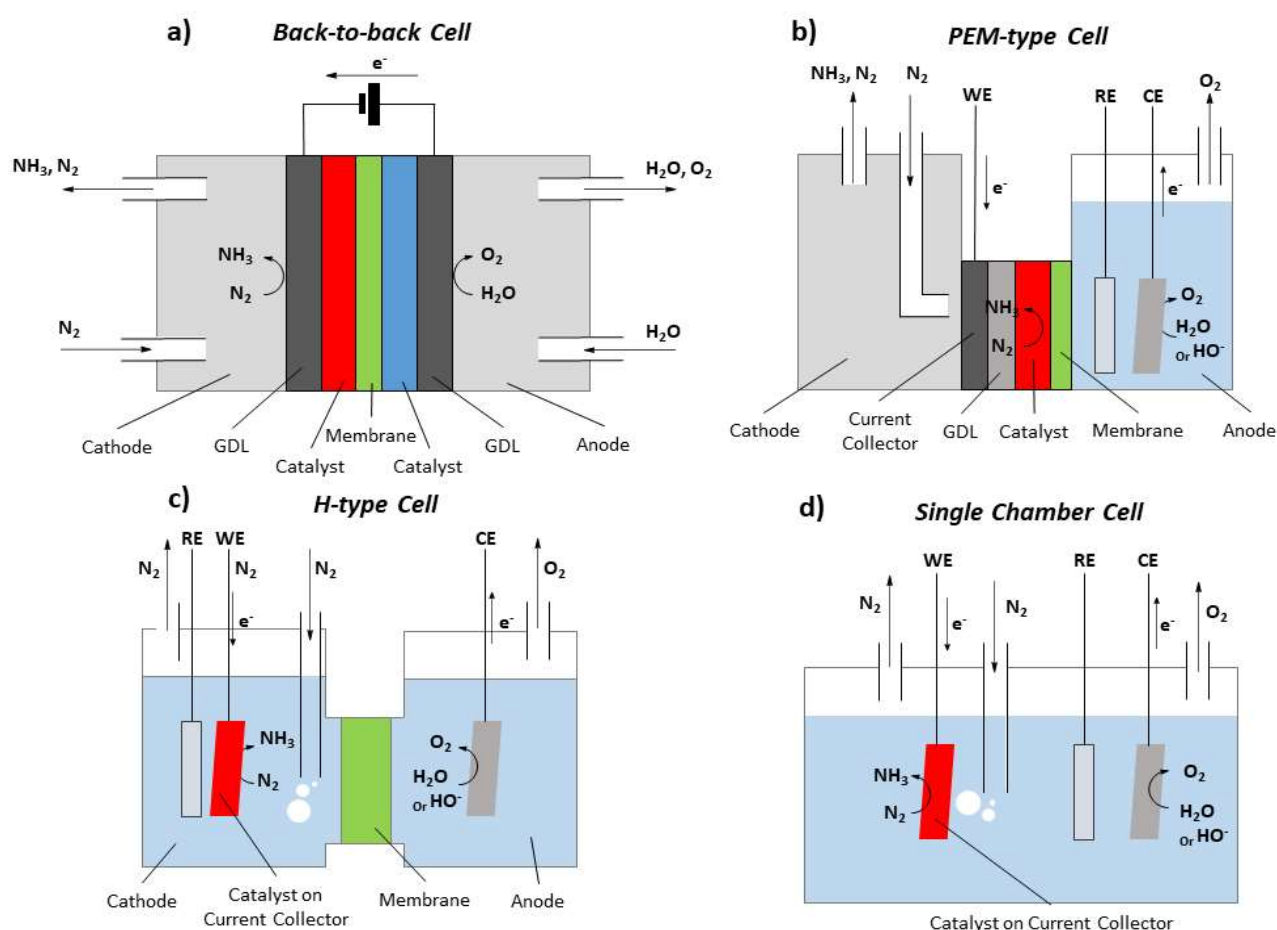


**Figure 1-9.** Scheme of the different types of electrochemical cells tested for the ambient dinitrogen reduction (a) Back-to-back cell, b) Proton-Electron-Membrane –type cell, c) Hydrogen-type cell and d) Single chamber cell, adapted from<sup>151</sup>.

Unfortunately such membranes are acidic and can therefore absorb ammonium ions ( $\text{NH}_4^+$ ) within their structure, which can be a considerable source of bias when quantifying ammonia generated from dinitrogen reduction. Moreover, the proton conductivity of the Nafion membranes decreases when exceeding  $80^\circ\text{C}$ , as the water content decreases within the membrane, resulting in slower kinetics, generally slowing down the synthesis of ammonia.

Back-to-back electrochemical type cells can also afford the use of liquid electrolytes, which extends the range of usable catalysts and electrolytes. Indeed, Kong *et al.*<sup>172</sup> recently reported the use of nano  $\gamma\text{-Fe}_2\text{O}_3$  in KOH electrolyte, achieving up to 1.9% Faraday efficiency (FE) with a weight-normalized production rate of  $12.5 \text{ nmol.h}^{-1}.\text{mg}_{\text{cat}}^{-1}$  at 0.0V vs RHE. They also deposited the same electrocatalyst onto porous carbon paper to generate the cathode, leading to an increase in the weight-normalized production rate up to  $55.9 \text{ nmol.h}^{-1}.\text{mg}_{\text{cat}}^{-1}$ . It suggests that this increase might be due to the high conductivity properties of the carbon paper or that the carbon paper has some intrinsic activity for the dinitrogen electroreduction to ammonia.

The Polymer Electrolyte Membrane (PEM) type cells were investigated as early as in 2000 by Kordali *et al.*<sup>173</sup>, where they utilized a ruthenium catalyst on a carbon support, achieving production rates of ammonia up to  $1.30 \mu\text{g.h}^{-1}.\text{cm}^{-2}$  at -1.02 V vs Ag/AgCl at  $90^\circ\text{C}$  with a current efficiency of 0.24% in 2.0 M KOH electrolyte. Recently, Chen *et al.*<sup>174</sup> reported the use of iron oxide supported on carbon nanotubes for the efficient electrochemical synthesis of ammonia utilizing a triple-phase type reactor. Where, gaseous nitrogen is supplied to the cathodic chamber, reaching the electrocatalysts deposited on a gas-diffusion layer (GDL), a highly porous and conductive carbon support. The protons generated at the

anode are conducted by the Nafion membrane to the active catalytic site. Hence, are to be brought to the catalyst deposited on GDL: on one side the electrons and  $N_2$  (by diffusion); and on the opposite side, the protons from the counter electrode (carried by the electrolyte). Succeeding in the optimisation of diverse parameters (such as iron loading, electrolyte, applied potential, temperature...), they reported on a 30 wt%  $Fe_2O_3$ -CNT catalyst, a rate production of  $NH_3$  of  $1.06 \cdot 10^{-11} \text{ mol.cm}^{-2} \cdot \text{s}^{-1}$  with a FE of 0.164% at -2.0V vs Ag/AgCl for their best performances<sup>175</sup>. Furthermore, they were able to stop ammonia from crossing the Nafion membrane towards the counter electrode electrolyte by introducing an additional GDL between the electrocatalyst and the Nafion membrane. Indeed, ammonia reaching the counter electrode could easily be oxidized and therefore the overall measured ammonia produced would be underestimated. Such intelligent cell design presents an elegant way to face some intrinsic challenges brought by the dinitrogen reduction, without yet worrying about the catalyst performances.

For the single chamber type cells, Amar et al.<sup>162</sup> utilized the well-studied  $Co_3Mo_3N$  catalyst in a single chamber type cell with a  $LiAlO_2$ -(Li, Na, K) $_2CO_3$  composite electrolyte. They managed successful ammonia synthesis with the best performance recorded at 450°C with a rate of production of  $3.27 \cdot 10^{-10} \text{ mol.s}^{-1} \cdot \text{cm}^{-2}$  when 0.8 V vs RHE were applied. Díez-Ramírez *et al.* reported Ag-doped  $Co_3Mo_3N$  to show some catalytic activity at high temperatures too<sup>171</sup>. Unfortunately, high temperatures are required in order to achieve sufficient protonic ion conductivity for the composite electrolyte, which would translate to high energy costs in the scale up of this process.

The main type of electrochemical cell that has been the most utilized is the H-type of cell, it is a well-known design that has been previously used in other electrochemical reaction

studies, notably for the carbon dioxide reduction reaction (CO<sub>2</sub>RR)<sup>176</sup>. Utilizing this H-type of cell, one can focus on the catalyst design rather than the cell design at first, as it offers an easy mean of comparison between reported studies. In this work the H-type cell is the cell design of choice.

### *Electrocatalyst Design*

When one thinks about designing an N<sub>2</sub>RR electrocatalyst efficiently; high surface to volume ratio, dispersion of catalytic site to avoid agglomeration, high porosity and good conductivity should be featured.

Previously, metal -organic frameworks (MOF)<sup>177,178</sup> were candidates of interest as they are well-defined self-assembled materials presenting both high porosity and high volumetric capacity per mass units, which overall are desired parameters for the development of N<sub>2</sub>RR electrocatalysts. The well-defined structure of the catalysts coordination environment can be tuned and offer varying catalytic properties of the metallic centre. The development of these electrocatalysts, such as MOF(Fe) were reported by Zhao *et al.*<sup>179</sup> with rates of formation and current efficiency of 2.12x10<sup>-9</sup> mol.s<sup>-1</sup>.cm<sup>-2</sup> and 1.43%, operating at -1.2 V and 90°C in 2 M KOH electrolyte, respectively. Unfortunately, most MOF assemblies suffer from poor water stability within operando conditions, and therefore these stability issues greatly limit the application of MOFs as electrocatalysts in aqueous media.

In order to benefit from the self-assembled materials properties, carbonization of such metal-organic frameworks, such as zeolites, can lead to the formation of a graphitized carbon matrix with or without presenting well-dispersed metallic centres. For example, porous nitrogen-doped carbon based electrocatalysts derived from the calcination of ZIF-8 precursors were also reported to have some activity for dinitrogen reduction reaction (N<sub>2</sub>RR)

by Mukherjee *et al.*<sup>169</sup> achieving  $\text{NH}_3$  production rates up to  $3.4 \times 10^{-6} \text{ mol.cm}^{-2}.\text{h}^{-1}$  with Faraday efficiency (FE) of 10.2% at -0.3 V vs. RHE under aqueous ambient conditions in 0.1 M KOH electrolyte<sup>169</sup>. Following the same trend, Liu *et al.* also investigated such materials and reported production rates of  $1.40 \text{ mmol.g}_{\text{cat}}^{-1}.\text{h}^{-1}$  at -0.9 V vs. RHE under ambient conditions in 0.05 M  $\text{H}_2\text{SO}_4$  electrolyte; suggesting by density functional theory (DFT) calculations that pyridinic and pyrrolic N as active sites for  $\text{N}_2\text{RR}$ <sup>180</sup>. Therefore, metal-free nitrogen-doped carbon materials electrocatalysts -that can be derived from carbonization of inexpensive bio-waste sources- can represent interesting candidates for sustainable electrocatalysts generation for ammonia synthesis.

### Computational Predictions

Nowadays, the use of computational studies for the evaluation of possible candidates as catalysts for  $\text{N}_2\text{RR}$  represent a major predictive tool in order to narrow down the number of these candidates that are worth being investigated experimentally. Based on DFT calculations carried out mainly by Abghoui *et al.*, metal nitrides (MN) such as ZrN, CrN, NbN, VN<sup>155,181</sup>,  $\text{Mo}_2\text{N}$ <sup>182,183</sup>, or even  $\text{MoC}_2$ <sup>184</sup> and zincblende<sup>185</sup>, were investigated for the dinitrogen electroreduction to ammonia. Indeed metal nitrides can be more active towards dinitrogen reduction over the hydrogen evolution reaction than their metallic counterparts. The required onset potential was predicted to follow a Mars-van-Krevelen (MvK)<sup>186</sup> mechanism (Fig.1-10).

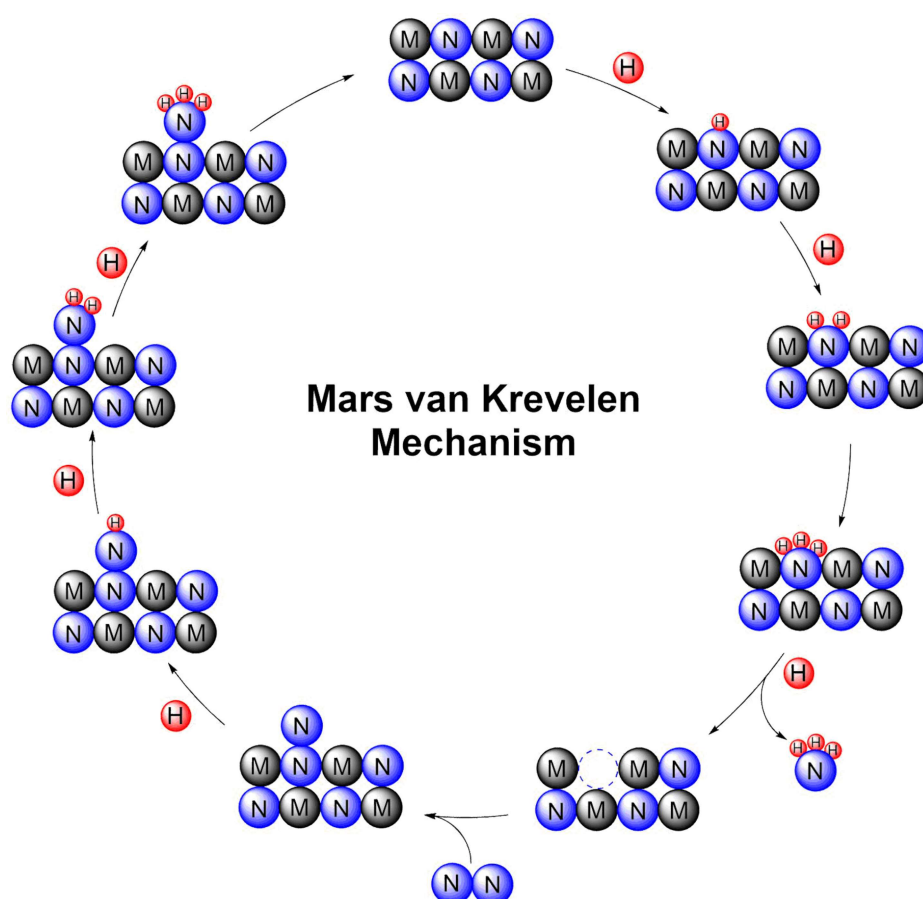


**Figure 1-10.** Schematic representation of the Mars van Krevelen mechanism on metal nitrides. M, N and H stand for metal, nitrogen and hydrogen, respectively.

In this mechanism the N atom from the metal nitride<sup>187</sup> is successively protonated and leaves as  $\text{NH}_3$ , leaving an empty active site for the next  $\text{N}_2$  to be adsorbed. The main challenges for such mechanism reside in the catalyst surface vacancy poisoning, and the likelihood of catalyst decomposition from the protonation of the metal-bonded nitride if it is not regenerated upon adsorption of an N-atom<sup>181</sup>. They investigated metal mononitrides in both zincblende<sup>185</sup> and rocksalt structure, and from this study the most promising catalysts were CrN, NbN, ZrN, and VN of the rocksalt (100) structure. The same group also investigated transition metals mononitrides of the rocksalt (111) facets, and from these DFT



calculations, MoN, WN, VN, CrN, and NbN were predicted to have low onset potentials for the dinitrogen reduction<sup>48</sup>. Unfortunately, only NbN was found able to regenerate itself, and therefore finish the all catalytic cycle for the dinitrogen reduction to ammonia under operating conditions. Indeed, the other transition metal nitrides would decompose to their metallic forms.

Whatever the catalytic pathway, dinitrogen reduction is non-trivial from a theoretical point of view both kinetically and thermodynamically. This leads to thinking that it will be even harder experimentally. Furthermore, one needs to be thorough regarding experimental procedures and use sufficient controls in order to ensure consistency and accurate measurements of  $\text{NH}_3$ , as sources of contamination are easily present in a laboratory environment<sup>188</sup>.

Consequently, one needs to keep in mind such parameters for the successful intelligent design of new highly selective and efficient electrocatalysts for ambient aqueous  $\text{N}_2\text{RR}$ .

### 1.3 Energy Storage Systems: Battery

In order to fully transition to a renewable energy grid, efficient energy storage systems (ESS) technologies need to be developed. By 2050, our worldwide electricity consumption is expected to double due to the ever-increasing population and energy demand. Indeed, depending on the scale and desired specific capacity; different technologies can be utilized. Underlying, is recognizing that inexpensive ESS are vital for economic development for a society based on renewable energy sources<sup>189</sup>.

Though ESS cannot address all above-mentioned challenges, it does offer a well-established approach for improving energy grid utilization and reliability. The role of the ESS in the grid is to supply electricity when and where it is needed. In the near future we are still unlikely to find a single technology that can repeatedly and efficiently store large quantities of electric energy at low cost, therefore a multitude of energy storing technologies are desirable to cope with the demand on every scale<sup>23,189–191</sup>. Each technology offers a distinct set of advantages and disadvantages, challenges and shortcomings<sup>192</sup>

Available energy storage technologies for large-scale applications are classified into four main groups: chemical, electrochemical, electrical and mechanical.

Today, 99% of the worldwide storage capacity is based on pumped hydroelectric systems where energy is stored in the form of gravitational potential energy, representing 127'00 MW of discharge power<sup>21,193</sup>. However, these localized systems necessitate a height difference in the landscape, usually a hill or a mountain, and water to be available in sufficient quantity. When such gigantic volumes of water are stored up-hill in pumped hydro storage systems, it represents a potential danger for the surrounding population, potentially devastating all surrounding life in case of a major incident. Other storage systems are of interest, within which, the batteries are one of the most promising candidates as portative energy storage systems. When such gigantic volumes of water are stored up-hill in pumped hydro storage systems, it represents a potential danger for the surrounding population, potentially devastating all surrounding life in case of a major incident. Other storage systems are of interest, within which, the batteries are one of the most promising candidates as portative energy storage systems.

Electrochemical storage systems are based on: chemical bonds of fuels (i.e.  $H_2$  fuel cells), electrochemical interfaces for supercapacitors or electrochemical capacitors, and on charge storage for the case of batteries. Herein, batteries will be the object of focus.

Batteries, regardless of their chemistry (aqueous or non-aqueous, Li or Na-based) store energy within the electrode's structure through charge transfer reactions<sup>194</sup>. In fuel cells, the energy is stored in the reactants that are fed to the cells, they are not rechargeable. Both systems differ from redox-flow cells/batteries<sup>191</sup>, where the energy is stored in redox species that are continuously circulating through the cells. Supercapacitors<sup>195</sup> have yet another different energy storage mechanism, via a capacitive process arising from an electrochemical double layer at the electrode-electrolyte interface.

Batteries usually consist of four active components: a cathode, an anode, a separator and an electrolyte, that connects both electrodes ionically. Although the configuration is simple, the interaction of components with one-another is very complex. Key parameters such as energy, specific capacity, cycle lifetime, efficiency, cost and safety have to be optimized simultaneously by intelligent design<sup>196</sup>. The complexity of battery systems rises even more when considering the chemical and electrochemical interactions of "inert" components such as the separator, the electrolyte, the electrolyte additives or the current collectors.

Batteries can be composed of one or several electrochemical cells that are connected in series and/or in parallel, providing the required voltage and capacity. Batteries can either be primary (non-rechargeable) or secondary (rechargeable). Herein, the primary batteries will be outside of the scope as they are not suitable for energy storage. In general, these secondary batteries present desirable features such as high round-trip efficiency, flexible power and

energy characteristics, pollution-free operation to cope with many grid functions, long cycle life, and low maintenance. Batteries have the advantage of being compacted, which is appropriate to use locally in order to provide additional control over the frequency to reduce the variations caused by intermittent sources of power such as wind or solar.

The energy of a battery  $E_{cell}$  (J) can be express as:

$$(1) E_{cell} = C_{cell} \cdot V_{cell}$$

Where,  $C_{cell}$  is the cell capacity (C), and  $V_{cell}$  is the cell voltage (V) defined by the difference between the positive electrode (cathode) and the negative electrode (anode) potentials. The capacity of the cell can be expressed as:

$$(2) \frac{1}{C_{cell}} = \frac{1}{C_a} + \frac{1}{C_c}$$

Where,  $C_a$  and  $C_c$  represent the capacity of the anode and the cathode respectively (C or A.s).

Nowadays, worldwide, over 200 installations use sodium/sulfur technology as energy storage systems, accounting for 315 MW of discharge power capacity<sup>197</sup>. Emerging storage systems such as low-cost redox flow batteries and high performing lithium-ion batteries (Li-ion) are considered for applications on different scales. Indeed, the techno-economical market analysis decides which storage system is the most suitable for a particular scale<sup>198</sup>. For example, light-weighed, fast charging li-ion batteries are suitable for portable devices<sup>199</sup>.

For the sake of briefness, only a few storage systems will be discussed, with an emphasis on Li-ion batteries, the focus of our research.

### 1.3.1 Li-ion Batteries

#### *History and Context*

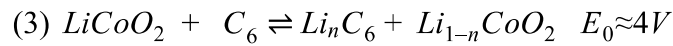
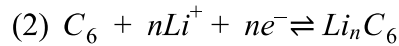
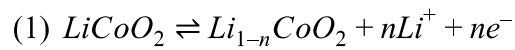
The battery technological upgrade lead to many noticeable societal changes. The successful commercialization of Li-ion batteries had a major impact on the development and widespread of portable electronics (portable computers, cell phones), transportations (Tesla®,...), or stationary storage applications<sup>200,201</sup>.

Lithium (Li), which was discovered by J. A. Arfweson in 1817<sup>202</sup>, is the first metal on the periodic table, belonging to the alkali metal group. It has the lowest density among metals ( $0.534\text{g}\cdot\text{cm}^{-3}$ ), and is one of the most reactive. It is nearly a century later that, in 1913, Lewis and Keyes<sup>203</sup> realized the electromotive power of Li, measuring a potential equivalent of 3.0564 V vs RHE. They declared that Li has "the highest electrode potential"; this statement is still true today and serves as the foundation for Li as the ultimate anode material for battery applications. However, this potential enables extremely high chemical and electrochemical reactions, most of which are undesired.

Lithium is a monovalent ion ( $\text{Li}^+$ ) and has a combination of small atomic weight, small radius, and low reduction potential which makes it the perfect candidate of in terms of gravimetric capacity ( $3,860\text{ mAh}\cdot\text{g}^{-1}$ ) and ionic diffusion for storage applications, with nearly no safe nor scalable elemental rivals<sup>204</sup>.

A first milestone in LIB was set by Harris<sup>205</sup> in 1958 where in his thesis, he evaluated the importance of using cyclic carbonate esters as non-protic non-aqueous solvents acting as electrolytes for the ionic conduction of  $\text{Li}^+$ . From the 1970s, Li metal anode primary batteries were developed, with the lithium-carbon monofluoride ( $\text{Li-CF}_x$ ) of Matsushita in 1973, followed by the commercial lithium-manganese dioxide primary cells of Sanyo in 1975<sup>206</sup>,

used as primary cells in small portable electronics. However, due to the lack of reversibility and the safety hazard linked to metallic Li, immense efforts were still needed to overtake the battery market. Based on the conceiving and development work of Asahi Kasei Co., Li-ion battery (LIB, rechargeable) technology was commercially introduced by Sony in the early 1990s<sup>207</sup>. Such batteries were based on the use of layered materials for Li-intercalation, such as graphite as anode material instead of Li metal, and of lithium cobalt oxide ( $\text{LiCoO}_2$ ), as cathode material. Li ions migrate across the electrolyte located between the two host structures, which serve as the positive and negative electrodes. Both half reactions of the cathode (1) and the anode (2), as well as the overall reaction of the battery (3) are illustrated as (Fig.1-11):



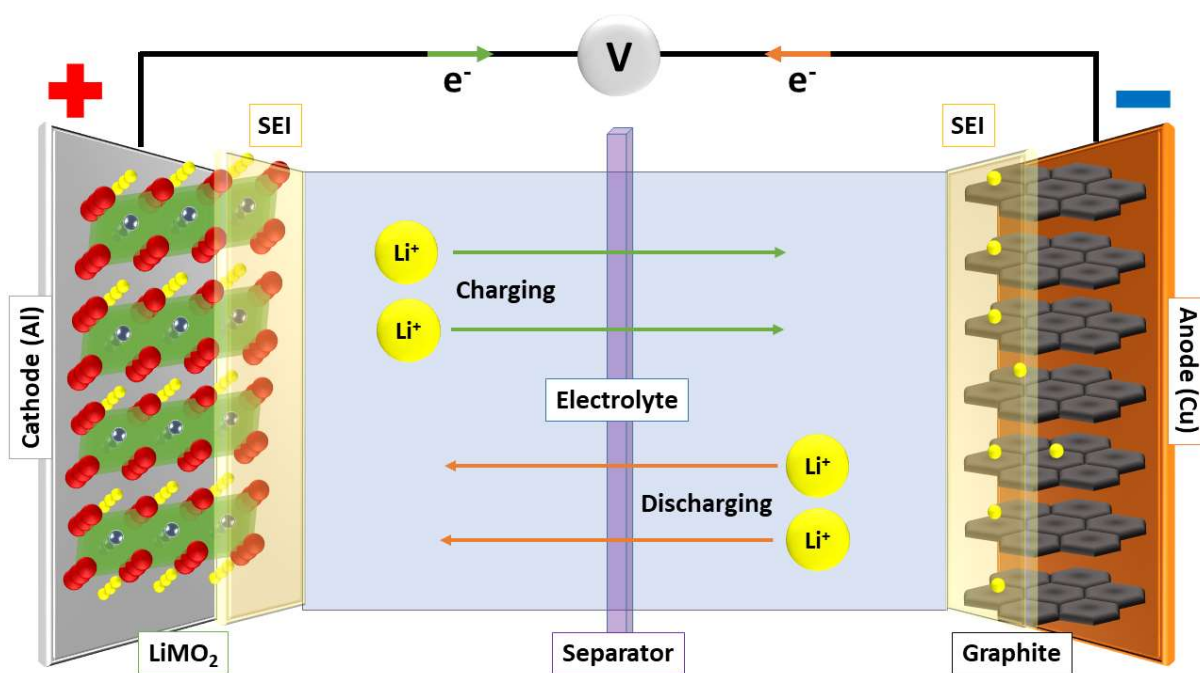


**Figure 1-11.** Schematic representation of charge-discharge process on a lithium-ion cell using graphite and  $\text{LiMO}_2$  electrodes.

Upon charging, an external voltage is applied across the anode and the cathode, driving the half reactions from left to right in (1) and (2). Lithium ions are formed from the lithium cobalt oxide at the cathode, diffuse across the electrolyte, and insert within the interlayer of the graphitic anode. For the formation of the lithium ion at the cathode, the cobalt is oxidized ( $\text{Co}^{3+}$  to  $\text{Co}^{4+}$ ), generating a free electron to maintain charge neutrality. These electrons travel through the wires connecting each electrode, and participate in the half-reaction of lithium insertion into graphite at the anode. The potential that has to be applied for charging is specific to both the anodic and cathodic materials, as well as the electrolyte composition. Upon discharge, the electrons follow from the anode to the cathode, generating a positive current that can be utilized to power electronic devices.

### *Thermodynamics and Principle*

The storage capacity of the battery is linked to the cell potential, as it is material dependent. The Gibbs free energy ( $\Delta G$ ) and the theoretical capacity ( $Q$ ) of electrode materials can be expressed as:

$$(4) \quad \Delta G = -nFE_0$$

$$(5) \quad Q = \frac{nF}{M}$$

Where,  $n$  is the number of reactive electrons,  $F$  is the Faraday constant ( $96485 \text{ C.mol}^{-1}$ ),  $E_0$  is the cell's voltage (V), and  $M$  is the molar weight of the material ( $\text{g.mol}^{-1}$ ). However, having a high cell voltage usually comes at the expense of safety, as high voltages are related to high activity leading to many unwanted and potentially dangerous side reactions, which is especially true in the case of Li-ion batteries with organic electrolytes.

A typical state-of-the-art Li-ion battery is composed of a graphite negative electrode (anode) and a transition-metal oxide ( $\text{LiMO}_2$ , where M is usually Co and/or Ni) as positive electrode (cathode), separated by a polypropylene or polyethylene thin film separator wetted in Li ion-conduction organic electrolyte. The typical electrolyte solution is  $\text{LiPF}_6$  dissolved in an organic carbonate solvent mixture, usually dimethyl carbonate (DMC), diethyl carbonate (DEC) and ethylene carbonate (EC). Thus, due to the extreme electrode potential of Li metal, leading to spontaneous chemical and electrochemical reactivity, it reacts with the organic electrolyte forming a solid electrolyte interface (SEI) of complex composition<sup>208,209</sup>. This SEI consists of solid products that conducts lithium ions, and that usually does not conduct electrons. This reactivity of Li metal forming this diversity of compound makes Li-based battery recycling extremely difficult. For every stripping/plating cycles, either the SEI is formed, either lithium ions may be deposited as "dead Li" or even form Li "dendrites", from



its preferential crystal growth, forming pointy nanowires that no longer participates in the cell reactions (Fig1-12). Both dead Li and dendrites still possesses an extreme reactivity, representing a real safety risk upon each additional charge/discharge cycle. Eventually, the dendrites may pierce the separator and get in contact with the cathode resulting in electrical short-circuiting, causing serious hazards, even explosions. Moreover, the reactions of Li with the carbonate electrolytes are exothermic and may lead to "thermal runaway" of the battery.

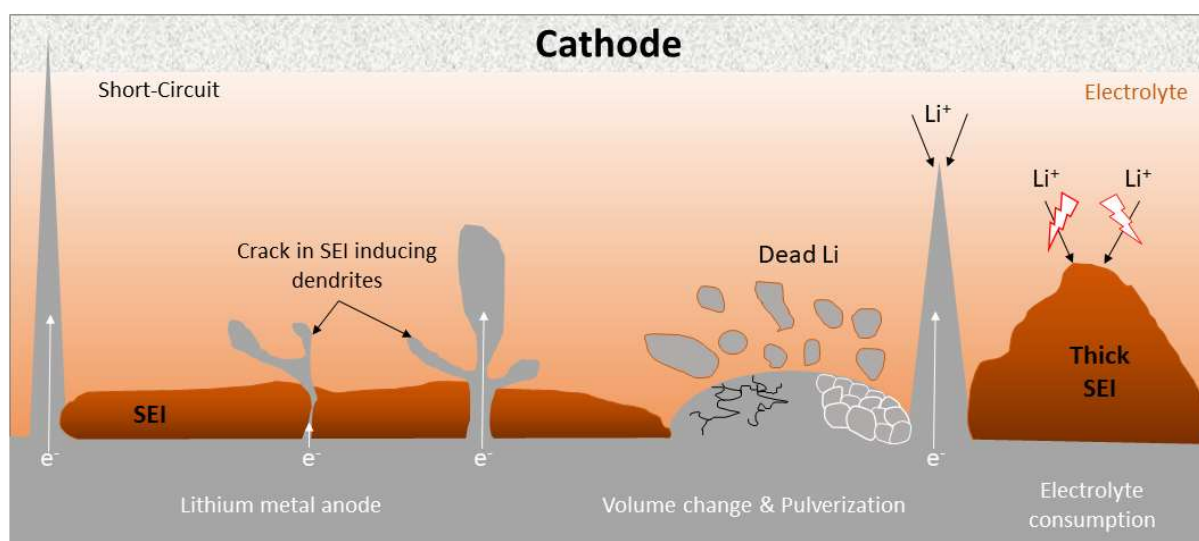
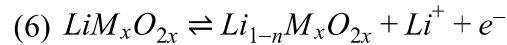


**Figure 1-12.** Mechanisms of Li unwanted side reactions leading to battery failure.

#### *Positive electrode (Cathodic) materials*

To cope with unwanted Li side reactions, i.e. SEI and dendrite formations, most of the strategies tried using negative electrode with higher potentials with respect to Li and consequently reduce the net cell voltage. To compensate with this cell voltage loss, cathode materials that exhibit high half-cell potentials and large capacities for Li insertion/intercalation were investigated<sup>210,211</sup>.

Most of the cathode materials<sup>211,212</sup> investigated for the last four decades were transition metal oxides mostly based on three different crystal structures namely: layered<sup>213</sup>, olivine<sup>214</sup> and spinel<sup>215</sup>. The layered and spinel arrangements can be described respectively by the general formula of  $\text{LiMO}_2$  (where  $\text{M} = \text{Co}, \text{Mn}, \text{Ni}$ ) and  $\text{LiM}_2\text{O}_4$  (where  $\text{M} = \text{Mn}, \text{Ni}$ ), reacting with lithium ions such as:



Transition metals<sup>216</sup> usually exhibit good  $\text{Li}^+$  conductivity as well as good electronic conductivity, as their multi-valent transition metals cations have different oxidation states available to electronic transitions. Also with appropriate doping, the electronic conductivity of these materials can be tuned, further opening the range of possible cathode materials<sup>217</sup>. Such materials usually depend on transition metals, such as cobalt (Co), that are scarce and/or toxic and can lead to safety hazards. On-going research focuses on the development of higher capacity, increased safety, and based on abundant and low-cost elements as cathode materials for sustainable and scalable consumer electronics. Materials synthesized from economically and ecologically sustainable processes and centred on abundant 3d metal redox elements such as manganese (Mn) ( $\text{LiMn}_2\text{O}_4$ ), Fe ( $\text{LiFePO}_4$ ,  $\text{Li}_2\text{FeSiO}_4$ ) and titanium (Ti) ( $\text{TiO}_2$ ,  $\text{Li}_4\text{Ti}_5\text{O}_{12}$ ) represent promising candidates<sup>218</sup>. However such cathode materials tend to have a low capacity<sup>219</sup>, and therefore Ni –which is fairly compatible with electrolytes- was introduced in order to increase the capacity ( $220\text{mA.h.g}^{-1}$ ), generating the  $\text{LiNi}_x\text{Mn}_y\text{Co}_{1-y-x}$  (NMC) cathode family<sup>220</sup>. However, as  $\text{Li}^+$  and  $\text{Ni}^{2+}$  are similar in size, and upon Li extraction,  $\text{Ni}^{2+}$  can occupy a  $\text{Li}^+$  site. Hence, this creates deformation of the layered structure, dissolution of the transition metal in the electrolyte, side reactions forming the SEI, resulting in capacity fading and poor cyclic performances<sup>221</sup>. In the case of  $\text{LiCoO}_2$ , a widely used cathode material, it

was found that metal oxide coatings would lead to increased performance by mitigation of some of the unwanted reactions<sup>222–224</sup>. This approach was further explored by depositing  $\text{Al}_2\text{O}_3$  coatings on NMC532 in chapter 3.

### Negative electrode (Anodic) materials

Although most batteries use the inexpensive, abundant graphite as layered anode material, it has limited specific capacity ( $372 \text{ mAh.g}^{-1}$ ) resulting in the opportunity for developing better materials. As mentioned above, using Li as anode materials comes with hazards that need to be addressed (Fig.1-12). Several approaches, such as Li insertion (as for graphite), conversion, or even alloying with other metals or semiconductors were investigated (Fig.1-13).

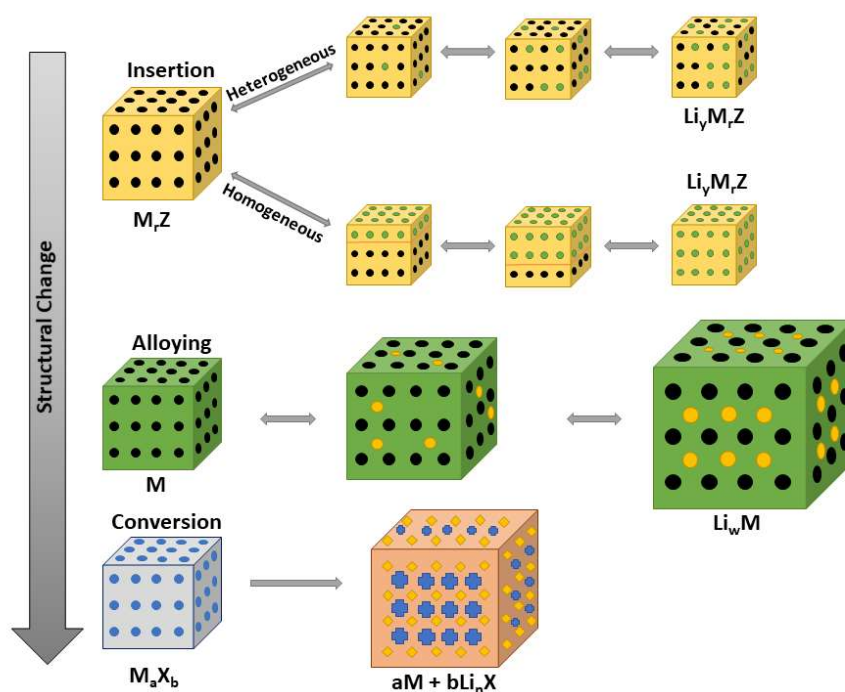
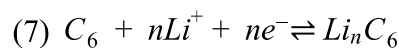


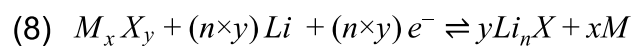
**Figure 1-13.** Mechanism of materials interacting with lithium.

Most of the commercial insertion-type anode materials are carbon based, utilizing the stack of hexagonally bonded sheets of graphite held by weak van der Waals forces<sup>225</sup>. Lithium ions are able to intercalate, around 0.05-0.1 V vs Li/Li<sup>+</sup>, both rapidly and reversibly in between graphite planes, occupying the interstitial sites according to the following reaction<sup>226,227</sup>:



But the graphitic carbon based anode suffer from a collection of competitive reactions, among which the co-intercalation of electrolyte molecules in the graphite structure, and the subsequent deterioration of such solvents, leading to the destruction of the graphitic structure overtime, the so-called "exfoliation"<sup>228</sup>.

Another type of material is the so-called conversion-type electrodes (anodes and/or cathode), that usually exhibit higher energy storage density, but suffer more from capacity fading than the intercalation-type materials<sup>229</sup>. Most conversion types have high theoretical capacity (ranging from 500 to 1500 mAh.g<sup>-1</sup>)<sup>230</sup>, higher than carbon anodes (372 mAh.g<sup>-1</sup>), and are easily available, abundant and inexpensive<sup>231</sup>. Conversion-type active materials, upon charging/discharging cycles, react reversibly as:

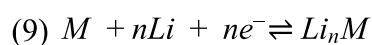


Where,  $M$  is a transition metal or a mix of transition metals (i.e.  $\text{Mn}_3\text{O}_4$ <sup>232</sup>,  $\text{Fe}_3\text{O}_4$ <sup>233</sup>, ...),  $X$  stands for an anion (i.e. oxygen, halogen, chalcogenide, ...) or a combination of anions, and  $\frac{n \times y}{x}$  is the formal oxidation state of  $M$ . Equation (8) describes the overall process, and can be compartmented into several intermittent stages and intermediate phases. Each individual active material has a unique path for charge and discharge stages and phases, in regard to parameters like lithiation/delithiation sequence, general composition and crystal structure<sup>231</sup>.

Usually, during the first lithiation/delithiation steps the conversion material will undergo irreversible changes, leading to a change in capacity and a hysteresis of the lithiation/delithiation potentials. The major drawbacks for using conversion-type materials for commercial batteries, compared to state-of-the-art, can be summed as<sup>234</sup>: low conductivity, short cycle life and voltage hysteresis. The low conductivity is intrinsic to most conversion materials, and it is leading to low active material utilization and low power performance<sup>235</sup>. The short cycle life can be accounted for by large volume expansion and continuous SEI formation upon each conversion step<sup>236</sup>. Furthermore, a hysteresis of lithiation/delithiation voltages is usually due to irreversible conversions during the first cycles, leading to low charge/discharge energy efficiency<sup>237</sup>. Finally,  $Li_nX$  species are often soluble in the electrolyte, further lowering the cycle life of the battery.

Thus, capacity fading of conversion-type materials has been attributed to the contact failure between the active material and current collector, or to the continuous breakdown of the SEI leading to fresh exposure to lithium and its unwanted side-reaction reducing the capacity upon each new charge/discharge cycle. Additionally, lithium can be trapped inside the bulk material, leading to further capacity fading<sup>238</sup>.

Another type of electrode materials are the alloys (or intermetallics), first addressed in early 1970s, where lithium reacts spontaneously with metals or semi-metallic elements to form alloys of various compositions<sup>239</sup>. They are promising for their high specific capacity and overall increased safety<sup>240</sup>. The reaction between lithium ions and the material, forming the alloy, can be described as:



Where,  $M$  is a metal ( $\text{Al}^{241}$ ,  $\text{Sn}^{242}$ ,...) or a semi-metal ( $\text{Si}^{243}$ ,...), and  $n$  is the number of electrons and lithium ions involved in the reaction. The most promising alloy candidates as anode materials for the next-generation of Li-ion batteries are aluminium (Al), tin (Sn)<sup>244,245</sup> and silicon (Si). They tend to have a high-capacity (three to ten times the one of commercial graphite,  $372 \text{ mAh.g}_\text{C}^{-1}$ ), but are suffering from severe volume expansion upon alloying with lithium (only +10% volume increase for  $\text{LiC}_6$  compared to  $\text{C}_6$ )<sup>226</sup>. Furthermore, Si and Al have an onset potential around 0.3-0.4 V vs  $\text{Li/Li}^+$  which increases the overall safety, preventing metallic lithium plating, without compromising the overall cell voltage. Aluminium alloys with a the formation of  $\text{LiAl}^{246}$  that can reach  $990 \text{ mAh.g}_\text{Al}^{-1}$  with a 100% increase in volume; tin, with the formation of  $\text{Li}_{22}\text{Sn}_5$ <sup>247</sup>, can reach around  $990 \text{ mAh.g}_\text{Sn}^{-1}$  undergoing a +250% volume expansion; and finally silicon, forming  $\text{Li}_{22}\text{Si}_5$ , has the highest theoretical capacity of  $4200 \text{ mAh.g}_\text{Si}^{-1}$ , thus suffering from a +300% increase in volume<sup>248</sup>. Even though silicon, a non-toxic, inexpensive, and abundant material, suffers from low electrical conductivity and drastic volume changes, it is regarded as the most promising candidate for next-generation LIB as for its high specific capacity and proper working voltage.

Thus, such huge volume changes upon lithiation/delithiation cycles are responsible for irreversible damage such as fracture and pulverization, electrical insulation, unstable and continuous SEI formation, and irreversible Li trapping<sup>249</sup> (Fig.1-14). During lithiation, an expansion happens at the phase boundary between  $\text{Li}_x\text{Si}$  and  $\text{Si}^{250}$ , leading to mechanical stress and anisotropic swelling. Over charge/discharge cycles, the repeated volume changes will eventually cause a mechanical fracture, leading to the pulverization of Si leading to the electric isolation of considerable amounts of active Si. In order to cope with the fracture and

pulverization, it has been proposed that reducing the size of the Si particles to nanoparticles would help coping with the induced mechanical stress<sup>251</sup>.

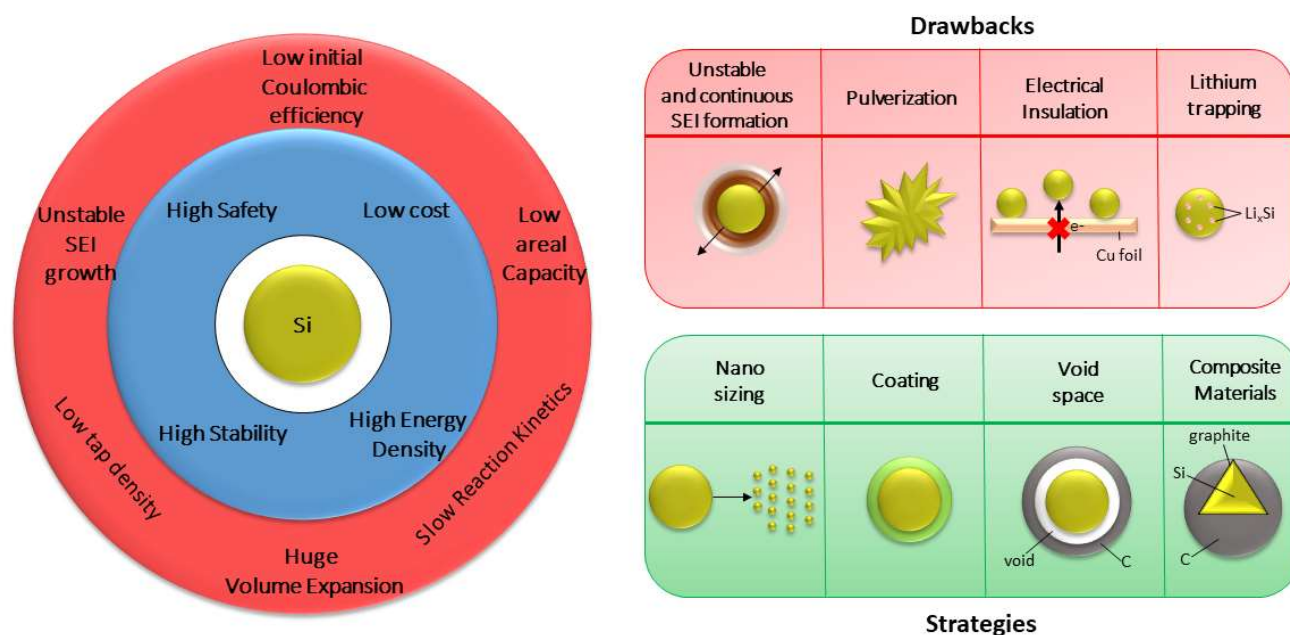


**Figure 1-14.** Si as anode for LIB, overview of advantages, drawbacks, shortcomings and coping strategies.

Additionally, the drastic volume changes usually destabilize the formed SEI, leading to a continuous SEI growth with dynamic volume changes upon cycling, as "fresh" reactive Li and Li<sub>x</sub>Si species become exposed to the electrolyte<sup>252</sup>. This continuous SEI layer formation consumes the electrolyte and the lithium ions, decreasing the capacity over time. SEI accumulation leads to increase in internal resistance, electrical isolation of Si particles to the current collector (Cu foil), and swelling of the battery, that can ultimately lead to fire and explosive hazards (battery exposed to air). Moreover, during the (de)alloying of silicon with lithium, it may lead to formation of defect sites, where the lithium can be trapped due to the complexity of phase transitions, generating irreversible structural transformations<sup>250,253–255</sup>.

In order to cope with the above-mentioned challenges and disadvantages of using silicon as anode material, while benefiting from its high specific capacity, intelligent strategies were developed (Fig.1-14).

Firstly, nano-sizing to reduce the mechanical stress on the particles upon multiple (de)alloying cycles<sup>251</sup>. Secondly, the introduction of void and/or porosity in the active material structure were investigated to manage the drastic volume changes by taking nature as a source of inspiration, yielding granada/pomegranate<sup>256,257</sup>, yolk-shell<sup>258,259</sup>, carob<sup>260</sup>, ant-nest<sup>261</sup>, coral<sup>262</sup>, sponges<sup>263</sup> and many more alike structures leading in improved charging time and performance. A third strategy is the creation of composite materials, usually coating the silicon nanoparticles with carbon/graphite materials<sup>264–266</sup>, or even other metals like copper<sup>265</sup> or silver<sup>267</sup>, in order to increase the Si electric conductivity and encapsulate overtime the generate dead material<sup>266</sup>.

Coatings, generating an artificial SEI, or encapsulating the Si particles within a confined space, were investigated with notably the use of metal organic frameworks (MOFs)<sup>268,269</sup>, zeolites<sup>270</sup>, sandwich like structure<sup>264</sup>, surface silicon oxides ( $\text{SiO}_x$ )<sup>271,272</sup> and many other intelligent designs. One that should be mentioned, and will be discussed further in chapter 4, is the use of atomic layer deposition (ALD) to deposit thin coatings<sup>273–278</sup>, usually transition-metal oxides ( $\text{Al}_2\text{O}_3$ ,  $\text{TiO}_2$ ,...) to create an artificial SEI and reduce the unwanted reactions between lithium and the electrolyte. Coping strategies above mentioned using Si as example can be generalized to any material (cathodic or anodic) suffering from similar drawbacks, and failures.

Yet another strategy highlights the importance of conductive carbon additives and binders for the optimization of electrical contact between active material and the current collector, reducing internal resistance, as well as for minimizing the electron mean free path.



Indeed, in order to coat the current collector (Cu foil) with the active material, an catalyst ink has to be prepared where: the active material (in this case Si nanoparticles) is mixed with conductive carbon (usually SuperP®, KetJen Black®, or Vulcan®,...) in an organic solvent (usually N-methyl-2-pyrrolidon) together with a binder (usually a polymer precursor like polyvinylidene fluoride or PVDF) that ensures sufficient adhesion of the ink to the current collector. The relative proportions are dependent on the surface of the active material and the ink composition may be tricky and a source of many approximations and problems, reducing the reproducibility of results.

A recent focus on the binders<sup>279</sup> has lead researchers to investigate compounds derived from the recycling of consumables, wood or food<sup>280</sup>, with for example water soluble carboxymethyl cellulose or rubber derived compounds<sup>281</sup>. The architecture of the binder seem to be correlated to its performance<sup>282,283</sup>. Conductive carbon additives also have a role to play, they ensure a short electron mean free path and generally contribute in reducing the internal resistance of the anode systems<sup>284,285</sup>. Strategies combining the binder and the conductive carbon matrix, generating a "conductive binder" were recently reported<sup>286</sup> and reviewed<sup>243,279,287,288</sup>.

Finally, doping<sup>267,289</sup> and decoration strategies were recently explored in order to improve reaction kinetics and increase the mechanical stability of the conductive matrix, which will be one object of focus in this thesis.

## 1.4 Context of the thesis

In order to transition to the Hydrogen economy and tackle the major challenges imposed by anthropogenic global climate change, research and innovation towards sustainability has to be pushed one step further. The use of rare-earth elements in many (electro)catalytic processes have to be replaced by more abundant elements together with catalyst size decrease -from nanoparticles to single atoms- to ensure scalability and atomic efficiency. In this context, Chapter 2 will address the incorporation of small amounts of Earth abundant metals for both aqueous ambient dinitrogen reduction to ammonia and acidic oxygen evolution, two crucial bottleneck reactions for the implementation of the Hydrogen economy. In Chapter 3, the incorporation of small amounts of metal in the conductive matrix of Si/C anode was explored, opening the path for performance enhancement without compromising the gravimetric capacity. Finally, Chapter 4 will investigate the use of atomic layer deposition to generate nanometer scale aluminium oxide coatings for the stabilization of solid-electrolyte interface in the case of a  $\text{LiNi}_{0.5}\text{Mn}_{0.3}\text{Co}_{0.2}$  cathode at high voltages (4.3-4.6 V) for the future of fast-charging lithium-ion batteries.

## 1.5 References

1. bp Statistical Review of World Energy 2020. 68 (2020).
2. Energy Transitions: Global and National Perspectives (Second expanded and updated edition) — Vaclav Smil.  
<http://vaclavsmil.com/2016/12/14/energy-transitions-global-and-national-perspectives-second-expanded-and-updated-edition/>.
3. Rennings, K. *et al. Sustainable Energy Consumption in Residential Buildings*. (Springer Science & Business Media, 2012).
4. Lahlou, S. *Case Studies in Sustainable Consumption and Production: Energy Use and the Built Environment*. (Greenleaf, 2011).
5. United Nations, Department of Economic and Social Affairs, & Population Division. *World population prospects Highlights, 2019 revision Highlights, 2019 revision*. (2019).
6. Carbon dioxide peaks near 420 parts per million at Mauna Loa observatory - Welcome to NOAA Research.  
<https://research.noaa.gov/article/ArtMID/587/ArticleID/2764/Coronavirus-response-barely-slows-rising-carbon-dioxide>.
7. Friedlingstein, P. *et al.* Global Carbon Budget 2019. *Earth System Science Data* **11**, 1783–1838 (2019).
8. Hansen, J. *et al.* Target Atmospheric CO<sub>2</sub>: Where Should Humanity Aim? 15.
9. L'Accord de Paris | CCNUCC.  
<https://unfccc.int/fr/processus-et-reunions/l-accord-de-paris/l-accord-de-paris>.
10. Matter, J. M. *et al.* Rapid carbon mineralization for permanent disposal of anthropogenic carbon dioxide emissions. *Science* **352**, 1312–1314 (2016).

11. Vechorkin, O., Hirt, N. & Hu, X. Carbon Dioxide as the C1 Source for Direct C–H Functionalization of Aromatic Heterocycles. *Org. Lett.* **12**, 3567–3569 (2010).
12. Fujihara, T. & Tsuji, Y. Carboxylation Reactions Using Carbon Dioxide as the C1 Source via Catalytically Generated Allyl Metal Intermediates. *Front. Chem.* **7**, (2019).
13. Barbarossa, V., Vanga, G., Viscardi, R. & Gattia, D. M. CO<sub>2</sub> as Carbon Source for Fuel Synthesis. *Energy Procedia* **45**, 1325–1329 (2014).
14. Panwar, N. L., Kaushik, S. C. & Kothari, S. Role of renewable energy sources in environmental protection: A review. *Renewable and Sustainable Energy Reviews* **15**, 1513–1524 (2011).
15. Lewis, N. S. Toward Cost-Effective Solar Energy Use. *Science* **315**, 798–801 (2007).
16. Kannan, N. & Vakeesan, D. Solar energy for future world: - A review. *Renewable and Sustainable Energy Reviews* **62**, 1092–1105 (2016).
17. Liu, M. *et al.* Review on concentrating solar power plants and new developments in high temperature thermal energy storage technologies. *Renewable and Sustainable Energy Reviews* **53**, 1411–1432 (2016).
18. Nayak, P. K., Mahesh, S., Snaith, H. J. & Cahen, D. Photovoltaic solar cell technologies: analysing the state of the art. *Nat Rev Mater* **4**, 269–285 (2019).
19. Zhang, H. L., Baeyens, J., Degreè, J. & Cacères, G. Concentrated solar power plants: Review and design methodology. *Renewable and Sustainable Energy Reviews* **22**, 466–481 (2013).
20. Shubbak, M. H. Advances in solar photovoltaics: Technology review and patent trends. *Renewable and Sustainable Energy Reviews* **115**, 109383 (2019).
21. Pumped-Storage Hydropower. *Energy.gov*  
<https://www.energy.gov/eere/water/pumped-storage-hydropower>.

22. Blakers, A., Stocks, M., Lu, B. & Cheng, C. A review of pumped hydro energy storage. *Prog. Energy* **3**, 022003 (2021).
23. Turner, J. A. A Realizable Renewable Energy Future. *Science* **285**, 687–689 (1999).
24. Nicoletti, G., Arcuri, N., Nicoletti, G. & Bruno, R. A technical and environmental comparison between hydrogen and some fossil fuels. *Energy Conversion and Management* **89**, 205–213 (2015).
25. Yue, M. *et al.* Hydrogen energy systems: A critical review of technologies, applications, trends and challenges. *Renewable and Sustainable Energy Reviews* **146**, 111180 (2021).
26. Abe, J. O., Popoola, A. P. I., Ajenifuja, E. & Popoola, O. M. Hydrogen energy, economy and storage: Review and recommendation. *International Journal of Hydrogen Energy* **44**, 15072–15086 (2019).
27. Rigden, J. S. & O’Connell, J. Hydrogen: The Essential Element. *Am. J. Phys.* **71**, 5 (2003).
28. Benfey, O. T. Prout’s hypothesis. 4 (1952).
29. Chadwick, J. The existence of a neutron. *Proceedings of the Royal Society of London. Series A, Containing Papers of a Mathematical and Physical Character* **136**, 692–708 (1932).
30. Bockris, J. O. A Hydrogen Economy. *Science* **176**, 1323–1323 (1972).
31. Dincer, I. & Acar, C. Review and evaluation of hydrogen production methods for better sustainability. *International Journal of Hydrogen Energy* **40**, 11094–11111 (2015).
32. Rand, D. A. J. A journey on the electrochemical road to sustainability. *J Solid State Electrochem* **15**, 1579–1622 (2011).
33. Acar, C. & Dincer, I. Review and evaluation of hydrogen production options for better environment. *Journal of Cleaner Production* **218**, 835–849 (2019).

34. Bartels, J. R., Pate, M. B. & Olson, N. K. An economic survey of hydrogen production from conventional and alternative energy sources. *International Journal of Hydrogen Energy* **35**, 8371–8384 (2010).
35. Dayton, D. C., Turk, B. & Gupta, R. Syngas Cleanup, Conditioning, and Utilization. in *Thermochemical Processing of Biomass* 125–174 (John Wiley & Sons, Ltd, 2019). doi:10.1002/9781119417637.ch5.
36. James, O. O., Mesubi, A. M., Ako, T. C. & Maity, S. Increasing carbon utilization in Fischer–Tropsch synthesis using H<sub>2</sub>-deficient or CO<sub>2</sub>-rich syngas feeds. *Fuel Processing Technology* **91**, 136–144 (2010).
37. Chisalita, D.-A., Petrescu, L. & Cormos, C.-C. Environmental evaluation of european ammonia production considering various hydrogen supply chains. *Renewable and Sustainable Energy Reviews* **130**, 109964 (2020).
38. Giddey, S., Badwal, S. P. S. & Kulkarni, A. Review of electrochemical ammonia production technologies and materials. *International Journal of Hydrogen Energy* **38**, 14576–14594 (2013).
39. Ozturk, M. & Dincer, I. An integrated system for ammonia production from renewable hydrogen: A case study. *International Journal of Hydrogen Energy* **46**, 5918–5925 (2021).
40. Sahu, R., Song, B. J., Im, J. S., Jeon, Y.-P. & Lee, C. W. A review of recent advances in catalytic hydrocracking of heavy residues. *Journal of Industrial and Engineering Chemistry* **27**, 12–24 (2015).
41. Zhang, L., Zhou, M., Wang, A. & Zhang, T. Selective Hydrogenation over Supported Metal Catalysts: From Nanoparticles to Single Atoms. *Chem. Rev.* **120**, 683–733 (2020).
42. Armaroli, N. & Balzani, V. The Hydrogen Issue. *ChemSusChem* **4**, 21–36 (2011).

43. Alanne, K. & Cao, S. Zero-energy hydrogen economy (ZEH2E) for buildings and communities including personal mobility. *Renewable and Sustainable Energy Reviews* **71**, 697–711 (2017).
44. Najjar, Y. S. H. Hydrogen safety: The road toward green technology. *International Journal of Hydrogen Energy* **38**, 10716–10728 (2013).
45. Mori, D. & Hirose, K. Recent challenges of hydrogen storage technologies for fuel cell vehicles. *International Journal of Hydrogen Energy* **34**, 4569–4574 (2009).
46. Aasadnia, M. & Mehrpooya, M. Large-scale liquid hydrogen production methods and approaches: A review. *Applied Energy* **212**, 57–83 (2018).
47. Orimo, S., Nakamori, Y., Eliseo, J. R., Züttel, A. & Jensen, C. M. Complex Hydrides for Hydrogen Storage. *Chem. Rev.* **107**, 4111–4132 (2007).
48. Mao, W. L. & Mao, H. Hydrogen storage in molecular compounds. *PNAS* **101**, 708–710 (2004).
49. Nijkamp, M. G., Raaymakers, J. E. M. J., van Dillen, A. J. & de Jong, K. P. Hydrogen storage using physisorption – materials demands. *Appl Phys A* **72**, 619–623 (2001).
50. Züttel, A. Materials for hydrogen storage. *Materials Today* **6**, 24–33 (2003).
51. Schlapbach, L. & Züttel, A. Hydrogen-storage materials for mobile applications. *Nature* **414**, 353–358 (2001).
52. Akal, D., Öztuna, S. & Büyükkakın, M. K. A review of hydrogen usage in internal combustion engines (gasoline-Lpg-diesel) from combustion performance aspect. *International Journal of Hydrogen Energy* **45**, 35257–35268 (2020).
53. Dodds, P. E. *et al.* Hydrogen and fuel cell technologies for heating: A review. *International Journal of Hydrogen Energy* **40**, 2065–2083 (2015).

54. Andújar, J. M. & Segura, F. Fuel cells: History and updating. A walk along two centuries. *Renewable and Sustainable Energy Reviews* **13**, 2309–2322 (2009).
55. Elmer, T., Worall, M., Wu, S. & Riffat, S. B. Fuel cell technology for domestic built environment applications: State of-the-art review. *Renewable and Sustainable Energy Reviews* **42**, 913–931 (2015).
56. Products | <https://www.fuelcellenergy.com/products/>.
57. Gülzow, E. Alkaline fuel cells: a critical view. *Journal of Power Sources* **61**, 99–104 (1996).
58. Giddey, S., Badwal, S. P. S., Kulkarni, A. & Munnings, C. A comprehensive review of direct carbon fuel cell technology. *Progress in Energy and Combustion Science* **38**, 360–399 (2012).
59. Dicks, A. L. Molten carbonate fuel cells. *Current Opinion in Solid State and Materials Science* **8**, 379–383 (2004).
60. Sammes, N., Bove, R. & Stahl, K. Phosphoric acid fuel cells: Fundamentals and applications. *Current Opinion in Solid State and Materials Science* **8**, 372–378 (2004).
61. Sharaf, O. Z. & Orhan, M. F. An overview of fuel cell technology: Fundamentals and applications. *Renewable and Sustainable Energy Reviews* **32**, 810–853 (2014).
62. Mahato, N., Banerjee, A., Gupta, A., Omar, S. & Balani, K. Progress in material selection for solid oxide fuel cell technology: A review. *Progress in Materials Science* **72**, 141–337 (2015).
63. Ruscic, B. *et al.* On the Enthalpy of Formation of Hydroxyl Radical and Gas-Phase Bond Dissociation Energies of Water and Hydroxyl. *J. Phys. Chem. A* **106**, 2727–2747 (2002).



64. Pearson, G. VII. Experiments and observations, made with the view of ascertaining the nature of the gaz produced by passing electric discharges through water. *Philosophical Transactions of the Royal Society of London* **87**, 142–158 (1797).
65. Bhardwaj, M. & Balasubramaniam, R. Uncoupled non-linear equations method for determining kinetic parameters in case of hydrogen evolution reaction following Volmer–Heyrovsky–Tafel mechanism and Volmer–Heyrovsky mechanism. *International Journal of Hydrogen Energy* **33**, 2178–2188 (2008).
66. Cheng, N. *et al.* Platinum single-atom and cluster catalysis of the hydrogen evolution reaction. *Nat Commun* **7**, 13638 (2016).
67. Eftekhari, A. Electrocatalysts for hydrogen evolution reaction. *International Journal of Hydrogen Energy* **42**, 11053–11077 (2017).
68. Vesborg, P. C. K., Seger, B. & Chorkendorff, I. Recent Development in Hydrogen Evolution Reaction Catalysts and Their Practical Implementation. *J. Phys. Chem. Lett.* **6**, 951–957 (2015).
69. Li, Y. *et al.* MoS<sub>2</sub> Nanoparticles Grown on Graphene: An Advanced Catalyst for the Hydrogen Evolution Reaction. *J. Am. Chem. Soc.* **133**, 7296–7299 (2011).
70. Suen, N.-T. *et al.* Electrocatalysis for the oxygen evolution reaction: recent development and future perspectives. *Chem. Soc. Rev.* **46**, 337–365 (2017).
71. Song, J. *et al.* A review on fundamentals for designing oxygen evolution electrocatalysts. *Chem. Soc. Rev.* **49**, 2196–2214 (2020).
72. Frydendal, R. *et al.* Benchmarking the Stability of Oxygen Evolution Reaction Catalysts: The Importance of Monitoring Mass Losses. *ChemElectroChem* **1**, 2075–2081 (2014).

73. McCrory, C. C. L. *et al.* Benchmarking Hydrogen Evolving Reaction and Oxygen Evolving Reaction Electrocatalysts for Solar Water Splitting Devices. *J. Am. Chem. Soc.* **137**, 4347–4357 (2015).
74. Lee, Y., Suntivich, J., May, K. J., Perry, E. E. & Shao-Horn, Y. Synthesis and Activities of Rutile IrO<sub>2</sub> and RuO<sub>2</sub> Nanoparticles for Oxygen Evolution in Acid and Alkaline Solutions. *J. Phys. Chem. Lett.* **3**, 399–404 (2012).
75. Reier, T., Oezaslan, M. & Strasser, P. Electrocatalytic Oxygen Evolution Reaction (OER) on Ru, Ir, and Pt Catalysts: A Comparative Study of Nanoparticles and Bulk Materials. *ACS Catal.* **2**, 1765–1772 (2012).
76. Audichon, T. *et al.* IrO<sub>2</sub> Coated on RuO<sub>2</sub> as Efficient and Stable Electroactive Nanocatalysts for Electrochemical Water Splitting. *J. Phys. Chem. C* **120**, 2562–2573 (2016).
77. Matsumoto, Y. & Sato, E. Electrocatalytic properties of transition metal oxides for oxygen evolution reaction. *Materials Chemistry and Physics* **14**, 397–426 (1986).
78. Angelinetta, C., Trasatti, S., Atanososka, Lj. D. & Atanasoski, R. T. Surface properties of RuO<sub>2</sub> + IrO<sub>2</sub> mixed oxide electrodes. *Journal of Electroanalytical Chemistry and Interfacial Electrochemistry* **214**, 535–546 (1986).
79. Kötzt, R., Lewerenz, H. J. & Stucki, S. XPS Studies of Oxygen Evolution on Ru and RuO<sub>2</sub> Anodes. *J. Electrochem. Soc.* **130**, 825 (1983).
80. Kötzt, R., Neff, H. & Stucki, S. Anodic Iridium Oxide Films: XPS-Studies of Oxidation State Changes and. *J. Electrochem. Soc.* **131**, 72 (1984).
81. Cherevko, S. Electrochemical dissolution of noble metals native oxides. *Journal of Electroanalytical Chemistry* **787**, 11–13 (2017).

82. Li, T. *et al.* Atomic-scale insights into surface species of electrocatalysts in three dimensions. *Nat Catal* **1**, 300–305 (2018).
83. Li, G. *et al.* Zeolite-templated  $\text{Ir}_x\text{Ru}_{1-x}\text{O}_2$  electrocatalysts for oxygen evolution reaction in solid polymer electrolyte water electrolyzers. *International Journal of Hydrogen Energy* **37**, 16786–16794 (2012).
84. Reksten, A. H., Thuv, H., Seland, F. & Sunde, S. The oxygen evolution reaction mechanism at  $\text{Ir}_x\text{Ru}_{1-x}\text{O}_2$  powders produced by hydrolysis synthesis. *Journal of Electroanalytical Chemistry* **819**, 547–561 (2018).
85. Ma, Z. *et al.* Reaction mechanism for oxygen evolution on  $\text{RuO}_2$ ,  $\text{IrO}_2$ , and  $\text{RuO}_2@\text{IrO}_2$  core-shell nanocatalysts. *Journal of Electroanalytical Chemistry* **819**, 296–305 (2018).
86. Lv, H. *et al.* Self-assembled  $\text{RuO}_2@\text{IrO}_x$  core-shell nanocomposite as high efficient anode catalyst for PEM water electrolyzer. *Applied Surface Science* **514**, 145943 (2020).
87. *Fact Sheet*. (2002).
88. Anderson, D. L. Chemical composition of the mantle. *Journal of Geophysical Research: Solid Earth* **88**, B41–B52 (1983).
89. Matthey, J. Pgm market report May 2021. 60 (2021).
90. Jamesh, M.-I. & Harb, M. Tuning the electronic structure of the earth-abundant electrocatalysts for oxygen evolution reaction (OER) to achieve efficient alkaline water splitting – A review. *Journal of Energy Chemistry* **56**, 299–342 (2021).
91. Yin, J. *et al.* Oxygen Vacancies Dominated  $\text{NiS}_2/\text{CoS}_2$  Interface Porous Nanowires for Portable Zn–Air Batteries Driven Water Splitting Devices. *Advanced Materials* **29**, 1704681 (2017).

92. Carmo, M., Fritz, D. L., Mergel, J. & Stolten, D. A comprehensive review on PEM water electrolysis. *International Journal of Hydrogen Energy* **38**, 4901–4934 (2013).
93. Trinke, P. *et al.* Hydrogen Crossover in PEM and Alkaline Water Electrolysis: Mechanisms, Direct Comparison and Mitigation Strategies. *J. Electrochem. Soc.* **165**, F502 (2018).
94. Schröder, V., Emonts, B., Janßen, H. & Schulze, H.-P. Explosion Limits of Hydrogen/Oxygen Mixtures at Initial Pressures up to 200 bar. *Chemical Engineering & Technology* **27**, 847–851 (2004).
95. Murthy, A. P., Madhavan, J. & Murugan, K. Recent advances in hydrogen evolution reaction catalysts on carbon/carbon-based supports in acid media. *Journal of Power Sources* **398**, 9–26 (2018).
96. Ďurovič, M., Hnát, J. & Bouzek, K. Electrocatalysts for the hydrogen evolution reaction in alkaline and neutral media. A comparative review. *Journal of Power Sources* **493**, 229708 (2021).
97. Grubb, W. T. Ionic Migration in Ion-exchange Membranes. *J. Phys. Chem.* **63**, 55–58 (1959).
98. Grubb, W. T. Batteries with Solid Ion Exchange Electrolytes: I . Secondary Cells Employing Metal Electrodes. *J. Electrochem. Soc.* **106**, 275 (1959).
99. Devanathan, R. Recent developments in proton exchange membranes for fuel cells. *Energy Environ. Sci.* **1**, 101–119 (2008).
100. Medina, P. & Santarelli, M. Analysis of water transport in a high pressure PEM electrolyzer. *International Journal of Hydrogen Energy* **35**, 5173–5186 (2010).
101. Barbir, F. PEM electrolysis for production of hydrogen from renewable energy sources. *Solar Energy* **78**, 661–669 (2005).

102. Ito, H., Maeda, T., Nakano, A. & Takenaka, H. Properties of Nafion membranes under PEM water electrolysis conditions. *International Journal of Hydrogen Energy* **36**, 10527–10540 (2011).
103. Ayers, K. E. *et al.* Research Advances towards Low Cost, High Efficiency PEM Electrolysis. *ECS Trans.* **33**, 3 (2010).
104. Reier, T., Nong, H. N., Teschner, D., Schlögl, R. & Strasser, P. Electrocatalytic Oxygen Evolution Reaction in Acidic Environments – Reaction Mechanisms and Catalysts. *Advanced Energy Materials* **7**, 1601275 (2017).
105. Man, I. C. *et al.* Universality in Oxygen Evolution Electrocatalysis on Oxide Surfaces. *ChemCatChem* **3**, 1159–1165 (2011).
106. Lin, Y. *et al.* Chromium-ruthenium oxide solid solution electrocatalyst for highly efficient oxygen evolution reaction in acidic media. *Nat Commun* **10**, 162 (2019).
107. Rossmeisl, J., Qu, Z.-W., Zhu, H., Kroes, G.-J. & Nørskov, J. K. Electrolysis of water on oxide surfaces. *Journal of Electroanalytical Chemistry* **607**, 83–89 (2007).
108. Etzi Coller Pascuzzi, M., Goryachev, A., Hofmann, J. P. & Hensen, E. J. M. Mn promotion of rutile TiO<sub>2</sub>-RuO<sub>2</sub> anodes for water oxidation in acidic media. *Applied Catalysis B: Environmental* **261**, 118225 (2020).
109. Chang, C.-J., Chu, Y.-C., Yan, H.-Y., Liao, Y.-F. & Chen, H. M. Revealing the structural transformation of rutile RuO<sub>2</sub> via in situ X-ray absorption spectroscopy during the oxygen evolution reaction. *Dalton Trans.* **48**, 7122–7129 (2019).
110. Diaz-Morales, O. *et al.* Iridium-based double perovskites for efficient water oxidation in acid media. *Nat Commun* **7**, 1–6 (2016).
111. Yang, L. *et al.* Efficient oxygen evolution electrocatalysis in acid by a perovskite with face-sharing IrO<sub>6</sub> octahedral dimers. *Nat Commun* **9**, 5236 (2018).

112. Kim, J. *et al.* High-Performance Pyrochlore-Type Yttrium Ruthenate Electrocatalyst for Oxygen Evolution Reaction in Acidic Media. *J. Am. Chem. Soc.* **139**, 12076–12083 (2017).
113. Rao, R. R. *et al.* Towards identifying the active sites on RuO<sub>2</sub>(110) in catalyzing oxygen evolution. *Energy Environ. Sci.* **10**, 2626–2637 (2017).
114. Stoerzinger, K. A. *et al.* Orientation-Dependent Oxygen Evolution on RuO<sub>2</sub> without Lattice Exchange. *ACS Energy Lett.* **2**, 876–881 (2017).
115. Dickens, C. F. & Nørskov, J. K. A Theoretical Investigation into the Role of Surface Defects for Oxygen Evolution on RuO<sub>2</sub>. *J. Phys. Chem. C* **121**, 18516–18524 (2017).
116. Wu, T. *et al.* Iron-facilitated dynamic active-site generation on spinel CoAl<sub>2</sub>O<sub>4</sub> with self-termination of surface reconstruction for water oxidation. *Nat Catal* **2**, 763–772 (2019).
117. Grimaud, A. *et al.* Activating lattice oxygen redox reactions in metal oxides to catalyse oxygen evolution. *Nature Chem* **9**, 457–465 (2017).
118. Grimaud, A. *et al.* Activation of surface oxygen sites on an iridium-based model catalyst for the oxygen evolution reaction. *Nat Energy* **2**, 1–10 (2016).
119. Bockris, J. O. & Otagawa, T. Mechanism of oxygen evolution on perovskites. *J. Phys. Chem.* **87**, 2960–2971 (1983).
120. Damjanovic, A. & Jovanovic, B. Anodic Oxide Films as Barriers to Charge Transfer in O<sub>2</sub> Evolution at Pt in Acid Solutions. *J. Electrochem. Soc.* **123**, 374 (1976).
121. Wohlfahrt-Mehrens, M. & Heitbaum, J. Oxygen evolution on Ru and RuO<sub>2</sub> electrodes studied using isotope labelling and on-line mass spectrometry. *Journal of Electroanalytical Chemistry and Interfacial Electrochemistry* **237**, 251–260 (1987).

122. Mefford, J. T. *et al.* Water electrolysis on  $\text{La}_{1-x}\text{Sr}_x\text{CoO}_{3-\delta}$  perovskite electrocatalysts. *Nat Commun* **7**, 11053 (2016).
123. Yoo, J. S., Rong, X., Liu, Y. & Kolpak, A. M. Role of Lattice Oxygen Participation in Understanding Trends in the Oxygen Evolution Reaction on Perovskites. *ACS Catal.* **8**, 4628–4636 (2018).
124. Macounová, K., Jirkovský, J., Makarova, M. V., Franc, J. & Krtíl, P. Oxygen evolution on  $\text{Ru}_{1-x}\text{Ni}_x\text{O}_2$  – nanocrystalline electrodes. *J Solid State Electrochem* **13**, 959–965 (2009).
125. Koper, M. T. M. Theory of multiple proton–electron transfer reactions and its implications for electrocatalysis. *Chem. Sci.* **4**, 2710–2723 (2013).
126. Rosca, V., Duca, M., de Groot, M. T. & Koper, M. T. M. Nitrogen Cycle Electrocatalysis. *Chem. Rev.* **109**, 2209–2244 (2009).
127. Smil, V. Detonator of the population explosion. *Nature* **400**, 415 (1999).
128. Socolow, R. H. Nitrogen management and the future of food: Lessons from the management of energy and carbon. *Proc Natl Acad Sci U S A* **96**, 6001–6008 (1999).
129. Zamfirescu, C. & Dincer, I. Using ammonia as a sustainable fuel. *Journal of Power Sources* **185**, 459–465 (2008).
130. Klerke, A., Christensen, C. H., Nørskov, J. K. & Vegge, T. Ammonia for hydrogen storage: challenges and opportunities. *J. Mater. Chem.* **18**, 2304–2310 (2008).
131. Shilov, A. E. Catalytic reduction of molecular nitrogen in solutions. *Russian Chemical Bulletin* **52**, 2555–2562 (2003).
132. Jia, H.-P. & Quadrelli, E. A. Mechanistic aspects of dinitrogen cleavage and hydrogenation to produce ammonia in catalysis and organometallic chemistry: relevance of metal hydride bonds and dihydrogen. *Chem. Soc. Rev.* **43**, 547–564 (2013).

133. Ham, C. J. M. van der, Koper, M. T. M. & Hetterscheid, D. G. H. Challenges in reduction of dinitrogen by proton and electron transfer. *Chem. Soc. Rev.* **43**, 5183–5191 (2014).
134. Cui, X. *et al.* Highly Selective Electrochemical Reduction of Dinitrogen to Ammonia at Ambient Temperature and Pressure over Iron Oxide Catalysts. *Chemistry – A European Journal* **0**,.
135. Liu, H. *Ammonia Synthesis Catalysts: Innovation and Practice*. (World Scientific, 2013).
136. Burgess, B. K. & Lowe, D. J. Mechanism of Molybdenum Nitrogenase. *Chem. Rev.* **96**, 2983–3012 (1996).
137. Einsle, O. *et al.* Nitrogenase MoFe-Protein at 1.16 Å Resolution: A Central Ligand in the FeMo-Cofactor. *Science* **297**, 1696–1700 (2002).
138. Lancaster, K. M. *et al.* X-ray Emission Spectroscopy Evidences a Central Carbon in the Nitrogenase Iron-Molybdenum Cofactor. *Science* **334**, 974–977 (2011).
139. Spatzal, T. *et al.* Evidence for Interstitial Carbon in Nitrogenase FeMo Cofactor. *Science* **334**, 940–940 (2011).
140. Hoffman, B. M., Lukoyanov, D., Yang, Z.-Y., Dean, D. R. & Seefeldt, L. C. Mechanism of Nitrogen Fixation by Nitrogenase: The Next Stage. *Chem. Rev.* **114**, 4041–4062 (2014).
141. Seefeldt, L. C., Hoffman, B. M. & Dean, D. R. Mechanism of Mo-Dependent Nitrogenase. *Annu. Rev. Biochem.* **78**, 701–722 (2009).
142. Schrock, R. R. Catalytic Reduction of Dinitrogen to Ammonia at a Single Molybdenum Center. *Acc. Chem. Res.* **38**, 955–962 (2005).



143. Yandulov, D. V. & Schrock, R. R. Studies Relevant to Catalytic Reduction of Dinitrogen to Ammonia by Molybdenum Triamidoamine Complexes. *Inorg. Chem.* **44**, 1103–1117 (2005).
144. Yandulov, D. V. & Schrock, R. R. Catalytic Reduction of Dinitrogen to Ammonia at a Single Molybdenum Center. *Science* **301**, 76–78 (2003).
145. Yandulov, D. V. & Schrock, R. R. Reduction of Dinitrogen to Ammonia at a Well-Protected Reaction Site in a Molybdenum Triamidoamine Complex. *J. Am. Chem. Soc.* **124**, 6252–6253 (2002).
146. Hetterscheid, D. G. H., Hanna, B. S. & Schrock, R. R. Molybdenum Triamidoamine Systems. Reactions Involving Dihydrogen Relevant to Catalytic Reduction of Dinitrogen. *Inorg. Chem.* **48**, 8569–8577 (2009).
147. Singh, A. R. *et al.* Electrochemical Ammonia Synthesis—The Selectivity Challenge. *ACS Catal.* **7**, 706–709 (2017).
148. Michalsky, R., Pfromm, P. H. & Steinfeld, A. Rational design of metal nitride redox materials for solar-driven ammonia synthesis. *Interface Focus* **5**, 20140084 (2015).
149. Guo, C., Ran, J., Vasileff, A. & Qiao, S.-Z. Rational design of electrocatalysts and photo(electro)catalysts for nitrogen reduction to ammonia (NH<sub>3</sub>) under ambient conditions. *Energy Environ. Sci.* **11**, 45–56 (2018).
150. Oshikiri, T., Ueno, K. & Misawa, H. Plasmon-Induced Ammonia Synthesis through Nitrogen Photofixation with Visible Light Irradiation. *Angewandte Chemie International Edition* **53**, 9802–9805 (2014).
151. Cui, X., Tang, C. & Zhang, Q. A Review of Electrocatalytic Reduction of Dinitrogen to Ammonia under Ambient Conditions. *Advanced Energy Materials* **8**, 1800369 (2018).

152. Montoya, J. H., Tsai, C., Vojvodic, A. & Nørskov, J. K. The Challenge of Electrochemical Ammonia Synthesis: A New Perspective on the Role of Nitrogen Scaling Relations. *ChemSusChem* **8**, 2180–2186 (2015).
153. Kyriakou, V., Garagounis, I., Vasileiou, E., Vourros, A. & Stoukides, M. Progress in the Electrochemical Synthesis of Ammonia. *Catalysis Today* **286**, 2–13 (2017).
154. Choi, C. *et al.* Suppression of Hydrogen Evolution Reaction in Electrochemical N<sub>2</sub> Reduction Using Single-Atom Catalysts: A Computational Guideline. *ACS Catal.* **8**, 7517–7525 (2018).
155. Abghoui, Y. & Skúlason, E. Onset potentials for different reaction mechanisms of nitrogen activation to ammonia on transition metal nitride electro-catalysts. *Catalysis Today* **286**, 69–77 (2017).
156. Nazemi, M., Panikkanvalappil, S. R. & El-Sayed, M. A. Enhancing the rate of electrochemical nitrogen reduction reaction for ammonia synthesis under ambient conditions using hollow gold nanocages. *Nano Energy* **49**, 316–323 (2018).
157. Wang, J. *et al.* Ambient ammonia synthesis via palladium-catalyzed electrohydrogenation of dinitrogen at low overpotential. *Nature Communications* **9**, (2018).
158. Shipman, M. A. & Symes, M. D. Recent progress towards the electrosynthesis of ammonia from sustainable resources. *Catalysis Today* **286**, 57–68 (2017).
159. Suryanto, B. H. R. *et al.* Rational Electrode–Electrolyte Design for Efficient Ammonia Electrosynthesis under Ambient Conditions. *ACS Energy Lett.* **3**, 1219–1224 (2018).
160. Zhang, R. *et al.* High-Efficiency Electrosynthesis of Ammonia with High Selectivity under Ambient Conditions Enabled by VN Nanosheet Array. *ACS Sustainable Chem. Eng.* **6**, 9545–9549 (2018).

161. Jeong, E.-Y. *et al.* Electrochemical Ammonia Synthesis Mediated by Titanocene Dichloride in Aqueous Electrolytes under Ambient Conditions. *ACS Sustainable Chem. Eng.* **5**, 9662–9666 (2017).
162. Amar, I. A., Lan, R., Petit, C. T. G. & Tao, S. Electrochemical Synthesis of Ammonia Based on Co<sub>3</sub>Mo<sub>3</sub>N Catalyst and LiAlO<sub>2</sub>–(Li,Na,K)<sub>2</sub>CO<sub>3</sub> Composite Electrolyte. *Electrocatalysis* **6**, 286–294 (2015).
163. Bao, D. *et al.* Electrochemical Reduction of N<sub>2</sub> under Ambient Conditions for Artificial N<sub>2</sub> Fixation and Renewable Energy Storage Using N<sub>2</sub>/NH<sub>3</sub> Cycle. *Advanced Materials* **29**, 1604799 (2017).
164. Katayama, A., Inomata, T., Ozawa, T. & Masuda, H. Electrochemical conversion of dinitrogen to ammonia induced by a metal complex–supported ionic liquid. *Electrochemistry Communications* **67**, 6–10 (2016).
165. Li, S.-J. *et al.* Amorphizing of Au Nanoparticles by CeO<sub>x</sub>–RGO Hybrid Support towards Highly Efficient Electrocatalyst for N<sub>2</sub> Reduction under Ambient Conditions. *Advanced Materials* **29**, 1700001 (2017).
166. Zhang, R. *et al.* Enabling Effective Electrocatalytic N<sub>2</sub> Conversion to NH<sub>3</sub> by TiO<sub>2</sub> Nanosheets Array under Ambient Conditions. **24**.
167. Licht, S. *et al.* Ammonia synthesis by N<sub>2</sub> and steam electrolysis in molten hydroxide suspensions of nanoscale Fe<sub>2</sub>O<sub>3</sub>. *Science* **345**, 637–640 (2014).
168. Zhang, Y. *et al.* High-Performance Electrohydrogenation of N<sub>2</sub> to NH<sub>3</sub> Catalyzed by Multishelled Hollow Cr<sub>2</sub>O<sub>3</sub> Microspheres under Ambient Conditions. *ACS Catal.* **8**, 8540–8544 (2018).

169. Mukherjee, S. *et al.* Metal-organic framework-derived nitrogen-doped highly disordered carbon for electrochemical ammonia synthesis using N<sub>2</sub> and H<sub>2</sub>O in alkaline electrolytes. *Nano Energy* **48**, 217–226 (2018).
170. Garagounis, I., Kyriakou, V., Skodra, A., Vasileiou, E. & Stoukides, M. Electrochemical Synthesis of Ammonia in Solid Electrolyte Cells. *Front. Energy Res.* **2**, (2014).
171. Díez-Ramírez, J. *et al.* Enhancement of Ammonia Synthesis on a Co<sub>3</sub>Mo<sub>3</sub>N-Ag Electrocatalyst in a K-βAl<sub>2</sub>O<sub>3</sub> Solid Electrolyte Cell. *ACS Sustainable Chem. Eng.* **5**, 8844–8851 (2017).
172. Kong, J. *et al.* Electrochemical Synthesis of NH<sub>3</sub> at Low Temperature and Atmospheric Pressure Using a γ-Fe<sub>2</sub>O<sub>3</sub> Catalyst. *ACS Sustainable Chem. Eng.* **5**, 10986–10995 (2017).
173. Kordali, V., Kyriacou, G. & Lambrou, C. Electrochemical synthesis of ammonia at atmospheric pressure and low temperature in a solid polymer electrolyte cell. *Chem. Commun.* **0**, 1673–1674 (2000).
174. Chen, S. *et al.* Electrocatalytic Synthesis of Ammonia at Room Temperature and Atmospheric Pressure from Water and Nitrogen on a Carbon-Nanotube-Based Electrocatalyst. *Angewandte Chemie International Edition* **56**, 2699–2703 (2017).
175. Chen, S. *et al.* Room-Temperature Electrocatalytic Synthesis of NH<sub>3</sub> from H<sub>2</sub>O and N<sub>2</sub> in a Gas–Liquid–Solid Three-Phase Reactor. *ACS Sustainable Chem. Eng.* **5**, 7393–7400 (2017).
176. Liang, S., Altaf, N., Huang, L., Gao, Y. & Wang, Q. Electrolytic cell design for electrochemical CO<sub>2</sub> reduction. *Journal of CO<sub>2</sub> Utilization* **35**, 90–105 (2020).

177. Liu, J., Zhu, D., Guo, C., Vasileff, A. & Qiao, S.-Z. Design Strategies toward Advanced MOF-Derived Electrocatalysts for Energy-Conversion Reactions. *Advanced Energy Materials* **7**, 1700518 (2017).
178. Zhang, R. *et al.* Metal–organic framework-derived shuttle-like V<sub>2</sub>O<sub>3</sub>/C for electrocatalytic N<sub>2</sub> reduction under ambient conditions. *Inorg. Chem. Front.* (2018) doi:10.1039/C8QI01145A.
179. Zhao, X. *et al.* Highly efficient metal–organic-framework catalysts for electrochemical synthesis of ammonia from N<sub>2</sub> (air) and water at low temperature and ambient pressure. *J Mater Sci* **52**, 10175–10185 (2017).
180. Liu, Y. *et al.* Facile Ammonia Synthesis from Electrocatalytic N<sub>2</sub> Reduction under Ambient Conditions on N-Doped Porous Carbon. *ACS Catal.* **8**, 1186–1191 (2018).
181. Abghoui, Y., Garden, A. L., Howalt, J. G., Vegge, T. & Skúlason, E. Electroreduction of N<sub>2</sub> to Ammonia at Ambient Conditions on Mononitrides of Zr, Nb, Cr, and V: A DFT Guide for Experiments. *ACS Catalysis* **6**, 635–646 (2016).
182. Matanović, I., Garzon, F. H. & Henson, N. J. Electro-reduction of nitrogen on molybdenum nitride: structure, energetics, and vibrational spectra from DFT. *Phys. Chem. Chem. Phys.* **16**, 3014–3026 (2014).
183. Li, Q., He, L., Sun, C. & Zhang, X. Computational Study of MoN<sub>2</sub> Monolayer as Electrochemical Catalysts for Nitrogen Reduction. *J. Phys. Chem. C* **121**, 27563–27568 (2017).
184. Li, Q., Qiu, S., He, L., Zhang, X. & Sun, C. Impact of H-termination on the nitrogen reduction reaction of molybdenum carbide as an electrochemical catalyst. *Phys. Chem. Chem. Phys.* (2018) doi:10.1039/C8CP04474K.

185. Abghoui, Y. & Skúlason, E. Computational Predictions of Catalytic Activity of Zincblende (110) Surfaces of Metal Nitrides for Electrochemical Ammonia Synthesis. *J. Phys. Chem. C* **121**, 6141–6151 (2017).
186. Abghoui, Y. & Skúlason, E. Electrochemical synthesis of ammonia via Mars-van Krevelen mechanism on the (111) facets of group III–VII transition metal mononitrides. *Catalysis Today* **286**, 78–84 (2017).
187. Qiao, Z., Johnson, D. & Djire, A. Challenges and opportunities for nitrogen reduction to ammonia on transitional metal nitrides via Mars-van Krevelen mechanism. *Cell Reports Physical Science* **2**, 100438 (2021).
188. Greenlee, L. F., Renner, J. N. & Foster, S. L. The Use of Controls for Consistent and Accurate Measurements of Electrocatalytic Ammonia Synthesis from Dinitrogen. *ACS Catal.* **8**, 7820–7827 (2018).
189. Luo, X., Wang, J., Dooner, M. & Clarke, J. Overview of current development in electrical energy storage technologies and the application potential in power system operation. *Applied Energy* **137**, 511–536 (2015).
190. Weber, A. Z. *et al.* Redox flow batteries: a review. *J Appl Electrochem* **41**, 1137 (2011).
191. Alotto, P., Guarnieri, M. & Moro, F. Redox flow batteries for the storage of renewable energy: A review. *Renewable and Sustainable Energy Reviews* **29**, 325–335 (2014).
192. Ibrahim, H., Ilinca, A. & Perron, J. Energy storage systems—Characteristics and comparisons. *Renewable and Sustainable Energy Reviews* **12**, 1221–1250 (2008).
193. Ralon, P. ELECTRICITY STORAGE AND RENEWABLES: COSTS AND MARKETS TO 2030. 16.
194. Abraham, K. M. Prospects and Limits of Energy Storage in Batteries. *J. Phys. Chem. Lett.* **6**, 830–844 (2015).

195. Poonam, Sharma, K., Arora, A. & Tripathi, S. K. Review of supercapacitors: Materials and devices. *Journal of Energy Storage* **21**, 801–825 (2019).
196. Xu, K. Electrolytes and Interphases in Li-Ion Batteries and Beyond. *Chem. Rev.* **114**, 11503–11618 (2014).
197. Wen, Z. *et al.* Research on sodium sulfur battery for energy storage. *Solid State Ionics* **179**, 1697–1701 (2008).
198. Liang, Y. *et al.* A review of rechargeable batteries for portable electronic devices. *InfoMat* **1**, 6–32 (2019).
199. Gröger, O., Gasteiger, H. A. & Suchsland, J.-P. Review—Electromobility: Batteries or Fuel Cells? *J. Electrochem. Soc.* **162**, A2605 (2015).
200. Joint Research Centre (European Commission), Tarvydas, D., Tsiropoulos, I. & Lebedeva, N. *Li-ion batteries for mobility and stationary storage applications: scenarios for costs and market growth*. (Publications Office of the European Union, 2018).
201. Joint Research Centre (European Commission), Steen, M., Di Persio, F., Boon-Brett, L. & Lebedeva, N. *EU competitiveness in advanced li-ion batteries for e-mobility and stationary storage applications: opportunities and actions*. (Publications Office of the European Union, 2017).
202. Winter, M., Barnett, B. & Xu, K. Before Li Ion Batteries. *Chem. Rev.* **118**, 11433–11456 (2018).
203. Lewis, G. N. & Keyes, F. G. THE POTENTIAL OF THE LITHIUM ELECTRODE. *J. Am. Chem. Soc.* **35**, 340–344 (1913).
204. Nitta, N., Wu, F., Lee, J. T. & Yushin, G. Li-ion battery materials: present and future. *Materials Today* **18**, 252–264 (2015).

205. Harris, W. S. *Electrochemical studies in cyclic esters*.  
<https://www.osti.gov/biblio/4305596-electrochemical-studies-cyclic-esters> (1958)  
doi:10.2172/4305596.
206. Julien, C., Mauger, A., Vijn, A. & Zaghib, K. Lithium Batteries. in *Lithium Batteries: Science and Technology* (eds. Julien, C., Mauger, A., Vijn, A. & Zaghib, K.) 29–68 (Springer International Publishing, 2016). doi:10.1007/978-3-319-19108-9\_2.
207. Ogumi, Z. & Wang, H. Carbon Anode Materials. in *Lithium-Ion Batteries: Science and Technologies* (eds. Yoshio, M., Brodd, R. J. & Kozawa, A.) 49–73 (Springer, 2009). doi:10.1007/978-0-387-34445-4\_3.
208. An, S. J. *et al.* The state of understanding of the lithium-ion-battery graphite solid electrolyte interphase (SEI) and its relationship to formation cycling. *Carbon* **105**, 52–76 (2016).
209. Wang, A., Kadam, S., Li, H., Shi, S. & Qi, Y. Review on modeling of the anode solid electrolyte interphase (SEI) for lithium-ion batteries. *npj Comput Mater* **4**, 1–26 (2018).
210. Whittingham, M. S. Lithium Batteries and Cathode Materials. *Chem. Rev.* **104**, 4271–4302 (2004).
211. Ellis, B. L., Lee, K. T. & Nazar, L. F. Positive Electrode Materials for Li-Ion and Li-Batteries. *Chem. Mater.* **22**, 691–714 (2010).
212. Julien, C. M., Mauger, A., Zaghib, K. & Groult, H. Comparative Issues of Cathode Materials for Li-Ion Batteries. *Inorganics* **2**, 132–154 (2014).
213. Chakraborty, A. *et al.* Layered Cathode Materials for Lithium-Ion Batteries: Review of Computational Studies on  $\text{LiNi}_{1-x-y}\text{Co}_x\text{Mn}_y\text{O}_2$  and  $\text{LiNi}_{1-x-y}\text{Co}_x\text{Al}_y\text{O}_2$ . *Chem. Mater.* **32**, 915–952 (2020).



214. Tolganbek, N., Yerkinbekova, Y., Kalybekkyzy, S., Bakenov, Z. & Mentbayeva, A. Current state of high voltage olivine structured LiMPO<sub>4</sub> cathode materials for energy storage applications: A review. *Journal of Alloys and Compounds* **882**, 160774 (2021).
215. Wu, F. *et al.* Spinel/Layered Heterostructured Cathode Material for High-Capacity and High-Rate Li-Ion Batteries. *Advanced Materials* **25**, 3722–3726 (2013).
216. Sun, H. & Zhao, K. Electronic Structure and Comparative Properties of Li<sub>Nix</sub>MnyCo<sub>z</sub>O<sub>2</sub> Cathode Materials. *J. Phys. Chem. C* **121**, 6002–6010 (2017).
217. Thackeray, M. An unexpected conductor. *Nature Mater* **1**, 81–82 (2002).
218. Tarascon, J.-M. Key challenges in future Li-battery research. *Philosophical Transactions of the Royal Society A: Mathematical, Physical and Engineering Sciences* **368**, 3227–3241 (2010).
219. He, P., Yu, H., Li, D. & Zhou, H. Layered lithium transition metal oxide cathodes towards high energy lithium-ion batteries. *J. Mater. Chem.* **22**, 3680–3695 (2012).
220. Liu, W. *et al.* Nickel-Rich Layered Lithium Transition-Metal Oxide for High-Energy Lithium-Ion Batteries. *Angewandte Chemie International Edition* **54**, 4440–4457 (2015).
221. Li, T. *et al.* Degradation Mechanisms and Mitigation Strategies of Nickel-Rich NMC-Based Lithium-Ion Batteries. *Electrochem. Energ. Rev.* **3**, 43–80 (2020).
222. Liu, G. Q. *et al.* Study of electrochemical properties of coating ZrO<sub>2</sub> on LiCoO<sub>2</sub>. *Journal of Alloys and Compounds* **496**, 512–516 (2010).
223. Liu, J. *et al.* Improving the Performances of LiCoO<sub>2</sub> Cathode Materials by Soaking Nano-Alumina in Commercial Electrolyte. *J. Electrochem. Soc.* **154**, A55 (2006).
224. Chen, Z. & Dahn, J. R. Studies of LiCoO<sub>2</sub> Coated with Metal Oxides. *Electrochem. Solid-State Lett.* **6**, A221 (2003).

225. Thinius, S., Islam, M. M., Heitjans, P. & Bredow, T. Theoretical Study of Li Migration in Lithium–Graphite Intercalation Compounds with Dispersion-Corrected DFT Methods. *J. Phys. Chem. C* **118**, 2273–2280 (2014).
226. Persson, K. *et al.* Lithium Diffusion in Graphitic Carbon. *J. Phys. Chem. Lett.* **1**, 1176–1180 (2010).
227. Wang, C. S., Wu, G. T. & Li, W. Z. Lithium insertion in ball-milled graphite. *Journal of Power Sources* **76**, 1–10 (1998).
228. Verma, P., Sasaki, T. & Novák, P. Chemical surface treatments for decreasing irreversible charge loss and preventing exfoliation of graphite in Li-ion batteries. *Electrochimica Acta* **82**, 233–242 (2012).
229. Wang, H. *et al.* Recent Advances in Conversion-Type Electrode Materials for Post Lithium-Ion Batteries. *ACS Materials Lett.* **3**, 956–977 (2021).
230. Yu, S.-H., Feng, X., Zhang, N., Seok, J. & Abruña, H. D. Understanding Conversion-Type Electrodes for Lithium Rechargeable Batteries. *Acc. Chem. Res.* **51**, 273–281 (2018).
231. Kraytsberg, A. & Ein-Eli, Y. A critical review-promises and barriers of conversion electrodes for Li-ion batteries. *J Solid State Electrochem* **21**, 1907–1923 (2017).
232. Lowe, M. A., Gao, J. & Abruña, H. D. In operando X-ray studies of the conversion reaction in Mn<sub>3</sub>O<sub>4</sub> lithium battery anodes. *J. Mater. Chem. A* **1**, 2094–2103 (2013).
233. He, K. *et al.* Visualizing non-equilibrium lithiation of spinel oxide via in situ transmission electron microscopy. *Nat Commun* **7**, 11441 (2016).
234. Meister, P. *et al.* Best Practice: Performance and Cost Evaluation of Lithium Ion Battery Active Materials with Special Emphasis on Energy Efficiency. *Chem. Mater.* **28**, 7203–7217 (2016).

235. Wu, Z.-S. *et al.* Graphene/metal oxide composite electrode materials for energy storage. *Nano Energy* **1**, 107–131 (2012).
236. Wu, H. B., Chen, J. S., Hng, H. H. & Lou, X. W. (David). Nanostructured metal oxide-based materials as advanced anodes for lithium-ion batteries. *Nanoscale* **4**, 2526–2542 (2012).
237. Wang, J., Zhou, H., Nanda, J. & Braun, P. V. Three-Dimensionally Mesostructured Fe<sub>2</sub>O<sub>3</sub> Electrodes with Good Rate Performance and Reduced Voltage Hysteresis. *Chem. Mater.* **27**, 2803–2811 (2015).
238. Li, J. *et al.* Phase evolution of conversion-type electrode for lithium ion batteries. *Nat Commun* **10**, 2224 (2019).
239. Dey, A. N. Electrochemical Alloying of Lithium in Organic Electrolytes. *J. Electrochem. Soc.* **118**, 1547 (1971).
240. Winter, M., Besenhard, J. O., Spahr, M. E. & Novák, P. Insertion Electrode Materials for Rechargeable Lithium Batteries. *Advanced Materials* **10**, 725–763 (1998).
241. Hamon, Y. *et al.* Aluminum negative electrode in lithium ion batteries. *Journal of Power Sources* **97–98**, 185–187 (2001).
242. Winter, M. & Besenhard, J. O. Electrochemical lithiation of tin and tin-based intermetallics and composites. *Electrochimica Acta* **45**, 31–50 (1999).
243. Erk, C., Brezesinski, T., Sommer, H., Schneider, R. & Janek, J. Toward Silicon Anodes for Next-Generation Lithium Ion Batteries: A Comparative Performance Study of Various Polymer Binders and Silicon Nanopowders. *ACS Appl. Mater. Interfaces* **5**, 7299–7307 (2013).

244. Lin, Z., Lan, X., Xiong, X. & Hu, R. Recent development of Sn–Fe-based materials as a substitute for Sn–Co–C anodes in Li-ion batteries: a review. *Mater. Chem. Front.* **5**, 1185–1204 (2021).
245. Liang, S., Cheng, Y.-J., Zhu, J., Xia, Y. & Müller-Buschbaum, P. A Chronicle Review of Nonsilicon (Sn, Sb, Ge)-Based Lithium/Sodium-Ion Battery Alloying Anodes. *Small Methods* **4**, 2000218 (2020).
246. Zhuang, H., Zhao, P., Li, G., Xu, Y. & Jia, X. Li–LiAl alloy composite with memory effect as high-performance lithium metal anode. *Journal of Power Sources* **455**, 227977 (2020).
247. Momma, T. *et al.* SnS<sub>2</sub> anode for rechargeable lithium battery. *Journal of Power Sources* **97–98**, 198–200 (2001).
248. Li, H. *et al.* Circumventing huge volume strain in alloy anodes of lithium batteries. *Nat Commun* **11**, 1584 (2020).
249. Chae, S., Ko, M., Kim, K., Ahn, K. & Cho, J. Confronting Issues of the Practical Implementation of Si Anode in High-Energy Lithium-Ion Batteries. *Joule* **1**, 47–60 (2017).
250. McDowell, M. T. *et al.* In Situ TEM of Two-Phase Lithiation of Amorphous Silicon Nanospheres. *Nano Lett.* **13**, 758–764 (2013).
251. Liu, X. H. *et al.* Size-Dependent Fracture of Silicon Nanoparticles During Lithiation. *ACS Nano* **6**, 1522–1531 (2012).
252. Kumar, R. *et al.* In Situ and Operando Investigations of Failure Mechanisms of the Solid Electrolyte Interphase on Silicon Electrodes. *ACS Energy Lett.* **1**, 689–697 (2016).
253. Gu, M. *et al.* Electronic Origin for the Phase Transition from Amorphous Li<sub>x</sub>Si to Crystalline Li<sub>15</sub>Si<sub>4</sub>. *ACS Nano* **7**, 6303–6309 (2013).

254. Wang, C.-M. *et al.* In Situ TEM Investigation of Congruent Phase Transition and Structural Evolution of Nanostructured Silicon/Carbon Anode for Lithium Ion Batteries. *Nano Lett.* **12**, 1624–1632 (2012).
255. Kim, H., Chou, C.-Y., Ekerdt, J. G. & Hwang, G. S. Structure and Properties of Li–Si Alloys: A First-Principles Study. *J. Phys. Chem. C* **115**, 2514–2521 (2011).
256. Guan, P. *et al.* Facile and Scalable Approach To Fabricate Granadilla-like Porous-Structured Silicon-Based Anode for Lithium Ion Batteries. *ACS Appl. Mater. Interfaces* **10**, 34283–34290 (2018).
257. Zhao, C. *et al.* Imaging of 3D morphological evolution of nanoporous silicon anode in lithium ion battery by X-ray nano-tomography. *Nano Energy* **52**, 381–390 (2018).
258. Guo, S., Hu, X., Hou, Y. & Wen, Z. Tunable Synthesis of Yolk–Shell Porous Silicon@Carbon for Optimizing Si/C-Based Anode of Lithium-Ion Batteries. *ACS Appl. Mater. Interfaces* **9**, 42084–42092 (2017).
259. Liu, N. *et al.* A Yolk-Shell Design for Stabilized and Scalable Li-Ion Battery Alloy Anodes. *Nano Lett.* **12**, 3315–3321 (2012).
260. Zhang, C. *et al.* A carob-inspired nanoscale design of yolk–shell Si@void@TiO<sub>2</sub>-CNF composite as anode material for high-performance lithium-ion batteries. *Dalton Trans.* **48**, 6846–6852 (2019).
261. An, W. *et al.* Scalable synthesis of ant-nest-like bulk porous silicon for high-performance lithium-ion battery anodes. *Nature Communications* **10**, 1447 (2019).
262. Wang, B. *et al.* Ultrafast-Charging Silicon-Based Coral-Like Network Anodes for Lithium-Ion Batteries with High Energy and Power Densities. *ACS Nano* **13**, 2307–2315 (2019).

263. Harpak, N. *et al.* Large-Scale Self-Catalyzed Spongelike Silicon Nano-Network-Based 3D Anodes for High-Capacity Lithium-Ion Batteries. *Nano Lett.* **19**, 1944–1954 (2019).
264. Chen, H. *et al.* Milled flake graphite/plasma nano-silicon@carbon composite with void sandwich structure for high performance as lithium ion battery anode at high temperature. *Carbon* **130**, 433–440 (2018).
265. Li, P., Hwang, J.-Y. & Sun, Y.-K. Nano/Microstructured Silicon–Graphite Composite Anode for High-Energy-Density Li-Ion Battery. *ACS Nano* **13**, 2624–2633 (2019).
266. Shen, X. *et al.* Research progress on silicon/carbon composite anode materials for lithium-ion battery. *Journal of Energy Chemistry* **27**, 1067–1090 (2018).
267. Hou, X., Zhang, M., Wang, J., Hu, S. & Liu, X. Deposition of silver nanoparticles into silicon/carbon composite as a high-performance anode material for Li-ion batteries. *J Solid State Electrochem* **19**, 3595–3604 (2015).
268. Han, Y. *et al.* Metal–Organic Frameworks (MOFs) as Sandwich Coating Cushion for Silicon Anode in Lithium Ion Batteries. *ACS Appl. Mater. Interfaces* **7**, 26608–26613 (2015).
269. Yoon, T. *et al.* Mesoporous Silicon Hollow Nanocubes Derived from Metal–Organic Framework Template for Advanced Lithium-Ion Battery Anode. *ACS Nano* **11**, 4808–4815 (2017).
270. Kim, N., Park, H., Yoon, N. & Lee, J. K. Zeolite-Templated Mesoporous Silicon Particles for Advanced Lithium-Ion Battery Anodes. *ACS Nano* **12**, 3853–3864 (2018).
271. Cao, C. *et al.* Solid Electrolyte Interphase on Native Oxide-Terminated Silicon Anodes for Li-Ion Batteries. *Joule* **3**, 762–781 (2019).
272. Liu, Z. *et al.* Silicon oxides: a promising family of anode materials for lithium-ion batteries. *Chem. Soc. Rev.* **48**, 285–309 (2019).

273. Lotfabad, E. M. *et al.* ALD TiO<sub>2</sub> coated silicon nanowires for lithium ion battery anodes with enhanced cycling stability and coulombic efficiency. *Phys. Chem. Chem. Phys.* **15**, 13646–13657 (2013).
274. Riley, L. A. *et al.* Conformal Surface Coatings to Enable High Volume Expansion Li-Ion Anode Materials. *ChemPhysChem* **11**, 2124–2130 (2010).
275. Li, Y. *et al.* Growth of conformal graphene cages on micrometre-sized silicon particles as stable battery anodes. *Nature Energy* **1**, 15029 (2016).
276. Lotfabad, E. M. *et al.* Si nanotubes ALD coated with TiO<sub>2</sub>, TiN or Al<sub>2</sub>O<sub>3</sub> as high performance lithium ion battery anodes. *J. Mater. Chem. A* **2**, 2504–2516 (2014).
277. Mattelaer, F., Vereecken, P. M., Dendooven, J. & Detavernier, C. The Influence of Ultrathin Amorphous ALD Alumina and Titania on the Rate Capability of Anatase TiO<sub>2</sub> and LiMn<sub>2</sub>O<sub>4</sub> Lithium Ion Battery Electrodes. *Advanced Materials Interfaces* **4**, 1601237 (2017).
278. Tiurin, O. & Ein-Eli, Y. A Critical Review: The Impact of the Battery Electrode Material Substrate on the Composition and Properties of Atomic Layer Deposition (ALD) Coatings. *Advanced Materials Interfaces* **6**, 1901455 (2019).
279. Shi, Y., Zhou, X. & Yu, G. Material and Structural Design of Novel Binder Systems for High-Energy, High-Power Lithium-Ion Batteries. *Acc. Chem. Res.* **50**, 2642–2652 (2017).
280. Zhao, H. *et al.* Mussel-Inspired Conductive Polymer Binder for Si-Alloy Anode in Lithium-Ion Batteries. *ACS Appl. Mater. Interfaces* **10**, 5440–5446 (2018).
281. Chang, W. J. *et al.* Direct Observation of Carboxymethyl Cellulose and Styrene–Butadiene Rubber Binder Distribution in Practical Graphite Anodes for Li-Ion Batteries. *ACS Appl. Mater. Interfaces* **11**, 41330–41337 (2019).

282. Cao, P.-F. *et al.* Effect of Binder Architecture on the Performance of Silicon/Graphite Composite Anodes for Lithium Ion Batteries. *ACS Appl. Mater. Interfaces* **10**, 3470–3478 (2018).
283. Chen, H. *et al.* Exploring Chemical, Mechanical, and Electrical Functionalities of Binders for Advanced Energy-Storage Devices. *Chem. Rev.* **118**, 8936–8982 (2018).
284. Wu, H. *et al.* Stable Li-ion battery anodes by *in-situ* polymerization of conducting hydrogel to conformally coat silicon nanoparticles. *Nature Communications* **4**, 1943 (2013).
285. Lee, K. *et al.* Polymeric binder based on PAA and conductive PANI for high performance silicon-based anodes. *RSC Adv.* **6**, 101622–101625 (2016).
286. Zeng, W. *et al.* Enhanced Ion Conductivity in Conducting Polymer Binder for High-Performance Silicon Anodes in Advanced Lithium-Ion Batteries. *Advanced Energy Materials* **8**, (2018).
287. Nguyen, V. A. & Kuss, C. Review—Conducting Polymer-Based Binders for Lithium-Ion Batteries and Beyond. *J. Electrochem. Soc.* **167**, 065501 (2020).
288. Higgins, T. M. *et al.* A Commercial Conducting Polymer as Both Binder and Conductive Additive for Silicon Nanoparticle-Based Lithium-Ion Battery Negative Electrodes. *ACS Nano* **10**, 3702–3713 (2016).
289. Yin, S. *et al.* Si/Ag/C Nanohybrids with in Situ Incorporation of Super-Small Silver Nanoparticles: Tiny Amount, Huge Impact. *ACS Nano* **12**, 861–875 (2018).



# Chapter 2: Single-Atom Electrocatalysts for electrochemical Dinitrogen Reduction and Atomic doping for Oxygen Evolution Reaction in acidic media

## 2.1 Introduction to Single atom catalysts

Catalysts are classified into two categories: heterogeneous catalysts and homogeneous catalysts. In heterogeneous catalyst, usually supported metal nanoparticles, only a fraction of the metal atoms are exposed (surface atoms) to the reactants, and the majority of the non-accessible catalytic atoms are either inert or can catalyse side reactions that can be damageable to the desired catalysis. Homogeneous catalysts, usually metal-ligand complexes, have tunable active sites (ligand design) and are associated with high turnover frequency (TOF) and selectivity for one or a family of specific reactions. However, they suffer from relatively low stability, complex design and poor recyclability, as they need to be separated from the wanted product to be reused. Within the catalyst domain, combining both advantages of homogeneous and heterogeneous catalysts while suppressing their limitations would give rise to the best kind of catalysts.

In the electrochemical catalysis field, it was proven that decreasing the size of nanoparticles has significant influence on its performances as catalytic site, therefore decreasing down to the metal cluster level where the structure can be atomically controlled should provide the necessary means to obtain 100% atomic efficiency in order to maximize the electrocatalytic performances<sup>1,2</sup>. Single atom catalysts (SACs) are composed of an isolated atom centre, acting as catalytic site, anchored on a support (usually carbon based)<sup>3,4</sup>. SACs have the advantage of presenting both the features of both heterogeneous and homogeneous catalysts. Furthermore, the strong interactions between the single metal atom and the support helps avoid agglomeration by stabilizing the atomic dispersion, by electron transfer for example<sup>5,6</sup>. Indeed, for SACs the support greatly affects the overall catalytic performances. Single-atom catalysts have proven to achieve promising performances in other

various electrocatalytic reactions<sup>7</sup>. It is therefore rational to think that some SACs should present some activity towards OER or N<sub>2</sub>RR.

However synthesizing and characterizing single atoms is not always an easy task experimentally, still it will remain a solid base for intelligent catalyst design. The tendency of metal atoms to agglomerate, especially during the carbonization process of carbon supports during synthesis, is a major challenge to achieve atomic dispersion. Synthetic approaches including mass selected soft landing<sup>8</sup> and atomic layer deposition (ALD)<sup>9</sup> are precise methods to control the formation of SACs. However they are generally very expensive in terms of technical equipment and afford only low yields, hence they cannot yet be scalable to industrial applications. Other methods such as co-precipitation and impregnation methods were also reported for the synthesis of SACs<sup>10,11</sup>: In order to synthesize high performance SACs, the optimization of precursors and supporting material, their interaction, and the general synthetic route is crucial.

One of the main challenges in the development of single atom catalysts is to prove the existence of the catalyst as single atoms. Indeed, a wide range of characterization techniques is needed in order to confirm the presence of SACs. Characterization techniques such as high-resolution tunnel electron microscopy (HR-TEM) and aberration-corrected high-angle annular dark field scanning transmission electron microscopy (HAADF-STEM) permit identification of SACs<sup>12</sup>. Further characterization by X-ray absorption near-edge spectroscopy (XANES), extended X-ray absorption fine structure (EXAFS), and X-ray photoelectron spectroscopy (XPS) can give more information about coordination environment, oxidation states, and binding mode of the SACs<sup>13</sup>. By combining the

information obtained from these characterization techniques the presence of single atoms can be confirmed.

In summary, the activity of the SAC either towards OER or N<sub>2</sub>RR is very much dependent on the coordination environment and the substrate<sup>14</sup>.

Furthermore, in the case of N<sub>2</sub>RR, one needs to be thorough regarding experimental procedures and use sufficient controls in order to ensure consistency and accurate measurements of NH<sub>3</sub>, as sources of contamination are easily present in a laboratory environment<sup>15</sup>.

## 2.2 Single Atom Electrocatalysts for Dinitrogen reduction (N<sub>2</sub>RR)

The development of SACs for N<sub>2</sub>RR at room temperature in aqueous media is crucial but tricky.

In 2014, Le *et al.*<sup>16</sup> reported the computational evaluation of the catalytic activity of a molybdenum-graphene-based electrocatalyst (Mo/N-doped graphene, simulated as C<sub>33</sub>H<sub>15</sub>MoN<sub>3</sub>) for the dinitrogen reduction to ammonia. From their study, they concluded that the Mo/N act as the active catalytic centre, and that the graphitic support acts as the electronic bridge for electrons transmission, and that peripheral graphene provides a reserve of electrons for the protonation and reduction steps. As suggested by Choi et al<sup>3</sup>, the utilization of SACs for N<sub>2</sub>RR activity might be fruitful. Indeed, single atom catalysts are said to have a high-energy surface, but have low stability and are prone to aggregate within the temperature range of carbonization. Moreover, SACs improved catalytic activity lies in the significant suppression of HER reaction, which they attributed to the highly unstable surface adsorption of \*H<sup>3</sup>. Although HER will still be dominant at sufficient negative potentials, H adsorption

will still be suppressed on SACs compared to bulk metal surfaces, resulting in expected increase selectivity towards  $\text{N}_2\text{RR}$ .

Thanks to the development of theoretical calculations, such as the density functional theory (DFT), it is possible to simulate the activity of a catalyst towards a reaction and therefore minimize the number of practical experiments. Thus, calculations never replace the actual lab-work, therefore it is important to use DFT as a source of inspiration for the intelligent design of new electrocatalysts, before performing the mandatory synthesis and electrochemical assessment.

In this chapter, we will discuss how, motivated by theoretical calculations, SACs were designed to overcome the challenges of  $\text{N}_2\text{RR}$  and acidic OER.

In 2017-2018, room temperature aqueous  $\text{N}_2\text{RR}$  received a new highlight as a hot research topic. Even if the reduction of dinitrogen to ammonia suffers from theoretical complications -i.e. selectivity problems and the N-N triple bond being non-polar with the highest bond dissociation energy<sup>17</sup>- new calculations emphasized the feasibility of the reaction using Mo atoms as the catalytic site. Indeed, from theoretical calculations,  $\text{MoS}_2$  -which can be related to the natural nitrogenase Fe-Mo cofactor ( $\text{Fe}_7\text{MoS}_9\text{C}$ )- was suggested by Zhang *et al.*<sup>18</sup> as being active towards  $\text{N}_2\text{RR}$ , and was reported to achieve a FE of 1.17% at -0.5V vs RHE in 0.1M  $\text{Na}_2\text{SO}_4$ , predicting unsaturated edge-Mo as the active site<sup>19</sup>. Defect-rich  $\text{MoS}_2$  being the active site suggests that going to atomic dispersion of molybdenum atoms on a support will increase its coordinating unsaturation, therefore increasing its activity. From DFT calculations, Chen *et al.*<sup>20</sup> reported that cobweb-like  $\text{MoC}_6$  should be active towards  $\text{N}_2\text{RR}$ , with an onset potential as low as -0.54V vs RHE. From their simulation they attributed the theorized activity to be linked to the selective stabilization of

$\text{N}_2\text{H}^*$  and destabilization of  $\text{NH}_2^*$  species. Single Mo on N-doped carbon was also calculated to be efficient by Ling *et al.*<sup>21</sup>, where  $\text{Mo}_1\text{-N}_1\text{C}_2$  could catalyse  $\text{N}_2\text{RR}$  via the enzymatic pathway with an overpotential as low as 0.24 V, and emphasizing the importance of coordinating Mo-N bond in the activity and selectivity of the catalysis. Thus, similar catalysts were also simulated by Chen *et al.*<sup>22</sup> to have high activity for the competing HER reaction. Although HER will still be dominant at sufficient negative potentials, H adsorption will still be suppressed on SACs compared to bulk metal surface, resulting in expected increase selectivity towards  $\text{N}_2\text{RR}$ <sup>3</sup>. In 2019, Ou *et al.*<sup>23</sup> reported DFT calculations supporting the efficiency of Mo SAC on N-doped black phosphorus, where they suggested  $\text{Mo}_1\text{N}_3$  to show the highest activity towards  $\text{N}_2\text{RR}$  with an ultra-low overpotential of 0.02 V via the associative distal pathway.

Based on this literature insight, it was clear that single atom molybdenum on N-doped carbon support was a promising lead towards efficient room temperature aqueous dinitrogen reduction to ammonia.

## 2.3 Results

### 2.3.1 Synthesis and Characterization

Adapted from the synthesis reported by Chen *et al.*<sup>22</sup>, molybdenum single atoms on N-doped carbon support were synthesized. Shortly, sodium molybdenum dihydrate was used to generate Mo SACs by carbonization in the presence of chitosan polymer (high molecular weight) -originally found in crustaceans' shell- which was used as bio-renewable precursors for the generation of the nitrogen-doped matrix. Silicon dioxide ( $\text{SiO}_2$ ) nanospheres were introduced as well in the mixture to ensure high porosity within the carbon matrix. Indeed, silica remained intact during the carbonization process, and the  $\text{SiO}_2$  nanospheres were embedded in the amorphous carbon, then the remains of silica were dissolved by etching with

high concentration of base (4 M NaOH, 60°C, stirring overnight). The obtained product was denoted Mo-N-C and was characterized and evaluated further for its electrocatalytic performances.

The pores that were introduced on the carbon matrix where the SiO<sub>2</sub> nanospheres used to reside, lead to a higher surface to volume ratio, increasing the number of single atoms in contact with the electrolyte. By controlling the size of the SiO<sub>2</sub> nanospheres, one can control the porous character of the carbon matrix.

The graphitization process and eventual presence of nanoparticles was monitored by X-ray diffraction, and the only peaks for C(002) and C(101) were recorded, resulting in successful carbonization of the chitosan. No peaks from crystalline metal oxides, metal nanoparticles, or any metallic species were observed. From the TEM results (Fig.2-1, c)), one can observe the multi-layered and porous structure of Mo-N-C, the SiO<sub>2</sub> etching created further porosity within the sample. STEM-EDX mapping revealed that the material is composed of C, N, O and Mo, with N and Mo being homogeneously dispersed (Fig.2-1, e), f)). This suggests the successful Mo impregnation and N doping of the carbon conductive matrix. Here the sample was carbonized under Ar flow, and more N doping could be introduced by changing to N<sub>2</sub>.

High-resolution X-ray photoelectron spectroscopy (XPS) spectra was recorded for Mo-N-C, revealing its chemical composition and the oxidation states. In the carbon region (C1s, Fig2-2, a)) the spectrum was deconvoluted in two main peaks: one corresponding to the C-C bonding at 284.8 eV and another one for the C-N functional groups at 286.5 eV, a third broader peak (in purple) was observed and attributed to the different type C-O, suggesting the presence of hydroxyl, carbonyl and carboxylic groups. The presence of oxygen functional

groups was not intentional, and is believed to come from using chitosan<sup>24,25</sup>. For the N1s region (Fig2-2, b)) three peaks were observed and attributed to pyridinic-N at 398.5 eV (green), another broad one for the pyrrolic-N at 401.1 eV (purple), a third one at 403.3 eV was attributed to NO<sub>x</sub> species (blue). The peak at 399.9 eV was attributed to porphyrin-like metal coordinated Mo-N<sub>x</sub> moieties, which is in accordance with the reported literature<sup>26</sup>. These N-bonding species are crucial for the anchoring of the Mo single atom as mentioned before<sup>21</sup>. The high-resolution spectra within the Mo 3d region was also acquired, with a recorded intensity enough to ensure its presence. Six different peaks were distinguished, to the best of my knowledge, in the region of 227 to 237 eV, respectively Mo<sup>δ+</sup> 3d<sub>5/2</sub> (orange), Mo<sup>4+</sup> 3d<sub>5/2</sub> (magenta), Mo<sup>δ+</sup> 3d<sub>3/2</sub> (light green), Mo<sup>6+</sup> 3d<sub>3/2</sub> (dark green), Mo<sup>4+</sup> 3d<sub>3/2</sub> (purple), and Mo<sup>6+</sup> 3d<sub>5/2</sub><sup>27-29</sup>. Thus, the intensity of the recorded spectra was low, with a high signal to noise ratio that can lead to errors in the peak deconvolution and assignment.



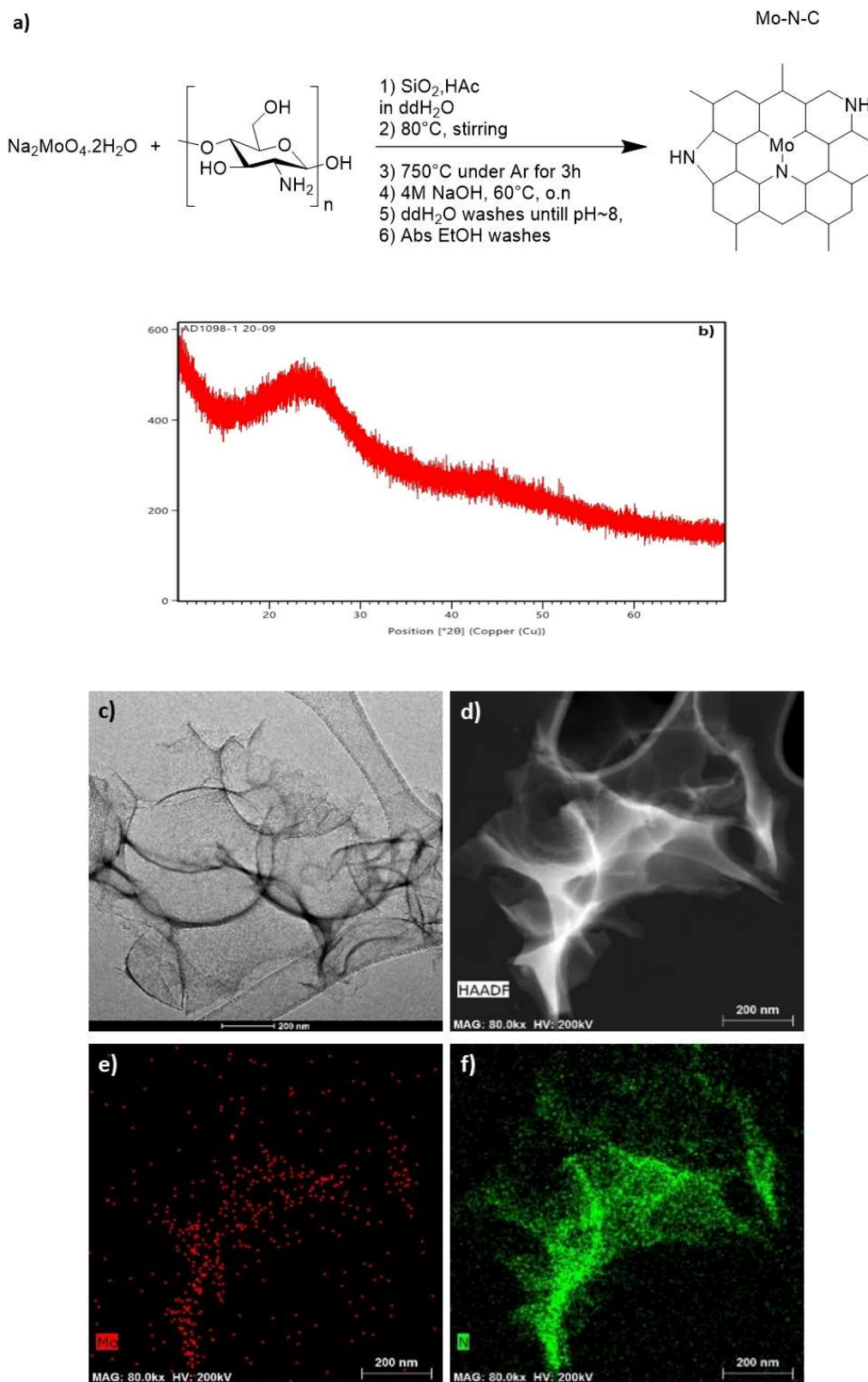


**Figure 2-1.** a) Synthesis scheme, b) recorded XRD pattern for Mo-N-C, c) TEM images, d) Aberration-corrected STEM-HAADF images, e) and f) STEM-EDS element mapping showing the distribution of Mo (red) and N (green), respectively.

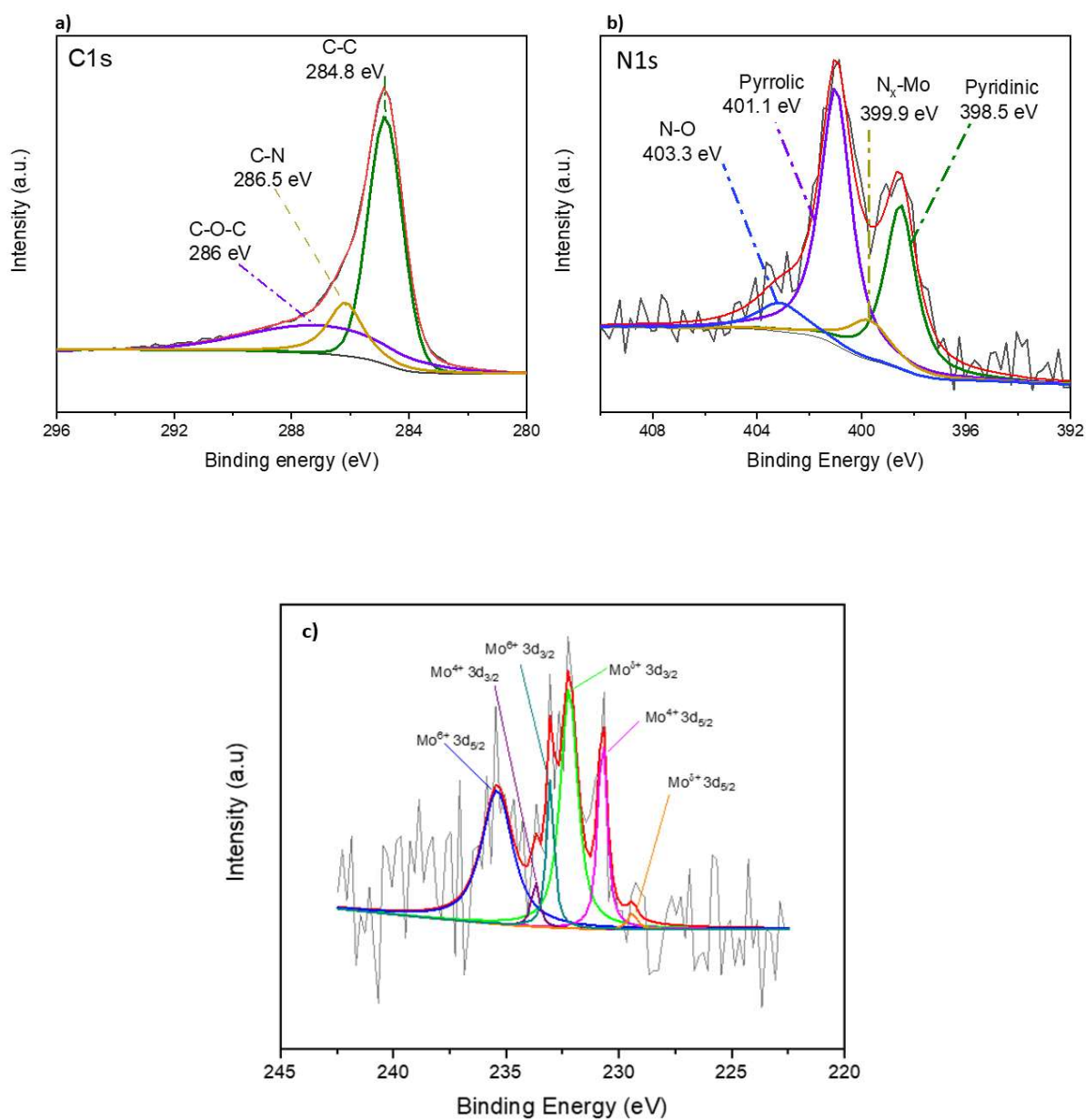


**Figure 2-2.** High-resolution XPS spectra of Mo-N-C powder for a) C1s region, b) N1s region and c) of Mo 3d region.

To confirm further the presence of Mo single atoms anchored on the N-doped conductive carbon matrix, high-resolution tunnel electron microscopy techniques were recorded (Fig2-3). As Molybdenum is quite light ( $Z = 42$ ), the contrast with the carbon

matrix is not as good as heavier metals when recording the HR-TEM images. Also, as the Mo atoms are dispersed evenly in the multi-layered, porous carbon matrix, and only the Mo which are in the focal of the electron probe will appear as sharp bright dots, the rest of them which are distributed outside of the focal will appear as bright blurry spots<sup>30</sup>. For the ease of reading, some Mo single atoms were circled in orange in the image below.

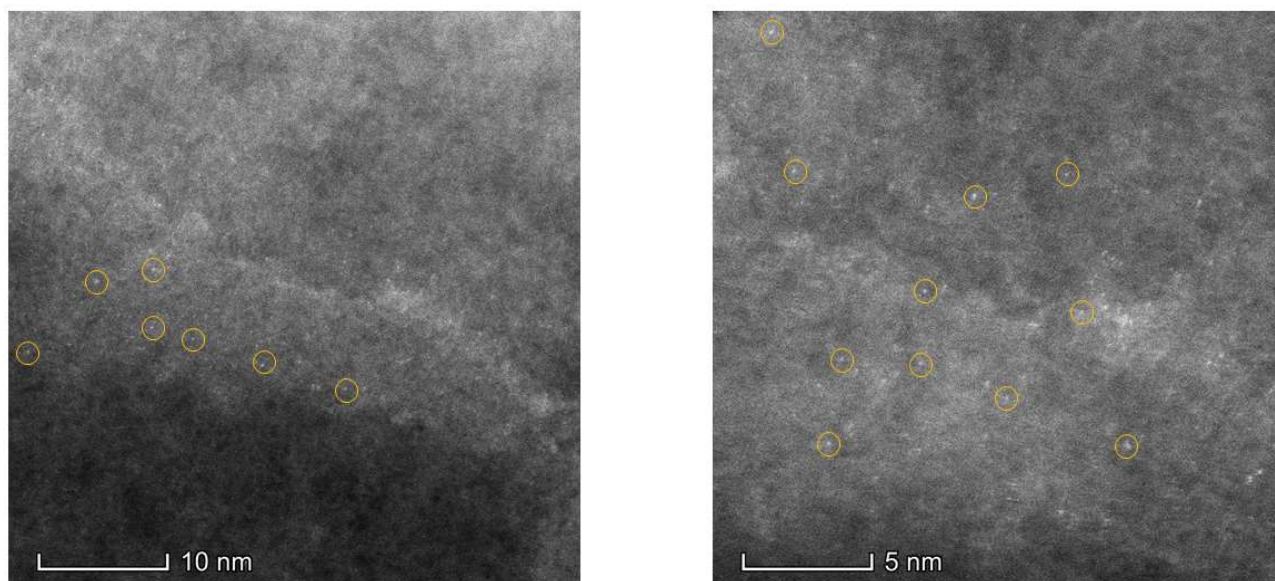


**Figure 2-3.** HR-TEM images of Mo-N-C.

The presence of Mo single atoms was confirmed, and in the recorded HR-TEM they were found to be homogeneously dispersed within the entire carbon matrix.

Results from the HR-TEM, Mo 3d and N1s region of the XPS spectrum, as well as the STEM-EDS spectrum are in accordance with each other. All above characterization results point in the direction that Mo-N-C is composed of Mo single atoms embedded in an N-doped carbon matrix.

### 2.3.2 Electrochemical Performances

In order to test the performances of the catalyst, it was dispersed as catalytic ink (3.5 mg<sub>cat</sub>, 1 mL bidistilled H<sub>2</sub>O, 250 µL isopropanol, 10 µL of 5% Nafion perfluorinated resin; yielding 2.78 mg<sub>cat</sub>.mL<sup>-1</sup>) and 100 µL were drop deposited on carbon cloth (1 cm<sup>2</sup>) and characterized electrochemically. The as-prepared catalyst-coated carbon cloths were used for the following electrochemical characterization, after activation by cyclic voltammetry (5 CV, from 0 to -1 V vs RHE). The electrolysis was performed in alkaline media (0.1 M KOH) as it limits the availability of protons, slowing down the kinetics of the competing HER reaction. Prior to electrochemical characterization, 0.1 M KOH electrolytes were purged with corresponding gas for at least 30 mins at 20 mL.min<sup>-1</sup>; the flowrate was kept constant during all experiments and stopped 30 mins after the end of the experiments. The nitrogen flow coming out of the electrochemical H-cell was bubbled through an acid trap solution (10 mL, 1 mM H<sub>2</sub>SO<sub>4</sub>) in order to trap gaseous ammonia as solvated ammonium (NH<sub>3(g)</sub> → NH<sub>4</sub><sup>+</sup><sub>(aq)</sub>). After the electrolysis, both working and counter electrolytes as well as acid trap solutions were analysed for ammonia concentration by the spectroscopic modified salicylate method by measuring the absorption at 660nm on a Cary60 UV-Vis spectrometer. The ammonia amounts were baseline corrected with respective electrolytes in order to remove background ammonia from the measurements.

Linear sweep voltammetry (LSV) was performed in working gas saturated aqueous 0.1M KOH electrolyte (30 mins under a constant flow of 20 mL.min<sup>-1</sup>). This experiment gives quickly an idea if a catalyst may show some activity towards N<sub>2</sub>RR by monitoring if a hysteresis in onset potential is observed when bubbling Ar compared to N<sub>2</sub>. In our case, after a quick activation and catalyst surface cleansing procedure, consisting in a linear sweep at 5

mV.s<sup>-1</sup> from 0 to -1.0 V vs RHE followed by five cycles of cyclic voltammetry (CV) at 10 mV.s<sup>-1</sup> between 0 and -0.6 V vs RHE.

Under nitrogen, the recorded potential to achieve -1 mA.cm<sup>-2</sup> was -0.347 V vs RHE, under argon reaching the same current density requires a potential of -0.747 V vs RHE. This result was preliminary and could indicate good N<sub>2</sub>RR performances.

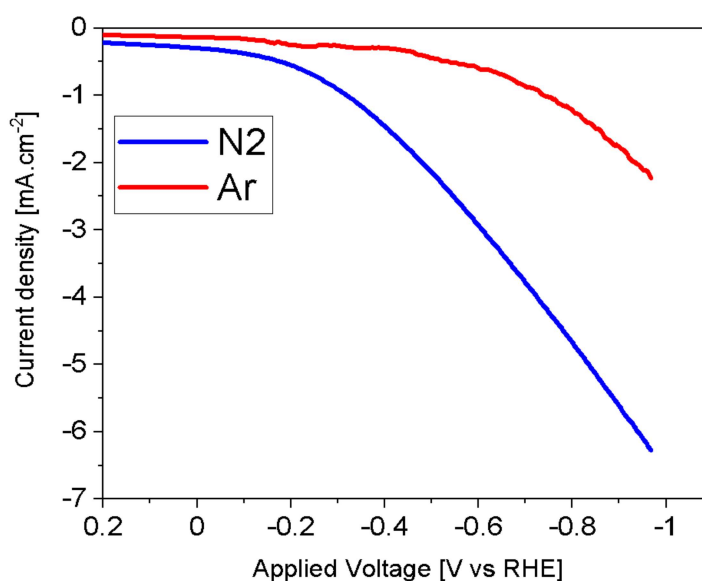


**Figure 2-4.** Linear Sweep Voltammetry results for Mo-N-C in N<sub>2</sub> and Ar saturated 0.1 M KOH.

To further control that the ammonia measured from spectroscopic measurements was produced from the reduction of dinitrogen, additional control experiments were necessary. At first a control experiment where argon gas (Ar) was fed for 14h to the H-cell, under the working potential of -0.277 V vs RHE was performed, and was used as a control experiment to ensure that the measured ammonia was produced from dinitrogen reduction. Unfortunately, ammonia can be present as an adsorbed species on the surface of materials or directly present

in the electrolytes yielding a background absorption. After 14h of experiment, only low amounts of ammonia (1.75  $\mu\text{g}$ ) were measured, and the rate of production for  $\text{NH}_3$  was found to be very low ( $24.5 \text{ nmol}_{\text{NH}_3} \cdot \text{mg}_{\text{cat}}^{-1} \cdot \text{h}^{-1}$ ) compared with the 1h experiment performed under  $\text{N}_2$  with the same applied potential, producing 6.25  $\mu\text{g}$  of ammonia at  $367.6 \text{ nmol}_{\text{NH}_3} \cdot \text{mg}_{\text{cat}}^{-1} \cdot \text{h}^{-1}$ .

To assess the stability and activity of Mo-N-C, 1h chronoamperometric experiments were performed, where the applied potential was kept constant and the current density was monitored. Indeed, accumulation of ammonia is necessary in order to have a relevant spectroscopic quantification, as the sources of contamination are diverse and can be consequent. Due to the gas bubbling, the electrodes were constantly moving leading to noisy recordings of electrochemical performances. Very small bubbles are preferable to prevent this issue; they can be obtained using a frit at the outlet of the bubbling tube.

The profile of the best performing conditions is displayed below, showing good stability over 1h. Also Faraday efficiencies (FE) were calculated for this supposed three-electron process based on the equation:

$$FE = \frac{3 \times F \times C_{\text{NH}_3} \times V}{17 \times Q}$$

Where,  $F$  is the Faraday constant ( $96485 \text{ C} \cdot \text{mol}^{-1}$ ),  $C_{\text{NH}_3}$  is the concentration measured ammonia ( $\text{mol} \cdot \text{L}^{-1}$ ),  $V$  the total volume (L) and  $Q$  is the total charge passed through the electrode (C). The molar ( $v_{\text{NH}_3}$ ) and mass ( $v_{\text{NH}_3}^m$ ) yield rates of  $\text{NH}_3$  at different applied potentials were calculated as:

$$v_{\text{NH}_3} = \frac{C_{\text{NH}_3} \times V}{t \times m_{\text{cat}}}$$

$$v_{NH_3}^m = \frac{17 \times C_{NH_3} \times V}{t \times m_{cat}}$$

Where,  $C_{NH_3}$  is the concentration measured ammonia (mol.L<sup>-1</sup>),  $V$  the total volume (L),  $t$  is the electrolysis time (1h), and  $m_{cat}$  is the mass of the catalyst (typically 0.3 mg). The reported NH<sub>3</sub> yield rates, FE, and error bars were determined based on measurements of three separately prepared electrodes under the same conditions. The recorded current densities were normalized to the geometric surface of the electrode using the ImageJ software.

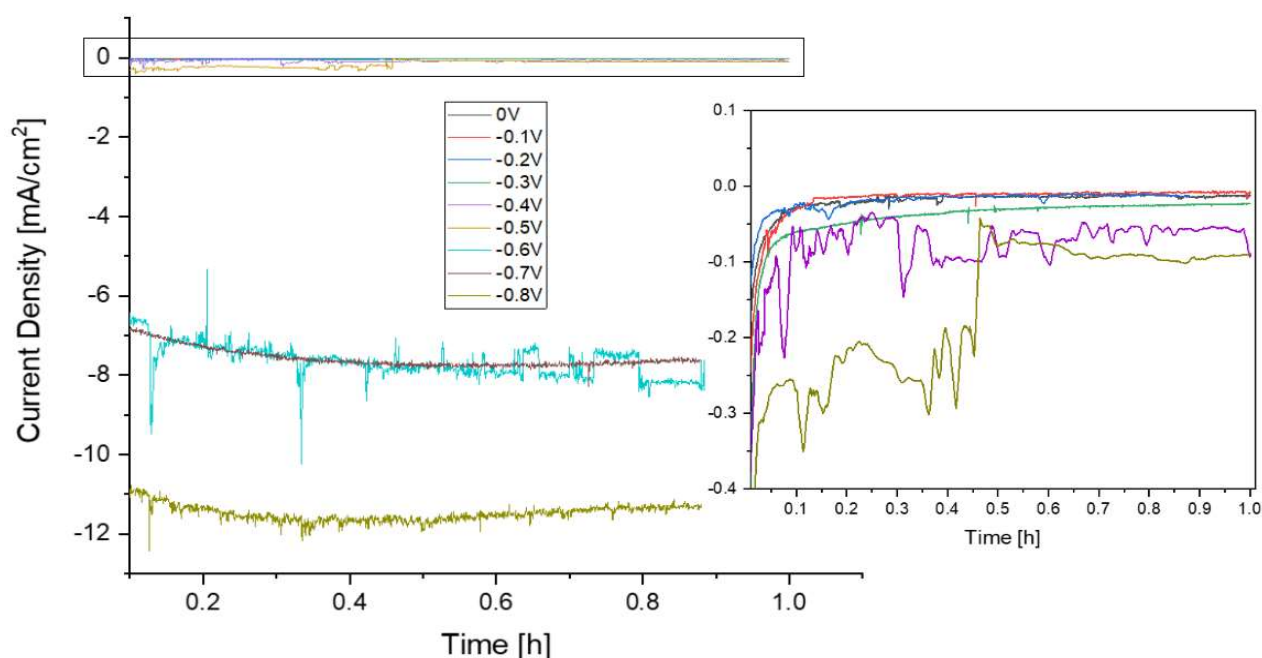


**Figure 2-5.** 1h electrolysis at constant voltage of Mo-N-C in N<sub>2</sub> saturated 0.1M KOH.

The best recorded performance for 1h electrolysis in 0.1 M KOH using Mo-N-C were achieved at -0.1V vs RHE, where ammonia was produced at the high averaged rate of 10.33 ( $\pm 1.36$ )  $\mu\text{g}_{NH_3} \cdot \text{mg}_{cat}^{-1} \cdot \text{h}^{-1}$  (Fig.2-5), with a record averaged FE of 37.9%. For the second and third best performing conditions, measured yield rate of ammonia was lower but still



consequent, ranging from  $6.36 (\pm 4.75) \mu\text{g}_{\text{NH}_3} \cdot \text{mg}_{\text{cat}}^{-1} \cdot \text{h}^{-1}$  to  $4.86 (\pm 0.37) \mu\text{g}_{\text{NH}_3} \cdot \text{mg}_{\text{cat}}^{-1} \cdot \text{h}^{-1}$  at -0.0V and -0.2V vs RHE, with a corresponding FE of 27.3% and 18.4%, respectively. Starting from -0.4 V vs RHE the FE decreased and the ammonia production rate increase. As more negative potential is applied, the competing HER reaction becomes more and more significant, drastically reducing the FE for  $\text{NH}_3$  production, with 0.7%, 0.3% and 0.08% at -0.6, -0.7 and -0.8 V vs RHE. The increase of the ammonia production rates were measured with significant error bars in between each samples, especially for -0.6 and -0.8 V vs RHE with respective yield rates of  $7.73 (\pm 5.72)$  and  $9.34 (\pm 5.48) \mu\text{g}_{\text{NH}_3} \cdot \text{mg}_{\text{cat}}^{-1} \cdot \text{h}^{-1}$ ; suggesting a degradation of the deposited catalyst or external sources of contamination. Thus, the three independent experiments performed at -0.7V vs RHE yielded  $8.12 (\pm 0.50) \mu\text{g}_{\text{NH}_3} \cdot \text{mg}_{\text{cat}}^{-1} \cdot \text{h}^{-1}$ . Also, it should be noted that from -0.6V vs RHE and below, the carbon cloth itself starts exhibiting some HER activity<sup>31,32</sup>, which will drastically decrease the FE for Mo-N-C, as the supplied electrons will not participate in the  $\text{N}_2\text{RR}$ .



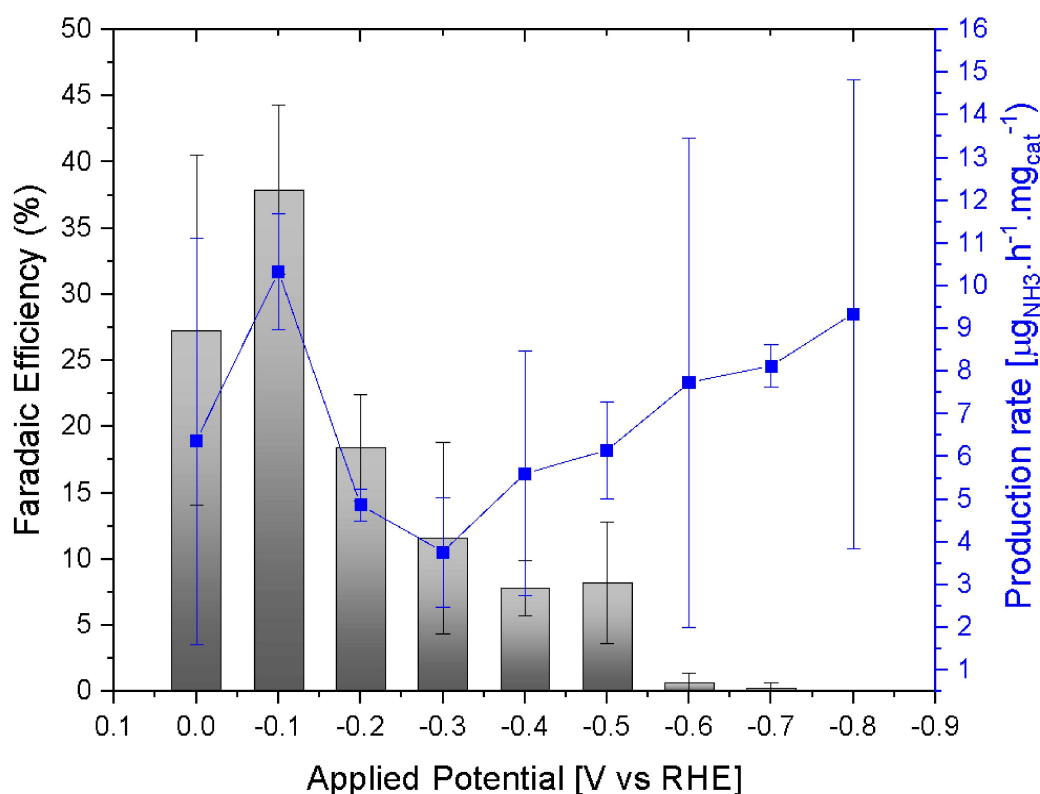


**Figure 2-6.** Calculated Faraday efficiencies and ammonia production rates for 1h electrolysis at constant voltage of Mo-N-C in  $\text{N}_2$  saturated 0.1M KOH.

As the above-obtained results were unsatisfactory, a new set of controls was performed. Where, a control catalyst ink was prepared exactly in the same fashion as for Mo-N-C, except no catalyst was added in the ink (Ctrl). This control aims at discriminating if the catalyst shows some activity towards  $\text{N}_2\text{RR}$  or if the spectroscopically measured ammonia could be produced from the carbon cloth itself, or as a contaminant of the nitrogen flow ( $\text{N}_2 > 99.9\%$ ). Another set of controls where argon ( $\text{Ar} > 99.99\%$ ) was bubbled through the cell was also performed. Without supplying nitrogen to the cell, the measured ammonia has to come from elsewhere than the  $\text{N}_2\text{RR}$ . This control will help distinguish between actual activity and measuring contaminants. The results of these control experiments are displayed in Figure 2-7.

Partial current densities were calculated according to:

$$j_{NH_3} = FE \times j$$

Where  $j_{NH_3}$  is the partial current density for ammonia (mA.cm<sup>-2</sup>),  $FE$  is the Faraday efficiency, and  $j$  is the geometrical current density (mA<sub>NH3</sub>.cm<sup>-2</sup>).

When comparing the Faraday efficiencies of Mo-N-C N<sub>2</sub> (blue) versus the Ar (red) in Figure 2-7 a), the ones under nitrogen flow were almost always higher than the ones using argon, with the exception of the performances recorded at -0.2 V vs RHE. Thus, when comparing the partial current densities for the production of ammonia (Fig.2-7 b)) the recorded results were similar and impossible to distinguish the best performing, as the error bars are significant in both conditions. One thing could be noted is that ammonia was always measured spectroscopically when Ar was used as feeding gas instead of N<sub>2</sub>, meaning that significant sources of contamination were present in both experiments. Furthermore, when comparing the FE of Mo-N-C with Ctrl using N<sub>2</sub> as feeding gas, one can see that the FE are higher for Ctrl at low potential, from 0 to -0.2V vs HRE, and lower at higher potentials, from -0.3 to -0.8 V vs RHE.

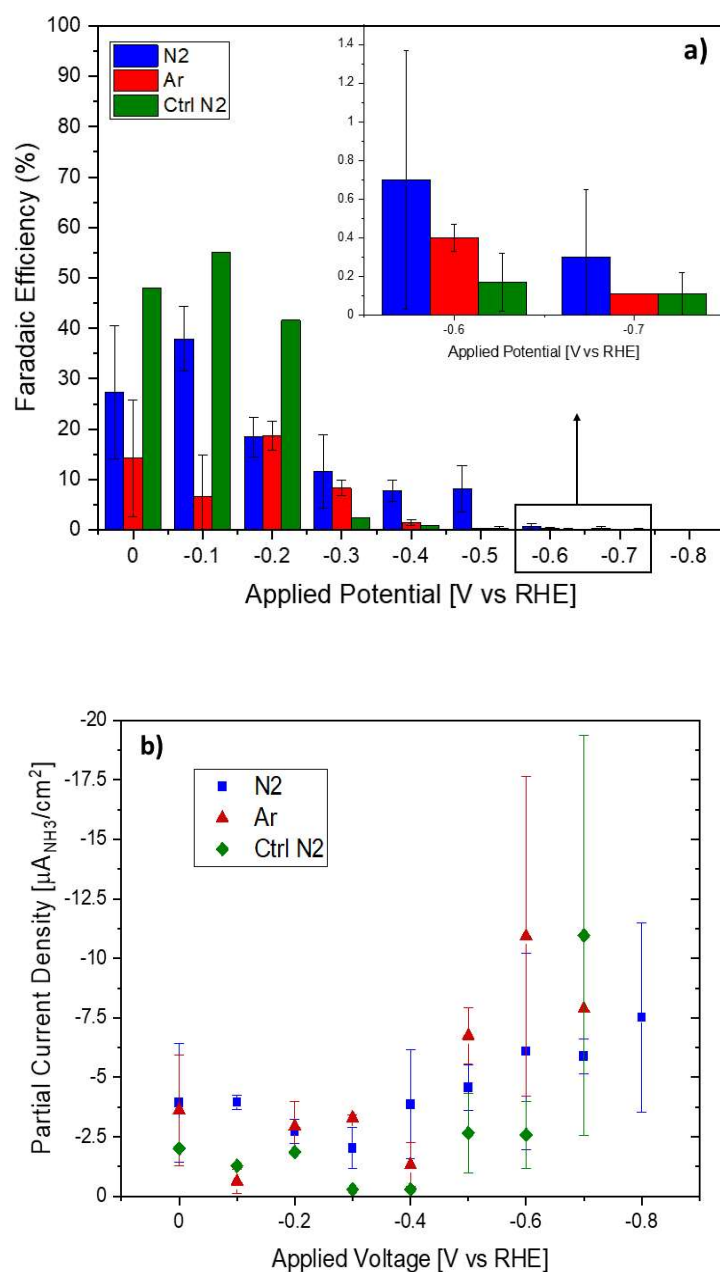


**Figure 2-7. a)** Calculated Faraday efficiencies and b) associated partial current densities for 1h electrolysis at constant voltage of Mo-N-C in N<sub>2</sub> (blue), Ar (red) and of Ctrl in N<sub>2</sub> (green) saturated 0.1M KOH.

This is probably because only limited current passes through the electrode at low negative potential, leading in an artificially high FE. The partial current densities for the production of ammonia using Ctrl were usually lower than the ones using Mo-N-C, as the carbon-cloth as a higher resistance and nearly no activity at low potentials limiting the

amount of electrons (i.e. current) passing through the electrode. The carbon cloth showed an increase in partial current density with potentials lower than -0.4 V vs RHE, supporting the hypothesis that the C-cloth is active towards HER. Together these control experiments shook the hypothesis of Mo-N-C having a high reproducible activity towards N<sub>2</sub>RR.

In order to see if the measured ammonia was coming from adsorption on the surface of catalysts, the time of the electrolysis was doubled from one to two hours. If the electrons supplied to the electrode are used in the reduction of nitrogen to ammonia the production should be consistent with time, meaning that the Faraday efficiency and the partial current density for ammonia production should be similar from one to the other (multiples of each other). The results of the experiment for 1h and 2h chronoamperometry at different applied voltages for Mo-N-C and Ctrl in nitrogen saturated 0.1 M KOH are displayed in Figure 2-8.

Here the difference is stunning, where for both Mo-N-C and Ctrl the Faraday efficiency and the partial current densities decreased drastically. For Mo-N-C at -0.1 V vs RHE the FE decreased from 37.9% to 6.6%, at -0.2 V vs RHE, from 18.4% to 3.0% at -0.2 V vs RHE, and at potentials lower than -0.4 V vs RHE to almost 0%, being 0.11%, 0.06%, 0.04% and 0.02% for -0.5, -0.6, -0.7 and -0.8 V vs RHE, respectively. The same trend was observed for the calculated partial current densities, decreasing from -3.94  $\mu\text{A}\cdot\text{cm}^{-2}$  to -0.15  $\mu\text{A}\cdot\text{cm}^{-2}$  at -0.1 V vs RHE when doubling the electrolysis time. For -0.6, -0.7 and -0.8 V vs RHE the current density decreased from -6.1  $\mu\text{A}\cdot\text{cm}^{-2}$  to -0.10  $\mu\text{A}\cdot\text{cm}^{-2}$ , from -5.9  $\mu\text{A}\cdot\text{cm}^{-2}$  to -0.21  $\mu\text{A}\cdot\text{cm}^{-2}$ , and from -7.51  $\mu\text{A}\cdot\text{cm}^{-2}$  to -0.12  $\mu\text{A}\cdot\text{cm}^{-2}$ , respectively. Thus, for Mo-N-C after 2h electrolysis, the current densities at lower potentials were higher than the ones recorded at -0.3 and -0.4 V vs RHE, which were -0.024  $\mu\text{A}\cdot\text{cm}^{-2}$  and -0.023  $\mu\text{A}\cdot\text{cm}^{-2}$ , respectively. This result suggest that at low applied potential the activity towards N<sub>2</sub>RR increased slightly. The

same similar trends were observed for the control experiments using Ctrl as the electrode. Altogether, this suggest that the spectroscopically measured ammonia was adsorbed on the surface of the electrode and desorbed upon immersion in the electrolyte.

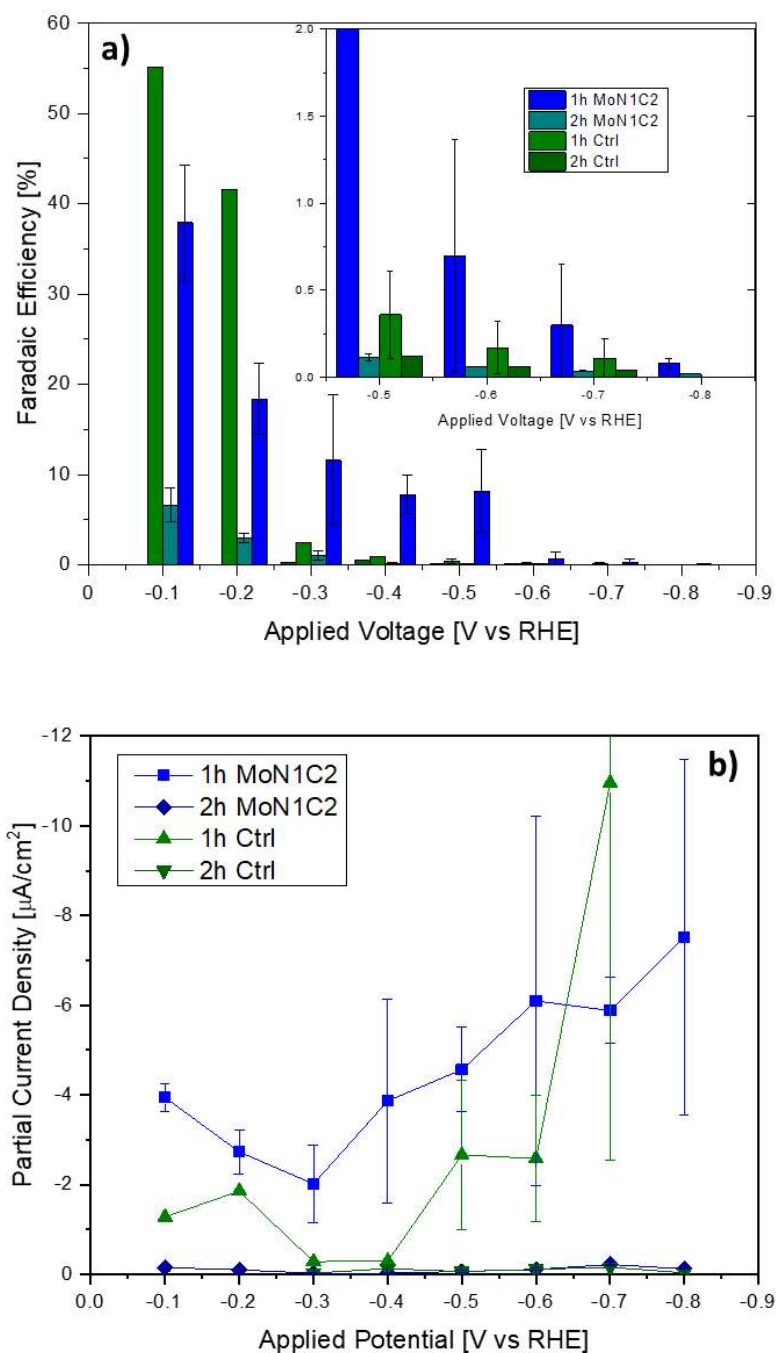


**Figure 2-8.** a) Calculated Faraday efficiencies and b) associated partial current densities for 1h and 2h electrolysis at constant voltage of Mo-N-C in  $\text{N}_2$  (blues), and of Ctrl in  $\text{N}_2$  (green) saturated 0.1M KOH.

As a final control experiment in order to probe the activity of Mo-N-C for N<sub>2</sub>RR, as suggested from theoretical calculations, an isotopic labelling experiment was set-up. The aim of the experiment is to use <sup>15</sup>N<sub>2</sub> as feeding gas -solvated as <sup>15</sup>NH<sub>4</sub><sup>+</sup> in 1mM H<sub>2</sub>SO<sub>4</sub> acid trap- as it can be directly detected and quantified via nuclear magnetic resonance (NMR)<sup>33,34</sup>. As NMR is not a very sensible detection method<sup>35</sup> -down to 0.1-0.01mM concentration- a long electrolysis experiment has to be performed to ensure a sufficient concentration of isotopically labelled <sup>15</sup>NH<sub>3</sub> species to be detected.

Therefore, a 48h electrolysis at -0.1V vs RHE was performed using Mo-N-C. In this experiment, <sup>15</sup>N<sub>2</sub> (98%) was fed at a rate of 20 mL.min<sup>-1</sup> through the cell saturating the 0.1 M KOH electrolyte, the acid trap and it was let out of the system for 30mins before the electrolysis. When the electrolyte was saturated with the <sup>15</sup>N<sub>2</sub>, the cell was sealed on the working electrode side, closing the connection to the gas flow and to the acid trap, then the electrolysis began. The electrolysis was performed for 45h in this closed cell fashion (I). Then a first purge with <sup>15</sup>N<sub>2</sub> was done, where the gas was fed at a rate of 20 mL.min<sup>-1</sup> for 10 mins, reopening the circuit, carrying isotopic ammonia to dissolve as <sup>15</sup>NH<sub>4</sub><sup>+</sup> ions in the acid trap solution. After 10mins, the system was sealed again and the electrolysis was left to perform for 50mins (II) in this fashion. This step was repeated one more time, where the <sup>15</sup>N<sub>2</sub> was fed at 20 mL.min<sup>-1</sup> for 10 mins, before sealing the cell again for another 50mins of electrolysis (III). Finally, for the last hour of electrolysis a fourth step (IV) where <sup>15</sup>N<sub>2</sub> was continuously fed at 20 mL.min<sup>-1</sup> to the opened system under electrolysis. In total -0.1 V vs RHE were applied for 48h consecutively. This complicated experimental design arises from the expense of using <sup>15</sup>N<sub>2</sub> as feeding gas (0.416 L of <sup>15</sup>N<sub>2</sub> at 98% purity compressed at 13.1 atm, or 5 L at 1 atm, is priced 2'300.- from Sigma-Aldrich).

The aim of phase (I) was to see if, in a closed system, after sufficient time the current density would drop, as the electrolyte will become less and less saturated with  $^{15}\text{N}_2$  if any ammonia was produced. Phase (II) and (III) were implemented to record the behaviour of the catalyst if the dissolved  $^{15}\text{N}_2$  was replenished in a close system. Finally, phase (IV), where  $^{15}\text{N}_2$  is continuously fed, was performed to record the catalytic behaviour of Mo-N-C upon re-saturation of the electrolyte with  $^{15}\text{N}_2$ , and if current densities corresponding to the first hour of electrolysis could be achieved again. The results of this experiment are displayed below in Figure 2-9.

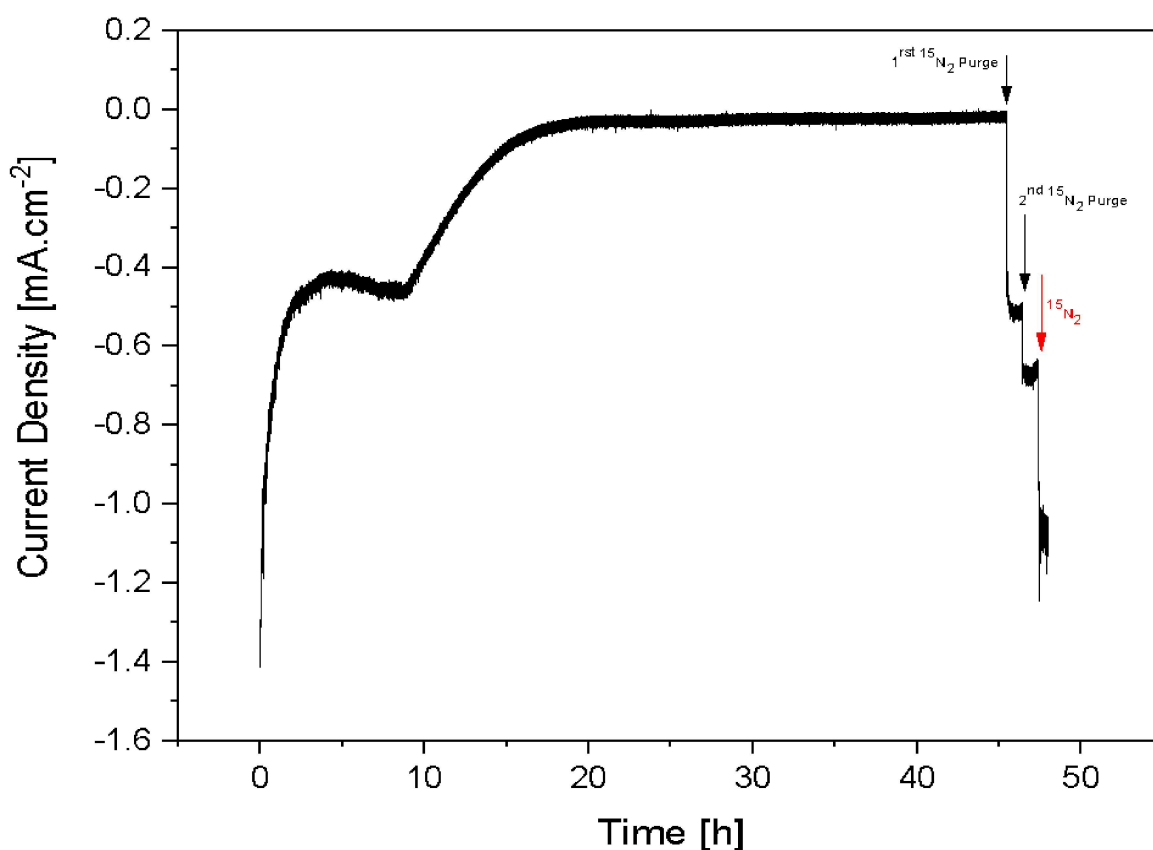


**Figure 2-9.**  $^{15}\text{N}_2$  isotopic labelling 48h electrolysis at -0.2 V vs RHE using Mo-N-C in 0.1M KOH.

Initially, when the electrolyte was saturated with  $^{15}\text{N}_2$ , a current density of  $-1.4 \text{ mA.cm}^{-2}$  was recorded, which was assigned to high activity towards reduction upon gas saturated electrolyte. This current density decreased quickly in absolute value with time and reached a plateau after 2h of electrolysis, at around  $-0.42 \text{ mA.cm}^{-2}$ . This current density was stable until 9h of electrolysis was reached. The plateau at  $-0.42 \text{ mA.cm}^{-2}$ , which is stable for around 7h, was assigned to the reduction of nitrogen to ammonia into non-saturated electrolyte. From this point in time, the absolute current density value decreases, at a slower rate, to near  $0 \text{ mA.cm}^{-2}$  by 20h of electrolysis. The decrease in current density arising after 9h of electrolysis was assigned to slower reaction rates as the electrolyte contains less and less dissolved  $^{15}\text{N}_2$  with time and the diminishment of dissolved  $^{15}\text{N}_2$  near the surface of the electrode. The current stayed at near  $0 \text{ mA.cm}^{-2}$ , until the first  $^{15}\text{N}_2$  purge of phase (II), occurring after 45h of electrolysis. One can hypothesize that there was no more dissolved  $^{15}\text{N}_2$  in the electrolyte until the first purge of  $^{15}\text{N}_2$ . Upon the first purge, the absolute current density value increased to about  $-0.50 \text{ mA.cm}^{-2}$ , which is comparable to the plateau at  $-0.42 \text{ mA.cm}^{-2}$  of phase (I), corresponding to electrolysis in  $0.1 \text{ M KOH}$  non-saturated with  $^{15}\text{N}_2$ . The turbulent replenishment of  $^{15}\text{N}_2$  in the electrolyte by bubbling helped mixing the electrolyte as well, which may play a role in the availability of  $^{15}\text{N}_2$  near the surface of the electrode. Upon the second purge, initiating phase (III), the absolute current density increased to  $-0.68 \text{ mA.cm}^{-2}$  in the first minutes, and decreased in absolute value to  $-0.64 \text{ mA.cm}^{-2}$  in the last minutes of this 50 mins phase. This current density increase in absolute value was directly correlated to the replenishment of dissolved  $^{15}\text{N}_2$  in the electrolyte. Moreover, the slight decrease of the current density at the end of phase (III),  $-0.68 \text{ mA.cm}^{-2}$  to  $-0.64 \text{ mA.cm}^{-2}$ , could be explained by the decrease in dissolved  $^{15}\text{N}_2$  generation of  $^{15}\text{NH}_3$ . For the final phase (IV), where  $^{15}\text{N}_2$  was continuously fed to the open cell, the current density stabilized around  $-1.08 \text{ mA.cm}^{-2}$  after



another sharp increase, which is comparable to the obtained initial current densities of phase (I), where the electrolyte was saturated with  $^{15}\text{N}_2$ . This current density can be associated with the maximum activity of Mo-N-C towards  $\text{N}_2\text{RR}$  in  $^{15}\text{N}_2$  saturated 0.1 M KOH.

Unfortunately, the recovered electrolyte and acid trap solution did not contain enough dissolved  $^{15}\text{NH}_4^+$  to be analysed quantitatively by NMR.

### 2.3.3 Other Samples: MOFs and ZIFs

Other catalysts based on metallic organic frameworks (MOFs) templates<sup>36</sup>, and then carbonized at high temperatures in order to generate metallic single-atom or dual-atoms embedded in a carboneous conductive matrix were synthesized. This work was inspired by previously reported literature<sup>37–39</sup>. SACs based on previously reported NENU-5<sup>40</sup>,  $\text{H}_3\text{PMo}_{12}\text{O}_{40}$  and  $\text{FeMoO}_4$  were successfully added by co-precipitation methods and annealed at 800°C under argon, yielding four catalysts denoted as  $\text{C}_x\text{-Cu}$ ,  $\text{MoC}_x\text{-Cu}$ ,  $\text{FeMoC}_x\text{-Cu}$  and  $\text{MoC}_x\text{-Cu-FeMo}$ . SACs based on previously reported ZIF-8<sup>41</sup>, yielding a metal-free and a Cu co-doped nitrogen-doped-carbon electrocatalyst, denoted as N-d-C and Cu-N-d-C. Regardless of the reported literature, none of the above listed catalysts showed promising activity towards  $\text{N}_2\text{RR}$  in alkaline electrolyte at ambient conditions.

### 2.3.4 Discussion

Regarding the future of ambient aqueous dinitrogen reduction, one should continue to investigate the use of single atom transition-metal based catalysts supported on nitrogen-doped carbon matrices. Indeed, the carbon matrix has a good conductivity and permits the anchoring of single atoms within defective sites. Single atoms present a 100% atomic efficiency, a metallic character leading to good conductivity, and through intelligent design the coordination sphere can be tuned by the carbonization conditions and the use of different precursors. Indeed, chitosan showed to be a good precursor for the generation of

nitrogen-doped carbon. Other bio-derived or bio-waste-derived materials could represent an efficient way to reutilize unwanted materials to create conductive carbon-based supports or even electrocatalysts with high selectivity and efficiency towards ammonia electrosynthesis.

The use of single atoms for efficient and selective  $\text{N}_2\text{RR}$  in ambient aqueous solutions was also supported by the latest reports using precious metals like  $\text{Ru}^{39,42}$  or  $\text{Au}^{43}$ . Other transition metals such as  $\text{Fe}^{44-46}$ ,  $\text{Co}^{47}$ ,  $\text{Cu}^{48}$  or even  $\text{Ti}^{49-51}$  can therefore be investigated as single-atoms, as they were previously predicted to show high performances for  $\text{N}_2\text{RR}$  by DFT by several different groups. Despite the progress, the yield rates of ammonia production for the above-mentioned single atom catalysts is still too low for practical applications. Indeed, unravelling the active site of the SACs is a major challenge in understanding the features needed to activate the highly stable  $\text{N}_2$ . Also, the competing HER reaction features much faster kinetics and lower activation barrier, leading to a poor FE towards  $\text{N}_2\text{RR}$  with increasing negative potentials. Surface engineering of the support could help reduce the HER activity<sup>3,52</sup>. Further investigation of metals displaying a high overpotential for the HER, like bismuth (Bi), tin (Sn) or even antimony (Sb), could be promising for  $\text{N}_2\text{RR}$ .

As displayed from my obtained results, the determination of the provenance of ammonia and its quantification is everything but trivial<sup>33,53,53,54</sup>. Indeed, the amount of ammonia produced is usually so small that it cannot precisely be attributed to electrosynthesis, as nearly everything is a source of contamination<sup>55</sup>. The usual indophenol and/or salicylate<sup>56</sup> detection methods are based on a two-step reaction generating a dye that will be quantified using UV-Vis. These methods are by essence indirect quantification methods and the correlation to the electrosynthesis of ammonia can be diluted along the process. Moreover, the selectivity challenge of  $\text{N}_2\text{RR}$  over favoured HER is colossal<sup>17</sup>.

In May 2019 -or a couple of months after this project was stopped- a ground-breaking article was published in Nature. In this article entitled "a rigorous electrochemical ammonia synthesis protocol with quantitative isotope measurements"<sup>57</sup> they listed all the possible contamination sources that are usually present in all publications prior to this one. The list is exhaustive, but a few should be mentioned such as: air (ammonia accumulates in electrolytes open to air), human breath, ion-conducting membranes (i.e. Nafion® being acidic can adsorb  $\text{NH}_4^+$ ), nitrogen-containing compounds and precursors (usually present in the synthesis of most SAC), the nitrogen and the argon feed gas. This already put in perspective previously reported results, including mine, that suffered from reproducibility. They continue saying that benchmarking protocols are needed to avoid false-claiming record results, with the systematic adoption of the  $^{15}\text{N}_2$  isotopic labelling experiment with quantitative detection by  $^1\text{H}$  NMR and FTIR<sup>58</sup>. In a herculean effort, they tested some of the pure-metal catalysts previously reported for  $\text{N}_2\text{RR}$  and found no activity for all of them. Since this publication, the frequency of published article of about  $\text{N}_2\text{RR}$  went down, as the price of the isotopic experiment is dissuasive and the number of control experiments needed to claim any result is astronomical.

The design of the electrochemical cell can also be improved, as the proton availability is one of the major determinant factors for the competitive HER, intelligent design should also be imputed in the design of the electrochemical apparatus. The utilization of gas diffusion layers in a triple phase reactor type of cell could result in higher selectivity and activity for  $\text{N}_2\text{RR}$  over HER<sup>59</sup>.

Finally, other types of materials could be used for the absorption and transport of ammonia in a Hydrogen Economy, such as metal hydrides, halides and borohydrides<sup>60</sup>.

### 2.3.5 Conclusion

Herein, on the basis of density functional theory calculations reported by Ling et al<sup>21</sup>, single atom Mo embedded in nitrogen-doped carbon (Mo-N-C) derived from the calcination of chitosan were successfully synthesized. The presence of Mo single atoms was confirmed directly by XPS and HR-TEM. The electrocatalyst was investigated for its ambient aqueous N<sub>2</sub>RR activity in 0.1 M KOH electrolyte, using H-type electrochemical cells. Ammonia concentrations were determined using the spectroscopic modified salicylate technique. Mo-N-C was believed to demonstrate a 'production' of 10.33 (±1.36)  $\mu\text{g}_{\text{NH}_3} \cdot \text{mg}_{\text{cat}}^{-1} \cdot \text{h}^{-1}$ , with an averaged FE of 37.9% at -0.1 V vs RHE in 0.1 M KOH. The isotopic labelling experiment showed direct correlation between the current density and the amount of dissolved <sup>15</sup>N<sub>2</sub> for 48h electrolysis at -0.1 V vs RHE. Unfortunately, the amount of ammonia produced was insufficient to perform direct quantification from <sup>1</sup>H NMR. These results represent evidence that dinitrogen reduction is extremely tricky as ammonia can come from various sources of contamination, increasing drastically the difficulty in assessing obtained results.

Thus, with sufficient controls, selective and active electrocatalysts derived from single atoms supported on nitrogen-doped carbon matrices could be promising candidates for future aqueous N<sub>2</sub>RR at ambient aqueous conditions.

### 2.3.6 Experimental Section

#### *Materials*

Hexadecyltrimethylammonium bromide (CTAB, 99%) was purchased from BioXtra, ammonia solution (25%) from VWR International GmbH, absolute ethanol from thermo-fischer, tetraethyl orthosilicate ( $\geq 99\%$ ) from Ivalua, Sodium hydroxide pellets (extrapure) from Chemie Brunschwig AG, Sodium molybdate dihydrate (99+%) and chitosan (high molecular weight flakes) from sigma-aldrich, glacial acetic acid from ABCR, argon (99.998%) and dinitrogen (99.995%) from carbagas AG, hydrogen peroxide (30%) and sulphuric acid (96%) from Reactolab,. Bidistilled water ( $18.2 \text{ M}\Omega\cdot\text{cm}^{-1}$ ) was used.

#### *Synthesis $\text{SiO}_2$ spheres*

0.5 g of cetrimonium bromide (CTAB), 1 mL of aqueous ammonia and 0.5 mL of tetraethyl orthosilicate were dissolved in a mixture of absolute EtOH (50 mL) and bidistilled water (75 mL) and left under stirring at room temperature for 58h. The precipitate was collected by centrifugation (6'000 rpm for 10 mins). Then, the recovered  $\text{SiO}_2$  were further dispersed in acetone and refluxed at  $80^\circ\text{C}$  for 1h, and collected by centrifugation (6'000 rpm for 10 mins). This procedure was repeated twice, in order to wash the  $\text{SiO}_2$  spheres completely off CTAB. The  $\text{SiO}_2$ -spheres were dried at  $80^\circ\text{C}$  overnight and used without further purification.

#### *Synthesis of Mo-N-C*

Sodium molybdate dihydrate ( $\text{Na}_2\text{MoO}_4\cdot 2\text{H}_2\text{O}$ , 4.5 mg), chitosan (216 mg),  $\text{SiO}_2$ -nanospheres (1,00 g), and 1 mL of glacial acetic acid were dissolved in 100 mL bidistilled water and left to dry under stirring at  $80^\circ\text{C}$  for 72h. Then, the recovered elastic precipitate was grounded and heated in a tubular furnace under Ar flow with a ramp of  $17.5$

$^{\circ}\text{C}.\text{min}^{-1}$ , and maintained at  $750^{\circ}\text{C}$  for 3h. The calcined product was recovered as a dark grey powder and was placed in 4 M NaOH at  $60^{\circ}\text{C}$  under stirring for 18h, in order to dissolve the  $\text{SiO}_2$  template. The precipitate was collected by centrifugation (6'000 rpm for 5 mins) and washed with sufficient amounts of bidistilled water, until  $\text{pH} < 8$ . Then the black solid was washed twice with absolute EtOH (6'000 rpm for 5 mins) and dried at  $80^{\circ}\text{C}$  overnight before further use and characterization. The recovered product was denoted Mo-N-C.

### *Electrochemical measurements*

Electrochemical characterizations, including cyclic voltammetry (CV), linear sweep voltammetry (LSV), chronopotentiometry (CA) were carried out on a BioLogic VSP (VPM3) electrochemical workstation using a three-electrode set-up, with a 117 Nafion membrane at ambient temperature. CV and LSV were performed at a scan rate of  $10\text{mV}.\text{s}^{-1}$  and  $5\text{mV}.\text{s}^{-1}$  respectively. All potentials are referenced to the reversible hydrogen electrode (RHE). The measured potential vs. Ag/AgCl in saturated KCl can be converted to the reversible hydrogen electrode (RHE) scale according to the Nernst equation:

$$(E_{RHE} = E_{\frac{\text{Ag}}{\text{AgCl}}} + 0.197V + 0.059\text{pH}).$$

Before any measurement, the electrolytes were purged with according gas for 30 mins to ensure gas saturation in the electrolyte. To reduce any chance of  $\text{NH}_3$  loss, the gas flow was bubbled through 10 mL of 1 mM  $\text{H}_2\text{SO}_4$  -an  $\text{NH}_3$  adsorber (acid trap)-. Before NRR tests, Nafion membranes were cut into  $2 \times 2\text{cm}^2$  and treated in aqueous  $\text{H}_2\text{O}_2$  (3%) at  $100^{\circ}\text{C}$  for 1h, then rinsed with bidistilled water, then immersed in bidistilled water at  $100^{\circ}\text{C}$  for 1h, followed by 1h in 0.5 M  $\text{H}_2\text{SO}_4$  at  $100^{\circ}\text{C}$ , before being rinsed with copious amounts of water, and finally they were immersed in bidistilled water at  $100^{\circ}\text{C}$  for another 1h, and then rinsed

with sufficient bidistilled water until reaching pH=7. Then they were stored in bidistilled water until further use.

### *Material Characterization*

TEM was performed using a FEI Tecnai Osiris TEM equipped with a high-brightness field emission gun (XFEG). Samples for TEM were prepared by drop-drying the samples from their diluted ethanol suspensions onto carbon-coated copper grids. Energy-dispersive X-ray spectroscopy (EDS) patterns and mapping images were taken on a FEI Tecnai Osiris TEM in a scanning TEM mode. The elemental ratio was calculated from the  $K\alpha$  peak area of each element, using ESPRIT2 (Bruker) software. HR-TEM was performed on an FEI Titan Themis 60-300 operated at 200kV with an aberration-corrected probe and using HAADF-STEM parameters. XRD patterns were recorded on a PANanalytical Aeris Research Edition with a filtered Cu- $K\alpha$  radiation (40kV, 15mA), and analysed by HighScore Plus software. Samples were concentrated in EtOH and drop-casted on a Si wafer prior to analysis. X-ray photoelectron spectroscopy (XPS) measurements were performed on a PHI5000 VersaProbe II XPS system by Physical Electronics (PHI) with a detection limit of one atomic percent. Monochromatic X-rays were generated by an Al  $K\alpha$  source (1486.7 eV). The diameter of the analyzed area was 10  $\mu\text{m}$ .

### Determination of $\text{NH}_3$

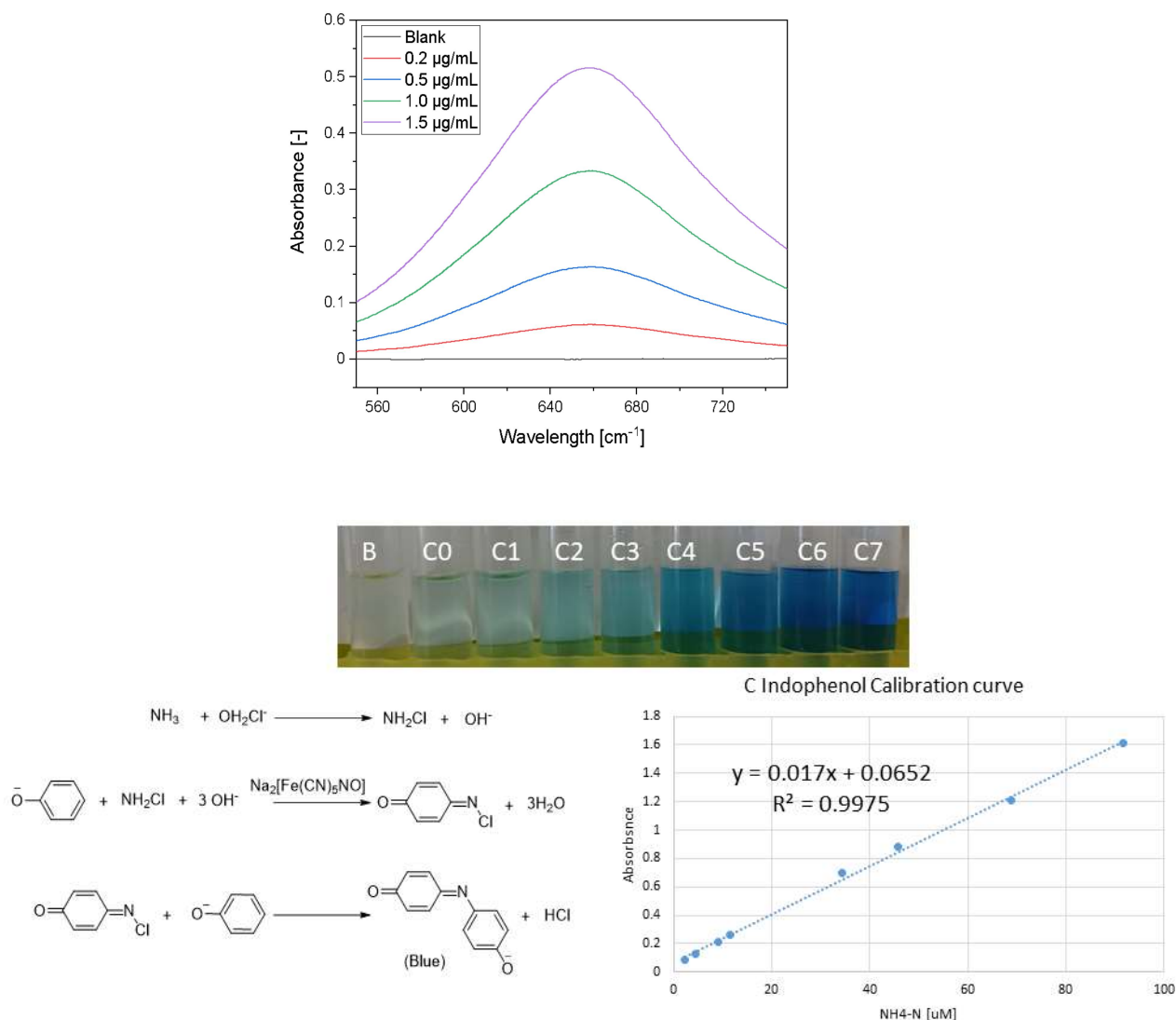


**Figure 2-10.** Calibration and reaction for Salicylate/Indophenol blue detection by UV-Vis.

Concentration of produced  $\text{NH}_3$  was spectrophotometrically determined by the modified indophenol blue method. In detail, 2 mL aliquot of the electrolytes (working, counter and acid trap) were removed from the corresponding electrochemical reaction compartments, and added to 2 mL of 1 M NaOH solution containing salicylic acid (5 wt%) and sodium citrate (5 wt%). Then, 1 mL of fresh 0.05 M NaClO and 0.2 mL of  $\text{Na}_2[\text{Fe}(\text{NO})(\text{CN})_5] \cdot 2\text{H}_2\text{O}$  (1 wt%)



were sequentially added to the previous solution. After standing at room temperature for exactly 1h in the dark, the UV-Vis absorption spectrum was recorded on a Carry60 Agilent spectrometer. The measurements were baseline corrected according to a concordant fresh control electrolyte sample and the indophenol blue/salicylate concentration was recorded at 660nm. The concentration-absorbance curves were calibrated, for each electrolyte tested, using standard  $\text{NH}_4\text{Cl}$  solutions with matter of precision.

### Cell Set-up

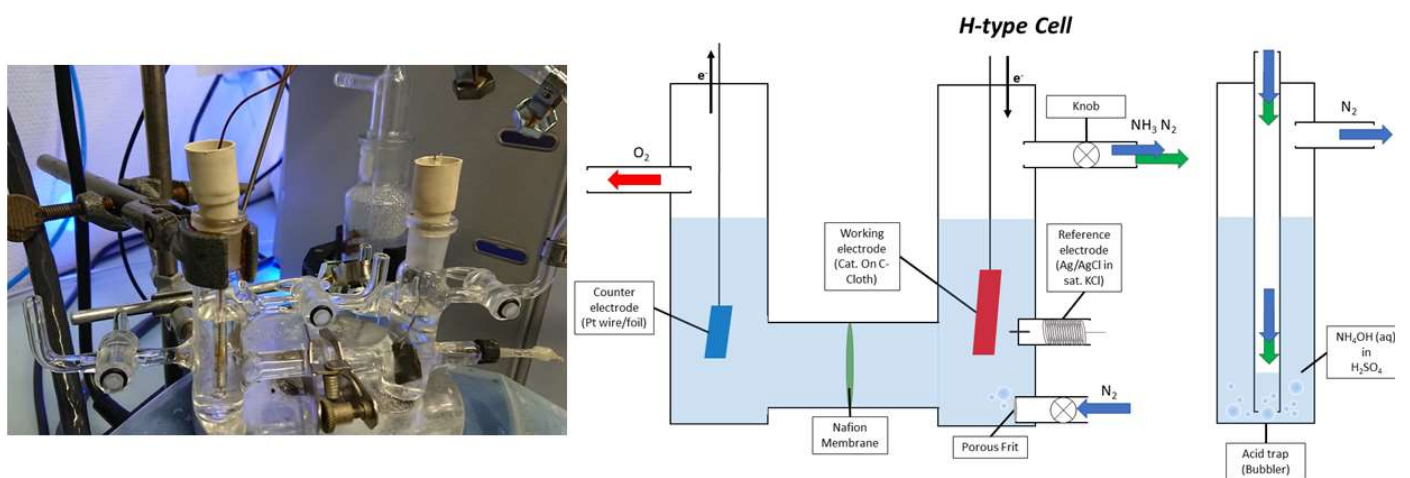


**Figure 2-11.** H-type Cell used with Nafion117 membrane.

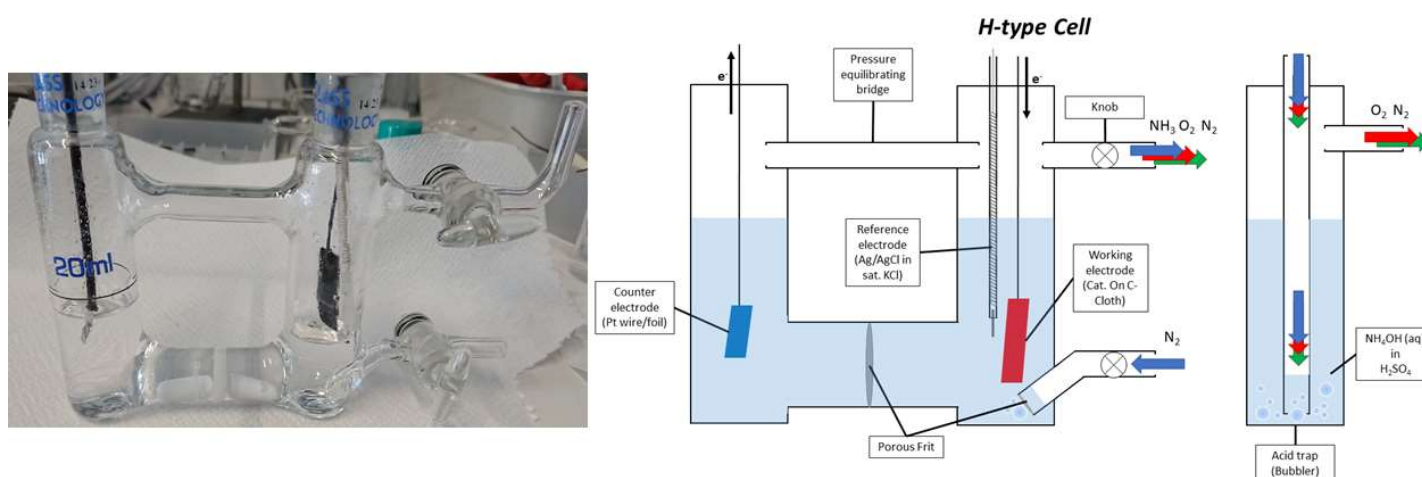


**Figure 2-12.** H-type Cell used with porous frit.

### *Contributions*

Albert Daubry synthesized the materials, performed the electrochemical tests, and the colorimetric quantifications. Albert Daubry designed the electrochemical cells. Dr. Lichen Bai performed the HR-TEM, TEM, HAADF and EDS-STEM mapping. Dr. Pierre Mettraux performed the XPS measurements.

## 2.4 Single-atom Electrocatalysts for Acidic Oxygen Evolution Reaction

As mentioned in the introduction, single-atom catalysts (SACs) are being researched worldwide for many electrocatalytic applications<sup>14</sup>, as their 100% atomic efficiency, high selectivity and activity are very attractive for scale-up application. Also, their well-defined structure and unique tunable electronic properties, arising from the metal-support interaction, that effectively dictate the binding energies of the intermediates to the metal centre, that accounts for its activity.

As Ru and Ir, the most active catalysts for OER, are scarce and expensive, downsizing from nanoparticles to single atoms would be beneficial. Thus, upon downsizing the nanoparticles the stability decreases as well, most reported SACs for OER utilize alkaline media, where under applied high-overpotential (typically >1.6 V vs RHE) the conditions are less harsh compared with acidic media. In the effort to replace those noble-metals, non-noble metals single atom electrocatalysts, such as Co<sup>61</sup>, Fe<sup>62</sup>, Mn<sup>63</sup>, and Ni<sup>64</sup>, graphed on nitrogen-doped carbon supports were reported for their activity in alkaline media.

Even though catalysts' performances are compared using the overpotential at 10 mA.cm<sup>-2</sup> ( $\eta_{10}^{\text{OER}}$ ), for practical applications they need to show low Tafel slopes at higher current densities (100-500 mA.cm<sup>-2</sup>).

As discussed before, Ru and Ir are the most active towards OER. Metal single atoms are not stable enough to withstand catalysis in acidic conditions, although Ru-N-C was reported<sup>65</sup> as efficient OER SAC in acid, which was believed to be stabilized by strong Ru-N bonding. The support is critical in the stability of the SAC, especially for acidic OER, where

formed metal oxides tend to be soluble in the electrolyte. Diluted surface alloys -precise atomic metal doping on a metallic support- were reported by Yao *et al.*<sup>66</sup> to have suppressed the dissolution of Ru by embedding Ru on PtCu<sub>x</sub>/Pt core-shell nanostructures. They observed that their collection of Ru<sub>1</sub> supported on PtCu alloys (Ru<sub>1</sub> on PtCu<sub>3</sub>, PtCu, Pt<sub>3</sub>Cu) exhibited faster kinetics and longer electrocatalytic lifetime compared with benchmarked RuO<sub>2</sub>. Other non-precious transition metals (Co, Ni, Fe, Mn ...) coordinated on carbon-based supports were reported for acidic OER, though with moderate activity and stability. In 2018, Zhang *et al.*<sup>64,67</sup> reported the use of anchored atomic Ni with a square-planar coordination environment on highly defective graphene (a-Ni@DG), that modified the electronic structure of anchored Ni, leading to a minimization of the reaction energy barrier and an increase in stability. Hetero-N-coordinated atomic cobalt bounded by pyridinic-N and amino-N ligands, were reported by Su *et al.*<sup>61</sup> to have low overpotential ( $\eta_{10}^{\text{OER}} = 265\text{mV}$ ) in 0.5 M H<sub>2</sub>SO<sub>4</sub> with an ultra-high TOF (2.8 s<sup>-1</sup>) and huge mass activity (7.6 A.mg<sup>-1</sup>), two orders of magnitude higher than commercial IrO<sub>2</sub>. 3d metals, such as Fe<sup>68</sup> and Mn<sup>63</sup>, in the square-planar configuration (M-N<sub>4</sub>) were also reported to have moderate activity towards OER. The type of coordinated nitrogen, graphitic and pyridinic N, were found to be respectively responsible for the conductivity and activity, which significantly affect OER performances. Fe-N<sub>4</sub> were reported to have  $\eta_{10}^{\text{OER}} = 294\text{ mV}$  in 0.5M H<sub>2</sub>SO<sub>4</sub>.

However, the reported literature for SACs for OER in acidic media is very limited due their intrinsic instability upon working potentials.

## 2.5 Results

### 2.5.1 Synthesis

In this study, a wet-impregnation method was used to synthesize metal-based single atoms dispersed on an oxidized carbon matrix. This synthesis is previously reported by Zheng *et al.*<sup>69</sup>, where they used carbon black material activated upon strong oxidizing conditions with nitric acid to generate surface oxygen species that will facilitate the adsorption of Ni<sup>2+</sup> ions, followed by a high temperature pyrolysis under inert atmosphere. Inspired by this efficient synthesis method, KetJen Black® (KJB), an highly electro-conductive carbon black material compared to widely used acetylene black (with electro-conductivity of 3.9 Ω.cm, and >1×10<sup>8</sup> Ω.cm, as 10 wt% in polycarbonate, respectively) consisting in hollow particles (80% void fraction) was used as carbon support. The hollow structure would facilitate the diffusion of generated O<sub>2</sub> within its structure. First, oxygen moieties were introduced by dispersing KJB in nitric acid solution (9 M) and heating at 90 °C overnight. The oxidized product was recovered by centrifugation as oxidized-KJB (Ox-KJB). It was then dispersed in water and the desired metal was slowly added overnight to the solution under vigorous stirring. The activated oxygen species as well as the high void fraction would ensure high loading of the metal ions to the surface of Ox-KJB. The metal-doped oxidized-KJB (M-Ox-KJB) were recovered by centrifugation, washed thoroughly and then dried. Finally these materials were mixed with urea (M-Ox-KJB 1:10 Urea), an abundant nitrogen source, and annealed under dinitrogen gas at elevated temperature (800°C). The schematics of the synthesis and catalyst ink composition are depicted in Figure 2-13. The detailed synthetic procedure is reported in section 2.3.6.

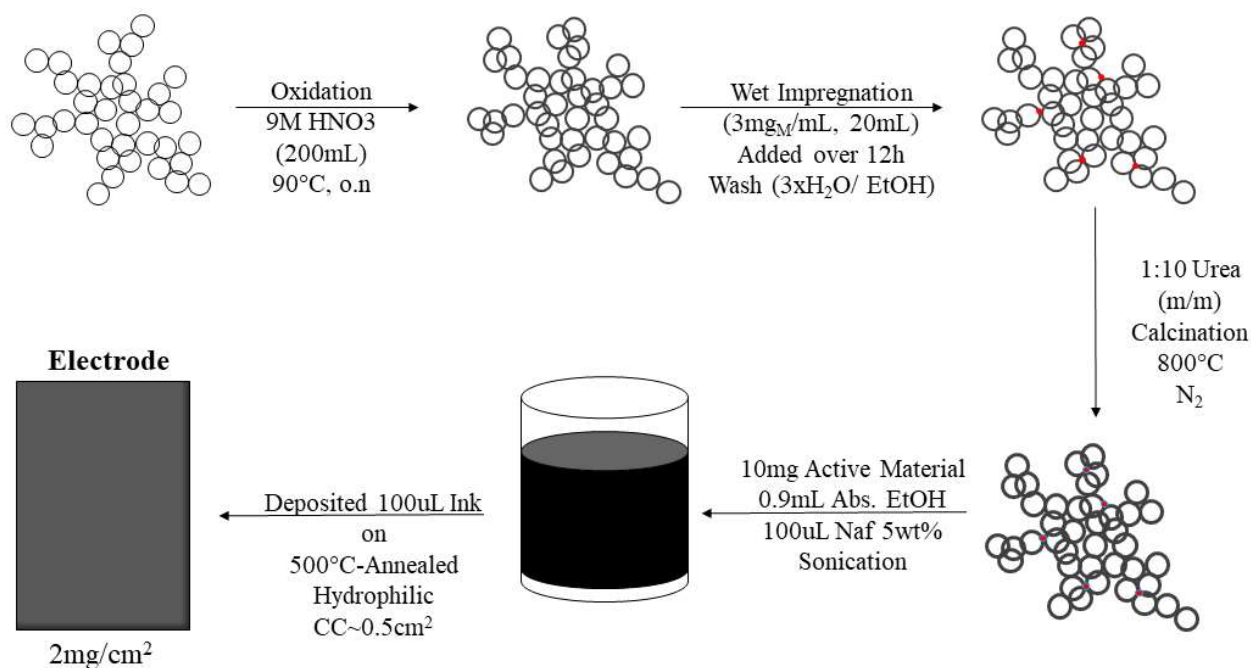


**Figure 2-13.** Scheme of the general synthesis of M-SAC-OxKJB, of the catalyst ink composition and of the catalyst drop-deposited on a hydrophilic carbon cloth.

### 2.5.2 Characterization

The structures and chemical composition spatial distribution of the KJB, Ox-KJB, Cu-Ox-KJB, Fe-Ox-KJB and Ni-Ox-KJB are investigated by TEM, HAADF, EDS and XPS in Figure 2-14 to Figure 2-18, respectively. KJB, Ox-KJB and Co-Ox-KJB will be discussed more thoroughly in chapter 3. In Figure 2-14 a) and b) confirm the existence of carbon particles with a mesoporous structure, which is similar across all the structures observed in both the pristine, Ox-KJB, Cu-Ox-KJB, Fe-Ox-KJB, and Ni-Ox-KJB. The HAADF images together with the EDS elemental mapping in Figure 2-14 c), d) and e) indicate the homogeneous distribution of carbon, and nitrogen within the pristine KJB sample. From the EDS survey spectrum (Fig.2-14 f)), a small oxygen peak was detected. The high-resolution XPS spectra of the C1s and O1s region, depicted in Fig2-14 g) and h), displays the presence of carbon bounded oxygen species. The XPS peaks in the C1s region are assigned respectively: C-C (sp<sup>2</sup>, 284.8eV), C-OH (285.8eV), C=O (287.1eV), and O-C=O (290.7eV).

The O1s profile from Figure 2-14 f) indicates the presence of organic species: C=O (532.3 eV), C-OH (533.9 eV); the peak observed at 538.2 eV was attributed to the remaining H<sub>2</sub>O within the sample.

From the TEM images of Ox-KJB in Figure 2-15 a) and b) -after oxidation treatment- the material still consisted of carbon particles with a mesoporous structure. It was found that the pores size had decreased which is further demonstrated and discussed in chapter 3. From the STEM-EDS mapping, the nitrogen and oxygen elements are still homogeneously distributed, as displayed in Fig.2-15 d) and e). When comparing KJB and Ox-KJB, it is worth noticing that the oxygen element profile increased significantly in intensity upon oxidation, it is attributed to the appearance of C-O and C=O functionalities on the surface of Ox-KJB. The C1s and O1s XPS spectra displayed an increase in the relative peaks attributed to C-OH (285.6 eV), C=O (287.8 eV), O-C=O (290.8 eV), as well as in C=O (532.0 eV) and C-OH (533.5 eV), respectively. The treatment with concentrated nitric acid at 90 °C efficiently increased the number of surface oxygen moieties with the carbon structure. The observed Cu peaks in the EDS survey of Fig.2-14 f) and Fig.2-15 f) were attributed to the carbon supported copper grids.



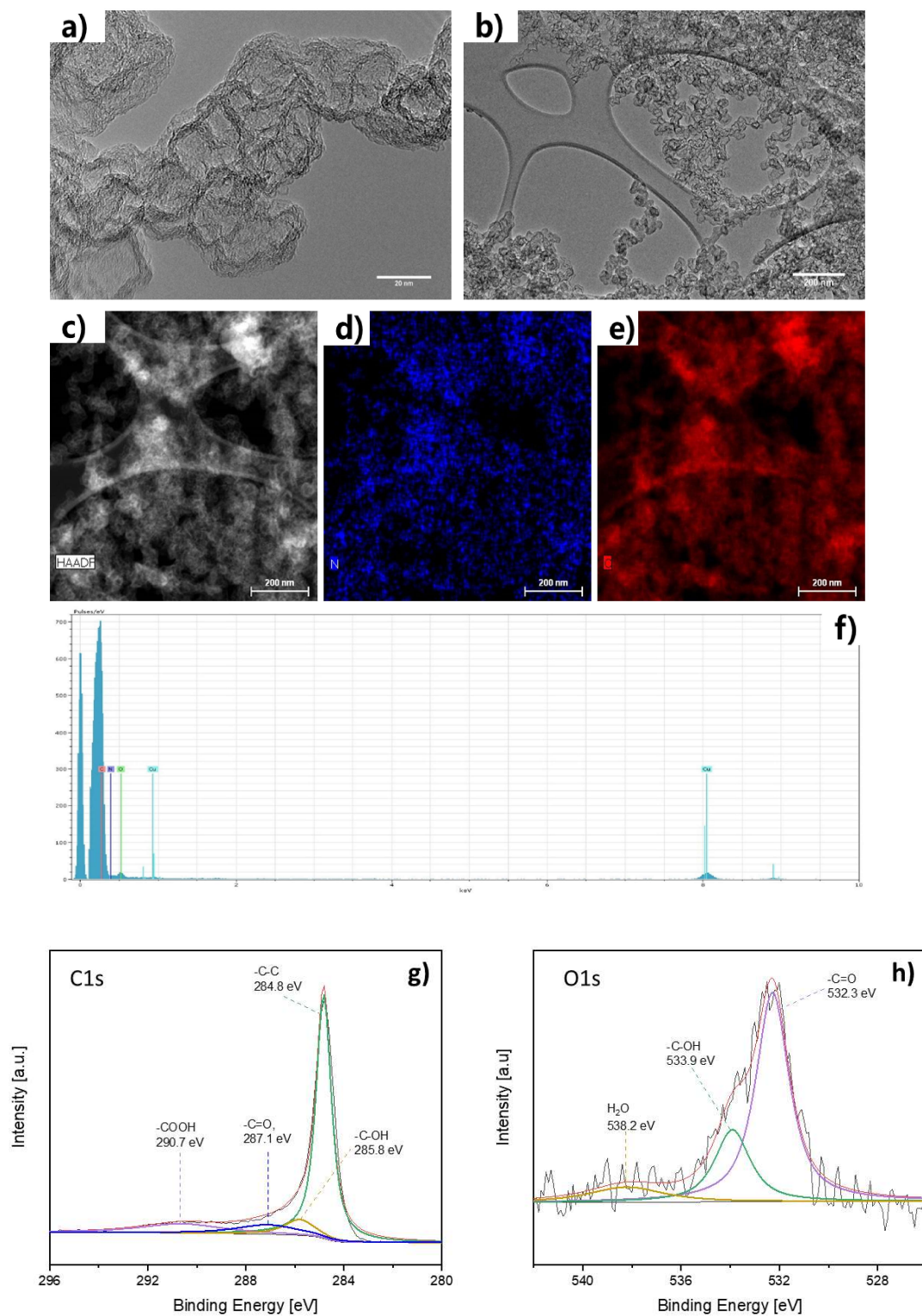


**Figure 2-14.** a-b) TEM images; c) HAADF images; d-e) EDS-STEM element mapping showing the distribution of C and O, respectively; f) EDS survey of KJB. g-h) High-resolution XPS spectra of C1s and O1s, respectively.



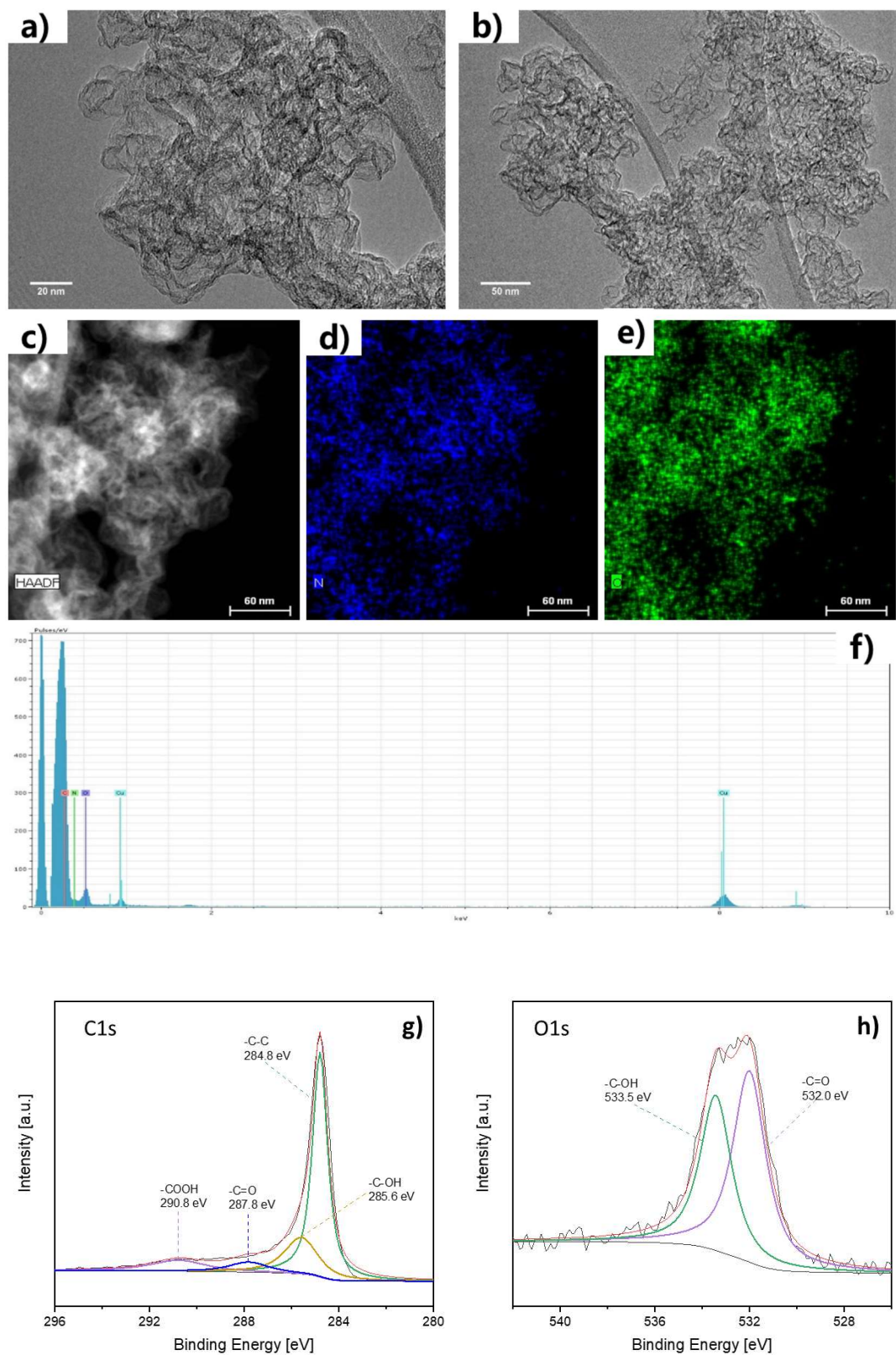


**Figure 2-15.** a-b) TEM images; c) HAADF images; d-e) EDS-STEM element mapping showing the distribution of C and O, respectively; f) EDS survey of Ox-KJB. g-h) High-resolution XPS spectra of C1s and O1s, respectively.

The structures and chemical composition spatial distribution results of the metal salts integration by wet-impregnation of Ox-KJB, followed by calcination is presence of urea yielding Cu-Ox-KJB, Fe-Ox-KJB, Ni-Ox-KJB are displayed below.

#### *Cu-Ox-KJB*

Cu-Ox-KJB, from the TEM images of Figure 2-16 a) and b), after impregnation with  $3\text{mg.mL}^{-1}$   $\text{Cu}(\text{NO}_3)_2 \cdot 2.5\text{H}_2\text{O}$ , and annealing, the material still consisted of carbon particles with a mesoporous layered structure. The HAADF images together with the EDS elemental mapping in Figure 2-16 c), d), e) and f) indicate the homogeneous distribution of nitrogen, and oxygen within the sample. The Cu EDS mapping did not show significant signal compared to the background. The C1s and O1s XPS spectra displayed an increase in the relative peaks, compared to pristine KJB, attributed to C-OH (285.5 eV), C=O (287.2 eV), O-C=O (290.3 eV), and in C=O (531.9 eV) and C-OH (533.5 eV), respectively. The peak at 537.3 eV was attributed to remaining water in the sample. The N1s high-resolution spectra was also collected, and the peaks were attributed to pyrrolic (400.3 eV), graphitic (402.4 eV) and nitrates moieties (406.3 eV). The Cu2p3 high-resolution spectra was also collected, but the signal to noise ratio did not permit the clear distinction of peaks. An atomic content obtained for long time XPS exposure of the sample gave a composition of: C1s (90.31%), N1s (0.86%), O1s (8.73%) and Cu2p3 (0.10%). The low amount of Cu in the Cu-Ox-KJB with a large specific surface area tends to weaken the XPS signal because XPS only detects the species residing at the sample surface and the KJB particle has an 80% void fraction.

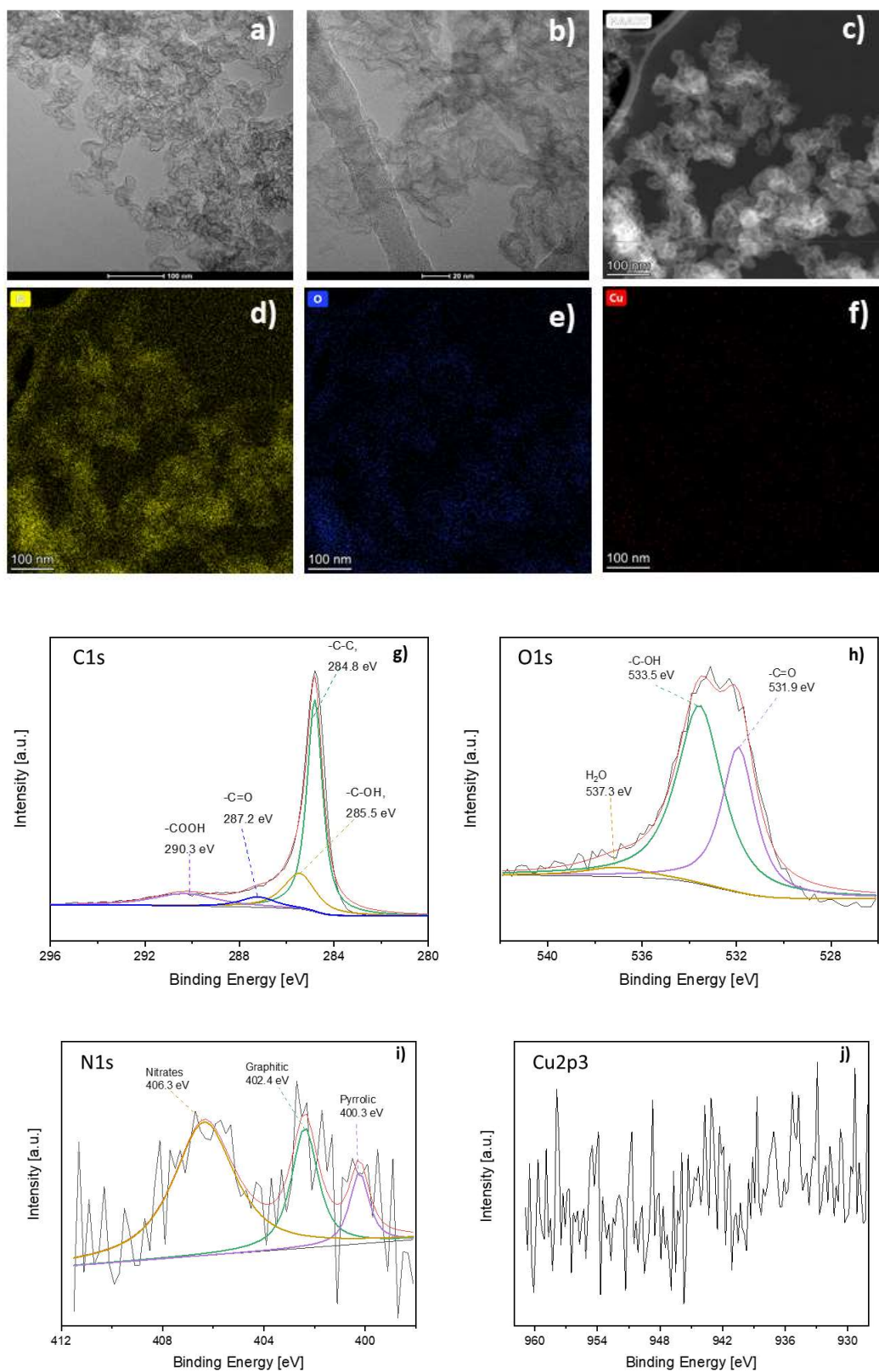


**Figure 2-16.** a-b) TEM images; c) HAADF images; d-f) EDS-STEM element mapping showing the distribution of N, O, and Cu in Cu-Ox-KJB, respectively. g-j) High-resolution XPS spectra of C1s, O1s, N1s and Cu2p3 respectively.

### *Fe-Ox-KJB*

Fe-Ox-KJB, from the TEM images of Figure 2-17 a) and b), after impregnation with  $3\text{mg.mL}^{-1}$   $\text{Fe}(\text{NO}_3)_3 \cdot 9\text{H}_2\text{O}$ , and annealing, the material still consisted of carbon particles with a mesoporous layered structure. The HAADF images together with the EDS elemental mapping in Figure 2-17 c), d), e) and f) indicate the homogeneous distribution of nitrogen, and oxygen within the sample. The oxygen signal was significantly lower with the other samples, even if the same Ox-KJB precursor was used for all the M-Ox-KJB synthesis. The Fe EDS mapping did not show significant signal compared to the background. The C1s and O1s XPS spectra displayed an increase in the relative peaks, compared to pristine KJB, attributed to C-OH (285.5 eV), C=O (287.2 eV), O-C=O (290.5 eV), and in C=O (531.9 eV) and C-OH (533.5 eV), respectively. The peak at 536.9 eV was attributed to remaining water in the sample. The N1s high-resolution spectra was also collected, and the peaks were attributed to pyrrolic (400.3 eV), graphitic (401.4 eV) and nitrates moieties (405.7 eV). The Fe2p3 high-resolution spectra was also collected, but the signal to noise ratio did not permit the clear distinction of peaks. An atomic content obtained for long time XPS exposure of the sample gave a composition of: C1s (90.93%), N1s (1.08%), O1s (7.86%) and Fe2p3 (0.13%). The low amount of Fe in the Fe-Ox-KJB with a large specific surface area tends to weaken the XPS signal because XPS only detects the species residing at the sample surface and the KJB particle has an 80% void fraction.



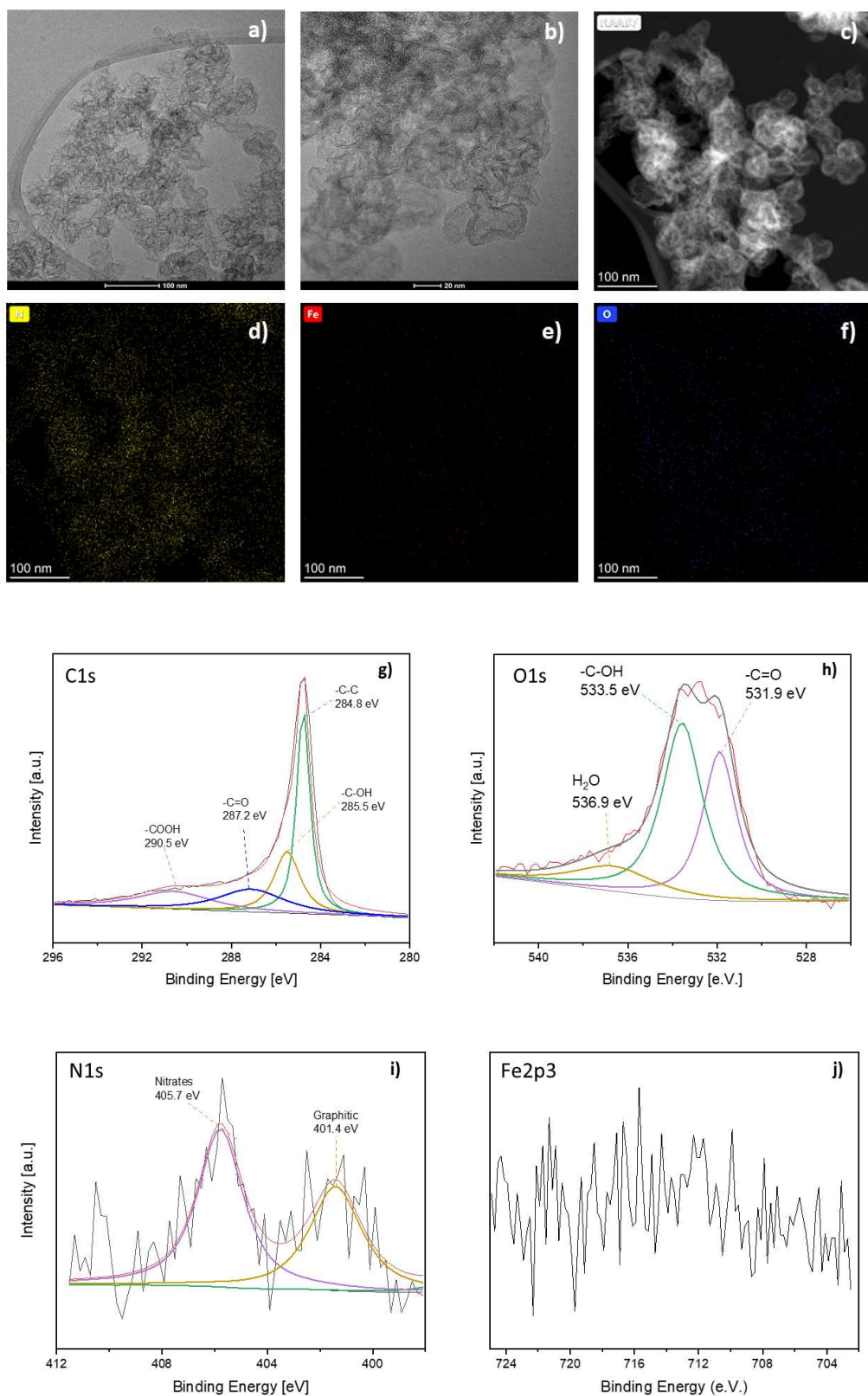


**Figure 2-17.** a-b) TEM images; c) HAADF images; d-f) STEM-EDS element mapping showing the distribution of N, Fe, and O in Fe-Ox-KJB, respectively. g-j) High-resolution XPS spectra of C1s, O1s, N1s and Fe2p3 respectively.

### *Ni-Ox-KJB*

Ni-Ox-KJB, from the TEM images of Figure 2-18 a) and b), after impregnation with  $3\text{mg.mL}^{-1}$   $\text{Ni}(\text{NO}_3)_2 \cdot 6\text{H}_2\text{O}$ , and annealing, the material still consisted of carbon particles with a mesoporous layered structure. The HAADF images together with the EDS elemental mapping in Figure 2-18 c), d), e) and f) indicate the homogeneous distribution of nitrogen, and oxygen within the sample. The oxygen signal was lower compared with Ox-KJB, even if the same Ox-KJB precursor was used for all the M-Ox-KJB synthesis. The Ni EDX map did not show significant signal compared to the background. The C1s and O1s XPS spectra displayed an increase in the relative peaks, compared to pristine KJB, attributed to C-OH (286.3 eV), C=O (288.7 eV), O-C=O (290.5 eV), and in C=O (531.7 eV) and C-OH (533.3 eV), respectively. The peak at 538.0 eV was attributed to remaining water in the sample. The N1s high-resolution spectra was also collected, and the peaks were attributed to pyrrolic (400.1 eV), graphitic (402.2 eV) and nitrates moieties (406.3 eV). The Ni2p3 high-resolution spectra was also collected, but the signal to noise ratio did not permit the clear distinction of peaks. An atomic content was obtained for long time XPS exposure of the sample gave a composition of: C1s (91.26%), N1s (0.73%), O1s (8.00%) and Ni2p3 (0.01%). The low amount of Ni in the Ni-Ox-KJB with a large specific surface area tends to weaken the XPS signal because XPS only detects the species residing at the sample surface and the KJB particle has an 80% void fraction. The incorporation of Ni ions in the carbon matrix is not evident from the XPS and EDS mapping.

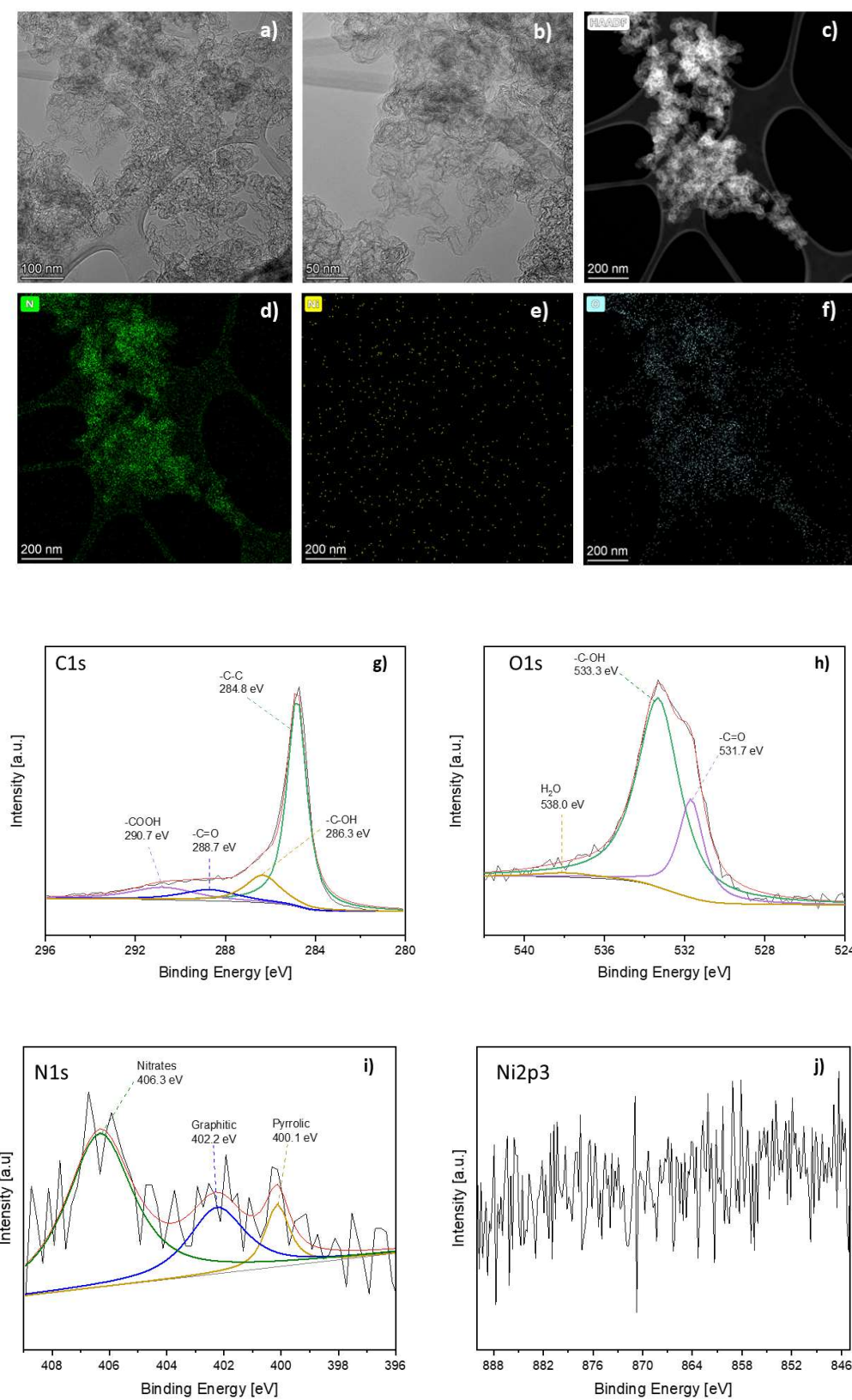


**Figure 2-18.** a-b) TEM images; c) HAADF images; d-f) EDS-STEM element mapping showing the distribution of N, Ni, and O in Ni-Ox-KJB, respectively. g-j) High-resolution XPS spectra of C1s, O1s, N1s and Ni2p3 respectively

Following the exact same synthetic procedure Al, Cr, Mn and Zn-Ox-KJB were obtained by utilizing instead  $3\text{mg.mL}^{-1}$  precursor solutions of  $\text{Al}(\text{NO}_3)_3.9\text{H}_2\text{O}$ ,  $\text{Cr}(\text{NO}_3)_3.9\text{H}_2\text{O}$ ,  $\text{Mn}(\text{NO}_3)_2.4\text{H}_2\text{O}$ , and  $\text{Zn}(\text{NO}_3)_2.6\text{H}_2\text{O}$ , respectively. The samples were further carbonized at  $800^\circ\text{C}$  under dinitrogen in the presence of urea (M-Ox-KJB 1:10 Urea).

### 2.5.3 Electrochemical Performance

A standard protocol was established in order to test the potential electrocatalytic activity of the samples deposited on a hydrophilic carbon cloth. At first, a pre-activation step consisting of 20 cycles of cyclic voltammetry (CV) at  $50\text{ mV.s}^{-1}$  from 0.6 to 1.6 V vs RHE, that would help remove impurities and clean the surface of the catalyst. Secondly, a pre-activity measurement consisting in a linear sweep (LSV) from 1.0 to 2.2 V vs RHE at  $5\text{ mV.s}^{-1}$ , yielding preliminary results about the OER activity. Thirdly, a stability test of 100 cycles of cyclic voltammetry at  $50\text{ mV.s}^{-1}$  from 0.9 to 1.6 V vs RHE, which aimed at monitoring the evolution within the current density along the experiment, probing for any physical degradation of the catalyst. Finally, as a fourth step a second LSV from 1.0 to 2.2 V vs RHE. From this last LSV curves parameters such as the overpotential and the Tafel slope at  $10\text{ mA.cm}^{-2}$  were calculated. All potentials were automatically iR compensated by the EC-Lab software. Ox-KJB and a control inks were made, and used as a reference to compare with the addition of impregnated metal ions and addition of active material, respectively. The results of this electrochemical performances measurements performed in Ar saturated  $0.1\text{M H}_2\text{SO}_4$ ,  $0.5\text{M H}_2\text{SO}_4$  and  $0.1\text{ HClO}_4$  are depicted in the figures below.

In  $0.1\text{M H}_2\text{SO}_4$  (Fig.2-19), the onset potential at which significant current density was observed from 1.7 V vs RHE. Ni-Ox-KJB was found to have the highest activity among all the other samples, achieving  $10\text{ mA.cm}^{-2}$  at 702 mV overpotential and displaying a Tafel slope of  $481\text{ mV.dec}^{-1}$ . Al-Ox-KJB, Cu-Ox-KJB and Fe-Ox-KJB displayed similar activity,



achieving  $10\text{mA}\cdot\text{cm}^{-2}$  at 778 mV, 765 mV, and 794 mV overpotential and displaying similar Tafel slopes of  $714\text{ mV}\cdot\text{dec}^{-1}$ ,  $651\text{ mV}\cdot\text{dec}^{-1}$  and  $686\text{ mV}\cdot\text{dec}^{-1}$ , respectively. Co-Ox-KJB and Ox-KJB had similar Tafel slopes at  $538\text{ mV}\cdot\text{dec}^{-1}$  and  $529\text{ mV}\cdot\text{dec}^{-1}$  and overpotentials of 871mV and 892mV, respectively. Zn, Mn and Cr based samples displayed the highest Tafel slopes at  $791\text{ mV}\cdot\text{dec}^{-1}$ ,  $920\text{ mV}\cdot\text{dec}^{-1}$  and  $1158\text{ mV}\cdot\text{dec}^{-1}$ , with overpotentials of 886 mV, 852mV and 867 mV, respectively.

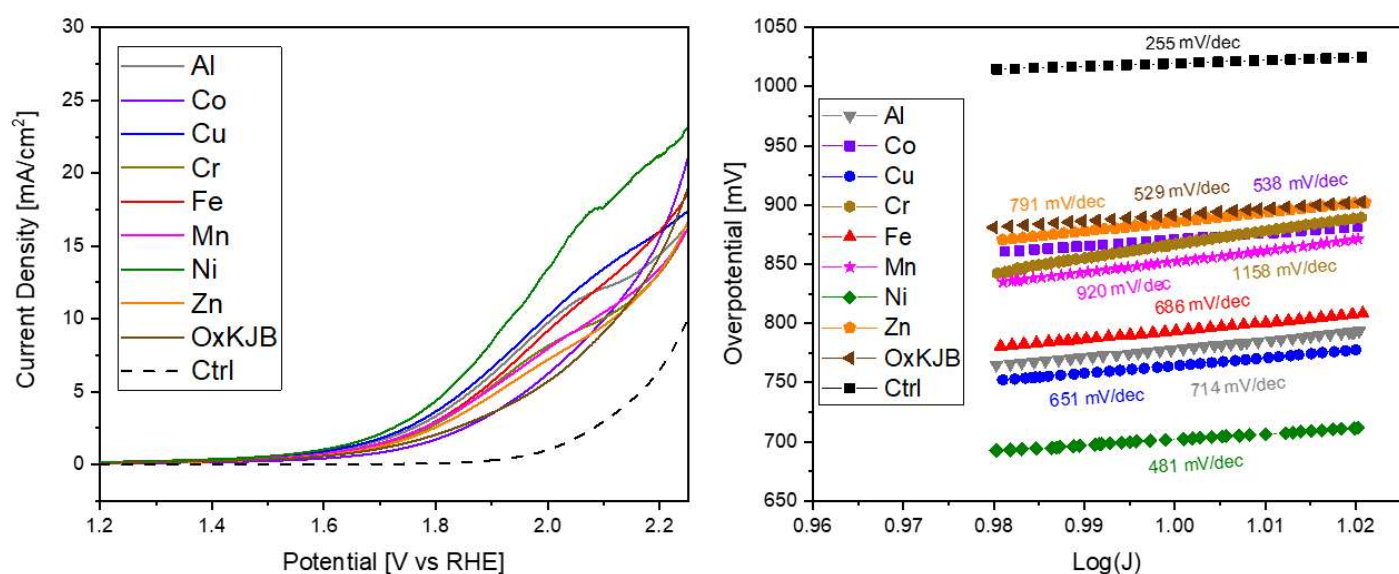


**Figure 2-19.** Linear sweep voltammetry at  $5\text{ mV}\cdot\text{s}^{-1}$ , obtained after the activation procedure (left) and related Tafel slopes @  $10\text{mA}\cdot\text{cm}^{-2}$  (right) for M-SAC-OxKJB in Ar saturated  $0.1\text{ M H}_2\text{SO}_4$ .

In  $0.5\text{M H}_2\text{SO}_4$  (Fig. 2-20, left), the onset potentials were found to be from 1.65 V vs RHE for the best performing samples, yielding overall smaller overpotentials than in  $0.1\text{ M H}_2\text{SO}_4$ . Cu-Ox-KJB was found to be the best performing sample in this electrolyte, reaching  $10\text{ mA}\cdot\text{cm}^{-2}$  at 573 mV overpotential and displaying a Tafel slope of  $345\text{ mV}\cdot\text{dec}^{-1}$ . The second best performing sample was Ni-Ox-KJB reaching  $10\text{ mA}\cdot\text{cm}^{-2}$  at 662 mV overpotential and displaying a Tafel slope of  $548\text{ mV}\cdot\text{dec}^{-1}$ . Co-Ox-KJB and Zn-Ox-KJB

presented similar overpotentials of 717 mV, but with very different Tafel slopes of 753 mV.dec<sup>-1</sup> and 909 mV.dec<sup>-1</sup>, respectively. Cr-Ox-KJB presented 775 mV overpotential for 1201 mV/dec<sup>-1</sup>; and Mn-Ox-KJB 812 mV for 1455 mV.dec<sup>-1</sup>. Interestingly Fe-Ox-KJB and Ox-KJB displayed similar Tafel slopes of 355 mV.dec<sup>-1</sup> and 404 mV.dec<sup>-1</sup> at 838 and 847 mV overpotentials. Al-Ox-KJB and Ctrl samples performed so poorly that they did not reach 10mA.cm<sup>-2</sup> upon application of 2.2V vs RHE.

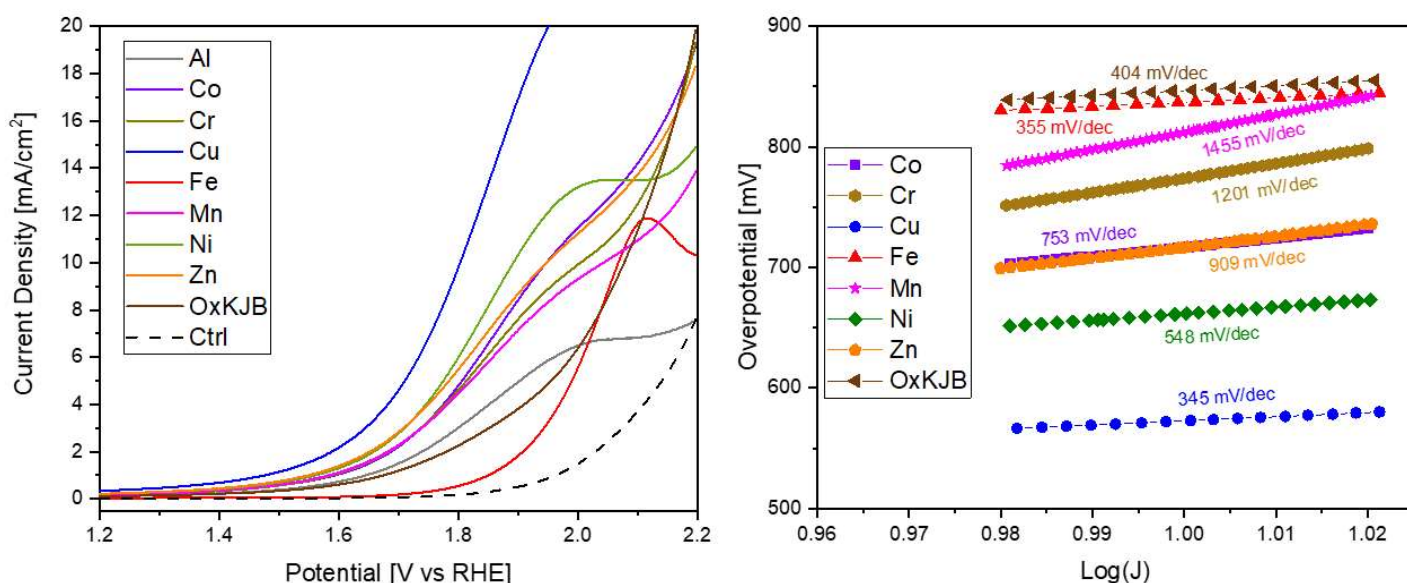


**Figure 2-20.** Linear sweep voltammetry at 5mV.s<sup>-1</sup>, obtained after the activation procedure (left) and related Tafel slopes @ 10mA.cm<sup>-2</sup> (right) for M-SAC-OxKJB in Ar saturated 0.5M H<sub>2</sub>SO<sub>4</sub>.

In 0.1 M HClO<sub>4</sub> (Fig.2-21, left), the onset potentials were found to start around 1.65 V vs RHE. The registered overpotentials were generally higher than in 0.5 M H<sub>2</sub>SO<sub>4</sub> and in 0.1 M H<sub>2</sub>SO<sub>4</sub> for most samples. Co-Ox-KJB was found to be the best performing sample in this electrolyte, reaching 10 mA.cm<sup>-2</sup> at 596 mV overpotential and displaying a Tafel slope of 236 mV.dec<sup>-1</sup>. The rest of the samples performed significantly worse with the second best sample, Ni-Ox-KJB, reaching 10 mA.cm<sup>-2</sup> at 756 mV overpotential and displaying a Tafel slope of

652 mV.dec<sup>-1</sup>. Al-Ox-KJB presented a similar Tafel slope of 651 mV.dec<sup>-1</sup>, but with an overpotential of 788 mV. Ox-KJB was found to have the second best Tafel slope of 352 mV.dec<sup>-1</sup> at a high overpotential of 852 mV.

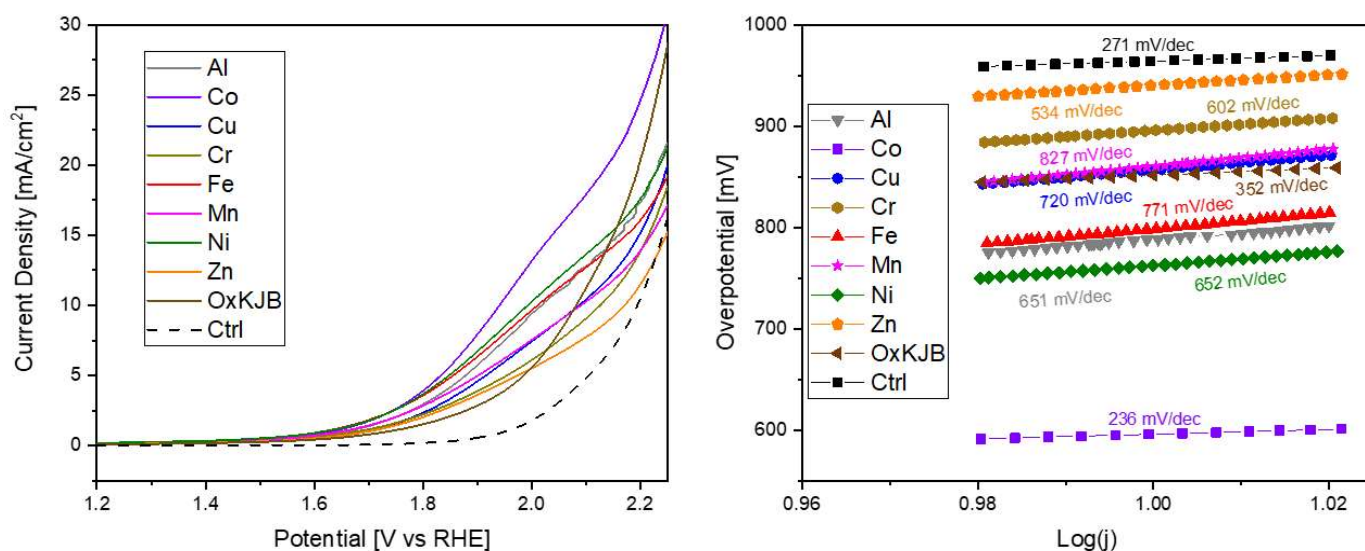


**Figure 2-21.** Linear sweep voltammetry at 5 mV.s<sup>-1</sup>, obtained after the activation procedure (left) and related Tafel slopes @ 10 mA.cm<sup>-2</sup> (right) for M-SAC-OxKJB in Ar saturated 0.1M HClO<sub>4</sub>.

The results obtained for the Tafel slopes and overpotential at 10mA.cm<sup>-2</sup> for the tested samples in the different tested electrolytes are recapped in table 2-1.

**Table 2-1.** Recap of the obtained overpotentials at 10mA.cm<sup>-2</sup> for M-SAC-OxKJB in different acidic electrolytes. The best performances are highlighted in bold for each electrolyte. Overpotentials are given in [mV]

Overpotential @10mA/cm <sup>2</sup>	Al	Co	Cr	Cu	Fe	Mn	Ni	Zn	OxKJB	Ctrl
<b>0,1M H<sub>2</sub>SO<sub>4</sub></b>	778	871	867	765	794	852	<b>702</b>	886	892	1020
<b>0,5M H<sub>2</sub>SO<sub>4</sub></b>	/	717	775	<b>573</b>	838	812	<b>662</b>	717	847	>>1000
<b>0,1M HClO<sub>4</sub></b>	788	<b>596</b>	896	857	798	860	756	941	852	965

#### 2.5.4 Discussion

Generally, in the case of acidic OER, an electrocatalyst with an overpotential in the range of 300-400 mV at 10 mA.cm<sup>-2</sup>, is to be considered excellent<sup>70</sup>. Among the tested samples, Ni-Ox-KJB was found to be one of the most promising results for acidic OER sulphuric acid electrolytes. Though the characterization of Ni ions in the sample was not obvious, the differences in activity with pristine Ox-KJB are clearly distinct. This was due to the incorporation of nickel salt. In 2018, Zhang<sup>64</sup> reported atomic Ni species trapped in graphene defect for OER and HER. Their reported performances of 270 mV overpotential at 10 mA/cm<sup>2</sup> in 0.5 M H<sub>2</sub>SO<sub>4</sub> were better than that of commercial IrO<sub>2</sub> (435 mV overpotential at 10 mA/cm<sup>2</sup> in 0.5 M H<sub>2</sub>SO<sub>4</sub>). Also, NiFe layered double hydroxide (LDH) unconventional  $\gamma$ -FeOOH/ $\gamma$ -NiOOH<sup>71</sup> are commonly used non-noble metal based electrocatalysts with high OER activity in alkaline media. The active site, either Fe or Ni atom, is still under debate<sup>72</sup>.

The performances obtained for Cu-Ox-KJB in 0.5 M H<sub>2</sub>SO<sub>4</sub> were the most promising among all M-Ox-KJB samples and conditions tested. Cu based materials were already reported to have some moderate activity for OER in alkaline media<sup>73</sup>. Cu<sub>3</sub>P/C was reported by Bai *et al*<sup>74</sup>. With an overpotential as low as 146 mV with a Tafel slope of 56 mV.dec<sup>-1</sup> at 10 mA.cm<sup>-2</sup> in 0.1 M KOH. 3D Cu<sub>2</sub>O-Cu hybrid foams were also reported to have high-performance for OER in alkaline media, with a low overpotential of 250 mV and a Tafel slope of 67.5 mV.dec<sup>-1</sup> at 10 mA.cm<sup>-2</sup> in 1.0 M KOH. Copper is also extensively used in the counter half-reaction of the carbon dioxide reduction to carbon monoxide and other C<sub>2</sub> products<sup>75</sup>.

The performances obtained for Co-Ox-KJB in 0.1 M HClO<sub>4</sub> were the most promising among all M-Ox-KJB samples. Cobalt spinel<sup>76</sup> (Co<sub>3</sub>O<sub>4</sub>) and cobalt titanate (Co<sub>2</sub>TiO<sub>4</sub>) were recently reported in the literature to have some activity for OER in 0.5 M H<sub>2</sub>SO<sub>4</sub> media<sup>77</sup>.

They reported cobalt titanate octahedral nanocrystals to reach 10 mA/cm<sup>2</sup> at 513 mV overpotential, 155 mV higher than the precious IrO<sub>2</sub>, and 336mV lower than Co<sub>3</sub>O<sub>4</sub> in the same conditions. It was also reported that cobalt doping in RuIr bifunctional nanocrystals<sup>78</sup> would greatly increase the stability of the catalyst in acidic media, supported by a 25h chronoamperometry experiments reaching 10 mA/cm<sup>2</sup> at 1.52 V vs RHE in 0.1 M HClO<sub>4</sub>.

In general all the calculated Tafel slopes, especially for the most active catalysts in acidic media, Co-Ox-KJB, Cu-Ox-KJB, and Ni-Ox-KJB, were significantly higher than for the expected conventional mechanism of OER (AEM, LOM) that typically range between 60 mV.dec<sup>-1</sup> and 120 mV.dec<sup>-1</sup>. However, the smallest Tafel slopes obtained 236 mV.dec<sup>-1</sup> in 0.1 M HClO<sub>4</sub>, 345 mV.dec<sup>-1</sup> in 0.5 M H<sub>2</sub>SO<sub>4</sub>, and 481 mV.dec<sup>-1</sup> in 0.1 M H<sub>2</sub>SO<sub>4</sub>, for Co-Ox-KJB, Cu-Ox-KJB and Ni-Ox-KJB, indicating for sluggish reaction mechanism. One probable explanation is the presence of other oxidation reactions such as the oxidation of carboxyl, carbonyls and carboxylic groups at the surface of the carbon oxidized matrix to form carbon dioxide (CO<sub>2</sub>). Also, N1s XPS spectra highlighted the presence of nitrate moieties at the surface of the catalyst that could also be further oxidized to nitrogen dioxide (NO<sub>2</sub>)<sup>79</sup>. Such processes were previously reported for the case of oxidized carbon nanotubes<sup>80</sup> and could explain partially the high Tafel slopes obtained as a mixture of all these possible side reactions additionally to the desired OER. Also, metal-free nitrogen-doped carbon materials were reported to have some activity towards OER in alkaline media<sup>81</sup> and in acidic media<sup>82</sup>. They argue that the incorporation of nitrogen-containing OER active sites by pyrolyzing carbon black in presence of imidazole-based ionic liquid would display 10 mA.cm<sup>-2</sup> at 1.70 V vs RHE with a Tafel slope of 226 mV.dec<sup>-1</sup>. They hypothesized that upon cyclic voltammetry aging in 0.5 M H<sub>2</sub>SO<sub>4</sub>, nitrogen species on the surface of the carbon black -perceived as the active site- were oxidized and would dissolve. Under high anodic potentials (1.7 V vs RHE)

the catalyst would quickly degrade. Also other surface reactions from adsorbed species could be potentially the cause of such high Tafel slopes.

Cobalt-Iron double-atom catalysts for OER in alkaline media were previously reported by our group<sup>83</sup> and hold a promiscuous method to generate stable and active atomically precise electrocatalysts to tackle the OER bottleneck.

Finally, for most of the worst performing catalysts, some of the deposited material was detached from the carbon cloth electrode during the 100 cycles of cyclic voltammetry, displaying a poor stability discouraging from performing long-term chronoamperometry (10h).

Up-to-now the best performing SAC catalysts in acid media reported to be somewhat stable still contain precious metals like Ru and Ir<sup>84,85</sup>. Recently, quadruple perovskite ruthenate  $\text{CaCu}_3\text{Ru}_4\text{O}_{12}$  were reported as high active materials for acidic OER<sup>86</sup> with an ultralow overpotential of 171 mV at 10  $\text{mA}\cdot\text{cm}^{-2}$  and a Tafel slope of 40  $\text{mV}\cdot\text{dec}^{-1}$  in 0.5 M  $\text{H}_2\text{SO}_4$ . They reported a greatly enhanced stability compared to state-of-the-art  $\text{RuO}_2$ . Similarly chromium-ruthenium oxide solid derived from MOF MIL-101 (Cr) were reported for their exceptional activity with an ultralow overpotential of 178 mV at 10  $\text{mA}\cdot\text{cm}^{-2}$  and Tafel slope of 58  $\text{mV}\cdot\text{dec}^{-1}$  in 0.5 M  $\text{H}_2\text{SO}_4$ <sup>87</sup>. They suggested that the superior stability arose from the integration of acid stable chromium oxide within the lattice. Altogether, this points out that the development of highly active and acid stable electrocatalysts for OER will pass by either doping or by the generation of mixed metal oxides coupling an OER active atom with a stable one.

### 2.5.5 Conclusion

In conclusion, various non-noble metal-ion based electrocatalysts supported on oxidized porous carbon conductive matrix were successfully synthesized by a simple three-step oxidation, wet-impregnation and calcination protocol. Such catalysts were found to suffer from high Tafel slopes, revealing slow kinetics and the possibility of other oxidation reactions occurring at high anodic potentials. Ni-Ox-KJB was found to have the highest activity in 0.1 M H<sub>2</sub>SO<sub>4</sub>, achieving 10 mA.cm<sup>-2</sup> at 702 mV overpotential and displaying a Tafel slope of 481 mV.dec<sup>-1</sup>. Co-Ox-KJB was found to be the best performing sample in 0.1 M HClO<sub>4</sub>, reaching 10 mA.cm<sup>-2</sup> at 596 mV overpotential and displaying a Tafel slope of 236 mV.dec<sup>-1</sup>. Cu-Ox-KJB was found to be the best performing sample in 0.5 M H<sub>2</sub>SO<sub>4</sub>, reaching 10 mA.cm<sup>-2</sup> at 573 mV overpotential and displaying a Tafel slope of 345 mV.dec<sup>-1</sup>. This overpotential was the lowest obtained throughout all the tested samples and conditions; unfortunately, it is still impracticable for real-life applications. Hopefully, doping with most active elements -Ir and Ru- may help achieve superior activity and maintain good stability over long term electrolysis.

### 2.5.6 Experimental Section

#### *Materials*

Nitric acid (65%) was obtained from Carlo Erba Reagents. KetJen Black carbon black (ECP600JP, 1292m<sup>2</sup>.g<sup>-1</sup> in Brunauer-Emmett-Teller surface area from the manufacturer) was obtained from Lion Corporation (Tokyo, Japan). Urea (99%) was purchased from Acros Organics. Al(NO<sub>3</sub>)<sub>3</sub>.9H<sub>2</sub>O (99+%), Co(NO<sub>3</sub>)<sub>2</sub>.6H<sub>2</sub>O (99+%), Cr(NO<sub>3</sub>)<sub>3</sub>.9H<sub>2</sub>O (99+%), Cu(NO<sub>3</sub>)<sub>2</sub>.2.5H<sub>2</sub>O (99+%), Fe(NO<sub>3</sub>)<sub>2</sub>.9H<sub>2</sub>O (99+%), Mn(NO<sub>3</sub>)<sub>2</sub>.4H<sub>2</sub>O (99+%), Ni(NO<sub>3</sub>)<sub>2</sub>.6H<sub>2</sub>O (99+%) and Zn(NO<sub>3</sub>)<sub>2</sub>.6H<sub>2</sub>O (99+%) were obtained from Sigma-Aldrich.

### *Synthesis of Ox-KJB*

KetJen Black (4.0 g) were dispersed in 200 mL 9 M  $\text{HNO}_3$  in a round bottom flask and heated under vigorous stirring at  $90^\circ\text{C}$  overnight (16h). A reflux system was installed to the round bottom flask to prevent fumes from saturating the hood. The product was recovered and washed with copious amount of bidistilled water ( $\text{ddH}_2\text{O}$ ) first by filtration until reaching a  $\text{pH} > 4$ , and then by centrifugation (3x50 mL  $\text{ddH}_2\text{O}$ , 2x50 mL absolute EtOH, 6'000 rpm for 5 mins). The recovered black product was then further dried in a vacuum oven at  $60^\circ\text{C}$  overnight (16h). The recovered dried black powder was denoted as Ox-KJB.

### *Synthesis of M-Ox-KJB*

First, 0.5 g of Ox-KJB were dispersed in 200 mL bidistilled water by sonication. Meanwhile, 20 mL of  $3 \text{ mg}_\text{M} \cdot \text{mL}^{-1}$  metal solution were prepared with the appropriate metal nitrate salts. Then, the 20 mL metal solution was added slowly, in 12h ( $0.028 \text{ mL} \cdot \text{min}^{-1}$ ), under vigorous stirring to the Ox-KJB dispersion. After complete addition the product was recovered by centrifugation (3x50 mL  $\text{ddH}_2\text{O}$ , 2x50 mL absolute EtOH, 6'000 rpm for 5 mins) and further dried in a vacuum oven at  $60^\circ\text{C}$  overnight (16h). The recovered product was denoted as M-Ox-KJB-WI.

Finally, typically 75 mg of M-Ox-KJB-WI were mixed with 750 mg urea (99+%) and placed in a ceramic crucible and annealed at  $800^\circ\text{C}$  under  $\text{N}_2$ , with a heating rate of  $5^\circ\text{C} \cdot \text{min}^{-1}$ . The samples were left to cool down to room temperature naturally, and then grounded to a fine black powder in an agate mortar. The recovered samples were denoted as M-Ox-KJB.

### *Electrochemical measurements*

Catalyst inks were prepared by mixing 0.9 mL absolute EtOH, 100  $\mu\text{L}$  5 wt% Nafion solution and 10 mg of active material. The ink was sonicated for at least 2h to ensure homogeneous



dispersion. Then 4×25 μL of the ink were deposited onto a carbon cloth (~0.5 cm<sup>2</sup>), and the electrodes were left to dry at 75 °C for 20 mins. The precise area of the carbon cloth electrode was determined by ImageJ and the current density was calculated accordingly.

Electrochemical characterizations, including cyclic voltammetry (CV), linear sweep voltammetry (LSV) were iR corrected and carried out on a BioLogic VSP (VMP3) electrochemical workstation using a three-electrode set-up in a single-chamber cell, using Pt foil as counter electrode and Ag/AgCl as reference electrode. CV and LSV were performed at a scan rate of 50 mV.s<sup>-1</sup> and 5 mV.s<sup>-1</sup> respectively. All potentials are referenced to the reversible hydrogen electrode (RHE) in this work. The measured potential vs. Ag/AgCl in saturated KCl can be converted to the reversible hydrogen electrode (RHE) scale according to the Nernst equation:

$$(E_{RHE} = E_{\frac{Ag}{AgCl}} + 0.197V + 0.059pH)$$

### *Material Characterization*

TEM was performed using a FEI Tecnai Osiris TEM equipped with a high-brightness field emission gun (XFEG). Samples for TEM were prepared by drop-drying the samples from their diluted ethanol suspensions onto carbon-coated copper grids. Energy-dispersive X-ray spectroscopy (EDS) patterns and mapping images were taken on a FEI Tecnai Osiris TEM in a scanning TEM mode. Elemental energy dispersive X-ray spectroscopy (EDS) mapping was used for elemental characterization, with simultaneously acquired high-angular annular dark field scanning transmission electron microscopy (HAADF-STEM) images showing atomic number and thickness contrast. The elemental ratio was calculated from the Kα peak area of each element, using the ESPRIT2 (Bruker) software. X-ray photoelectron spectroscopy (XPS) measurements were performed on a PHI5000 VersaProbe II XPS system by Physical

Electronics (PHI) with a detection limit of 1 atomic percent. Monochromatic X-rays were generated by an Al K $\alpha$  source (1486.7 eV). The diameter of the analyzed area was 10  $\mu\text{m}$ .

### *Contributions*

Albert Daubry synthesized the materials and performed the electrochemical tests. Albert Daubry designed the electrochemical cells. Dr. Lichen Bai performed the HR-TEM, TEM, HAADF and EDS-STEM mapping. Dr. Pierre Mettraux performed the XPS measurements.

## 2.6 References

1. Yoo, E. *et al.* Enhanced Electrocatalytic Activity of Pt Subnanoclusters on Graphene Nanosheet Surface. *Nano Lett.* **9**, 2255–2259 (2009).
2. Yao, H. *et al.* Electrocatalytic Oxidation of Alcohols, Tripropylamine, and DNA with Ligand-Free Gold Nanoclusters on Nitrided Carbon. *ChemElectroChem* **3**, 2100–2109 (2016).
3. Choi, C. *et al.* Suppression of Hydrogen Evolution Reaction in Electrochemical N<sub>2</sub> Reduction Using Single-Atom Catalysts: A Computational Guideline. *ACS Catal.* **8**, 7517–7525 (2018).
4. Zhao, J. & Chen, Z. Single Mo Atom Supported on Defective Boron Nitride Monolayer as an Efficient Electrocatalyst for Nitrogen Fixation: A Computational Study. *J. Am. Chem. Soc.* **139**, 12480–12487 (2017).
5. Choi, C. H. *et al.* Tuning selectivity of electrochemical reactions by atomically dispersed platinum catalyst. *Nature Communications* **7**, 10922 (2016).
6. Liu, S. & Huang, S. Theoretical insights into the activation of O<sub>2</sub> by Pt single atom and Pt<sub>4</sub> nanocluster on functionalized graphene support: Critical role of Pt positive polarized charges. *Carbon* **115**, 11–17 (2017).
7. Cheng, N., Zhang, L., Doyle-Davis, K. & Sun, X. Single-Atom Catalysts: From Design to Application. *Electrochem. Energ. Rev.* **2**, 539–573 (2019).
8. Abbet, S. *et al.* Acetylene Cyclotrimerization on Supported Size-Selected Pd<sub>n</sub> Clusters ( $1 \leq n \leq 30$ ): One Atom Is Enough! *J. Am. Chem. Soc.* **122**, 3453–3457 (2000).

9. Single-Atom Pd1/Graphene Catalyst Achieved by Atomic Layer Deposition: Remarkable Performance in Selective Hydrogenation of 1,3-Butadiene - Journal of the American Chemical Society (ACS Publications).  
<https://pubs.acs.org/doi/10.1021/jacs.5b06485>.
10. Zhang, L., Han, L., Liu, H., Liu, X. & Luo, J. Potential-Cycling Synthesis of Single Platinum Atoms for Efficient Hydrogen Evolution in Neutral Media. *Angewandte Chemie International Edition* **56**, 13694–13698 (2017).
11. Kwak, J. H., Kovarik, L. & Szanyi, J. Heterogeneous Catalysis on Atomically Dispersed Supported Metals: CO<sub>2</sub> Reduction on Multifunctional Pd Catalysts. *ACS Catal.* **3**, 2094–2100 (2013).
12. Liu, J. *et al.* Tackling CO Poisoning with Single-Atom Alloy Catalysts. *J. Am. Chem. Soc.* **138**, 6396–6399 (2016).
13. Long, R. *et al.* Isolation of Cu Atoms in Pd Lattice: Forming Highly Selective Sites for Photocatalytic Conversion of CO<sub>2</sub> to CH<sub>4</sub>. *J. Am. Chem. Soc.* **139**, 4486–4492 (2017).
14. Wang, Y. *et al.* Advanced Electrocatalysts with Single-Metal-Atom Active Sites. *Chem. Rev.* **120**, 12217–12314 (2020).
15. Greenlee, L. F., Renner, J. N. & Foster, S. L. The Use of Controls for Consistent and Accurate Measurements of Electrocatalytic Ammonia Synthesis from Dinitrogen. *ACS Catal.* **8**, 7820–7827 (2018).
16. Le, Y.-Q., Gu, J. & Tian, W. Q. Nitrogen-fixation catalyst based on graphene: every part counts. *Chem. Commun.* **50**, 13319–13322 (2014).
17. Singh, A. R. *et al.* Electrochemical Ammonia Synthesis—The Selectivity Challenge. *ACS Catal.* **7**, 706–709 (2017).

18. Zhang, L. *et al.* Electrochemical Ammonia Synthesis via Nitrogen Reduction Reaction on a MoS<sub>2</sub> Catalyst: Theoretical and Experimental Studies. *Advanced Materials* **30**, 1800191 (2018).
19. Li, X. *et al.* Boosted Electrocatalytic N<sub>2</sub> Reduction to NH<sub>3</sub> by Defect-Rich MoS<sub>2</sub> Nanoflower. *Advanced Energy Materials* **0**, 1801357.
20. Chen, Z. W., Lang, X. Y. & Jiang, Q. Discovery of cobweb-like MoC<sub>6</sub> and its application for nitrogen fixation. *J. Mater. Chem. A* **6**, 9623–9628 (2018).
21. Ling, C., Bai, X., Ouyang, Y., Du, A. & Wang, J. Single Molybdenum Atom Anchored on N-Doped Carbon as a Promising Electrocatalyst for Nitrogen Reduction into Ammonia at Ambient Conditions. *J. Phys. Chem. C* **122**, 16842–16847 (2018).
22. Chen, W. *et al.* Rational Design of Single Molybdenum Atoms Anchored on N-Doped Carbon for Effective Hydrogen Evolution Reaction. *Angewandte Chemie International Edition* **56**, 16086–16090 (2017).
23. Ou, P. *et al.* Single molybdenum center supported on N-doped black phosphorus as an efficient electrocatalyst for nitrogen fixation. *Nanoscale* **11**, 13600–13611 (2019).
24. Daniyal, W. M. E. M. M. *et al.* X-ray Photoelectron Spectroscopy Analysis of Chitosan–Graphene Oxide-Based Composite Thin Films for Potential Optical Sensing Applications. *Polymers* **13**, 478 (2021).
25. Li, P.-C. *et al.* Fabrication and Characterization of Chitosan Nanoparticle-Incorporated Quaternized Poly(Vinyl Alcohol) Composite Membranes as Solid Electrolytes for Direct Methanol Alkaline Fuel Cells. *Electrochimica Acta* **187**, 616–628 (2016).
26. Ju, W. *et al.* Understanding activity and selectivity of metal-nitrogen-doped carbon catalysts for electrochemical reduction of CO<sub>2</sub>. *Nat Commun* **8**, 944 (2017).

27. Choi, J.-G. & Thompson, L. T. XPS study of as-prepared and reduced molybdenum oxides. *Applied Surface Science* **93**, 143–149 (1996).
28. Gruenert, W. *et al.* Analysis of molybdenum(3d) XPS spectra of supported molybdenum catalysts: an alternative approach. *J. Phys. Chem.* **95**, 1323–1328 (1991).
29. Wu, H. & Lian, K. The Development of Pseudocapacitive Molybdenum Oxynitride Electrodes for Supercapacitors. *ECS Trans.* **58**, 67 (2014).
30. Chen, P. *et al.* Atomically Dispersed Iron–Nitrogen Species as Electrocatalysts for Bifunctional Oxygen Evolution and Reduction Reactions. *Angewandte Chemie International Edition* **56**, 610–614 (2017).
31. Cao, J. *et al.* A Co/CoO hybrid rooted on carbon cloth as an efficient electrocatalyst for the hydrogen evolution reaction in alkaline solution. *Sustainable Energy & Fuels* **4**, 1924–1932 (2020).
32. Liu, T. *et al.* Ru<sub>2</sub>P Nanoparticle Decorated P/N-Doped Carbon Nanofibers on Carbon Cloth as a Robust Hierarchical Electrocatalyst with Platinum-Comparable Activity toward Hydrogen Evolution. *ACS Appl. Energy Mater.* **1**, 3143–3150 (2018).
33. Nielander, A. C. *et al.* A Versatile Method for Ammonia Detection in a Range of Relevant Electrolytes via Direct Nuclear Magnetic Resonance Techniques. *ACS Catal.* **9**, 5797–5802 (2019).
34. Kolen, M., Smith, W. A. & Mulder, F. M. Accelerating <sup>1</sup>H NMR Detection of Aqueous Ammonia. *ACS Omega* **6**, 5698–5704 (2021).
35. Tsedilin, A. M. *et al.* How sensitive and accurate are routine NMR and MS measurements? *Mendeleev Communications* **25**, 454–456 (2015).

36. Mukherjee, S. *et al.* Metal-organic framework-derived nitrogen-doped highly disordered carbon for electrochemical ammonia synthesis using N<sub>2</sub> and H<sub>2</sub>O in alkaline electrolytes. *Nano Energy* **48**, 217–226 (2018).
37. Zhao, X. *et al.* Highly efficient metal–organic-framework catalysts for electrochemical synthesis of ammonia from N<sub>2</sub> (air) and water at low temperature and ambient pressure. *J Mater Sci* **52**, 10175–10185 (2017).
38. Qin, J.-S. *et al.* Ultrastable Polymolybdate-Based Metal–Organic Frameworks as Highly Active Electrocatalysts for Hydrogen Generation from Water. *J. Am. Chem. Soc.* **137**, 7169–7177 (2015).
39. Geng, Z. *et al.* Achieving a Record-High Yield Rate of 120.9 for N<sub>2</sub> Electrochemical Reduction over Ru Single-Atom Catalysts. *Advanced Materials* **0**, 1803498.
40. Wu, H. B., Xia, B. Y., Yu, L., Yu, X.-Y. & Lou, X. W. (David). Porous molybdenum carbide nano-octahedrons synthesized via confined carburization in metal-organic frameworks for efficient hydrogen production. *Nature Communications* **6**, 6512 (2015).
41. Liu, Y. *et al.* Facile Ammonia Synthesis from Electrocatalytic N<sub>2</sub> Reduction under Ambient Conditions on N-Doped Porous Carbon. *ACS Catal.* **8**, 1186–1191 (2018).
42. Tao, H. *et al.* Nitrogen Fixation by Ru Single-Atom Electrocatalytic Reduction. *Chem* **5**, 204–214 (2019).
43. Qin, Q., Heil, T., Antonietti, M. & Oschatz, M. Single-Site Gold Catalysts on Hierarchical N-Doped Porous Noble Carbon for Enhanced Electrochemical Reduction of Nitrogen. *Small Methods* **2**, 1800202 (2018).
44. Kong, J. *et al.* Electrochemical Synthesis of NH<sub>3</sub> at Low Temperature and Atmospheric Pressure Using a  $\gamma$ -Fe<sub>2</sub>O<sub>3</sub> Catalyst. *ACS Sustainable Chem. Eng.* **5**, 10986–10995 (2017).

45. Cui, B. *et al.* Electrochemical synthesis of ammonia directly from N<sub>2</sub> and water over iron-based catalysts supported on activated carbon. *Green Chem.* **19**, 298–304 (2017).
46. Wang, M. *et al.* Over 56.55% Faraday efficiency of ambient ammonia synthesis enabled by positively shifting the reaction potential. *Nat Commun* **10**, 341 (2019).
47. Liu, Y. *et al.* Electrochemical reduction of N<sub>2</sub> to ammonia on Co single atom embedded N-doped porous carbon under ambient conditions. *J. Mater. Chem. A* **7**, 26358–26363 (2019).
48. Zang, W. *et al.* Copper Single Atoms Anchored in Porous Nitrogen-Doped Carbon as Efficient pH-Universal Catalysts for the Nitrogen Reduction Reaction. *ACS Catal.* **9**, 10166–10173 (2019).
49. Zhang, R. *et al.* Enabling Effective Electrocatalytic N<sub>2</sub> Conversion to NH<sub>3</sub> by TiO<sub>2</sub> Nanosheets Array under Ambient Conditions. **24**.
50. Xia, J. *et al.* Boosting electrosynthesis of ammonia on surface-engineered MXene Ti<sub>3</sub>C<sub>2</sub>. *Nano Energy* **72**, 104681 (2020).
51. Cao, N. *et al.* Electrochemical nitrogen fixation via bimetallic Sn-Ti sites on defective titanium oxide catalysts. *Journal of Colloid and Interface Science* **588**, 242–247 (2021).
52. Lee, H. K. *et al.* Favoring the unfavored: Selective electrochemical nitrogen fixation using a reticular chemistry approach. *Science Advances* **4**, eaar3208 (2018).
53. American Public Health Association *et al.* *Standard methods for the examination of water and wastewater*. (2017).
54. Catalano, G. An improved method for the determination of ammonia in seawater. *Marine Chemistry* **20**, 289–295 (1987).
55. Lan, R., Irvine, J. T. S. & Tao, S. Synthesis of ammonia directly from air and water at ambient temperature and pressure. *Sci Rep* **3**, 1145 (2013).



56. Zhou, L. & Boyd, C. E. Comparison of Nessler, phenate, salicylate and ion selective electrode procedures for determination of total ammonia nitrogen in aquaculture. *Aquaculture* **450**, 187–193 (2016).
57. Andersen, S. Z. *et al.* A rigorous electrochemical ammonia synthesis protocol with quantitative isotope measurements. *Nature* **1** (2019) doi:10.1038/s41586-019-1260-x.
58. McEnaney, J. M. *et al.* Ammonia synthesis from N<sub>2</sub> and H<sub>2</sub>O using a lithium cycling electrification strategy at atmospheric pressure. *Energy Environ. Sci.* **10**, 1621–1630 (2017).
59. Chen, S. *et al.* Room-Temperature Electrocatalytic Synthesis of NH<sub>3</sub> from H<sub>2</sub>O and N<sub>2</sub> in a Gas–Liquid–Solid Three-Phase Reactor. *ACS Sustainable Chem. Eng.* **5**, 7393–7400 (2017).
60. Zhang, T., Miyaoka, H., Miyaoka, H., Ichikawa, T. & Kojima, Y. Review on Ammonia Absorption Materials: Metal Hydrides, Halides, and Borohydrides. *ACS Appl. Energy Mater.* **1**, 232–242 (2018).
61. Su, H. *et al.* Hetero-N-Coordinated Co Single Sites with High Turnover Frequency for Efficient Electrocatalytic Oxygen Evolution in an Acidic Medium. *ACS Energy Lett.* **4**, 1816–1822 (2019).
62. Pan, Y. *et al.* A Bimetallic Zn/Fe Polyphthalocyanine-Derived Single-Atom Fe-N<sub>4</sub> Catalytic Site: A Superior Trifunctional Catalyst for Overall Water Splitting and Zn–Air Batteries. *Angewandte Chemie International Edition* **57**, 8614–8618 (2018).
63. Guan, J. *et al.* Water oxidation on a mononuclear manganese heterogeneous catalyst. *Nat Catal* **1**, 870–877 (2018).
64. Zhang, L. *et al.* Graphene Defects Trap Atomic Ni Species for Hydrogen and Oxygen Evolution Reactions. *Chem* **4**, 285–297 (2018).

65. Cao, L. *et al.* Dynamic oxygen adsorption on single-atomic Ruthenium catalyst with high performance for acidic oxygen evolution reaction. *Nat Commun* **10**, 4849 (2019).
66. Yao, Y. *et al.* Engineering the electronic structure of single atom Ru sites via compressive strain boosts acidic water oxidation electrocatalysis. *Nat Catal* **2**, 304–313 (2019).
67. Zhang, H. *et al.* Unveiling the Activity Origin of Electrocatalytic Oxygen Evolution over Isolated Ni Atoms Supported on a N-Doped Carbon Matrix. *Advanced Materials* **31**, 1904548 (2019).
68. Lei, C. *et al.* Fe N<sub>4</sub> Sites Embedded into Carbon Nanofiber Integrated with Electrochemically Exfoliated Graphene for Oxygen Evolution in Acidic Medium. *Advanced Energy Materials* **8**, 1801912 (2018).
69. Zheng, T. *et al.* Large-Scale and Highly Selective CO<sub>2</sub> Electrocatalytic Reduction on Nickel Single-Atom Catalyst. *Joule* **3**, 265–278 (2019).
70. Tahir, M. *et al.* Electrocatalytic oxygen evolution reaction for energy conversion and storage: A comprehensive review. *Nano Energy* **37**, 136–157 (2017).
71. Song, F. *et al.* An Unconventional Iron Nickel Catalyst for the Oxygen Evolution Reaction. *ACS Cent. Sci.* **5**, 558–568 (2019).
72. Bai, L., Lee, S. & Hu, X. Spectroscopic and Electrokinetic Evidence for a Bifunctional Mechanism of the Oxygen Evolution Reaction\*\*. *Angewandte Chemie International Edition* **60**, 3095–3103 (2021).
73. Zhou, Z., Li, X., Li, Q., Zhao, Y. & Pang, H. Copper-based materials as highly active electrocatalysts for the oxygen evolution reaction. *Materials Today Chemistry* **11**, 169–196 (2019).

74. Bai, Y. *et al.* Strengthened Synergistic Effect of Metallic MxPy (M = Co, Ni, and Cu) and Carbon Layer via Peapod-Like Architecture for Both Hydrogen and Oxygen Evolution Reactions. *Small* **13**, 1603718 (2017).
75. Kim, J. *et al.* Branched Copper Oxide Nanoparticles Induce Highly Selective Ethylene Production by Electrochemical Carbon Dioxide Reduction. *J. Am. Chem. Soc.* **141**, 6986–6994 (2019).
76. Yang, X. *et al.* Highly acid-durable carbon coated Co<sub>3</sub>O<sub>4</sub> nanoarrays as efficient oxygen evolution electrocatalysts. *Nano Energy* **25**, 42–50 (2016).
77. Anantharaj, S., Karthick, K. & Kundu, S. Spinel Cobalt Titanium Binary Oxide as an All-Non-Precious Water Oxidation Electrocatalyst in Acid. *Inorg. Chem.* **58**, 8570–8576 (2019).
78. Shan, J., Ling, T., Davey, K., Zheng, Y. & Qiao, S.-Z. Transition-Metal-Doped RuIr Bifunctional Nanocrystals for Overall Water Splitting in Acidic Environments. *Advanced Materials* **31**, 1900510 (2019).
79. Sousa, J. P. S., Pereira, M. F. R. & Figueiredo, J. L. NO oxidation over nitrogen doped carbon xerogels. *Applied Catalysis B: Environmental* **125**, 398–408 (2012).
80. Arkhipova, E. A. *et al.* Structural evolution of nitrogen-doped carbon nanotubes: From synthesis and oxidation to thermal defunctionalization. *Carbon* **125**, 20–31 (2017).
81. Zhao, Y., Nakamura, R., Kamiya, K., Nakanishi, S. & Hashimoto, K. Nitrogen-doped carbon nanomaterials as non-metal electrocatalysts for water oxidation. *Nat Commun* **4**, 2390 (2013).
82. Zhu, Y., Zhang, T. & Lee, J. Y. Nitrogenated-Graphite-Encapsulated Carbon Black as a Metal-Free Electrocatalyst for the Oxygen Evolution Reaction in Acid. *ChemElectroChem* **5**, 583–588 (2018).

83. Bai, L., Hsu, C.-S., Alexander, D. T. L., Chen, H. M. & Hu, X. A Cobalt–Iron Double-Atom Catalyst for the Oxygen Evolution Reaction. *J. Am. Chem. Soc.* **141**, 14190–14199 (2019).
84. Frydendal, R. *et al.* Benchmarking the Stability of Oxygen Evolution Reaction Catalysts: The Importance of Monitoring Mass Losses. *ChemElectroChem* **1**, 2075–2081 (2014).
85. McCrory, C. C. L. *et al.* Benchmarking Hydrogen Evolving Reaction and Oxygen Evolving Reaction Electrocatalysts for Solar Water Splitting Devices. *J. Am. Chem. Soc.* **137**, 4347–4357 (2015).
86. Miao, X. *et al.* Quadruple perovskite ruthenate as a highly efficient catalyst for acidic water oxidation. *Nat Commun* **10**, 3809 (2019).
87. Lin, Y. *et al.* Chromium-ruthenium oxide solid solution electrocatalyst for highly efficient oxygen evolution reaction in acidic media. *Nat Commun* **10**, 162 (2019).

# Chapter 3: Co-incorporated Carbon Black for Lithium-ion Batteries

This presented in this chapter were adapted from:

"Lithium-Ion Battery Negative Electrode with Enhanced Rate Performance by Metal Incorporated Carbon Conductive Agent" currently under revision and in collaboration with the group of Prof. Yajun Cheng in Ningbo Institute of technology and engineering.

### 3.1 Introduction to Electron conductive Carbon agents

Lithium-ion batteries have found wide applications in consumer electronics<sup>1</sup>, electric vehicles, and smart grids<sup>2</sup>. The reversible capacity of the electrode is critical to determine the energy density of the battery. Besides utilization of new materials with high theoretical capacities<sup>3-5</sup>, developing alternative strategies to increase actual capacities exhibited by the conventional electrode holds great promise for practical applications<sup>6,7</sup>. Electron conductive agents such as acetylene carbon have been extensively used to fabricate electrodes<sup>8</sup>. With the help of carbon, an electronic conductive network is built which enables charge carrier transportation within the electrode. The electron conductive network plays an important role in the electrochemical kinetics and overall electrochemical performance of the batteries<sup>9</sup>. However, the development of electron conductive agents have been rarely explored.

The group of Prof. Cheng recently reported that in situ incorporation of a tiny amount of silver nanoparticles to the silicon/carbon nanohybrid negative electrode improved its rate performance<sup>10</sup>. The embedded silver nanoparticles increased the charge carrier mobility rather than charge carrier density, resulting in improved electron conductivity of the silicon/carbon electrode.

Inspired by this work, we probed whether incorporation of small amounts of metal species into electron conductive carbon matrices could improve the electrochemical performance of the negative electrode. The reversible capacities and rate performance of silicon/carbon negative electrodes were improved significantly compared to electrodes using the conventional KetJen Black® as the electron conductive agent. A similar improvement

was found for the Super-P® based electron conductive carbon matrix, indicating a generality of this approach.

## 3.2 Results

### 3.2.1 Characterization

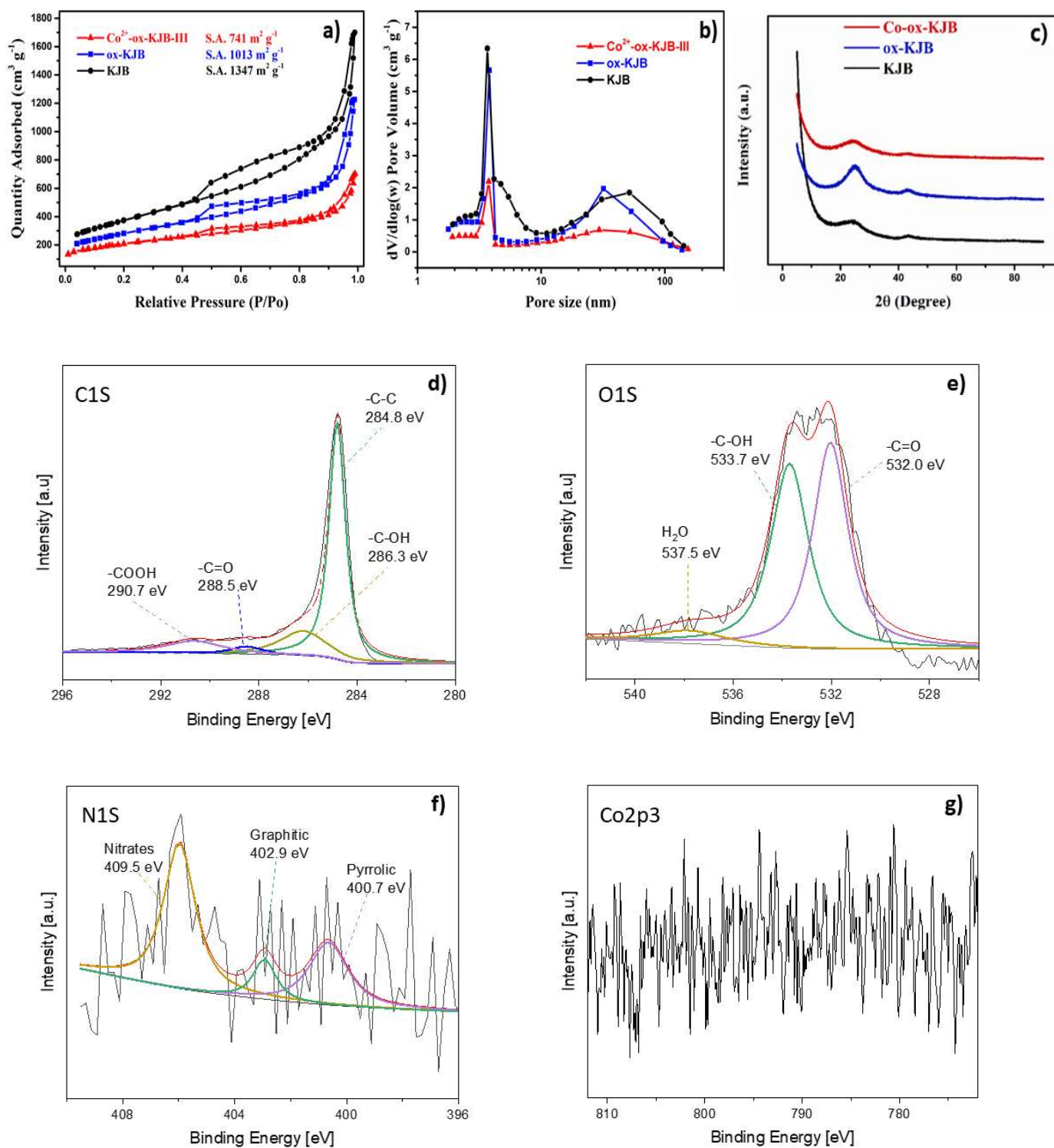
Figure 3-1 a) shows the nitrogen adsorption/desorption isotherm curves of the pristine, oxidized, and oxidized KJB incorporated with cobalt. All three curves show typical type-II hysteresis indicating the existence of mesoporous structures, which was confirmed by the pore size distribution profiles displayed in Figure 3-1 b)<sup>11</sup>. The pristine KJB exhibits the specific surface area of 1357 m<sup>2</sup>/g. It was decreased to 1013 m<sup>2</sup>/g after oxidation treatment because the internal cohesion force tends to be enhanced by surface functional groups introduced by the oxidation process. Incorporation of the cobalt salt further decreased the specific surface area to 741 m<sup>2</sup>/g due to further enhanced cohesion force by the metal ions. Figure 3-1 b) indicates the existence of mesopores with a broad size distribution in the pristine KJB because most of the pores in the KJB were created by particle packing. After oxidation, the pore size distribution was significantly narrowed because the number of the pores is diminished by the enhanced inter-particle cohesion force. Compared to the pristine and Ox-KJB samples, the Co-Ox-KJB sample showed even a more narrow pore size distribution, where the amount of pores with a diameter larger than 10 nm had largely decreased. The pore size distribution profiles are in a good agreement with the specific surface area data, which indicates that the oxidation and metal ion incorporation modified the surface property and inter particle interactions within the KJB powder.

The broad peak exhibited in XRD results (Fig.3-1 c)) suggests the existence of a local graphitic structure in the KJB powder. The peak position is slightly shifted towards the high two-theta region compared to those of typical graphite materials<sup>12-14</sup>, suggesting that the

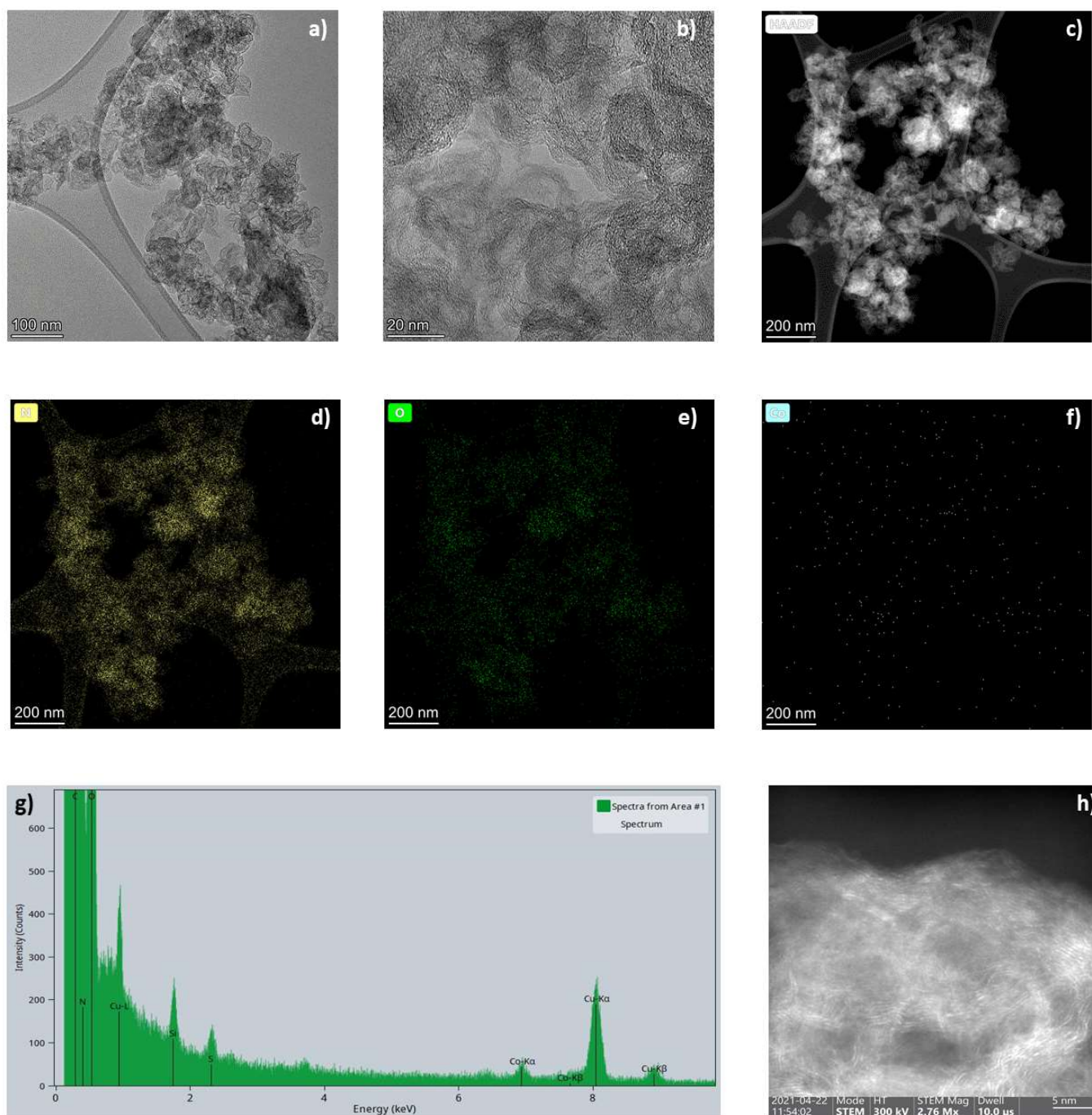
inter-plane distance of the local graphitic structure in KJB is expanded slightly<sup>15</sup>. The XPS profiles of C1s, Co2p, O1s, and N1s spectra of the Co-Ox-KJB are displayed in Figure 1d to 1g. The peaks from C1s are assigned to respectively: C-C ( $sp^2$ , 284.8eV); C-OH (286.3eV), C=O (288.5eV); O-C=O (290.7eV), indicating the incorporation of oxygen-containing functional groups upon nitric acid oxidation<sup>15</sup>. However, no clear signal is observed from the Co2p profile. The low amount of cobalt (around 0.8 % by mass by ICP) in the KJB with a large specific surface area and void fraction tends to weaken the XPS signal because XPS only detects the species residing at the sample surface. The O1s profile from Figure 1f indicates the presence of organic species: C=O (532.0 eV), C-OH (533.7 eV); the peak observed at 537.5 eV was attributed to the remaining H<sub>2</sub>O within the sample<sup>16-18</sup>.

The structures and chemical composition spatial distribution of the Co-Ox-KJB were investigated by TEM, HAADF, HR-LAADF, and EDS (Figure 3-2). Figure 3-2 a) and b) confirm the existence of carbon particles with a mesoporous structure, which are similar to the structures observed in both the pristine and Ox-KJB (Fig.2-11 a)-b) and Fig.2-12 a)-b)). The HAADF images together with the EDS elemental mapping in (Fig.3-2 c)-g)) indicate the homogeneous distribution of carbon, nitrogen, and oxygen within the sample. Collected signal for cobalt was weak compared to the background (Fig.3-2 f)). It is worth noticing that the nitrogen and oxygen elements can also be detected in the pristine KJB (Fig.2-11 h)), which are homogeneously distributed at the surface of the pristine KJB. Averaged EDS mapping from HR-TEM on a 700×700 nm<sup>2</sup> was collected with long exposure, and a small peak from the K<sub>α</sub> line confirmed the presence of Co (Fig.3-2 g)). Carbon graphitic planes were observed by HR-LAADF (Fig.3-2 h)), and no Co nanoparticles were found.





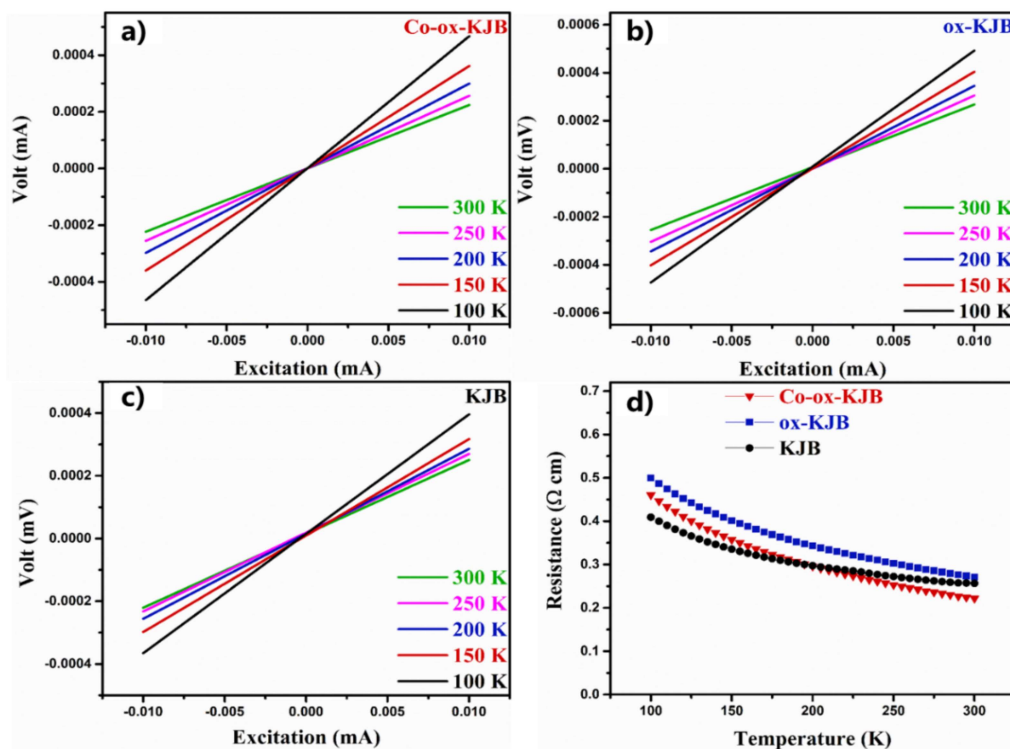
**Figure 3-1.** a) Nitrogen adsorption/desorption isotherm curves of Co-Ox-KJB (red), Ox-KJB (blue) and KJB (black). b) Pore size distribution curves of Co-Ox-KJB (red), Ox-KJB (blue) and KJB (black). c) XRD Pattern of Co-Ox-KJB (red), Ox-KJB (blue) and KJB (black). d-g) High resolution XPS spectra for d) C 1s, e) Co 2p, f) O 1s and g) N 1s regions of Co-Ox-KJB, respectively.



**Figure 3-2.** a-b) TEM images of Co-Ox-KJB. c) HAADF images of Co-Ox-KJB. d-f) STEM-EDS element mapping showing the distribution of N , O, and Co of Co-Ox-KJB, respectively. g) STEM-EDS survey from HR-TEM and h) LAADF of Co-Ox-KJB.

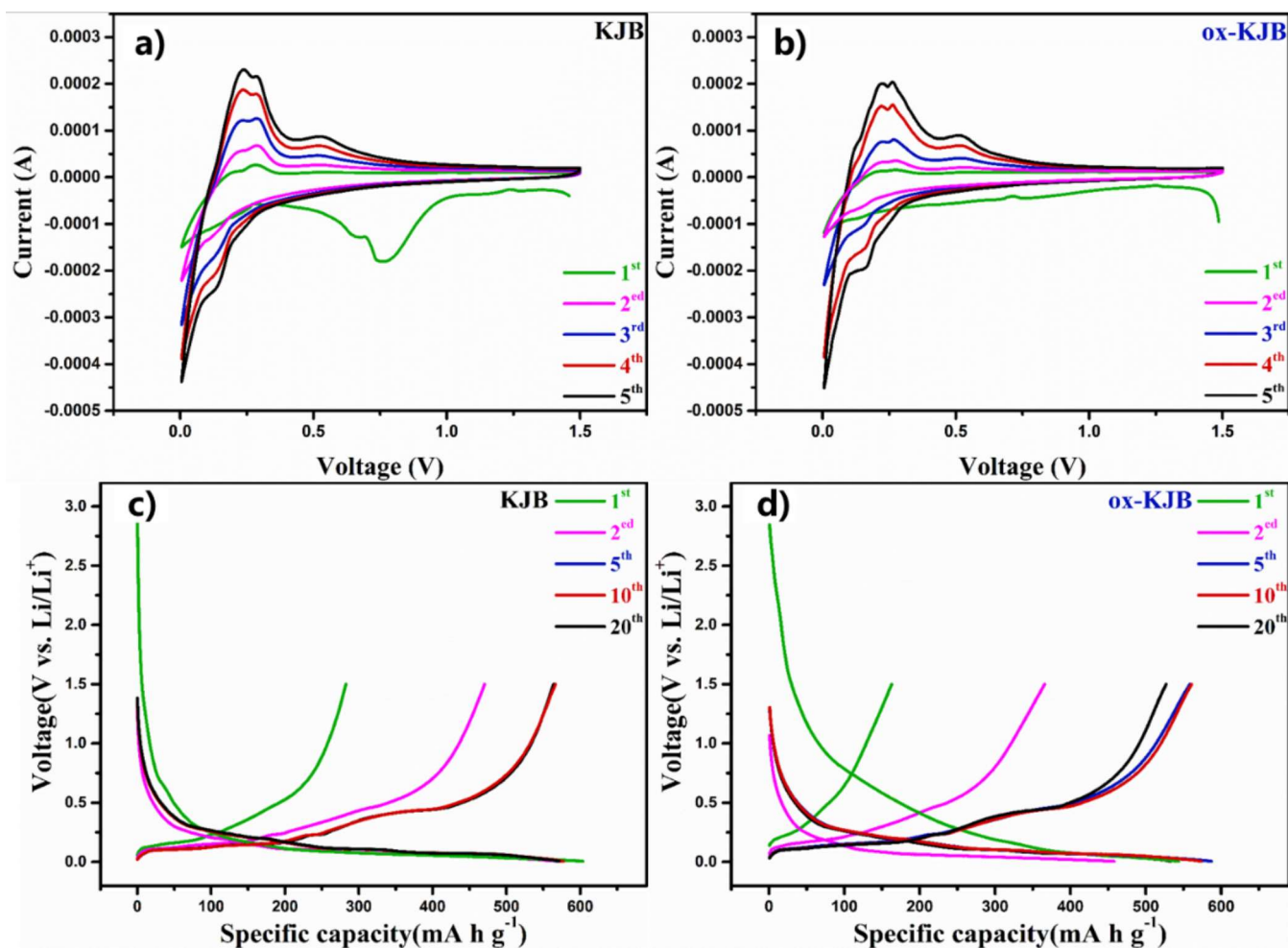
### 1.1.1 Electrochemical Performances

Figure 3-3 a-c) displays the temperature-dependent I-V curves and d) the corresponding temperature-dependent resistivity of the pristine KJB, Ox-KJB, and Co-Ox-KJB. The I-V curves (Figure 3-3a-c) exhibited an ohmic character, which suggests that the dominant charge carrier transportation mechanism for the KJB, Ox-KJB, and Co-Ox-KJB is band-like rather than a hopping process. The monotonical increase of the resistivity upon decreasing temperature suggests that the samples are semiconductive in nature<sup>10</sup>. The resistivity profiles indicate that the Ox-KJB had the highest resistivity values at the temperature from 300 K to 100 K. Indeed, the oxidation process partially destroyed the local graphitic structure of KJB, decreasing the charge carrier transportation ability<sup>19</sup>. When cobalt ions were incorporated into the Ox-KJB, the resistivity is decreased compared to the bare Ox-KJB. This result suggests that the addition of cobalt into the defects of Ox-KJB matrix was beneficial for the electron conductivity. At 200 K or above, Co-Ox-KJB is more conductive than pristine KJB.



**Figure 3-3.** a-c) Typical  $I-V$  curves of Co-Ox-KJB, Ox-KJB and KJB at different temperatures. d) Temperature-dependent resistivity profiles of Co-Ox-KJB, Ox-KJB and KJB at different temperatures.

The cyclic voltammetry profile of the first five cycles of a half-cell with Co-Ox-KJB is displayed in Figure 3-5 a). The broad cathodic peak at around 0.2 V corresponds to the lithiation of silicon to form amorphous  $\text{Li}_x\text{Si}$ . The anodic peaks at 0.35 and 0.50 V are associated with the successive transitions from highly lithiated Si to less-lithiated and further non-lithiated Si. These CV patterns are similar to the profiles observed in typical Si/C composite electrodes<sup>20,21</sup>. The use of the Co-Ox-KJB did not modify the fundamental lithiation/delithiation process.



**Figure 3-4.** a-b) CV curves of pristine KJB and Ox-KJB. c-d) Discharge and charge curves of pristine KJB and Ox-KJB at 0.05 A g<sup>-1</sup>.

The CV profiles of the pristine KJB show a broad peak at around 0.6 V - 0.8 V in the first cathodic process due to the formation of the SEI layer (Fig.3-4a)<sup>22,23</sup>. The intensity of this peak was significantly diminished in the CV curves of Ox-KJB -which are similar to those of the Co-Ox-KJB- it was attributed to decrease in specific surface areas (Fig.3-4 b). The discharge/charge profiles of the Co-Ox-KJB (Fig.3-5 b)) display characteristic lithiation/delithiation plateaus, in accordance with CV. The lithiation/delithiation capacities are increased gradually indicating an activation process for the first few cycles, which is also



observed in both pristine KJB and Ox-KJB samples (Fig.3-4 c-d)). This activation originated from a gradually enhanced electrolyte wetting process within the Si/C electrode, resulting from the large specific surface areas KJB. After five cycles, the lithiation/delithiation capacity of Co-Ox-KJB reached 626/644 mAh g<sup>-1</sup> (Fig.3-5 b)), which is typical for a Si/C electrode.

The cyclic performances of the Si/C anodes using KJB, Ox-KJB, and Co-Ox-KJB as conductive agents are displayed in Figure 3-5 c). The Si/C electrode with the Ox-KJB had the lowest reversible capacities and the worst stability over 100 cycles. The significant decrease of the specific surface area of Ox-KJB also limited the surface coverage of the Si/C particles, suppressing charge carrier transportation within the electrode. With cobalt incorporated into Ox-KJB, the reversible capacities were higher than those of the Ox-KJB, and even slightly higher than those of the pristine KJB. After 100 cycles at 0.05 A.g<sup>-1</sup>, the reversible capacity was maintained at 501 mA.h.g<sup>-1</sup> with the Co-Ox-KJB, higher than that of the pristine KJB and Ox-KJB, at 447 mA.h.g<sup>-1</sup> and 370 mA.h.g<sup>-1</sup>, respectively. The capacity retention ratio after 100 cycles using Co-Ox-KJB was around 80.0 %, which is slightly higher than the Si/C electrode with unmodified KJB at around 74.5%. The specific surface area of the Co-Ox-KJB was significantly decreased and the local graphitic structure was deteriorated by incorporating oxygen surface functional groups compared to KJB. Hence, the enhanced performance in terms of reversible capacities and capacity retention ratio was attributed to the enhanced electron conductivity by the metal incorporation into Ox-KJB.

The rate performances of KJB, Ox-KJB, and Co-Ox-KJB are displayed in Figure 3-5 d). The pristine KJB sample showed inferior capacities at various current densities except at 0.05 A.g<sup>-1</sup>. Considering that the pristine KJB possesses a good electron conductivity as well as a

large specific surface area, the measured lower capacities at the current densities above 0.10 A.g<sup>-1</sup> suggested that other factors influenced the electrochemical performance. The introduction of oxygen surface functional groups in Ox-KJB -by acid treatment- enhanced its affinity towards the electrolyte solution. We hypothesized that the surface wetting by the electrolyte solution and further desolvation process were promoted by this modification, leading to accelerated electrochemical kinetics and improved rate performance at higher current densities (from 0.50 A.g<sup>-1</sup> and above). With cobalt incorporation into Ox-KJB, the capacities were even further increased. We expect that the cobalt ions were reduced *in situ* to form elemental cobalt during the lithiation process<sup>24-26</sup>, being at the origin of the enhanced electronic conductivity of the Co-Ox-KJB.

Hence, the accelerated electrochemical kinetics and rate performance were attributed to the synergetic effect of the combination of the increased electron conductivity, improved electrolyte wetting, and enhanced desolvation process.

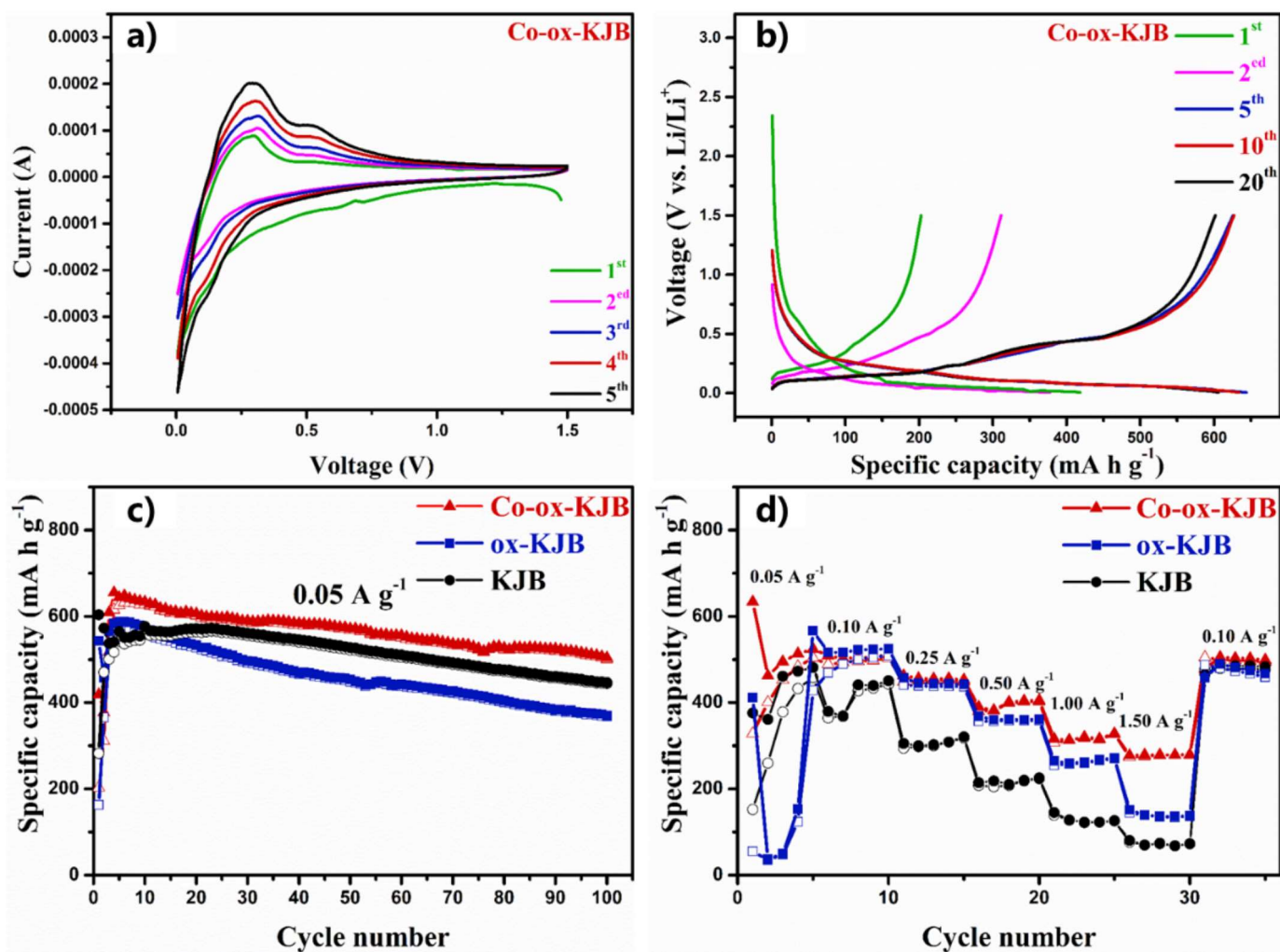


**Figure 3-5.** a) CV curves and b) Discharge and charge curves of Co-Ox-KJB at 50 mA g<sup>-1</sup>. c) Long-term cycling performance at 50 mA g<sup>-1</sup> of Co-Ox-KJB (red), Ox-KJB (blue) and KJB (black). d) Rate capability test from 0.05 A g<sup>-1</sup> to 1.50 A g<sup>-1</sup>, followed by returning to 0.10 A g<sup>-1</sup> with 5 cycles of Co-Ox-KJB (red), Ox-KJB (blue) and KJB (black).

The applicability of our approach was also investigated with SuperP, another typical electron conductive agent used in the fabrication of lithium-ion batteries. As shown in Figure 3-6 a-b), spherical like carbon particles were observed by TEM in the Co-Ox-super P sample, whose particle size seems larger than that of the KJB. A clear signal for cobalt was detected by EDS (Fig.3-6 d)), together with homogeneous distribution of the nitrogen, oxygen, and carbon. Apparently, more cobalt ions are incorporated into the super P than the KJB. XPS



data confirm the existence of the cobalt ion, whose signal is more pronounced than that of the Co-Ox-KJB (Fig.3-6 k)).

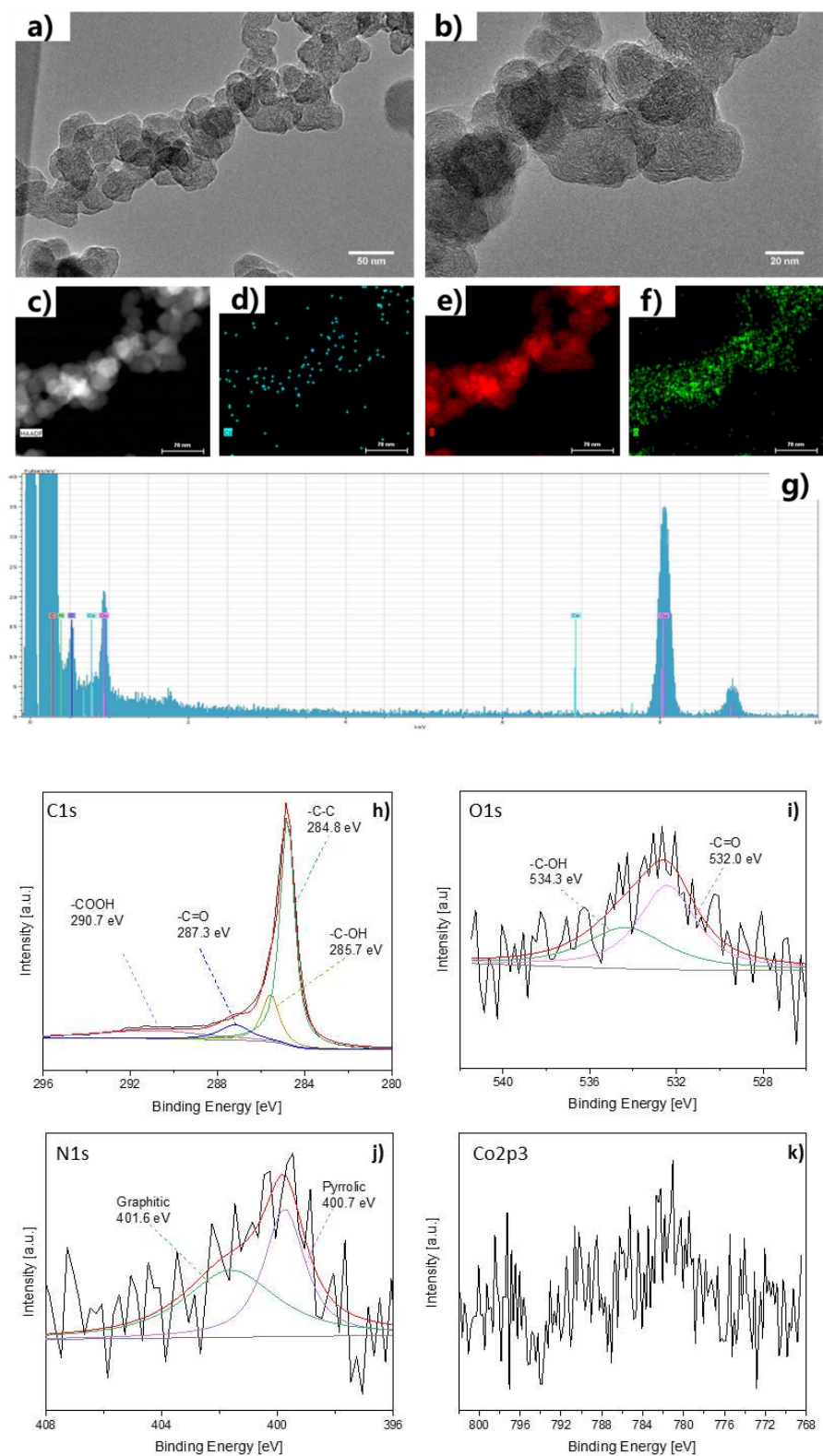


**Figure 3-6.** a-b) TEM images, c) HAADF images d-f) EDS element mapping showing the distribution of Co, C and O of Co-Ox-super P, respectively. g) EDX image of Co-Ox-super P. h-k) High resolution XPS spectra for h) C1s, i) O1s, j) N1s and k) Co2p regions of Co-Ox-SuperP, respectively.

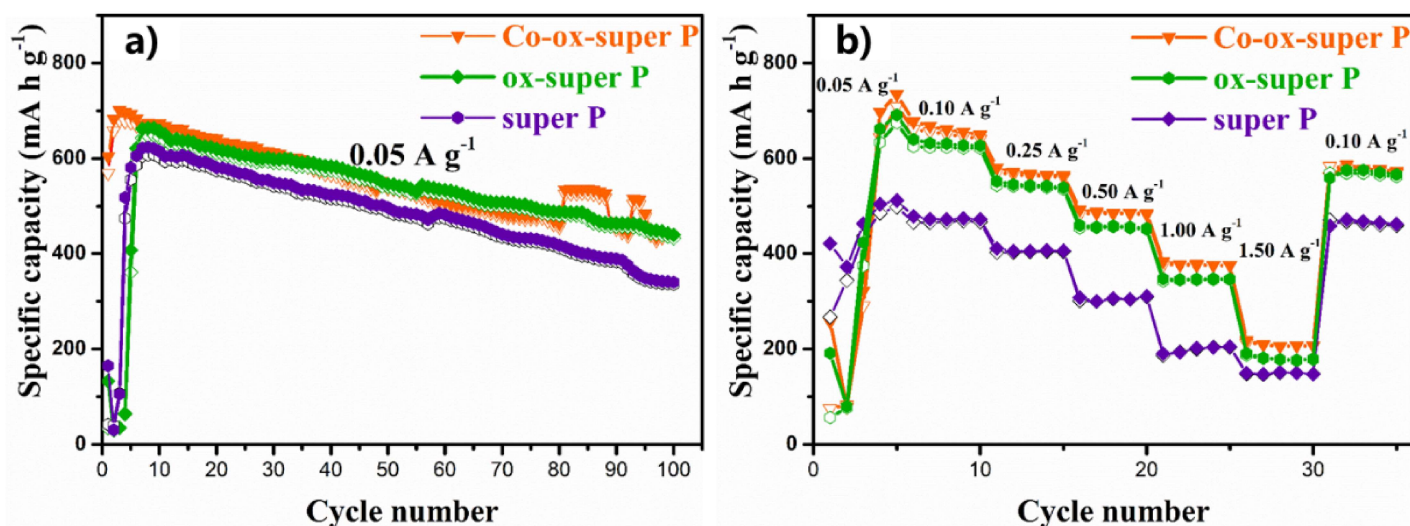


**Figure 3-7.** Cyclic (a) and rate (b) performance of the Si/C electrode with pristine SuperP, ox-super P, and Co-Ox-SuperP.

The cyclic performances of the Si/C electrodes using the pristine SuperP, Ox-SuperP, and Co-Ox-SuperP are displayed in Figure 3-7. The Si/C electrode with the pristine SuperP shows slightly less reversible capacities compared to the Ox-SuperP and Co-Ox-SuperP. An activation process was observed in all of the three samples. However, the Co-Ox-SuperP undergoes the least activation process, which is likely due to a decreased specific surface area after oxidation and cobalt incorporation. Further rate performance test results showed that both Ox-SuperP and Co-Ox-SuperP can effectively increase the reversible capacities at the current densities from  $0.10 \text{ A g}^{-1}$  to  $1.50 \text{ A g}^{-1}$ , compared to pristine SuperP. Compared to the Ox-SuperP, the cobalt incorporation further lifts the reversible capacities with the current densities from  $0.10 \text{ A g}^{-1}$  to  $1.50 \text{ A g}^{-1}$ . These data confirm that the oxidation and further cobalt incorporation into SuperP can effectively improve the rate performance of the Si/C electrode over a wider current density range. Thus, the extent of the capacity increase by the

cobalt incorporation into the SuperP was found to be less than for KJB, possibly due to a lower specific surface area of SuperP compared with KJB.

Inspired by the above results, we also prepared other M-Ox-KJB, where M = Cu, Fe and Ni, following similar procedures. Si/C electrodes using these conductive matrices showed poorer performance compared to pristine conductive agents. The reversible capacities of the samples with the M-Ox-KJB were lesser than with pristine KJB. Regarding the rate performance, the Si/C with the Cu-Ox-KJB exhibited better rate performance than the other M-Ox-KJB samples. While the capacity difference among the Fe-Ox-KJB, Ni-Ox-KJB, and pristine KJB being quite small (Fig.3-8).

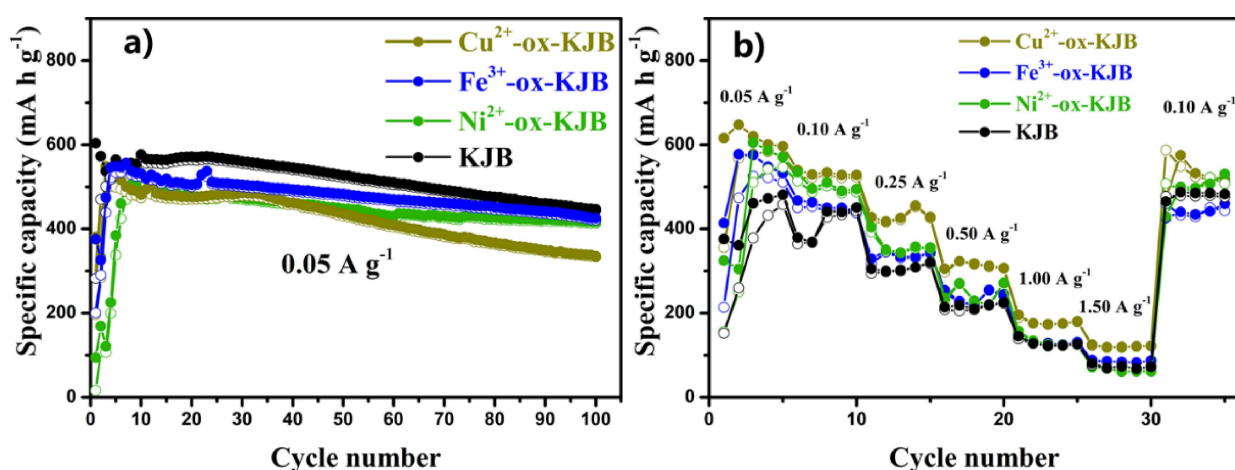


**Figure 3-8.** Cyclic (a) and rate (b) performance of the Si/C electrode with pristine KJB, Cu-Ox-KJB, Fe-Ox-KJB, and Ni-Ox-KJB.

From  $0.10 \text{ A.g}^{-1}$  and above Ox-KJB incorporated with copper displayed higher specific capacities than pristine KJB. Though it was found to perform less than pristine for longer cyclic performances at  $0.05 \text{ A.g}^{-1}$ .

## 1.2 Discussion

In order to deposit active material on a current collector, a slurry is made with three main components: an active material, a binder and conductive additives. Here the incorporation of 0.8% by mass of cobalt in the oxidized KJB was found to be beneficial for discharge/charge at current densities higher than  $0.50 \text{ A.g}^{-1}$ . Though the oxidation of the carbon matrix displayed higher resistance when comparing Ox-KJB to KJB. Cobalt incorporated Ox-KJB displayed a higher resistance at low temperature and a higher one at higher temperatures. The average capacity of the Si/C anode increased by 180% at  $1.5 \text{ A.g}^{-1}$  with the incorporation of cobalt compared to pristine KJB ( $297 \text{ mAh.g}^{-1}$  vs  $73 \text{ mAh.g}^{-1}$ , respectively). We hypothesize that the Co incorporation is beneficial for the electronic conductivity of the carbon matrix. However, the oxidation of SuperP agent was found to be beneficial at lower current densities, where an improvement in the specific capacity can be observed from  $0.10 \text{ A.g}^{-1}$ , as well upon incorporation of cobalt. As the oxidation causes an increase in resistance, it may also allow an improved affinity towards the electrolyte and enhanced desolvation process. The incorporation of Co may also play a role in the overall mechanical properties of the carbon conductive agent.

Nowadays, carbon nanotubes (CNT)<sup>27</sup>, graphene<sup>28–30</sup>, or poly-3,4-ethylenedioxythiophene/polystyrene sulfonate (PEDOT:PSS)<sup>31</sup> are used as additives in the slurry to enhance the electron conductivity. PEDOT:PSS -a p-type conductive polymer- is used as a stable conductive coating with good flexibility and mechanical properties<sup>32</sup>. The good mechanical and chemical stability, combined with excellent conductivity and thermal stability lead to the wide adoption of CNT in the world of nanoelectronics<sup>33</sup>. Thus, the more conductive additives are used in the slurry, the less of active material per mass, leading to an

increase in the total mass of the battery without increasing the specific capacity. Indeed, our approach consisting in the incorporation of small amounts of metallic ions is a promising way to enhance the conductivity and mechanical properties of the conductive additive, without reducing the amount of active material in the slurry nor influence the total mass of the battery.

### 1.3 Conclusion

In conclusion, a new concept has been established to improve the rate performance of the lithium-ion battery. A tiny amount (around 0.8 % by mass) of cobalt ions are incorporated into oxidized electron conductive agents (Ketjen black and super P), which effectively increase the reversible capacities of the Si/C composite anode at high current densities. The enhancement is attributed to enhanced electron conductivity, improved electrolyte wetting, and enhanced desolvation process. This work provides a new approach to improve the rate performance of the lithium-ion battery.

### 1.4 Experimental Section

#### *Acknowledgements*

This research is supported by EPFL, the National Natural Science Foundation of China (21773279, 22075305, 52061135110), the Key Research Program of the Chinese Academy of Sciences (ZDRW\_CN\_2020-1), and the Ningbo Science & Technology Innovation 2025 Major Project (2019B10050, 2019B10113), and Key Laboratory of Bio-based Polymeric Materials of Zhejiang Province.

## *Materials*

All chemicals were used as received without further purification. Ketjen Black ECP600JP was purchased from Lion specialty Chemicals Co. Sodium alginate with analytical grade was purchased from Aladdin Chemical. Ltd. Sodium Alginate (SA) was bought from Sigma Aldrich. Silicon/carbon composite was donated by BAK Power Battery. Nitric Acid (65%) was purchased from Carlo Erba Reagents. Cobalt nitrate hexahydrate (99%+) and urea (99%) were purchased from Acros Organics. The solvents include bidistilled water ( $18.2\text{M}\Omega\cdot\text{cm}^{-1}$ ) and absolute ethanol (Abs. EtOH, Fluka).

## *Synthesis of Ox-KJB*

KetJen Black (4.0 g) were dispersed in 200 mL 9 M  $\text{HNO}_3$  in a round bottom flask and heated under vigorous stirring at  $90^\circ\text{C}$  overnight (16h). A reflux system was installed to the round bottom flask to prevent fumes from saturating the hood. The product was recovered and washed with copious amount of bidistilled water ( $\text{ddH}_2\text{O}$ ) first by filtration until reaching a  $\text{pH}>4$ , and then by centrifugation (3x50 mL  $\text{ddH}_2\text{O}$ , 2x50 mL absolute EtOH, 6'000 rpm for 5 mins). The recovered black product was then further dried in a vacuum oven at  $60^\circ\text{C}$  overnight (16h). The recovered dried black powder was denoted as Ox-KJB.

## *Synthesis of Co-Ox-KJB*

KetJen Black (0.6 g) and  $\text{Co}(\text{NO}_3)_2\cdot 6\text{H}_2\text{O}$  (13.0mg) were dispersed in 30mL 9M  $\text{HNO}_3$  by sonication, the mixture left to stir overnight at  $90^\circ\text{C}$ . Then, the surfactant was discarded from the recovered sample, and the product was washed and concentrated by centrifugation (3x 50 mL double distilled  $\text{H}_2\text{O}$ , 2x 50 mL Abs. EtOH). Recovered product was further dried at  $60^\circ\text{C}$  overnight in a vacuum oven. The obtained product was denoted as Co-Ox-KJB.

Ox-KJB was obtained following a similar protocol, without the addition of  $\text{Co}(\text{NO}_3)_2 \cdot 6\text{H}_2\text{O}$  to the solution.

### *Characterization*

TEM was performed using a FEI Tecnai Osiris TEM equipped with a high-brightness field emission gun (XFEG). Samples for TEM were prepared by drop-drying the samples from their diluted ethanol suspensions onto carbon-coated copper grids. Energy-dispersive X-ray spectroscopy (EDS) patterns and mapping images were taken on a FEI Tecnai Osiris TEM in a scanning TEM mode. Elemental energy dispersive X-ray spectroscopy (EDS) mapping was used for elemental characterization, with simultaneously acquired high-angular annular dark field scanning transmission electron microscopy (HAADF-STEM) images showing atomic number and thickness contrast. The high-resolution TEM, and low-angular annular dark field scanning transmission electron microscopy (LAADF-STEM) were acquired simultaneously on FEI Titan Themis Cubed operated at 300kV and a beam current at 60pA. The elemental ratio was calculated from the  $K\alpha$  peak area of each element, using the ESPRIT2 (Bruker) software. X-ray photoelectron spectroscopy (XPS) measurements were performed on a PHI5000 VersaProbe II XPS system by Physical Electronics (PHI) with a detection limit of 1 atomic percent. Monochromatic X-rays were generated by an Al  $K\alpha$  source (1486.7 eV). The diameter of the analyzed area was 10  $\mu\text{m}$ .

The amount of cobalt incorporated into Ketjen black was measured by Inductively coupled plasma (ICP). 0.1 g of the sample was dissolved in 5 ml of nitric acid assisted with microwaves, which was further diluted to 50 ml for the ICP test.

### *Electrochemical Measurements*

Standard 2032-type coin cells were fabricated. Slurry was prepared by manual mixing of the active material, Ketjen black, and Sodium Alginate (SA) binder with a mass ratio of 6:2:2



in deionized water. Thereafter, the slurry was cast on a piece of copper foil, followed by drying at 80 °C in vacuum for 12 h. The mass loading density of the active material was from 1.0 mg cm<sup>-2</sup> to 1.6 mg cm<sup>-2</sup>. Half-cells were fabricated using lithium foils as counter electrodes. Electrolyte from Zhangjiagang Guotai-Huarong Chemical New Material Co., Ltd. was used. The rate performance was measured at the current density sequence of 0.1 C, 0.2 C, 0.5 C, 1.0 C, 2.0 C, 3.0 C, and 0.2 C in the voltage range between 1.5 V and 0.005 V (vs. Li/Li<sup>+</sup>) (five cycles at each current density, 1 C = 500 mAh g<sup>-1</sup>). The cyclic measurement was carried out at a current density of 0.1 C in the same voltage range for 100 rounds. The specific capacity was calculated on the basis of the active material only. Cyclic voltammetry (CV) test was conducted with a Solartron Analytical at a scanning rate of 0.1 mV s<sup>-1</sup> with the voltage range between 0.005 V and 1.5 V.

### *Contributions*

Albert Daubry synthesized the materials and the analysis of the characterization. Dr. Lichen Bai performed the TEM, HAADF and EDS-STEM mapping. Dr. Pierre Mettraux performed the XPS measurements. Dr. Victor Boureau performed the HR-TEM and LAADF-STEM. Prof. Yajun Cheng and his group assembled the batteries and performed the electrochemical tests. Prof. Xile Hi, Prof Yajun Cheng, Zhuijin Xu, Yonggao Xia and Albert Daubry analysed the data and wrote the corresponding manuscript.

## 1.5 Références

1. Liang, Y. *et al.* A review of rechargeable batteries for portable electronic devices. *InfoMat* **1**, 6–32 (2019).
2. Dunn, B., Kamath, H. & Tarascon, J.-M. Electrical Energy Storage for the Grid: A Battery of Choices. *Science* **334**, 928–935 (2011).
3. Zuo, X., Zhu, J., Müller-Buschbaum, P. & Cheng, Y.-J. Silicon based lithium-ion battery anodes: A chronicle perspective review. *Nano Energy* **31**, 113–143 (2017).
4. Qiu, B. *et al.* Gas–solid interfacial modification of oxygen activity in layered oxide cathodes for lithium-ion batteries. *Nat Commun* **7**, 12108 (2016).
5. Choi, J. U., Voronina, N., Sun, Y.-K. & Myung, S.-T. Recent Progress and Perspective of Advanced High-Energy Co-Less Ni-Rich Cathodes for Li-Ion Batteries: Yesterday, Today, and Tomorrow. *Advanced Energy Materials* **10**, 2002027 (2020).
6. Kim, S.-H. *et al.* Ultrahigh-Energy-Density Flexible Lithium-Metal Full Cells based on Conductive Fibrous Skeletons. *Advanced Energy Materials* **11**, 2100531 (2021).
7. Tsai, S.-H., Tsou, Y.-L., Yang, C.-W., Chen, T.-Y. & Lee, C.-Y. Applications of different nano-sized conductive materials in high energy density pouch type lithium ion batteries. *Electrochimica Acta* **362**, 137166 (2020).
8. Tsai, S.-H. *et al.* Applications of Long-Length Carbon Nano-Tube (L-CNT) as Conductive Materials in High Energy Density Pouch Type Lithium Ion Batteries. *Polymers* **12**, 1471 (2020).
9. Zhou, Y. *et al.* Preparation and Electrochemical Properties of Multicomponent Conductive-Nanocarbon Additives for LFP Battery. *NANO* **15**, 2050093 (2020).

10. Yin, S. *et al.* Si/Ag/C Nanohybrids with in Situ Incorporation of Super-Small Silver Nanoparticles: Tiny Amount, Huge Impact. *ACS Nano* **12**, 861–875 (2018).
11. Sing, K. S. W. Reporting physisorption data for gas/solid systems with special reference to the determination of surface area and porosity (Recommendations 1984). *Pure Appl. Chem.* **57**, 603–619 (1985).
12. Lee, J.-S. *et al.* Ketjenblack Carbon Supported Amorphous Manganese Oxides Nanowires as Highly Efficient Electrocatalyst for Oxygen Reduction Reaction in Alkaline Solutions. *Nano Lett.* **11**, 5362–5366 (2011).
13. Lee, J.-S., Park, G. S., Kim, S. T., Liu, M. & Cho, J. A Highly Efficient Electrocatalyst for the Oxygen Reduction Reaction: N-Doped Ketjenblack Incorporated into Fe/Fe<sub>3</sub>C-Functionalized Melamine Foam. *Angewandte Chemie International Edition* **52**, 1026–1030 (2013).
14. Kuroda, S., Tabori, N., Sakuraba, M. & Sato, Y. Charge–discharge properties of a cathode prepared with ketjen black as the electro-conductive additive in lithium ion batteries. *Journal of Power Sources* **119–121**, 924–928 (2003).
15. Xiao, Q., Zhang, J., Xiao, C., Si, Z. & Tan, X. Solar photocatalytic degradation of methylene blue in carbon-doped TiO<sub>2</sub> nanoparticles suspension. *Solar Energy* **82**, 706–713 (2008).
16. Sidor, K. *et al.* Tailoring Properties of Resol Resin-Derived Spherical Carbons for Adsorption of Phenol from Aqueous Solution. *Molecules* **26**, 1736 (2021).
17. Liu, W. *et al.* Oxidative dehydrogenation on nanocarbon: Effect of heteroatom doping. *Applied Catalysis B: Environmental* **258**, 117982 (2019).

18. Li, J. *et al.* Improving the Alkene Selectivity of Nanocarbon-Catalyzed Oxidative Dehydrogenation of n-Butane by Refinement of Oxygen Species. *ACS Catal.* **7**, 7305–7311 (2017).
19. Hettler, S. *et al.* In-situ reduction by Joule heating and measurement of electrical conductivity of graphene oxide in a transmission electron microscope. *2D Mater.* **8**, 031001 (2021).
20. Li, P., Hwang, J.-Y. & Sun, Y.-K. Nano/Microstructured Silicon–Graphite Composite Anode for High-Energy-Density Li-Ion Battery. *ACS Nano* **13**, 2624–2633 (2019).
21. Zhang, C. *et al.* 3D Porous Silicon/N-Doped Carbon Composite Derived from Bamboo Charcoal as High-Performance Anode Material for Lithium-Ion Batteries. *ACS Sustainable Chem. Eng.* **6**, 9930–9939 (2018).
22. Feng, X. *et al.* Untangling the respective effects of heteroatom-doped carbon materials in batteries, supercapacitors and the ORR to design high performance materials. *Energy Environ. Sci.* **14**, 2036–2089 (2021).
23. Cao, C. *et al.* Solid Electrolyte Interphase on Native Oxide-Terminated Silicon Anodes for Li-Ion Batteries. *Joule* **3**, 762–781 (2019).
24. Cao, Z., Yang, Y., Qin, J., He, J. & Su, Z. Co<sub>3</sub>O<sub>4</sub> Polyhedron@MnO<sub>2</sub> Nanotube Composite as Anode for High-Performance Lithium-Ion Batteries. *Small* **17**, 2008165 (2021).
25. Sun, B. *et al.* Synergistic engineering of defects and architecture in Co<sub>3</sub>O<sub>4</sub>@C nanosheets toward Li/Na ion batteries with enhanced pseudocapacitances. *Nano Energy* **78**, 105366 (2020).
26. Ni, L. *et al.* In situ visualizing the interplay between the separator and potassium dendrite growth by synchrotron X-ray tomography. *Nano Energy* **83**, 105841 (2021).

27. Lee, S. H., Huang, C., Johnston, C. & Grant, P. S. Spray printing and optimization of anodes and cathodes for high performance Li-Ion batteries. *Electrochimica Acta* **292**, 546–557 (2018).
28. Wu, Z.-S. *et al.* Graphene/metal oxide composite electrode materials for energy storage. *Nano Energy* **1**, 107–131 (2012).
29. Agyeman, D. A., Song, K., Lee, G.-H., Park, M. & Kang, Y.-M. Carbon-Coated Si Nanoparticles Anchored between Reduced Graphene Oxides as an Extremely Reversible Anode Material for High Energy-Density Li-Ion Battery. *Advanced Energy Materials* **6**, 1600904 (2016).
30. Kucinskis, G., Bajars, G. & Kleperis, J. Graphene in lithium ion battery cathode materials: A review. *Journal of Power Sources* **240**, 66–79 (2013).
31. Eliseeva, S. N., Apraksin, R. V., Tolstopjatova, E. G. & Kondratiev, V. V. Electrochemical impedance spectroscopy characterization of LiFePO<sub>4</sub> cathode material with carboxymethylcellulose and poly-3,4-ethylenedioxythiophene/polystyrene sulfonate. *Electrochimica Acta* **227**, 357–366 (2017).
32. Fan, X. *et al.* PEDOT:PSS for Flexible and Stretchable Electronics: Modifications, Strategies, and Applications. *Advanced Science* **6**, 1900813 (2019).
33. Che, Y. *et al.* Review of carbon nanotube nanoelectronics and macroelectronics. *Semicond. Sci. Technol.* **29**, 073001 (2014).

# Chapter 2: Atomic Layered Deposition of Aluminium Oxide for stabilizing $\text{LiNi}_{0.5}\text{Co}_{0.2}\text{Mn}_{0.3}\text{O}_2$ cathode in Lithium-ion Batteries

Results presented in this chapter were obtained in collaboration with the group of Prof. Yajun Cheng in Ningbo Institute of technology and engineering.

## 2.1 Introduction to Atomic Layer Deposition

The term Atomic layer deposition (ALD) was introduced back in 2000; before that, ALD was referred to as atomic layer epitaxy (ALE). The history of ALE started in Finland in 1974, with the pioneer work of Tuomo Suntola. Six years later, the first scientific literature report on ALE was published<sup>1,2</sup>.

ALD is a subtype of chemical vapour deposition (CVD), where the substrate is exposed sequentially to reagents -usually a metal precursor and an oxidizer- leading to thin film growth by self-limited surface reactions<sup>3</sup>. Figure 4.1 depicts the mechanism of  $\text{Al}_2\text{O}_3$  film growth by ALD, using trimethylaluminium(III) and water as precursors. Where, the first step of the process consists of a reaction between the surface of the substrate and the saturated precursor, usually an organometallic complex. The organometallic will chemisorb on the substrate's surface reactive sites. Theoretically, all the surface reactive sites are saturated with the precursor, self-limiting the growth of the film to a monolayer. In practice, not all surface active sites are accessible to sterically hindered organometallic precursors, leading to some inhomogeneity. The second step consists of the purge of the excess precursor with inert gas, yielding an organometallic covered surface. For the next step, the second precursor -usually an oxidant- will be pulsed in the chamber to react with the first one, forming the desired layered product. The final step is another purge to flush all remaining unreacted species and unwanted by-products.

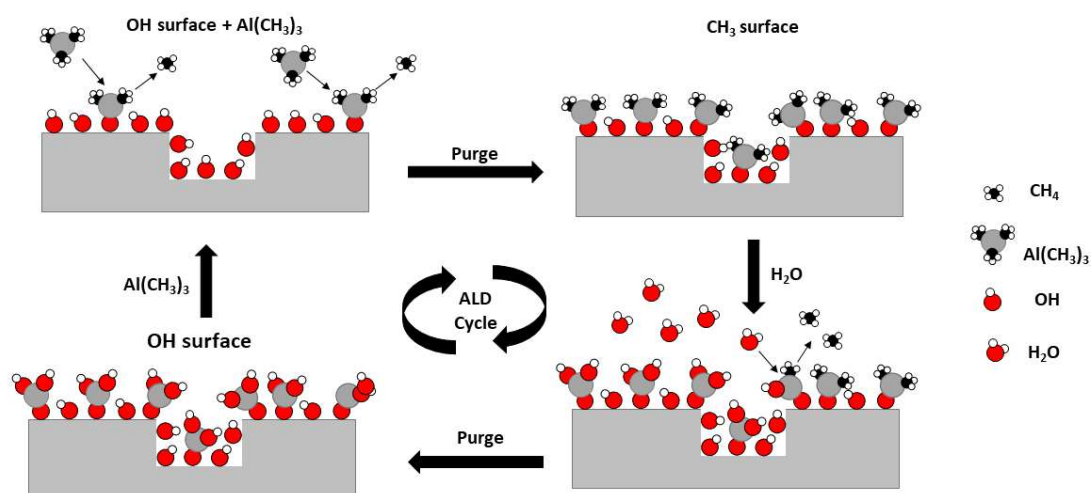


**Figure 4-1.** Sequence for  $\text{Al}_2\text{O}_3$  deposition by ALD

Combined, the four steps make an ALD cycle that can be repeated for a layer by layer film growth. Keeping consistent ALD parameters, precursors and conditions, the ALD cycles occur via saturated coverage steps, yielding a film thickness growth consistent with each cycle. A growth per cycle (GPC) rate can be calculated accordingly. Moreover, as the ALD process is performed under vacuum (around 1mbar), the carrying inert gas (in our case  $\text{N}_2$ ) is in the viscous flow regime. In this regime, the gas can easily carry the reactants to the reactive surface and through its pores, as well as carry away any stagnant unreacted molecules, during the gas purge steps. ALD therefore permits the layered formation of high-aspect ratio nanostructures in an entirely tuneable fashion<sup>3</sup>. Additionally, ALD permits precise composition control. By tailoring ALD cycles for different inorganic precursors, "super cycles" which are composed of multiple ALD processes (one for each different inorganic precursors) generate mixed layered composition, such as zinc tin oxide (ZTO)<sup>4</sup> and strontium titanate ( $\text{SrTiO}_3$ )<sup>5</sup> and many more<sup>6,7</sup>. Thus, it is not yet possible to grow every material by ALD. Reactants and oxidants that will generate the desired layered material must be available or synthesizable. Depending on the element the choice of reactant might be very



limited or non-existent, as it should exist in a gas phase at moderate temperatures (25-350°C). It is important to consider that neither the reactant nor its by-products generated from surface reactions should damage nor dissolve the deposited film, the substrate nor the ALD deposition chamber.

Thanks to the above-mentioned advantages of using ALD to deposit thin and uniform films, it is widely used in microelectronics and energy industries. As the application range of ALD is vast, and that is why it has become a popular tool to develop nano-coatings and thin films in industry. One of the most popular applications of ALD is in the deposition of thin-films in the semi-conductor manufacturing industry, where with each year, components are being miniaturized and consistent and repeatable film-coating in accordance with the high standard of performance for consumer electronics is needed. Recently, the industrial transistor fabrication, research and development utilizes ALD to deposit pinhole-free conformal thin films with a high degree of precision over thickness and dielectric constants<sup>8,9</sup>. Industrial ALD's importance greatly improved in regards to reducing the power consumption and increasing the speed of devices, by increasing the electron and hole mobility with next-generation transistors<sup>10,11</sup>.

ALD is also employed in the field of photovoltaics<sup>12</sup>, for the deposition of rear contact passivating layers<sup>13</sup>, tuning the electrode work function in organic solar cells<sup>14</sup>, or as a barrier to prevent electron-hole recombination in the field of dye sensitized solar cells<sup>15</sup>.

ALD also presents advantages for the generation of nanostructured electrodes and interface engineering resulting in (1) reduction of unwanted side reactions at the SEI<sup>16</sup>, (2) enhanced cyclic stability and (3) higher stability at high discharge rates (C), (4) overall increase safety<sup>17,18</sup>. Notably, ALD was extensively explored for the stabilization of Si-anodes

in LIB, aiming at drastic volume expansion during cycling and continuous unstable SEI formation<sup>19–21</sup>. Aluminum oxide ( $\text{Al}_2\text{O}_3$ ) deposited by ALD directly on lithium metal increased the battery performances, durability, and safety as air-exposed Li metal was stable with only 14nm of layered aluminium oxide deposited. In 2011, Liu *et al.*<sup>22</sup> studied the (de)lithiation of 4-5nm  $\text{Al}_2\text{O}_3$  surface layers deposited on aluminium nanowires by in-situ transmission electron microscopy. They reported the formation of stable Li-Al-O glass tubes with a thickness of 6-10nm (volume expansion of 100%) through elastic and plastic deformation, generating a mechanically robust solid electrolyte with exceptional ion conduction, while causing  $\text{Li}^+$  loss.

Since the potentials of  $\text{LiC}_6$  and Si anode materials are nearing that of lithium metal, further improvement to lower the anode potentials are extremely difficult. To further increase the voltage of the LIB to around 5V, cathode materials such as  $\text{LiNi}_{0.5}\text{Mn}_{1.5}\text{O}_4$  and  $\text{LiCoMnPO}_4$  are explored<sup>23</sup>. In particular layered  $\text{LiNi}_{0.5}\text{Co}_{0.2}\text{Mn}_{0.3}\text{O}_2$  (NCM523) is a promising high energy candidate due to its high capacity at high voltages and good electrochemical stability<sup>24–26</sup>. NMC-based cathodes can be produced at low cost<sup>27</sup> and benefit from incorporating three transition metals: cobalt (Co) and manganese (Mn) offering a layered structure and good structural integrity, and nickel (Ni) providing high specific capacities. However, the low stability of electrolytes at cell voltages higher than 4.4V diminishes their commercial application, and solutions need to be implemented to cope with the undesired side reactions<sup>28–30</sup>.

In this chapter, ultrathin  $\text{Al}_2\text{O}_3$  films were deposited by conventional ALD on  $\text{LiNi}_{0.5}\text{Co}_{0.2}\text{Mn}_{0.3}\text{O}_2$  (NCM523) cathode material for high voltage (4.3-4.6V) applications, displaying superior cyclability and overall performances.

## 2.2 ALD Principle and Set-up

The atomic layer deposition system used in this chapter was custom built. The setup is composed of a tubular heating chamber heated by an electrical resistance brand wrapping (Fig.4.2), a block manifold, a turbine pump, a pressure sensor and control panel using LabView. Different precursors can be loaded in impervious cylinders that attach to the block manifold. Two gas lines go through the block manifold, carrying the precursor's vapours to the vacuum chamber. The block manifold is composed of pneumatic valves that are controlled electronically with a high degree of precision. Indeed, the pulse length of each precursor can be controlled by the amount of time where the valve is opened. Both the block and the cylinders can be heated independently to desired temperatures by electrical resistance brand wrapping and heated jacket respectively. The carrying gas, here  $N_2$ , can be controlled by mass-flow, transporting the precursor vapour to the deposition chamber through lines ending with showerhead tubes, enabling delivery directly on top of the substrate. A pressure sensor is connected to the deposition chamber in order to precisely monitor the difference in pressure inside the chamber for each peak pulse of the precursor. All precursors and desired parameters, such as the nitrogen flow, the temperature of the chamber, the block, and the precursor cylinders; as well as the pump speed or the length of valve actuation are controlled by a centralized panel using a custom software coded with the LabView software. The software was modified in order to allow fast opening and closing of the valves while isolating the chamber from the pump, allowing for longer exposure time of the substrate to the precursors. Finally, an additional function was added to the software to monitor the status of the valve, as they can get clogged with precursors with repeated usage.

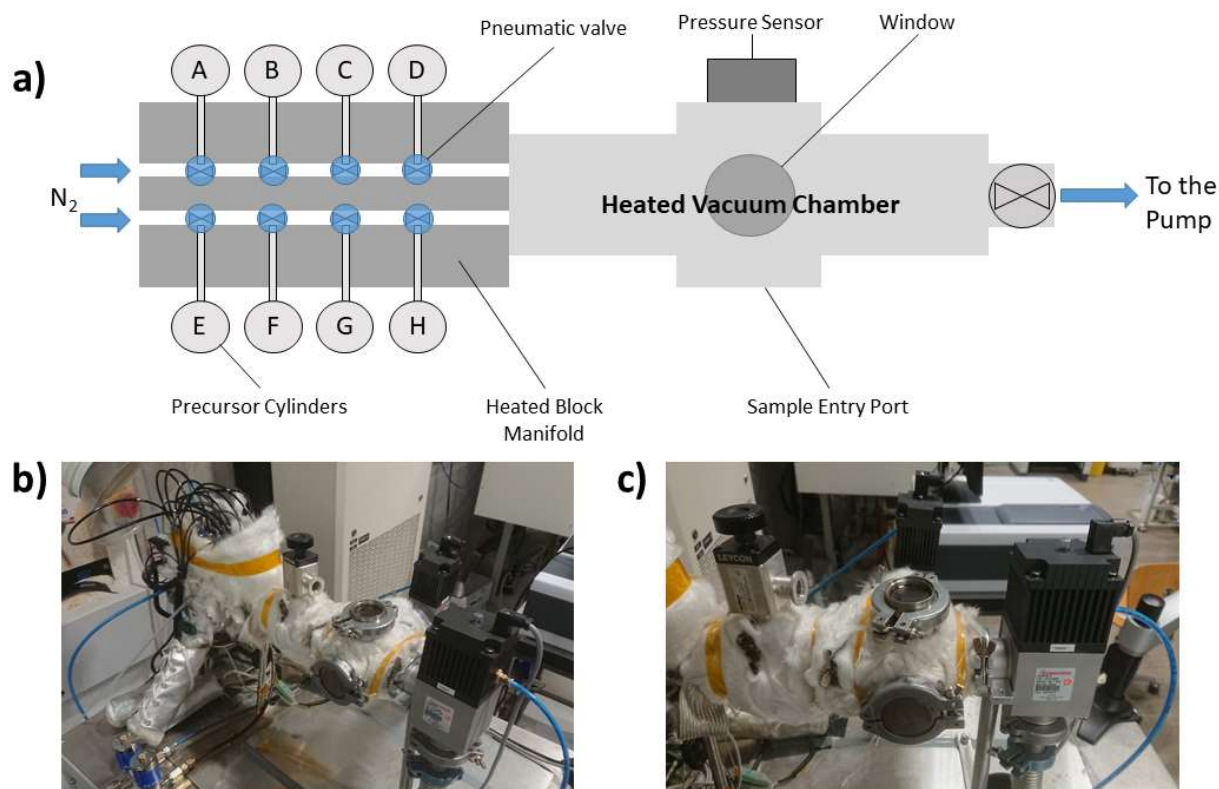


**Figure 4-2.** a) Schematic top-view representation of the ALD set-up, b) Picture of the overall system and, c) Glass wool covered vacuum chamber.

## 2.3 Results:

### 2.3.1 Calibration

Using this setup, thin homogeneous films of  $Al_2O_3$  were obtained. This metal oxide was obtained by oxidizing a low-boiling point organometallic precursor with hydrogen peroxide ( $H_2O_2$ ) as oxidant. The growth per cycle (GPC) using our custom ALD setup was calculated by scanning electron microscopy and X-ray photoelectron spectroscopy. The conditions used for the formation of aluminium oxide are summarized in Table 4.1.

**Table 4-1.** Conditions used and calculated growth per cycle (GPC) rate for Al<sub>2</sub>O<sub>3</sub> deposition

Material	Metal Precursor	Abbreviation	Metal Temperature [°C]	Oxidant	Oxidant Temperature [°C]	Chamber Temperature [°C]	GPC from XPS [nm/cycle]
Al <sub>2</sub> O <sub>3</sub>	Trimethylaluminium(III)	TMA	30	30% H <sub>2</sub> O <sub>2</sub>	30	120	0.236

In order to determine the thickness of the obtained film two different characterization techniques were used. At first, 400 Al<sub>2</sub>O<sub>3</sub> ALD cycles were deposited on a clean Si (100) wafer substrate, which was cut using a diamond blade, and the cross section was analysed by SEM (Fig.4-3 e)). Height measurements at three independent areas of two separate wafers were performed and the GPC was obtained from the average of these six measurements. The surface of the wafer was found to have some small inhomogeneity of deposition, which was attributed to the accumulation of small imperfections in the deposition with increasing cycle number. The average GPC was calculated to be at 0.19nm.cycle<sup>-1</sup>.

Additionally, four samples were 26, 79, 158 and 316 Al<sub>2</sub>O<sub>3</sub> ALD cycles were deposited on clean Si (100) wafers and the depth profile of the deposition was analysed by XPS sputtering. An argon ion (Ar<sup>+</sup>) beam at 2kV was shoot on a 4×4mm<sup>2</sup> surface at a sputtering speed of 2.7nm.min<sup>-1</sup>, etching in a layer-by-layer fashion the deposited material, and revealing the subsurface composition in function of depth (Fig.4-3 a), b), c) and d). XPS profiling provides quantified information on each analyzed layer. Before removing material from the sample area, an XPS spectrum is acquired, and then the ion beam etches the squared surface, then another XPS spectrum is recorded. This process was repeated until the signal for Al2p faded until disappearing, while the Si2p increased. The results of the atomic composition obtained

by in-depth XPS sputtering are displayed in Fig.4-3 a), b), c), and d). GPC of  $0.236\text{nm}\cdot\text{cycle}^{-1}$  was calculated from the depth profile and is reported in Fig.4-3 f).

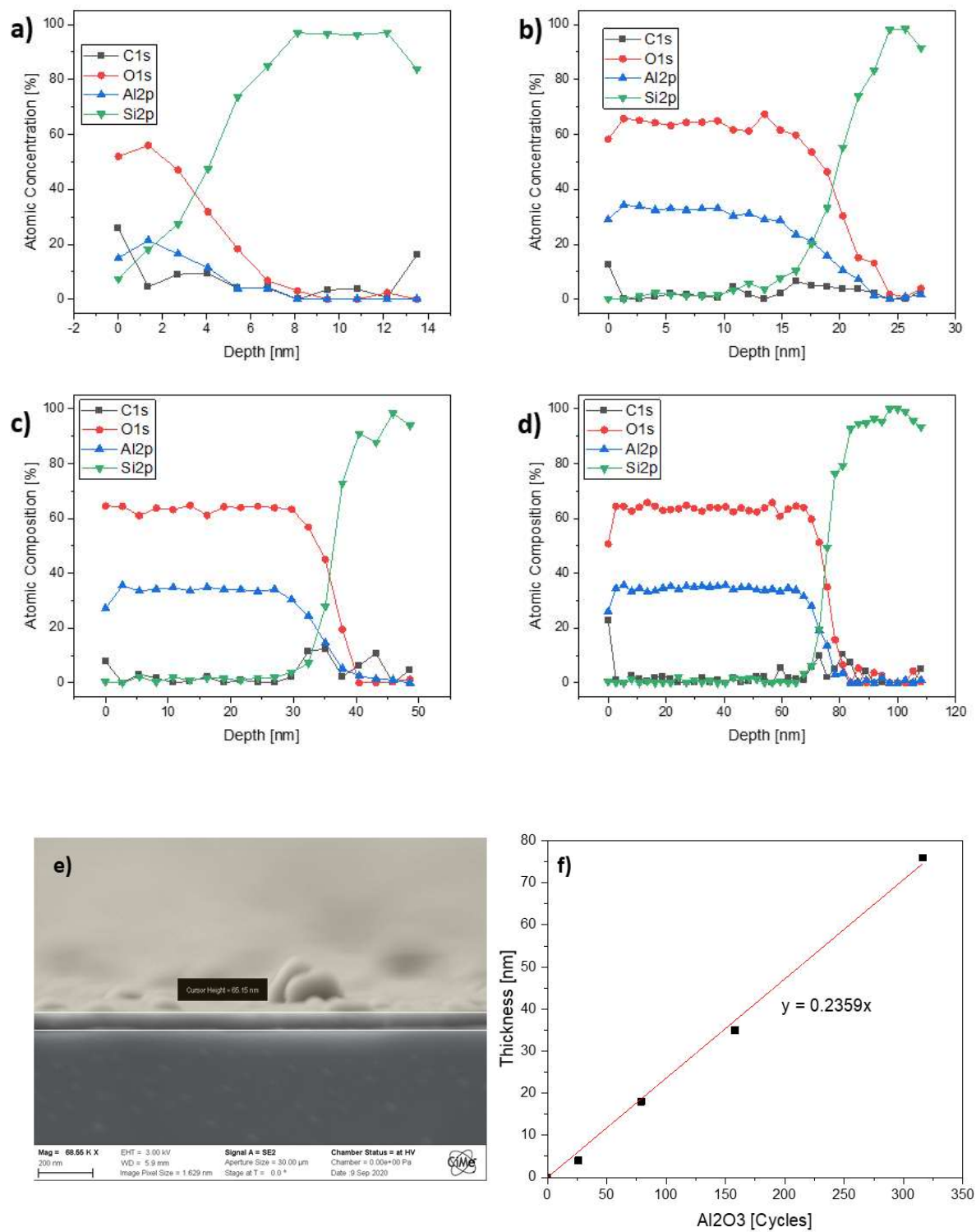


**Figure 4-3.** Atomic concentration of C, O, Al, and Si for a) 26, b) 79, c) 158 and d) 316  $\text{Al}_2\text{O}_3$  ALD cycles; e) SEM image of 400  $\text{Al}_2\text{O}_3$  ALD cycles; f) Growth per cycle rate of  $\text{Al}_2\text{O}_3$  deposited on Si (100) wafer substrate.

### 2.3.2 Electrochemical Performances

Aluminium foil coated with NCM523 cathode material were sent to us by our collaborator in China, Prof. Yajun Cheng and his group, and were subjected to different  $\text{Al}_2\text{O}_3$  ALD coating here in Lausanne. Other samples, such as NCM811 and  $\text{TiNbO}_4$ , were also subjected to  $\text{Al}_2\text{O}_3$  or  $\text{TiO}_2$  coatings and are undergoing long-term cyclability tests.

The pristine NCM523 electrodes were placed in the reaction chamber. Pre-pumping and heating of the chamber and block manifold until reaching  $<0.04\text{mbar}$ ,  $130^\circ\text{C}$  and  $50^\circ\text{C}$ , respectively. TMA and  $\text{H}_2\text{O}_2$  precursors were heated at  $30^\circ\text{C}$ , then the  $\text{N}_2$  flow rate was adjusted to  $20\text{mL}\cdot\text{min}^{-1}$ , yielding a background pressure of  $0.17\text{-}0.20\text{mbar}$ . Then, the ALD  $\text{Al}_2\text{O}_3$  reaction cycle was decoupled in the following steps: (1) 10s of pumping time, (2) 0.1s TMA pulse, (3) purging the chamber with the pure nitrogen flow for 15s, which was enough to attain the background pressure and remove by-products, (4) 0.5s  $\text{H}_2\text{O}_2$  pulse, (5) purging the chamber with the pure nitrogen flow for 15s, which was enough to attain the background pressure and remove by-products. This sequence constitutes an ALD cycle. 2, 4, 6, 8, 10 ALD cycles were performed on five similar electrodes before being shipped to Ningbo for further testing. The samples were denoted as NCM523- $\text{Al}_2\text{O}_3$ -(X), where X is the number of ALD cycles.

For electrochemical measurements, CR-2032-type coin cells were manufactured in dry-Ar glovebox ( $\text{H}_2\text{O}$  and  $\text{O}_2$  lesser than 1ppm), within which NCM523 (cathode), lithium foil (anode) and Celgard-2400 (separator) were used. The electrolyte was composed of 1M

LiPF<sub>6</sub> salt dissolved in a mixture of ethylene carbonate (EC) and dimethyl carbonate (DMC) with the volume ratio of 3:7, respectively.

The rate performance was measured at the current density sequence of 0.1 C, 0.2 C, 0.5 C, 1.0 C, 2.0 C, 5.0 C, 0.2 C and 1.0 C in the voltage range between 4.3 V and 4.6 V (vs. Li/Li<sup>+</sup>) (five cycles at each current density, 1.0 C = 170 mAh g<sup>-1</sup>). Galvanostatic charge/discharge tests were carried out at room temperature, varying the voltage between 4.3V and 4.6 V. The current density was set at 0.2 C for the initial three cycles and 1.0 C thereafter for the remaining cycles. The specific capacity was calculated on the basis of the active material only.

The results of obtained rate performances are displayed in Figure 4-4 a-e). The estimated thickness for 2, 4, 6, 8 and 10 cycles Al<sub>2</sub>O<sub>3</sub> ALD are estimated at 0.472nm, 0.974nm, 1.416nm, 1.888nm and 2,359nm respectively. Fig4-4 a-e) displays initial specific capacities nearing 180 mAh.g<sup>-1</sup> for the first five cycles in all NCM523-Al<sub>2</sub>O<sub>3</sub>-(X), specifically NCM523-Al<sub>2</sub>O<sub>3</sub>-(2) with 176 mAh.g<sup>-1</sup>, NCM523-Al<sub>2</sub>O<sub>3</sub>-(4) with 176 mAh.g<sup>-1</sup>, NCM523-Al<sub>2</sub>O<sub>3</sub>-(6) with 172 mAh.g<sup>-1</sup>, NCM523-Al<sub>2</sub>O<sub>3</sub>-(8) with 173 mAh.g<sup>-1</sup>, NCM523-Al<sub>2</sub>O<sub>3</sub>-(1) with 173 mAh.g<sup>-1</sup> and pristine with 173 mAh.g<sup>-1</sup>. After 140 cycles at 1.0 C the capacity retention was about 85% for NCM523-Al<sub>2</sub>O<sub>3</sub>-(X) samples, and just above 75% for pristine. NCM523-Al<sub>2</sub>O<sub>3</sub>-(4), NCM523-Al<sub>2</sub>O<sub>3</sub>-(2) and NCM523-Al<sub>2</sub>O<sub>3</sub>-(10), in this order, presented higher specific capacity retention during the cycling process. For all the NCM523-Al<sub>2</sub>O<sub>3</sub>-(X), the Coulombic efficiency (CE) was >98% after 140 cycles, similar results were found for the pristine sample. During the first five cycles, initial capacity fadings were observed and attributed to irreversible interfacial reactions. The samples present improved specific capacity and Coulombic efficiency compared to pristine NCM523,



indicating that ultra-thin  $\text{Al}_2\text{O}_3$  coatings benefits in cyclability were not detrimental to lowering the overall performances.

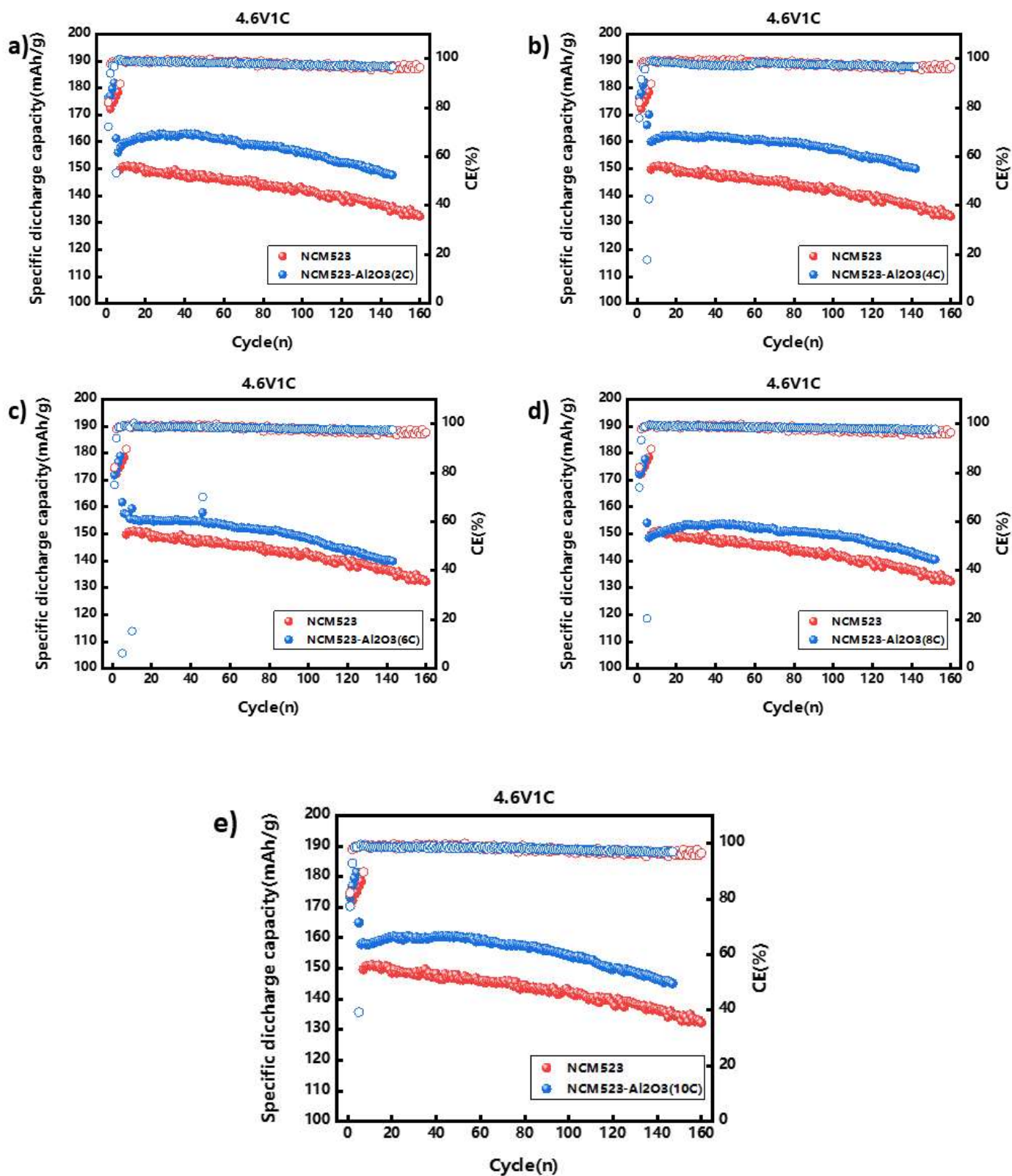


**Figure 4-4.** Capacity retention and Coulombic efficiency for a) NCM523-Al<sub>2</sub>O<sub>3</sub>-(2), b) NCM523-Al<sub>2</sub>O<sub>3</sub>-(4), c) NCM523-Al<sub>2</sub>O<sub>3</sub>-(6), d) NCM523-Al<sub>2</sub>O<sub>3</sub>-(8), e) NCM523-Al<sub>2</sub>O<sub>3</sub>-(10) cycling at 1.0 C.

The results of obtained rate performances are displayed in Figure 4-5 a-e). At 0.1 C, 0.2 C and 0.5 C the pristine displayed a higher specific capacity for the first 5 cycles. At 0.1 C a difference of about 20mAh.g<sup>-1</sup> can be observed for all Al<sub>2</sub>O<sub>3</sub> coated electrodes. At 0.5 C NCM523-Al<sub>2</sub>O<sub>3</sub>-(2), NCM523-Al<sub>2</sub>O<sub>3</sub>-(6), and NCM523-Al<sub>2</sub>O<sub>3</sub>-(10) displayed specific capacity of about 175mAh.g<sup>-1</sup> which is similar than for pristine sample. NCM523-Al<sub>2</sub>O<sub>3</sub>-(4) and NCM523-Al<sub>2</sub>O<sub>3</sub>-(8) displayed specific capacity lower than pristine. At higher current density, 1.0 C and above, all the Al<sub>2</sub>O<sub>3</sub> coated samples displayed higher specific capacity than the pristine NCM523. At 5.0 C the difference in specific capacity is large, especially for NCM523-Al<sub>2</sub>O<sub>3</sub>-(6) and NCM523-Al<sub>2</sub>O<sub>3</sub>-(10) that display an increase of about 20 mAh.g<sup>-1</sup> and 35 mAh.g<sup>-1</sup> compared to uncoated NCM523, respectively. Additionally, NCM523-Al<sub>2</sub>O<sub>3</sub>-(6) and NCM523-Al<sub>2</sub>O<sub>3</sub>-(10) displayed higher recovered specific capacity at 1.0 C for the last 35 charge-discharge cycles. The specific capacity retained for the last 35 cycles at 1.0 C was comparable to the obtained value of about 150mAh.g<sup>-1</sup> for the cycles 15 to 20 performed at 1.0 C as well, as for the pristine sample the specific capacity had decreased. NCM523-Al<sub>2</sub>O<sub>3</sub>-(2) and NCM523-Al<sub>2</sub>O<sub>3</sub>-(4) displayed similar recovered performance as pristine for 35 cycles at 1.0 C, and NCM523-Al<sub>2</sub>O<sub>3</sub>-(8) poorer performance for the last 25 cycles at 1.0 C. At high current densities for these samples, the kinetics of (de)lithiation gave rise to lower specific capacity due to irreversible interfacial modifications within the cathode interface.

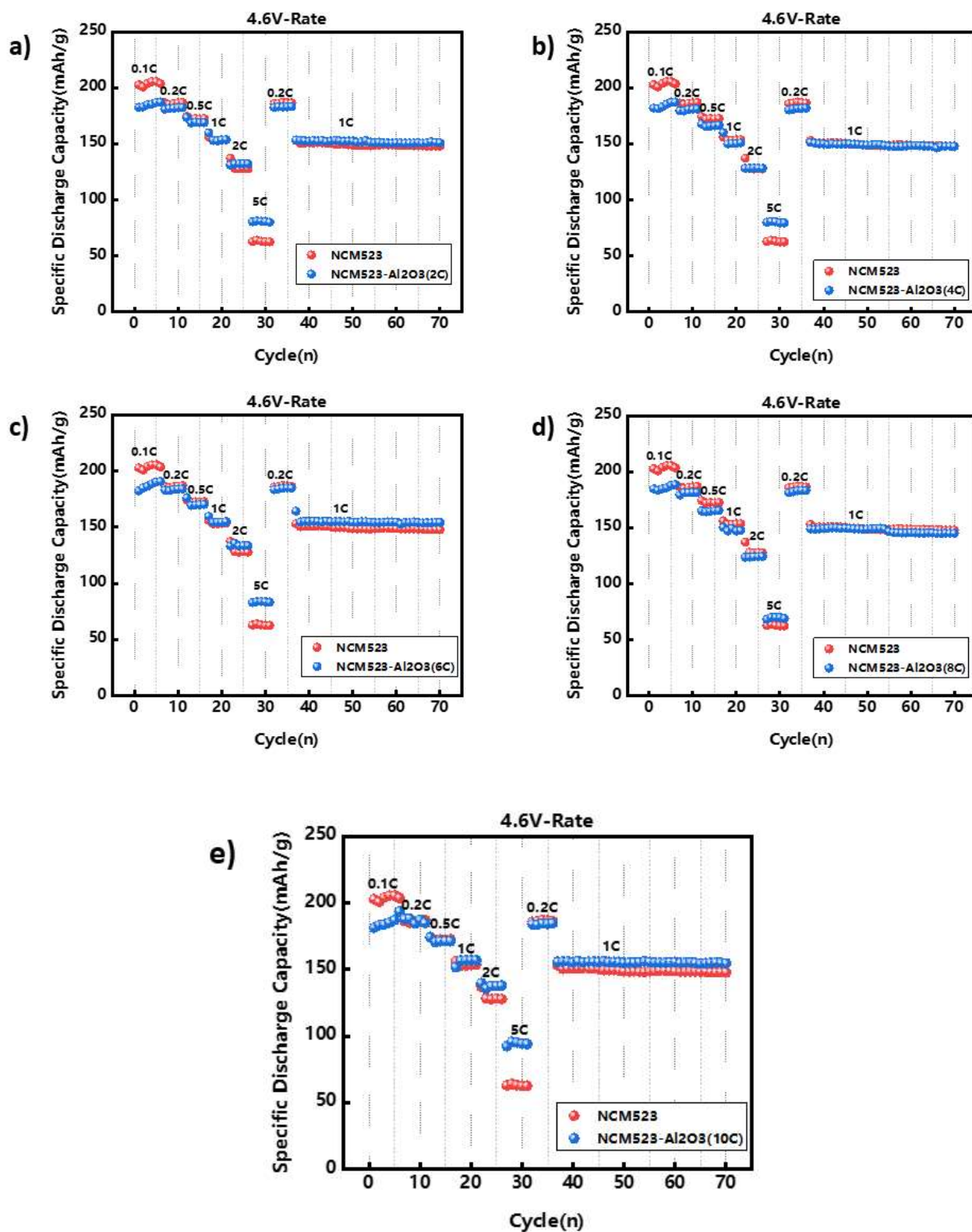


**Figure 4-5.** Rate performance of a) NCM523-Al<sub>2</sub>O<sub>3</sub>-(2), b) NCM523-Al<sub>2</sub>O<sub>3</sub>-(4), c) NCM523-Al<sub>2</sub>O<sub>3</sub>-(6), d) NCM523-Al<sub>2</sub>O<sub>3</sub>-(8), e) NCM523-Al<sub>2</sub>O<sub>3</sub>-(10) at various current densities from 0.1 to 5.0 C.

## 2.4 Discussion

Upon manufacturing and storage of NCM cathode material, side reactions with air and moisture take place, leaving contaminating species on the surface of the electrode. Once the battery is assembled, these surface residual species can react with electrolyte, forming insulating materials at the electrode-electrolyte interface. To synthesize Ni-rich layered compounds, an excess amount of lithium is necessary, and residual lithium on the surface of the material reacts with air to form hydroxides (LiOH) and carbonates (Li<sub>2</sub>CO<sub>3</sub>)<sup>31,32</sup>.

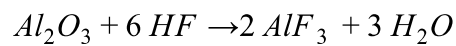
Additionally, upon charge (delithiation), highly reactive Ni<sup>4+</sup> species are formed which can react and accelerate the decomposition of the electrolyte, resulting in the formation of a thick solid-state electrolyte resistive interface. The compounds formed depend on the electrolyte composition. At high voltages, the reactive Ni<sup>4+</sup> can cause formation of highly reactive oxygen<sup>33</sup> species and CO<sub>2</sub> evolution from electrolyte decomposition<sup>34</sup>, which increases the pressure inside the battery leading to serious safety issues<sup>35</sup>.

The observed initial capacity loss in the first charge-discharge cycles is debated (Fig.4-4 a-e)), some account it to parasitic irreversible surface reactions, which increases with higher manganese content<sup>36</sup>. Others believe it is due to the formation of an over-lithiated Li<sub>2</sub>MO<sub>2</sub> phase with slow lithium diffusion kinetics, which is a reversible process upon discharge at low potentials (<2.0V)<sup>37</sup>.

Using Ni-rich cathode materials, capacity and voltage gradually fade, which is believed to arise from layered structure disordering. Upon charge-discharge cycles, partial reduction of transition metals causes local structure changes of this interlayer space<sup>38</sup>, due to the migration of the transition-metal layer to the lithium layer<sup>39</sup>. This cation migration is referred to as the cation mixing<sup>40</sup>, which leads to the formation of cracks<sup>41</sup> in the cathode

material followed by NCM dissolution and degradation<sup>42,43</sup>. Therefore, sub-nanometer ultra-thin coatings are desirable, as they can reduce the mechanical stress caused upon cation mixing and efficiently reduce detrimental surface reactions<sup>44</sup>.

Also, LiPF<sub>6</sub>, the dominant lithium salt in LIB, decomposes in the presence of moisture to form a wide range of products, including the highly corrosive HF. Hydrofluoric acid (HF) is believed to be responsible for the dissolution of transition metals and corrosion of the cathode materials<sup>45</sup>. Oxide coatings<sup>46</sup>, and notably Al<sub>2</sub>O<sub>3</sub>, can serve as active HF scavengers<sup>47</sup>, protecting the cathode material by reducing its local acidity such as:



In order to clarify which combination of the aboved-listed advantages of ultra-thin Al<sub>2</sub>O<sub>3</sub> coating leads to improved cyclability and specific capacity at high current densities (1.0 C and above), *operando* analysis techniques such as: elemental analysis, such as EDX mapping can help unravel the chemical overall chemical composition. *Operando* XPS and X-ray absorption spectroscopy (XAS) for the formation of the SEI and associated valence changes and oxidation states of the transition metals. *Operando* XRD to monitor the crystal structure changes upon charge-discharge cycles, monitoring for potential dependent (ir)reversible changes in the layered crystal structure. SEM and TEM techniques for the microscopic structure of the material and plausible damage to it from cation mixing and cracking.

## 2.5 Conclusion

Sub and nanometer thick  $\text{Al}_2\text{O}_3$  coatings on NCM523 cathodes were successfully deposited thanks to our homemade ALD apparatus. Prepared samples were tested for their rate performances and specific capacities within a high voltage window, between 4.3V and 4.6 V.

In summary, NCM523- $\text{Al}_2\text{O}_3$ -(6) and NCM523- $\text{Al}_2\text{O}_3$ -(10) were the most promising samples for enhanced high-voltage cycling, with estimated  $\text{Al}_2\text{O}_3$  thickness of 1.416 nm and 2,359 nm, respectively. At low current densities, 0.1 C to 0.5 C, the pristine sample displayed higher specific capacity compared to coated samples. At high current density, 1.0 C and above, all the  $\text{Al}_2\text{O}_3$  coating was beneficial, displaying higher specific capacity than the pristine NCM523. At 5.0 C the difference in specific capacity was the largest, where NCM523- $\text{Al}_2\text{O}_3$ -(6) and NCM523- $\text{Al}_2\text{O}_3$ -(10) displayed an increase of about 20  $\text{mAh.g}^{-1}$  and 35  $\text{mAh.g}^{-1}$  compared to uncoated NCM523, respectively. On-going electrochemical and material characterizations will soon help unravel the mechanism behind the performance enhancement. ALD-deposited  $\text{Al}_2\text{O}_3$ , were also previously reported to retard interfacial reactions between  $\text{LiNi}_{0.5}\text{Mn}_{0.3}\text{Co}_{0.2}\text{O}_2$  and electrolyte<sup>48</sup>.

Fast charging devices (high current densities) are essential for the implementation of electric vehicles, for greener mobility solutions in a Hydrogen economy<sup>49,50</sup>. Ultra-thin oxides by ALD deposition may represent an efficient and scalable way to tackle some of the drawbacks entitled to high-voltage cathode materials.

## 2.6 Experimental Section

### 2.6.1 Deposition procedure

#### *Determination of GPC*

All reagents were obtained commercially and used without any further purification. In order to calibrate the GPC of  $\text{Al}_2\text{O}_3$ , deposition on mirror polished Si (100) wafer substrates was done. The Si(100) wafers were first thoroughly cleaned with acetone in order to remove any organic contamination, before being dried in air. Measurements of layer thickness were done by cross section SEM. For each sample, the thickness was measured at least three different positions of the cross section and the average of these measurements was taken as the thickness of the material layer. The layer deposition measurements were made using ImageJ.

#### *$\text{Al}_2\text{O}_3$ deposition protocols*

Trimethylaluminium (TMA, 98 %, Strem) and hydrogen peroxide ( $\text{H}_2\text{O}_2$ , 30 wt.% in water, Sigma Aldrich) were used as Al and O precursors, respectively. All precursors were loaded in stainless steel cylinders. TMA and  $\text{H}_2\text{O}_2$  were heated to 30°C prior to deposition. The deposition sequences were as followed for the  $\text{Al}_2\text{O}_3$  deposition: (1) 10s nitrogen purge (flow of  $20\text{ml}\cdot\text{min}^{-1}$ ), (2) TMA pulse of 0.1 s, followed by (3) a 15 s nitrogen purge (flow of  $20\text{ml}\cdot\text{min}^{-1}$ ), followed by (4) a  $\text{H}_2\text{O}_2$  pulse of 0.5 s and by (5) a 15 s nitrogen purge (flow of  $20\text{ml}\cdot\text{min}^{-1}$ ) were used. The vacuum chamber was held at 130°C, and the block manifold at 50°C. Steps (1)-(5) represent one ALD cycle.

#### *Materials*

All chemicals were used as received without further purification. Single crystal  $\text{LiNi}_{0.5}\text{Co}_{0.2}\text{Mn}_{0.3}\text{O}_2$  (NCM 523) was acquired by Ningbo Ronbay New Technology Co., Ltd., China. Poly (vinylidene fluoride) (PVDF) was provided by Solvay. N-methyl-2-pyrrolidone (NMP, 99% purity) was purchased from Aladdin Reagent Co., Ltd., China. Conductive



carbon black (Super P) was acquired from SCM Chem. Shanghai, China. Lithium metal foil (500  $\mu\text{m}$ ) was purchased from Dongguan Shanshan Battery Materials Co., Ltd. The electrolyte solution containing 1.0 M of  $\text{LiPF}_6$  in a solvent mixture of ethylene carbonate (EC) and dimethyl carbonate (DMC) with the volume ratio of 3:7 was acquired from Zhangjiagang Guotai-Huarong Commercial New Material Co., Ltd.

#### *Electrode fabrication and battery assembly*

The cathode slurry was prepared by mixing NCM 523, PVDF and Super P in NMP solvent with mass ratio of 8:1:1. The prepared slurry was stirred for four hours at 600 rpm and then the homogeneously mixed slurry was cast onto aluminium foil, blade coated, and vacuum dried at 80  $^{\circ}\text{C}$  for about 12 h sequentially.

Next, the dried electrode was pressed and punched into circular pieces with a diameter of 14mm (active material loading 5.3  $\text{mg}\cdot\text{cm}^{-2}$ ). After further drying at 80  $^{\circ}\text{C}$  for 4 h, standard Li/NCM523 half-cells were assembled in an argon-filled glovebox. 2032-type coin cells consisting of NCM523 cathode, PP-PE-PP separator (Celgard 2400), lithium foil counter electrode and electrolyte (100  $\mu\text{L}$ ) were assembled in an argon-filled glovebox (MBRAUN,  $\text{H}_2\text{O} \leq 0.1$  ppm,  $\text{O}_2 \leq 0.1$  ppm).

#### *Electrochemical measurements*

The performance was measured on LAND cell test system (Wuhan, China) after the NCM523/Li ion cells were rested for 12 h. Galvanostatic charge/discharge tests at room temperature were carried out with the voltage between 4.3V and 4.6 V. The current density was set at 0.2 C for the initial three cycles and 1.0 C thereafter for the remaining cycles

(1 C = 170 mAh.g<sup>-1</sup>). Regarding the rate performance test, the cells were cycled at 0.1 C, 0.2 C, 0.5 C, 1C, 2 C, 5 C, 0.2 C, and 1.0 C for five charge-discharge cycles each.

## 2.7 References

1. Puurunen, R. L. A Short History of Atomic Layer Deposition: Tuomo Suntola's Atomic Layer Epitaxy. *Chemical Vapor Deposition* **20**, 332–344 (2014).
2. Ahonen, M., Pessa, M. & Suntola, T. A study of ZnTe films grown on glass substrates using an atomic layer evaporation method. *Thin Solid Films* **65**, 301–307 (1980).
3. George, S. M. Atomic Layer Deposition: An Overview. *Chem. Rev.* **110**, 111–131 (2010).
4. Hultqvist, A., Edoff, M. & Törndahl, T. Evaluation of Zn Sn O buffer layers for CuIn<sub>0.5</sub>Ga<sub>0.5</sub>Se<sub>2</sub> solar cells. *Progress in Photovoltaics: Research and Applications* **19**, 478–481 (2011).
5. Kosola, A., Putkonen, M., Johansson, L.-S. & Niinistö, L. Effect of annealing in processing of strontium titanate thin films by ALD. *Applied Surface Science* **211**, 102–112 (2003).
6. Pore, V., Hatanpää, T., Ritala, M. & Leskelä, M. Atomic Layer Deposition of Metal Tellurides and Selenides Using Alkylsilyl Compounds of Tellurium and Selenium. *J. Am. Chem. Soc.* **131**, 3478–3480 (2009).
7. Uusi-Esko, K. & Karppinen, M. Extensive Series of Hexagonal and Orthorhombic RMnO<sub>3</sub> (R = Y, La, Sm, Tb, Yb, Lu) Thin Films by Atomic Layer Deposition. *Chem. Mater.* **23**, 1835–1840 (2011).
8. Mistry, K. *et al.* A 45nm Logic Technology with High-k+Metal Gate Transistors, Strained Silicon, 9 Cu Interconnect Layers, 193nm Dry Patterning, and 100% Pb-free Packaging. in *2007 IEEE International Electron Devices Meeting* 247–250 (2007). doi:10.1109/IEDM.2007.4418914.

9. Auth, C. *et al.* A 22nm high performance and low-power CMOS technology featuring fully-depleted tri-gate transistors, self-aligned contacts and high density MIM capacitors. in *2012 Symposium on VLSI Technology (VLSIT)* 131–132 (2012). doi:10.1109/VLSIT.2012.6242496.
10. Liu, B. *et al.* Germanium Multiple-Gate Field-Effect Transistors Formed on Germanium-on-Insulator Substrate. *IEEE Transactions on Electron Devices* **60**, 1852–1860 (2013).
11. Ye, P. D. Main determinants for III–V metal-oxide-semiconductor field-effect transistors (invited). *Journal of Vacuum Science & Technology A* **26**, 697–704 (2008).
12. Delft, J. A. van, Garcia-Alonso, D. & Kessels, W. M. M. Atomic layer deposition for photovoltaics: applications and prospects for solar cell manufacturing. *Semicond. Sci. Technol.* **27**, 074002 (2012).
13. Benick, J. *et al.* High efficiency n-type Si solar cells on Al<sub>2</sub>O<sub>3</sub>-passivated boron emitters. *Appl. Phys. Lett.* **92**, 253504 (2008).
14. Frankenstein, H., Leng, C. Z., Losego, M. D. & Frey, G. L. Atomic layer deposition of ZnO electron transporting layers directly onto the active layer of organic solar cells. *Organic Electronics* **64**, 37–46 (2019).
15. Palomares, E., Clifford, J. N., Haque, S. A., Lutz, T. & Durrant, J. R. Control of Charge Recombination Dynamics in Dye Sensitized Solar Cells by the Use of Conformally Deposited Metal Oxide Blocking Layers. *J. Am. Chem. Soc.* **125**, 475–482 (2003).
16. Hy, S. *et al.* Stabilizing Nanosized Si Anodes with the Synergetic Usage of Atomic Layer Deposition and Electrolyte Additives for Li-Ion Batteries. *ACS Appl. Mater. Interfaces* **7**, 13801–13807 (2015).

17. Riley, L. A. *et al.* Conformal Surface Coatings to Enable High Volume Expansion Li-Ion Anode Materials. *ChemPhysChem* **11**, 2124–2130 (2010).
18. Jung, Y. S. *et al.* Ultrathin Direct Atomic Layer Deposition on Composite Electrodes for Highly Durable and Safe Li-Ion Batteries. *Advanced Materials* **22**, 2172–2176 (2010).
19. Lotfabad, E. M. *et al.* ALD TiO<sub>2</sub> coated silicon nanowires for lithium ion battery anodes with enhanced cycling stability and coulombic efficiency. *Phys. Chem. Chem. Phys.* **15**, 13646–13657 (2013).
20. Lotfabad, E. M. *et al.* Si nanotubes ALD coated with TiO<sub>2</sub>, TiN or Al<sub>2</sub>O<sub>3</sub> as high performance lithium ion battery anodes. *J. Mater. Chem. A* **2**, 2504–2516 (2014).
21. Kohandehghan, A. *et al.* Silicon nanowire lithium-ion battery anodes with ALD deposited TiN coatings demonstrate a major improvement in cycling performance. *J. Mater. Chem. A* **1**, 12850–12861 (2013).
22. Liu, Y. *et al.* In Situ Transmission Electron Microscopy Observation of Pulverization of Aluminum Nanowires and Evolution of the Thin Surface Al<sub>2</sub>O<sub>3</sub> Layers during Lithiation–Delithiation Cycles. *Nano Lett.* **11**, 4188–4194 (2011).
23. Julien, C. M., Mauger, A., Zaghib, K. & Groult, H. Comparative Issues of Cathode Materials for Li-Ion Batteries. *Inorganics* **2**, 132–154 (2014).
24. Chakraborty, A. *et al.* Layered Cathode Materials for Lithium-Ion Batteries: Review of Computational Studies on LiNi<sub>1-x-y</sub>CoxMnyO<sub>2</sub> and LiNi<sub>1-x-y</sub>CoxAl<sub>y</sub>O<sub>2</sub>. *Chem. Mater.* **32**, 915–952 (2020).
25. Ahn, J. *et al.* Ultrathin ZrO<sub>2</sub> on LiNi<sub>0.5</sub>Mn<sub>0.3</sub>Co<sub>0.2</sub>O<sub>2</sub> electrode surface via atomic layer deposition for high-voltage operation in lithium-ion batteries. *Applied Surface Science* **484**, 701–709 (2019).

26. He, M. *et al.* High Voltage LiNi<sub>0.5</sub>Mn<sub>0.3</sub>Co<sub>0.2</sub>O<sub>2</sub>/Graphite Cell Cycled at 4.6 V with a FEC/HFDEC-Based Electrolyte. *Advanced Energy Materials* **7**, 1700109 (2017).
27. Ahmed, S., Nelson, P. A., Gallagher, K. G., Susarla, N. & Dees, D. W. Cost and energy demand of producing nickel manganese cobalt cathode material for lithium ion batteries. *Journal of Power Sources* **342**, 733–740 (2017).
28. Nagahama, M., Hasegawa, N. & Okada, S. High Voltage Performances of Li<sub>2</sub>NiPO<sub>4</sub>F Cathode with Dinitrile-Based Electrolytes. *J. Electrochem. Soc.* **157**, A748 (2010).
29. Sun, X.-G. & Angell, C. A. New sulfone electrolytes for rechargeable lithium batteries.: Part I. Oligoether-containing sulfones. *Electrochemistry Communications* **7**, 261–266 (2005).
30. Tornheim, A. *et al.* Effect of electrolyte composition on rock salt surface degradation in NMC cathodes during high-voltage potentiostatic holds. *Nano Energy* **55**, 216–225 (2019).
31. Li, J. *et al.* The Impact of Electrolyte Additives and Upper Cut-off Voltage on the Formation of a Rocksalt Surface Layer in LiNi<sub>0.8</sub>Mn<sub>0.1</sub>Co<sub>0.1</sub>O<sub>2</sub> Electrodes. *J. Electrochem. Soc.* **164**, A655 (2017).
32. Li, T. *et al.* Degradation Mechanisms and Mitigation Strategies of Nickel-Rich NMC-Based Lithium-Ion Batteries. *Electrochem. Energ. Rev.* **3**, 43–80 (2020).
33. Wandt, J., Freiberg, A. T. S., Ogrodnik, A. & Gasteiger, H. A. Singlet oxygen evolution from layered transition metal oxide cathode materials and its implications for lithium-ion batteries. *Materials Today* **21**, 825–833 (2018).
34. Hatsukade, T., Schiele, A., Hartmann, P., Brezesinski, T. & Janek, J. Origin of Carbon Dioxide Evolved during Cycling of Nickel-Rich Layered NCM Cathodes. *ACS Appl. Mater. Interfaces* **10**, 38892–38899 (2018).

35. Xiong, D. J. *et al.* Measuring Oxygen Release from Delithiated  $\text{LiNi}_x\text{Mn}_y\text{Co}_{1-x-y}\text{O}_2$  and Its Effects on the Performance of High Voltage Li-Ion Cells. *J. Electrochem. Soc.* **164**, A3025 (2017).
36. Choi, J. & Manthiram, A. Investigation of the Irreversible Capacity Loss in the Layered  $\text{LiNi}_{1/3}\text{Mn}_{1/3}\text{Co}_{1/3}\text{O}_2$  Cathodes. *Electrochem. Solid-State Lett.* **8**, C102 (2005).
37. Kang, S.-H., Abraham, D. P., Yoon, W.-S., Nam, K.-W. & Yang, X.-Q. First-cycle irreversibility of layered Li–Ni–Co–Mn oxide cathode in Li-ion batteries. *Electrochimica Acta* **54**, 684–689 (2008).
38. Sun, H. & Zhao, K. Electronic Structure and Comparative Properties of  $\text{LiNi}_x\text{Mn}_y\text{Co}_z\text{O}_2$  Cathode Materials. *J. Phys. Chem. C* **121**, 6002–6010 (2017).
39. Yan, P., Zheng, J., Zhang, J.-G. & Wang, C. Atomic Resolution Structural and Chemical Imaging Revealing the Sequential Migration of Ni, Co, and Mn upon the Battery Cycling of Layered Cathode. *Nano Lett.* **17**, 3946–3951 (2017).
40. Lee, J. *et al.* Unlocking the Potential of Cation-Disordered Oxides for Rechargeable Lithium Batteries. *Science* **343**, 519–522 (2014).
41. Yan, P. *et al.* Intragranular cracking as a critical barrier for high-voltage usage of layer-structured cathode for lithium-ion batteries. *Nat Commun* **8**, 14101 (2017).
42. Jung, R., Metzger, M., Maglia, F., Stinner, C. & Gasteiger, H. A. Oxygen Release and Its Effect on the Cycling Stability of  $\text{LiNi}_x\text{Mn}_y\text{Co}_z\text{O}_2$  (NMC) Cathode Materials for Li-Ion Batteries. *J. Electrochem. Soc.* **164**, A1361 (2017).
43. Li, J., Downie, L. E., Ma, L., Qiu, W. & Dahn, J. R. Study of the Failure Mechanisms of  $\text{LiNi}_{0.8}\text{Mn}_{0.1}\text{Co}_{0.1}\text{O}_2$  Cathode Material for Lithium Ion Batteries. *J. Electrochem. Soc.* **162**, A1401 (2015).

44. Chen, Z., Qin, Y., Amine, K. & Sun, Y.-K. Role of surface coating on cathode materials for lithium-ion batteries. *J. Mater. Chem.* **20**, 7606–7612 (2010).
45. Zhou, Z.-B., Takeda, M., Fujii, T. & Ue, M. Li [ C 2 F 5 BF 3 ] as an Electrolyte Salt for 4 V Class Lithium-Ion Cells. *J. Electrochem. Soc.* **152**, A351 (2005).
46. Sun, Y.-K., Lee, Y.-S., Yoshio, M. & Amine, K. Synthesis and Electrochemical Properties of ZnO-Coated LiNi<sub>0.5</sub>Mn<sub>1.5</sub>O<sub>4</sub> Spinel as 5 V Cathode Material for Lithium Secondary Batteries. *Electrochem. Solid-State Lett.* **5**, A99 (2002).
47. Liu, J. *et al.* Improving the Performances of LiCoO<sub>2</sub> Cathode Materials by Soaking Nano-Alumina in Commercial Electrolyte. *J. Electrochem. Soc.* **154**, A55 (2006).
48. Su, Y. *et al.* Enhancing the High-Voltage Cycling Performance of LiNi<sub>0.5</sub>Mn<sub>0.3</sub>Co<sub>0.2</sub>O<sub>2</sub> by Retarding Its Interfacial Reaction with an Electrolyte by Atomic-Layer-Deposited Al<sub>2</sub>O<sub>3</sub>. *ACS Appl. Mater. Interfaces* **7**, 25105–25112 (2015).
49. Iturrondobeitia, A. *et al.* Post-Mortem Analysis of Calendar-Aged 16 Ah NMC/Graphite Pouch Cells for EV Application. *ACS Publications*  
<https://pubs.acs.org/doi/full/10.1021/acs.jpcc.7b05416> (2017)  
doi:10.1021/acs.jpcc.7b05416.
50. Xia, Y., Zheng, J., Wang, C. & Gu, M. Designing principle for Ni-rich cathode materials with high energy density for practical applications. *Nano Energy* **49**, 434–452 (2018).



# Conclusion and Outlooks

For the future of humanity, tackling the environmental crisis is urgent. Our energy consumption relying mostly on fossil fuels is still increasing, as well as the population. In order to avoid future conflicts due to massive migrations and food shortages, energetic solutions based on renewable sources are needed urgently. Solutions in the field of water splitting, food production and energy storage are desperately necessary. In this thesis, efforts have been made to study such questions and try to bring answers to them, from the point of view of electrochemistry and energy.

In Chapter 2, the exploration of atomic doping for the development of new electrocatalysts for dinitrogen reduction to ammonia and oxygen evolution in acidic conditions at ambient conditions was investigated.

In the case of dinitrogen reduction, molybdenum single atoms on a nitrogen-doped graphitic support were successfully synthesized and characterized. The ability to synthesize ammonia by Mo single atoms was tested in alkaline media (0.1M KOH), as predicted by several DFT studies. The quantification of ammonia was found to be extremely complicated as nearly everything can be a source of contamination as demonstrated by Andersen *et al.*<sup>1</sup>, leaving expensive isotopic labelling experiments as only direct production for accurate quantification of <sup>15</sup>N-ammonia by <sup>1</sup>H NMR. Unfortunately, sufficient ammonia needs to be produced in order to afford a concentration high enough for the appearance of <sup>15</sup>N-ammonium peaks. Hence, ammonia electrosynthesis is still immature for real-life application -replacing

the Haber-Bosch process in a near future-. This work participated in the worldwide effort to accomplish this achievement, though with moderate success.

Acidic OER is extremely tricky as well, due to the low stability of known catalysts at high oxidative potentials. In this work, earth-abundant metal doping on highly conductive carbon was synthesized by simple wet-impregnation followed by annealing. These catalysts presented moderate activity towards OER and the kinetic insights (Tafel slope) lead to think that other reactions than the desired oxygen evolution were happening, leading in the degradation of the electrocatalysts. The acidic conditions are desired to achieve higher current densities in PEM electrolyzers, facilitating the kinetics of the coupled HER reaction and scale-up of hydrogen production from water.

In Chapter 3, we have learned that the same earth-abundant metal doping on conductive carbon could be used as highly conductive additives to enhance the performances at high current densities of Si/C anodes in lithium-ion batteries. The structure of the electron conductive network plays a significant role in the electrochemical kinetics and rate performances. Cobalt doping of 0.8% by mass was found to be the most beneficial, with an average capacity increase of 180% at 1.5 A.g<sup>-1</sup> (279 mA h g<sup>-1</sup> and 73 mA h g<sup>-1</sup>, for Co-Ox-KJB and KJB, respectively). The metal ion incorporation was found to improve the affinity towards the electrolyte, enhance the desolvation process and increase electron conductivity which, combined, results in an improvement of rate performances. This approach was found to be generalized to several carbon conductive agents (KJB, SuperP), and different metals incorporation (copper, iron and nickel). This performance enhancement -without compromising the gravimetric capacity- is a significant approach for the future development of fast-charging batteries for portable devices and vehicles.

Finally, in Chapter 4 ultrathin films (nanometer scale) of aluminium oxide were deposited on the surface of NMC523 cathode electrodes by atomic layer deposition. This protective layer was found to be beneficial at higher current densities (1.0 C and above) where at 5.0 C NCM523-Al<sub>2</sub>O<sub>3</sub>-(6) and NCM523-Al<sub>2</sub>O<sub>3</sub>-(10) displayed an increase of about 20 mAh.g<sup>-1</sup> and 35 mAh.g<sup>-1</sup> compared to uncoated NCM523, respectively. The mitigation of surface side reactions between lithium species and the electrolyte as well as the prevention of the dissolution of the transition metals (Ni, Co and Mn) was accounted for by the protective oxide layer –again without much impact on the gravimetric density of the electrode-. Indeed, the implementation of higher voltage cathode materials is usually detrimental to the overall safety of the battery, which is a major drawback for successful commercialization.

If we want to limit the predicted global warming to 2 °C by the end of the century (Paris agreement)<sup>2</sup>, a great effort combining academia, industry and politics is urgent. Indeed, we all live in the same boat: "Earth". The disastrous consequences of our careless energy consumption are now to be seen, with the new record temperature of 54.4 °C for the past century, measured in Furnace Creek (California, USA) on the 9<sup>th</sup> of July 2021. Solutions to transition from fossil fuels to more renewable sources of energy exists<sup>3-5</sup>, but geopolitical and economic concerns hinder their implementation. Fossil fuels are depleting and their consumption should be the driving force to create and implement a sustainable Hydrogen Economy.

*"The best energy, is the one that we do not consume [...]"*

Nathalie Kosciusko-Morizet, former French minister of Ecology, 2011.

Overall, this thesis is a small step towards implementation of a sustainable future, but a big step for Albert.



## References

1. Andersen, S. Z. *et al.* A rigorous electrochemical ammonia synthesis protocol with quantitative isotope measurements. *Nature* 1 (2019) doi:10.1038/s41586-019-1260-x.
2. L'Accord de Paris | CCNUCC.  
<https://unfccc.int/fr/processus-et-reunions/l-accord-de-paris/l-accord-de-paris>.
3. Abe, J. O., Popoola, A. P. I., Ajenifuja, E. & Popoola, O. M. Hydrogen energy, economy and storage: Review and recommendation. *International Journal of Hydrogen Energy* **44**, 15072–15086 (2019).
4. Alanne, K. & Cao, S. Zero-energy hydrogen economy (ZEH2E) for buildings and communities including personal mobility. *Renewable and Sustainable Energy Reviews* **71**, 697–711 (2017).
5. Ralon, P. ELECTRICITY STORAGE AND RENEWABLES: COSTS AND MARKETS TO 2030. 16.

# Transcript of Results



Vice-présidence académique  
Service académique

Relevé des résultats (16.08.2021) pour / Statement of results (16.08.2021) for

**Daubry Albert Claude Jean-Pierre**

## Thesis

Programme doctoral : Chimie et génie chimique

Doctoral program: Chemistry and Chemical Engineering

Matricule fédéral : 12-819-548

Federal number

Matières	Forme Forms	Langue enseign. Teaching Language	Session	Note ou (moyenne) Grade or (average)	Crédits ou (Coeff) Credits or (Coeff)	Crédits obtenus Obtained credits	
Thesis							
Program courses					12	12	Réussi Passed
Doctoral courses						11	
Core courses						11	
Challenges and Opportunities in Energy Research	EO	EN	03.2018	R Passed	2	2	
Electrochemistry of metals and semiconductors	E	EN	08.2021	R Passed	2	2	
Hands-on with Research Data Management in Chemistry	TP	EN	01.2021	R Passed	1	1	
Highlights in Energy Research : Characterization of materials for sustainable energy (2)	M	EN	08.2021	R Passed	1	1	
Interfacial Electrochemistry of Metals and Semiconductors for Energy Conversion and Storage 1- Basic concepts	MULTI	EN	07.2018	R Passed	2	2	
Leading research M in Chemical Engineering (1)	M	EN	08.2019	R Passed	1	1	
Leading research M in Chemical Engineering (2)	M	EN	08.2019	R Passed	1	1	
Scientific Writing (EDCH) (1) (Fall)	TP	EN	12.2020	R Passed	1	1	
Other doctoral courses (EDOC)						1	
Scanning electron microscopy techniques (b)	E	EN	07.2020	R Passed	1	1	

# Curriculum Vitae

## Albert DAUBRY

My aim as a young scientist is to lead towards sustainability and efficiency through technology and innovation



### CONTACT INFO



Chemin de l'Union 7  
Prilly, 1008



+41 78 745 90 66



albdaubry@gmail.com



albertdaubry

### LANGUAGES

- ✓ English - C1+
- ✓ French - Langue Maternelle
- ✓ Spanish - A1+
- ✓ German - Notions

### TECHNICAL SKILLS

- ✓ Lab Management
- ✓ Atomic Layer Deposition/Coatings
- ✓ Electrochemical characterization
- ✓ (In)Organic Synthesis
- ✓ X-rays (EDX, XPS, XRD)
- ✓ E-Microscopy (SEM, TEM)
- ✓ Biochemistry (UV-Vis, IR, SDS-PAGE, AFM)
- ✓ Inert Gas (Ar & N<sub>2</sub>)

### SOFTWARES

- ✓ ChemDraw
- ✓ MestreNova
- ✓ Zotero
- ✓ ImageJ
- ✓ OriginPro
- ✓ HighScore

### EXPERIENCE

10/17-10/21

- **Researcher** • EPFL, Laboratory of Inorganic Synthesis and Catalysis (LSCI), Lausanne  
Development of new inexpensive materials tested as state-of-the-art electrocatalysts  
Deposition of protective oxide coatings increasing the lifetime of batteries  
Implementation of a Li-ion battery lab equipment, maintenance work and establishment of procedures  
Teaching assistant for practical chemistry to 1st year students (Excellence Teaching Award)  
Management of Lab ordering and Inventory (2017-2020). Person of Contact for external relations and communication

08/16

- **Undergraduate Researcher** • EPFL, Laboratory of Organometallic and Medicinal Chemistry, Lausanne  
Verification of previously reported catalytic results  
Production of a summary report and presentation of scientific conclusions

04/16

- **Booth Agent** • Suisse Technology Partners AG, Lausanne  
Active listening and proposition of analytical solutions to Scientific Customers

07-08/14 & 08/15

- **Pilot in SAP Outsourcing** • OxYa France, Issy-Les-Moulineaux  
Monitoring and reactive reporting of issues to administration and customers  
Scrupulous following of escalation procedures

### EDUCATION

10/17 – 10/21

- **EPFL** • Lausanne, Switzerland  
PhD in Electrochemistry and Li-Ion Batteries:  
"Atomic doping and coating for electrocatalysis and Li-ion batteries"

09/16 – 04/17

- **McGill** • Montréal, Québec  
Master Project: "Conjugation of Highly Selective targeting ligands on DNA Nanotubes"

08/15 – 07/16

- **EPFL** • Lausanne, Switzerland  
M. Sc. "Molecular and Biological Chemistry" including two projects

09/14 – 06/15

- **Lunds Universitet** • Lund, Sweden  
B. Sc. "Molecular and Biological Chemistry", 3<sup>rd</sup> Year Exchange Student

09/12 – 07/14

- **EPFL** • Lausanne, Switzerland  
B. Sc. in "Chemistry and Chemical Engineering"

### COMPETENCES

- Project Management
- Scientific Communication
- Teaching/Learning
- Culturally Astute
- Team Building
- Creativity